

UNIVERSITY OF OKLAHOMA

GRADUATE COLLEGE

RELATIONSHIPS BETWEEN MONTHLY AGROCLIMATE VARIABILITY AND
LOCAL CROP YIELD IN THE CENTRAL AND EASTERN UNITED STATES
AND SOUTHERN CANADA

A DISSERTATION

SUBMITTED TO THE GRADUATE FACULTY

in partial fulfillment of the requirements for the

Degree of

DOCTOR OF PHILOSOPHY

By

REED TIMMER
Norman, Oklahoma
2015

RELATIONSHIPS BETWEEN MONTHLY AGROCLIMATE VARIABILITY AND
LOCAL CROP YIELD IN THE CENTRAL AND EASTERN UNITED STATES
AND SOUTHERN CANADA

A DISSERTATION APPROVED FOR THE
SCHOOL OF METEOROLOGY

BY

Dr. Lance Leslie, Chair

Dr. Michael Richman, Co-chair

Dr. Jeffrey Basara

Dr. Renee McPherson

Dr. Frederick Carr

© Copyright by REED TIMMER 2015
All Rights Reserved.

This research and dissertation are dedicated to my late mentor, Dr. Peter Lamb, who passed away last summer. Dr. Lamb was so much more than my graduate research advisor over the last 13 years, and without his wise guidance, advice, and incredible patience, I would not be the scientist (and even storm chaser) I am today. Dr. Lamb did not settle for anything but the absolute best work his students, and while very demanding as an advisor, these high standards force his research assistants to realize what they are truly capable of. Even the 10-hour Saturday exams in Climate Dynamics that seemed so brutal at the time, in hindsight, were attended entirely for that purpose. If you took one of Dr. Lamb's classes you know what I am talking about – I've never devoted so much effort to any other class, and never have had much expected from me as a student.

Working as Dr. Lamb's research assistant extended well beyond growing as a meteorologist, but to succeed his students had to develop a way of life with a deep-rooted work ethic, and belief in your own ability that only he could bring out. He was the professor that the average student complained about so often when they accidentally enrolled in one of his classes, but that was because average was never an acceptable standard for Dr. Lamb. The students that remained at the end of those classes (i.e., Climate Dynamics) were certainly pushed to their limit, but we all realized what we were truly capable of by the end. I knew that if I wanted to be the best meteorologist and researcher I could be, that Dr. Lamb was the perfect advisor to make that happen. While most students hope to graduate from college quickly, I wish that I could have the opportunity to work under Dr. Lamb as his graduate research assistant for yet another decade.

I'll be forever grateful for Dr. Lamb taking the chance on me as a graduate student in 2003, despite having somewhat of a reckless storm chasing reputation at OU. As I slowly got to know Dr. Lamb through working with him on my PhD research and our many side projects, I realized that he was even better person than professor/advisor that will do anything for you once you gain his respect. I wish Dr. Lamb could have seen this completed project in person, as I know he would have been proud to see how far I've come as his student. I'm honored to have known him, and will continue to work my hardest in life and as a meteorologist to finish the work he started as my advisor.

Acknowledgements

I would first like to thank my current advisor Dr. Lance Leslie for the opportunity to defend my Dissertation, despite my first year of graduate school being over 12 years ago. He truly has made my future as a scientist in this field possible by providing the pivotal support and inspiration that was needed to finish this substantial project, which we began with Dr. Lamb in 2006. I also have been very lucky to have participated in every one of Dr. Leslie's courses over the years, and he is responsible for the emergence of my "side interest" in the fluid dynamics of vortices. Lance's computational fluid dynamics course along with our recent project on the measurement of vertical winds inside tornadoes with mobile radar, has given my passion of storm chasing a whole new meaning.

Even less than a year ago, the completion of my PhD still seemed so far away and insurmountable, to the point that I was even questioning whether or not I was still capable. Then, all the doubt vanished after meeting the love of my life and storm chasing partner, my fiancé and meteorologist Maria Molina. Without Maria's help getting back on track with the end of my research and writing of the Dissertation, it might have been another decade before I would get the opportunity to write this Acknowledgements section. She has given me the happiest year of my life, and also the most productive with her unrelenting support, positivity, and a sense of adventure that even exceeds my own. I wish I met her years ago, but am so excited about the future post-graduate school as we continue to grow as people, meteorologists, and chasers. December 26, 2015, our wedding day in Nicaragua, cannot come soon enough!

I'd also like to thank my incredibly patient committee members who I've grown to respect to greatly over the years, with Drs. Richman and Basara guiding my graduate research since the Energy Weather Project in 2003. Even though it was incredibly confusing and complex material at the time, Dr. Richman's multivariate statistics course during my Masters at OU has based the research of every project I've been involved in, from the climatology of Australian Dust to the prediction of tornadoes through my PhD. He made statistics fun and exciting through his unique creative ability to apply that mathematics to interesting, real-world meteorological problems. I also am so grateful to have enjoyed his many side hobbies, such as the cultivation of ornamental cacti and salt water aquarium/fish/corals.

Dr. Basara and I's beginning was much more tumultuous, especially after I wrote a "hot check" for \$2.00 to he and his golfing partner after suffering a meltdown on the 18th hole. His passion for our science has always been infectious, and I realized that immediately on the first day of his Synoptic Meteorology class. His innovative ideas and suggestions for my research all these years definitely took my dissertation to a whole new level. I always had the goal of completing my PhD in as fast as Jeff's record 2 year pace, but I blew by that goal by 5-6 years, unfortunately.

I'd also like to thank Drs. Carr and McPherson, who saved the day by agreeing to serve as my committee members only months ago. Even during that short time, their contribution to this work is so apparent, and I'll be forever grateful for the opportunity they made possible. It seems just like yesterday when I was a freshman at OU, and Dr. Carr the Director of the School of Meteorology pulled me aside in the Map Room and asked about an embarrassing front-page picture in the school newspaper that involved

body paint and an OU basketball game. I've always looked up to both Dr. Carr and McPherson while hoping to follow in their footsteps after graduate school.

Also, I'd like express my deepest of thanks to my few very close friends that have been with me every stop of the way through 17 years of college, storm chasing, and even intercepting tornadoes by armored vehicle. I never could have balanced school and my passion for chasing storms without Dr. Lamb's Administrative Assistant, Luwanda Byrd. There were so many times throughout graduate school, especially during spring storm season, when I found myself multiple states away from Norman with an immediate deadline to submit a critical problem set or paper, and Luwanda would save the day and help me satisfy my obligations. Through years of baling me out of tight situations and our conversations in between meetings with Dr. Lamb, she became a close friend as well.

Thank you especially to my long-time storm chasing partners Dick McGowan and Joel Taylor (and now Maria), who had to drive so many miles between target areas while I sat in the backseat, working on problem sets and studying for exams. Your constant words of encouragement and the countless times you have been there for me when times were rough will never be forgotten.

And finally, the most pivotal of all, I'd like to thank my mom, who helped me realize so early on my passion and even borderline obsession for the sciences. If it weren't for my first bug net and insect book, I never would have collected moths and Scarab Beetles for the next 10 years, and I enjoyed every second of it. My mom helped bring out my deep-rooted curiosity for nature and science, and somehow supported without hesitation every single one of my crazy ideas since childhood (except for the

chasing of Hurricanes since Katrina and a few other extreme cases). My mom was right all along -- She always said that if I do what I love for a living, I would never have to work a day in my life. Because of her, I can honestly say I've lived very close to that ideal through my entire 17 years at the University of Oklahoma. NEVER stop chasing.

Table of Contents

Acknowledgements	iv
List of Tables	xii
List of Figures	xiii
Abstract	xvi
Chapter 1. Introduction	
<i>a. Historical Background</i>	1
<i>b. Previous Pacific Climate System Research Relevant to U.S. Agriculture</i>	6
<i>c. Present Treatment of the Pacific Climate System and Previous Agrometeorological Research</i>	11
<i>d. Present Objectives and Related Agrometeorological Research</i>	18
Chapter 2. Analysis of Pacific Ocean Sea Surface Temperature Patterns	
<i>a. Background</i>	24
<i>b. Pacific Ocean Sea Surface Temperature (SST) Data Set</i>	26
<i>c. Principal Component Analysis</i>	27
<i>d. Characteristic Pacific Ocean SST Anomaly Patterns</i>	32
Chapter 3. North American Growing Season Agroclimate Variables	
<i>a. Expert Opinion Background</i>	43
<i>b. Climate Data Sets</i>	47
<i>c. Growing Degree Days (GDD)</i>	49
<i>d. Precipitation</i>	55
<i>e. Palmer Drought Index (PDI)</i>	
(i) Concept of Drought	57

(ii) Development of Palmer Drought Indices	58
(iii) Present Application of Palmer Drought Index (PDI)	66
<i>f. Extreme Mid-Summer Heat</i>	70
<i>g. Agroclimate Teleconnections with Pacific Ocean SST Patterns</i>	72
Chapter 4. Monthly Growing Degree Day (GDD) Teleconnections	
<i>a. Background</i>	74
<i>b. Methodology</i>	75
<i>c. Mature ENSO</i>	78
<i>d. Decaying ENSO</i>	90
<i>e. Pacific Decadal Oscillation (PDO)</i>	97
<i>f. North Pacific Oscillation (NPO)</i>	103
<i>g. Summary</i>	109
Chapter 5. Monthly Precipitation Teleconnections	
<i>a. Background</i>	115
<i>b. Methodology</i>	116
<i>c. Mature ENSO</i>	117
<i>d. Decaying ENSO</i>	129
<i>e. Pacific Decadal Oscillation (PDO)</i>	145
<i>f. North Pacific Oscillation</i>	160
<i>g. Summary</i>	166
Chapter 6. Monthly Palmer Drought Index (PDI) Teleconnections	
<i>a. Background</i>	179
<i>b. Methodology</i>	181

<i>c. Mature ENSO</i>	182
<i>d. Pacific Decadal Oscillation</i>	187
<i>e. North Pacific Oscillation</i>	193
<i>f. Summary</i>	197
Chapter 7. Local Crop Yield Impacts from Agroclimate Extremes	
<i>a. Background</i>	200
<i>b. AAPEX Farm Specifics and Local Crop Yield Histories</i>	208
<i>c. Agroclimate and Local Crop Yield Co-variability</i>	218
<i>d. Crop Yield Impacts from Agroclimate Extremes</i>	224
Chapter 8. Predictability and Conclusions	
<i>a. Local Predictability of Agroclimate Extremes</i>	236
<i>b. Key Results and Suggested Future Work</i>	239
References	248
Appendix	
<i>a. AAPEX Crop Significance in U.S. and Canadian Agriculture</i>	261
<i>b. Focus Crop Physiological Adaptations to Prevailing Agroclimate</i>	266
i. Soybeans	267
ii. Feed Corn	273
iii. Upland Cotton	278
iv. Cereal Grains (Spring Wheat and Grain Sorghum)	284
<i>c. AAPEX Farm Growing Region Summaries</i>	
i. AAPEX Farmer #1, Soybeans, Southern Ontario	291

ii. AAPEX Farmer #2, Feed Corn, Southern Minnesota 292

iii. AAPEX Farmer #3, Upland Cotton, Southern Texas and
North Carolina 293

iv. AAPEX Farmer #4, Grain Sorghum, Texas Panhandle296

v. AAPEX Farmer #5, Spring Wheat, Central Montana297

List of Tables

Table 1. Optimum number of UPCs retained and rotated	32
Table 2. AAPEX farm and focus crop information	44
Table 3. Palmer Drought Index ranges for each moisture	63
Table 4. Critical temperature thresholds above which	71
Table 5. Typical date ranges for critical farming phases	211
Table 6. Brief descriptions of weather-sensitive phenomena	212
Table 7. Annual crop yield and production averages	214
Table 8. Correlations between monthly and total growing	223
Table 9. Typical data ranges for critical farming phases	236
Table 10. Pacific Ocean SST mode and growing season	242
Table 11. Critical soybean growth phases and number of days	269
Table 12. Critical corn growth phases and number of days	276
Table 13. Critical upland cotton growth phases and number of	281
Table 14. Critical spring wheat growth phases and number	286
Table 15. Critical grain sorghum growth phases and number	288

List of Figures

Figure 1.	Geographical locations of the commercial farms	19
Figure 2.	January-March SST VPC loading patterns	31
Figure 3.	Pacific Ocean SST anomaly patterns extracted	33
Figure 4.	Same as figure 3 but for 3-month SST periods	34
Figure 5.	Geographical distribution of the primary stations	48
Figure 6.	Long-term mean (1949-2000) growing	51
Figure 7.	Examples of monthly PDI patterns	68
Figure 8.	Monthly spring (March-June) GDD composite	79
Figure 9.	Same as for figure 8 except for 3-month	80
Figure 10.	Same as for figure 8 except for mid-summer	85
Figure 11.	Same as for figure 8 except for late summer-to-fall	87
Figure 12.	Same as for figure 8 except for late summer-to-fall	88
Figure 13.	Monthly summer (June-August) GDD composite	92
Figure 14.	Same as for figure 13 except for monthly	93
Figure 15.	Same as for figure 13 except for 6-month	96
Figure 16.	Monthly spring-to-summer (April-August) GDD	98
Figure 17.	Same as for figure 16 except for monthly	99
Figure 18.	Same as for figure 16 except for monthly	101
Figure 19.	Same as for figure 16 except for monthly	102
Figure 20.	Monthly spring-to-summer (April-August)	104
Figure 21.	Same as for figure 20 except for monthly	105

Figure 22.	Same as for figure 20 except for monthly	108
Figure 23.	Generalization of the main GDD composite	114
Figure 24.	Monthly spring (March-April) precipitation	118
Figure 25.	Same as figure 24 except for 3-month	119
Figure 26.	Same as figure 24 except for monthly	125
Figure 27.	Monthly spring (March-May) precipitation	130
Figure 28.	Same as for figure 27 except for mid-summer	135
Figure 29.	Same as for figure 27 except for September	142
Figure 30.	Monthly spring-to-summer (April-July) precipitation	149
Figure 31.	Same as for figure 30 except for monthly	152
Figure 32.	Same as for figure 30 except for monthly	157
Figure 33.	Monthly spring-to-summer (March-July)	163
Figure 34.	Same as for figure 33 except for monthly	165
Figure 35.	Generalization of the main precipitation	175
Figure 36.	March-October monthly composite PDI	184
Figure 37.	March-October monthly composite PDI	185
Figure 38.	April-September monthly composite PDI	188
Figure 39.	April-September monthly composite PDI	189
Figure 40.	April-September monthly composite PDI	191
Figure 41.	April-September monthly composite PDI	192
Figure 42.	April-October monthly composite PDI	195
Figure 43.	April-October monthly composite PDI	196
Figure 44.	Flow chart of the meteorological and non-meteorological	201

Figure 45.	Geographical locations of the six AAPEX	209
Figure 46.	Annual raw (left) and de-trended (right) county	216
Figure 47.	Growing season GDD and precipitation anomalies	220
Figure 48.	Raw and average crop yield residuals for the ten highest	225
Figure 49.	Raw and average crop yield residuals for the ten highest	228
Figure 50.	Raw and average crop yield residuals for the ten highest	231
Figure 51.	Raw and average crop yield residuals for the 15 highest	233

Abstract

Short-term agroclimate is defined here as the monthly-to-seasonal meteorological, geological, biological, and psychological factors that modulate local and regional crop yield. Modern agricultural production in the central and eastern United States and southern Canada accounts for a vast majority of the global food supply as the leading producer annually for corn (~80%), soybeans (~50%) and the cereal grains (> 20%), since the new millennium (U.S. Grains Council, 2010; American Soybeans Association, 2014; EPA, 2014). Hence, the worldwide socioeconomic significance of study region (Fig. 1) crop production in the midst of ruthless monthly-to-seasonal agroclimate variability is ever increasing, and especially the mitigation of crop yield losses from growing season climate extremes such as heat waves and severe agricultural droughts and pluvials. The recently infamous Droughts of 1988 and 2012-14 are the two most costly natural disasters in U.S. history ahead of even Hurricane Katrina (2005) and Super Storm Sandy (2012), followed shortly by the agriculturally devastating Flood of 1993 in the Upper Mississippi River Basin, and show the enhanced sensitivity of modern farming to short-term agroclimate extremes.

The present study represents the meteorological aspects of locally and regionally impactful agroclimate variability with growing season (March-October) monthly growing degree day (GDD) totals, precipitation anomalies, the Palmer Drought Indices (PDI), and midsummer extreme heat above crop-specific pollen sterilization thresholds; as based on the recently extended Lamb-Richman daily temperature and precipitation data sets for eastern North America (Skinner et al., 1999; Timmer and Lamb, 2007), and

NCDC's monthly PDI data by U.S. Climate Division (Karl et al., 1986; Heddinhaus and Sabol, 1991; NCDC, 2014). Five managers of large commercial farms across North America and prominent members of the Association of Agricultural Production Executives (AAPEX) provided expert opinion input on the relative severity of these agroclimate extremes from planting through harvest at six widely separated farming locations, cultivating five different focus crops (corn, soybeans, cotton, sorghum, spring wheat). These six AAPEX farming locations base the present study's exhaustive analyses of local crop yield-agroclimate relationships, motivated to identify periods within the growing season when monthly extremes in GDD, precipitation, PDI, and temperature during flowering are most impactful.

The local and regional predictability of growing season (March-October) monthly extremes in GDD, precipitation, and PDI across the central/eastern U.S. and southern Canada are assessed via time-lagged teleconnections with 3- and 6-month modes of Pacific Ocean SST variability. Several strong monthly-to-seasonal teleconnection patterns were identified for these agroclimate extremes with not only mature and transitional El Niño/La Niña patterns, but also the cold and warm phases of the Pacific Decadal Oscillation (PDO) and North Pacific Oscillation (NPO) as uniquely clarified with present treatment of Varimax-rotated Principal Component Analysis (PCA). The most prominent teleconnections include the ENSO Spring GDD ("ESG") and ENSO Spring Precipitation ("ESP") anomaly patterns, especially with winter-spring 3-month mature El Niño modes and the corresponding wetness (monthly precipitation anomalies > 1.25 inches) and anomalously low GDD composite totals across the Great Plains Region and southern U.S (GDD < -30); as well as large-scale moderate to severe

agricultural drought indicated throughout the study region associated with preceding or concurrent cold-phase PDO.

Overall, the most impactful (both detrimental and beneficial) aspects of growing season agroclimate variability at the six AAPEX farming locations are summer (June-August) GDD monthly anomalies for all crops and spring (March-April) GDD for South Texas cotton yields; midsummer (June-July) monthly PDI for central Montana spring wheat; and the monthly totals of days with daily mean temperatures above highly-specific pollen sterilization thresholds for all focus crops except for southern Ontario soybeans. Each of these specific growing season extremes in agroclimate show predictability using particularly the mature ENSO and PDO modes of January-March and March-May Pacific Ocean SST variability.

Chapter 1. Introduction

a. Historical Background

Weather and climate extremes have been hardships for North American farmers since the beginning of recorded history, with severe drought, heat waves, and floods having catastrophic impacts on small subsistence farms to whole societies. Even as far back as A.D. 800, archaeological surveys have revealed primitive irrigation systems designed by the ancient Pueblo Tribes of the Southwest U.S. to control flooding and cope with periods of dryness (Neely, 1997; Doolittle and Neely, 1998; Doolittle, 2000). However, prior to the advent of modern large-scale irrigation practices and other farming technologies, agrarian societies such as the Pueblo were largely at the mercy of short- and long-term regional climate variations. Historical records, supported by tree ring climate data, indicate that several severe, multi-year droughts nearly led to the demise of the entire ancient Pueblo civilization, including the “Great Pueblo Drought” of 1276-1299 and the six year drought and famine of 1666-1671 (Johnson, 1996, 2008; Encyclopedia Britannica, 2009).

Following the United States Civil War, awareness of the impacts of extreme weather and climate on agriculture in the U.S. increased substantially after President Ulysses S. Grant passed a resolution on February 9, 1870, for the creation of a new service in the War Department called the United States Weather Bureau dedicated to taking meteorological observations (Heddinghaus and Le Comte, 1992). This resolution was initiated after a series of intense storms had caused substantial damage and loss of life in the Great Lakes shipping industry in the late 1860s, and also resulted in a long-term publication called the *Weekly Weather Chronicle*, which reported weekly

weather and climate summaries that substantially benefited United States farmers for decades (Heddinghaus and Le Comte, 1992).

Given their relevance to agriculture interests, assessments of national crop and livestock conditions later were added to the weekly weather and climate summaries, and the title was changed to the *Weekly Weather and Crop Bulletin* in 1887. By this time, substantial resources also were being provided for the large-scale implementation of a network of weather observers, instruments, and telegraph lines for communication. Still in circulation today, the existence of the *Weekly Weather and Crop Bulletin* permitted objective documentation of the most anthropogenically significant droughts in modern American History, beginning with the severe drought from the late 1880s into the early 1890s that initially hampered agricultural expansion over the Great Plains after the Civil War (Woodhouse and Overpeck, 1998).

Climate extremes have not always been detrimental to early U.S. agriculture, however, as a 13-year pluvial period prevailed across much of the Central and Eastern U.S. during 1905-1917 with very favorable conditions for farming, which facilitated an agricultural boom in the Great Plains Region (Fye et al., 2004). This agricultural boom led to extensive farming that destroyed native prairie grasses before the time of erosion control, which set the stage for one of the worst natural disasters in U.S. history, the Dust Bowl. Severe drought conditions plagued the Great Plains from 1929 to as late as 1940 during the Dust Bowl, forcing hundreds of thousands of people to evacuate their homes with millions of acres of farmland destroyed (Ludlum, 1971; Fye et al., 2004; Andreadis, 2005). A little over a decade later, another historic drought gripped the nation from the Rocky Mountains to the Appalachians during 1952-56, causing

agricultural production over the Great Plains to drop by as much as 50%, with most of the region declared as federal disaster areas (Ludlum, 1971; NOAA, 2003; Fye et al., 2004).

Thus, during the first half of the 20th century, prior to the appearance of large-scale irrigation in the U.S., farmers did not have the technology to cope with extended periods of dryness. Because of this technological inadequacy, the benefit of accurate seasonal-to-decadal climate forecasts to American farmers would have been limited during these early times, with a timely prediction of the Dust Bowl being little more than a precursor of inevitable crop failure. In contrast, during the recent times of continually improving agricultural technology and especially since the implementation of advanced, large-scale irrigation systems in the Great Plains beginning in the 1950s, farmers are much more capable of dealing with climate extremes (Kucharik and Ramankutty, 2004). Other more recent farming strategies such as advanced fertilization techniques, pest and weed control, and plant breeding have enabled farmers to also take maximum advantage of periods with ideal growing conditions. Given these added options for modern farmers to mitigate climate-related risk, the need for accurate, tailored climate information on the monthly, seasonal, and interannual time-scales has increased dramatically since the time of the Dust Bowl, as this information can more effectively be used to maximize field production, profit margins, and ultimately the food supply.

Despite modern farming technologies and the availability (sometimes) of accurate seasonal-to-interannual climate forecasts, climate extremes still can be devastating to the agriculture sector. The 1988 heatwave and drought and 1993 floods

in the central U.S. are representative examples of modern natural disasters, even though they were of much shorter durations than both the Dust Bowl and 1950s drought. From a financial perspective, the 1988 drought is deemed the worst natural disaster in U.S. history, causing an estimated \$30 billion in agricultural losses with 10,000 deaths attributed to heat stress (Trenberth et al., 1988; Ropelewki, 1988; Trenberth and Branstator, 1992). The flood of 1993, which was focused over the Upper Mississippi River Basin or the heart of the U.S. Corn Belt, resulted in \$15-20 billion in damage as rainfall totals there were the largest of the 20th century for the 2- to 12-month periods encompassing the 1993 summer (Kunkel et al., 1994, 1995). The floods of 1993 show that abundant rainfall is not always a positive development for agriculture, especially given excessive rainfall rates over short periods of time.

The drought of 1988 and the flood of 1993 are examples of climate extremes that even the most advanced farming technologies largely could not overcome, especially in the hardest hit areas. Hence, many farmers seek crop insurance or engage in agriculture futures trading to minimize the financial risk from climate variability and various economic factors, luxuries the farmers of the Dust Bowl did not have. It is important to note that agriculture insurance rate development and regulation of insurance rates are based on historical climate data, and not anticipation of future weather events. Therefore, farmers can optimize their coverage per unit area and for yield guarantees, based on accurate climate information, to reduce risk even further when needed (Fosse and Changnon, 1993). Agriculture futures markets, on the other hand, are more intended to reduce the year-to-year variability in commodity prices

rather than protect against total crop loss, by allowing farmers the option of a predetermined fixed price for their crops at harvest (Parcell and Pierce, 2009).

Since crop prices and production costs are highly dependent on weather and climate, and are impacted particularly by climate extremes such as drought and excessively hot temperatures, predictive information for these extremes acquired prior to the growing season can help farmers tailor the use of futures contracts to further minimize climate-related risk for their crops. Additionally, climate extremes are much more detrimental to year-to-year yields when they coincide with crop growth phases characterized by heightened sensitivities to moisture shortages and extreme heat, such as flowering/pollination and fruit/grain development. Thus, predictive information for growing season climate is much more valuable to farmers when supplemented with crop- and location-specific knowledge on the timing of these critical time windows, as well as the crop yield impacts from different aspects of extreme climate. Given this knowledge, farmers can more effectively manage equipment and labor, as well as the above farming practices employed to minimize the negative impacts on crop yield from extreme agroclimate. The present study provides this information by quantifying the relationships between climate extremes and crop yields at monthly intervals during the growing season, on the local level for different crop varieties and growing climates. Teleconnections between North American agroclimate and Pacific Ocean sea surface temperature (SST) patterns also are investigated because of their predictive potential.

b. Previous Pacific Climate System Research Relevant to U.S. Agriculture

A large part of North American monthly, seasonal, interannual, decadal, and even multi-decadal climate variability now can be at least partially attributed to various modes of Pacific Ocean SST variability. This includes the longer-term extreme moisture regimes of 1900-1960 mentioned above, as well as monthly and seasonal periods of extreme climate.

For the decadal time-scale, Fye et al. (2004) calculated composite Pacific Ocean SST anomaly patterns for the aforementioned pluvial period (1905-1917), the Dust Bowl (1929-1940), and the extended post-World War II drought (1946-1956). Their findings showed that both dry periods were associated with La Niña conditions in the Tropical Pacific Ocean, as well as the presence of a cool-phase of the Pacific Decadal Oscillation (PDO, Barlow et al., 2001). The pluvial period of the early 1900s, on the other hand, was accompanied by a consistent El Niño pattern that would have favored an enhanced Subtropical Jet Stream into the western U.S., a warm-phase of the PDO, as well as cold SSTs across the central North Pacific (negative North Pacific Oscillation, NPO, Barlow et al., 2001; Fye et al., 2004). This linkage for three of the most agriculturally-significant climate regimes in recorded U.S. history, as demonstrated by Fye et al. (2004), was part of the motivation for using the Pacific Climate System as a starting point and framework for the North American agrometeorological analyses performed in the present study.

For the monthly-to-seasonal time-scale, both the 1988 drought and the 1993 floods in the central U.S. also have been linked to Pacific Ocean SST patterns in previous research (Ropelewski, 1988; Trenberth et al., 1988; Trenberth and Branstator,

1992; Kunkel et al., 1995; Trenberth and Guillemot, 1996; Ting and Wang, 1997; Bates et al., 2001). Specifically, each of these studies discusses how the development of the 1988 drought (1993 flood) in the Central U.S. in spring coincided with the emergence a strong La Niña (moderate El Niño). However, Trenberth et al. (1988) emphasized how the 1988 drought was a unique case, because positive SST anomalies just southeast of Hawaii played a pivotal role in the development and maintenance of the massive anticyclone over the western U.S., in addition to the role played by cold La Niña waters that emerged in the eastern tropical Pacific that March. These contrasting SST anomalies enhanced further the meridional SST gradient from the tropics through the subtropics that contributed to the blocking pattern downstream.

Despite the observed associations of these infamous 1988 and 1993 periods of extreme warm-season climate in the U.S. Heartland with (respectively) strong/unique La Niña and El Niño events that peaked during the preceding winter-spring, Livezey et al. (1997) disagreed with this theorized causal relationship between Pacific SST anomaly patterns in the tropics and North American climate, especially for the following warm season. However, Livezey focused solely on ENSO phases identified by SST anomalies in the central Tropical Pacific for assessing warm season climate teleconnections over North America. In contrast, Trenberth (1988) argued that subtle differences in the location, strength, timing, and sign of the tropical and subtropical SST anomaly regions comprising strong winter-spring La Niña/El Niño conditions can have profound impacts on the "downstream" warm season teleconnections. These demonstrated complexities and subtleties in the associations between tropical and extratropical SST anomalies for two of the most impactful seasons of extreme climate

in modern U.S. history motivated the separate treatment here of ENSO-related SST variability patterns focused in the central and eastern Tropical Pacific. This approach included assessing how differences in time evolution of these patterns from winter through summer affects North American climate during the subsequent growing season.

Not only is North American climate influenced by SST anomaly patterns in the tropical Pacific, but extratropical SST anomaly patterns in the North Pacific Ocean also can induce atmospheric anomalies over North America during both winter and summer. Since North America is located downstream of the North Pacific Ocean relative to the prevailing westerlies, some of the most robust atmosphere-ocean teleconnections outside of the tropics affect North America (Horel and Wallace, 1981; Hoskins and Karoly, 1981; Wallace and Gutzler, 1981; Namias et al., 1988). Horel and Wallace (1981) showed that the proximity of the Polar Front Jet Stream to SST anomalies in the tropical Pacific is key for downstream Rossby Wave development and propagation into mid-latitudes, hence contributing to stronger winter than summer teleconnections for El Niño and La Niña. Therefore, as the Polar Front Jet Stream migrates north to high latitudes during summer, SST anomalies in the extratropics become increasingly important compared to the tropical Pacific for the development of teleconnections in North American warm-season climate. Accordingly, Wallace and Gutzler (1981) identified robust warm season teleconnections in geopotential height and mean sea level pressure between North America and the subtropical Pacific Ocean, and Namias et al. (1976, 1988) showed teleconnections of similar robustness for the higher latitudes of the North Pacific. Hence, the present study focuses on SST variability in both the tropical and extratropical North Pacific Ocean.

The many modes of North Pacific SST variability evolve relatively slowly (months to years) given the very large size of the Pacific Ocean, especially in the tropics where individual El Niño/La Niña events typically last over a year (Rasmusson and Carpenter, 1981). Namias et al. (1988) indicated that extratropical North Pacific SST patterns also can have impressive persistence of several months, contributing to the robust and coherent teleconnections with North American climate extending into the warm season, intensified further by the co-location of the extreme northern Pacific SST anomalies and upper-level flow patterns at this point in the seasonal cycle (Oakley and Redmond, 2014; Yeh et al., 2015). Thus, given this SST pattern persistence in both the tropics and extratropics, observed and expected Pacific SST anomalies can be an invaluable tool in developing predictive climate information on monthly to decadal time-scales for the North American summer growing season.

This relationship of monthly and seasonal North American climate variability to the Pacific Ocean Climate System has been well documented in many previous studies, a majority of which focused on the more coherent and pronounced winter teleconnections and emphasized tropical Pacific forcing (Ropelewski and Halpert, 1986; Mantua et al., 1997; Gershunov and Barnett, 1998; Goodrich, 2004). A majority of the relatively few investigations involving warm-season North American climate teleconnections with the Pacific Climate System also focus primarily on El Niño/La Niña (Bunkers et al., 1996; Montroy et al., 1998; Hu and Feng, 2001; Smith et al., 2007; Zhang et al., 2011; Gilford et al., 2013) and ignore Pacific Ocean SST variability in the northern extratropics. However, Ting and Wang (1997), Barlow et al. (2001), and DeFlorio et al. (2013) included both the tropical and extratropical North Pacific Ocean

when extracting patterns of SST variability and relating them to North American warm-season (June-August) climate. They found that the strongest teleconnections were with the PDO and NPO, especially for July-August precipitation in the Central U.S. These stronger extratropical, warm-season North Pacific SST associations, compared with Tropical Pacific SST variability such as El Niño/La Niña, were suggested to result from the distinctive maturation and persistence of PDO and NPO SST anomalies during summer (Barlow et al., 2001). In contrast, El Niño/La Niña events typically mature during Northern Hemisphere winter (Rasmusson and Carpenter, 1982).

Each of the above studies involving warm-season teleconnections (e.g., Bunkers et al., 1996; Ting and Wang, 1997; Montroy et al., 1998; Barlow et al., 2001; Hu and Feng, 2001) explored only concurrent or short-lag (1-2 month) associations. However, this contemporary focus not only eliminates the ability to extract lagged relationships of sufficient lead-time to be useful to farmers, but also fails to reflect the intraseasonal evolution of the SST patterns, and thus their impact on North American climate. This inadequacy limits farmers' ability to make critical, climate-sensitive decisions months before the impacts of climate are realized, actions that are needed to optimize their farming strategies and mitigate the negative impacts from extreme climate (Meza et al., 2008).

Hill et al. (2000) is one of the few studies that treat the temporal evolution of Pacific SST patterns and resulting impacts on North American climate and agriculture (winter and spring wheat), but the Southern Oscillation Index (SOI) phase is the only aspect of the Pacific Climate System considered. This was accomplished not only by considering the concurrent and immediately preceding SOI value, but also the month-

to-month SOI trend (consistently negative, consistently positive, rapidly falling, rapidly rising, near zero). Notably, Hill et al. (2000) determined that this five-phase system involving the recent SOI trend was much more valuable than the raw SOI for many winter and spring wheat producers from the U.S. Southern Great Plains to the Canadian Prairies. Strong relationships between the SOI/El Niño SSTs and agricultural production extend well beyond North America, as identified in Nicholls (1986) and Cane et al. (1994) for northeast Australia sorghum and Zimbabwe maize, respectively. These studies also identified the effectiveness of using SOI values and eastern Tropical Pacific SSTs preceding the growing seasons of these crops, respectively, to predict year-to-year crop yield. Thus, the time evolution of Pacific Ocean SST patterns, but for the entire basin, and their lagged teleconnections with warm season North American climate is a focus of the present study, the rationale for which is developed further in the next section.

c. Present Treatment of the Pacific Climate System and Previous Agrometeorological Research

Motivated by the more comprehensive analyses of the Pacific Climate System by Ting and Wang (1997) and Barlow et al. (2001), the present study explores all major tropical and extratropical modes of Pacific Ocean SST variability for teleconnections with agroclimate in representative locations in the U.S. east of the Rocky Mountains and southern Ontario. These modes are derived using rotated Principal Component Analysis (PCA) of monthly Pacific Ocean SST data between 20°S and 60°N for six 3- and 6-month time periods extending from late boreal fall through the following boreal summer (preceding and concurrent with the North American growing season) --

November-April, April-September, January-June, January-March, March-May, and June-August. This treatment of Pacific Ocean SST variability was employed to capture the seasonal temporal and spatial evolution of the predominant SST modes and to extract concurrent and lagged teleconnections of sufficient lead-time so farmers can adapt their production strategies to reduce climate-related risk and maximize yields. The Pacific SST patterns used in this study represent El Niño/La Niña, PDO, and NPO, and their teleconnections with North American agroclimate are quantified from the regional level down to the farm-scale. This approach supplements in several ways the previous agrometeorological research outlined below.

A vast majority of previous research exploring the associations between North American agriculture and Pacific Ocean SST patterns has two characteristics. First, it focuses primarily on the El Niño-Southern Oscillation phenomenon (e.g., Solow et al., 1998; Hill et al., 1999, 2000; Mavromatis et al., 2002; Mauget and Ko, 2008), with other modes of SST variability such as the PDO and NPO largely being ignored despite their demonstrated strong teleconnections with warm-season North American climate (e.g., Namias et al., 1988; Ting and Wang, 1997; Barlow et al., 2001). Second, most previous agrometeorological research also involves the impacts of extreme climate on North American agricultural production at only the regional or national levels (e.g. Richman and Easterling, 1988; Solow et al., 1998; Hill et al., 2000; Heim et al., 2003; Mauget and Ko, 2008). However, studies tailored to the local and farm-scale levels -- such as Mjelde et al. (1993), Hill et al. (1999), and Mavromatis et al. (2002) -- supplement the above regional and national agrometeorological studies in two important ways. They provide both a better understanding of the crop-specific impacts (e.g.,

identify climate-sensitive crop growth phases and quantify yield impacts) of large-scale extreme climate on regional and national agriculture, and also furnish local climate information that can be directly useful for individual farmers and specific crops.

Specifically, Mavromatis et al. (2002) explored the relationships between ENSO and peanut yields for four farming locations in northern Florida and southern Georgia, and discovered that peanut production can be increased by up to 8% by planting crops later during El Niño events and earlier during La Niñas. Hill et al. (1999) similarly showed that Texas sorghum farmers could substantially increase field production by adapting farming strategies (e.g., planting date, applied Nitrogen fertilizer) based on knowledge of SO phase. Mjelde et al. (1993) calculated expected economic values for east-central Illinois corn production ($\$ \text{ acre}^{-1}$) using a dynamic programming model for five different seasonal climate forecast scenarios (ranging from “very good” to “very poor”). The greatest potential economic value achieved was for high forecast quality of “poor” extreme climate conditions that negatively impact crop yields, rather than for high forecast quality of “good” climate conditions. These studies quantified the impacts of local growing season climate on field production using crop yield simulation and decision-making models (Lamb et al., 2011), and provide substantial insight into how local farmers can optimize their farming strategies based on climate information to maximize crop yields. Research of this type can help bridge the aforementioned gap between the above regional/national agrometeorological research and the operations of North American farmers, and provide motivation to more comprehensively quantify the effects of extreme seasonal climate on local crop production.

The value of short-term climate information/predictions tailored for the North American farmer is maximized only when combined with a comprehensive understanding of the specific agricultural impacts from regional climate variability, as well as the ability to adjust farm management decisions based on this information to effectively modulate these agronomic impacts (Lamb, 1981; Sonka and Lamb, 1987; Lamb et al., 2011). This importance of a comprehensive and interdisciplinary approach in developing seasonal climate prediction schemes, and the resulting enhancement of this societal value for climate-impacted sectors such as agriculture and energy, motivated the development of a 3-step framework in Lamb (1981) that has since been employed in a number of applied climate studies, including in the regional agroclimate analyses of the present study (Sonka et al., 1982; Sonka and Lamb, 1987; Hansen et al., 2002; Lamb et al., 2011). These interdisciplinary principles outlined in Lamb (1981)'s 3-step framework encouraged the present study's substantial focus on expert opinion input from several commercial farmers that are each experts and highly successful in their field.

To focus and maximize the utility of agrometeorological studies for the end user, it is essential to obtain feedback from farmers whose livelihoods are directly impacted by extreme seasonal climate. A promising example is the "expert systems" method described in Richman and Easterling (1988), where nine corn crop-weather experts were interviewed intensively to identify which corn production management practices and phenological growth stages were most sensitive to moisture availability and heat stress. From this expert systems process, Richman and Easterling (1988) identified climate conditions that negatively impact Midwest corn yields during four

phases of the growing season. These four climate conditions/phases were: (i) dry and/or warm preceding winters (resulting in inadequate soil moisture recharge); (ii) wet and cold mid-to-late springs (causing delayed field preparation and planting, accelerated nitrogen loss, impeded vertical root system development, and increased soil compaction); (iii) dry or hot mid-to-late summers (associated with soil moisture deficiencies and pollen sterilization); and (iv) wet and/or cold falls (resulting in harvest delays/field losses and increased likelihood of early freezes).

The development phases of most crops -- germination, initial growth, maturation, flowering, reproduction, harvest -- each respond very differently to extreme weather and climate. Two climate variables generally important for maturation of all crops are soil moisture, which is supplied by precipitation and/or irrigation, and surface air temperature, since extreme high temperatures during summer often are associated with soil moisture deficiencies and drought. Hot temperatures during mid-summer also sterilize pollen during crop flowering and hamper the plant reproduction process (Richman and Easterling, 1988). In fact, the timing of nearly all of the above crop maturation phases from germination to harvest are dependent on the seasonally evolving air temperature, as plants grow in a stepwise manner proportional to accumulated heat (Griffin and Honeycutt, 2000; Cox, 2006). Thus, seasonal climate prediction information on not only extreme temperature and soil moisture, but also the likelihood of more moderate temperature ranges that modulate crop maturation rates, can be of substantial benefit for farmers seeking to both limit climate-related risk and take full advantage of ideal growing conditions.

Despite the close relationship between temperature and nearly all crop maturation phases, much agrometeorological research has involved soil moisture climatology, especially for drought and extreme wetness, and its impact on local to national agricultural production (e.g., Richman and Easterling, 1988; Isard and Easterling, 1989; Heim et al., 2003). Heim et al. (2003) focused on the relationship between soil moisture and corn and soybean production on the national level, by developing the Moisture Stress Index (MSI). The MSI was developed to quantify the impacts on U.S. agricultural production from periods of extreme drought and wetness occurring in different growing regions. It is based on a traditional measure of agricultural drought and wetness termed the Palmer Z Index ($Z \leq -2$ for catastrophic drought to $Z \geq +5$ for extreme wetness; Palmer, 1965). The relative effects of regional soil moisture anomalies on national agricultural yield then are assessed using Climate Division MSI values weighted by 10-year mean crop production. Correlations as large as -0.78 and -0.73 were obtained for national corn and soybean production, respectively, for the 1970-2000 period using the July-August MSI, which is consistent with the aforementioned importance of soil moisture during the mid-summer reproductive period of both these crops (Heim et al., 2003). While the national focus of Heim et al. (2003) is useful for the overall U.S. agribusiness sector, it does not provide information on the vital local-to-regional climate-crop yield relationships that can be used by farmers to adjust crop- and location-specific farm management practices to maximize crop yields.

Consistent with this need, Richman and Easterling (1988) and Isard and Easterling (1989) focused on local and regional corn agroclimate in Illinois, with the sole motivation of developing climate information useful to local farmers there.

Specifically, these studies quantified the relationships between different measures of soil moisture on local to regional crop production in the U.S. Corn Belt (mainly Illinois). Richman and Easterling (1988) used a very innovative multivariate statistical technique, Procrustes Target Analysis (PTA), to develop precipitation-based indices that showed significant correlations with corn yield down to the county level. For example, they obtained correlation magnitudes as high as 0.75 with Carroll County, Illinois, de-trended corn yield for the 1966-1980 period. Isard and Easterling (1989) developed a simple linear regression model that also incorporated the Palmer Drought Index (PDI) -- indicative of its wide use to measure agricultural drought/wetness in climate research and in the agribusiness sector -- to quantify the relationship between monthly-seasonal soil moisture anomalies and U.S. crop yield. Significant correlations (up to +0.60) with corn yield were found for the 1960-1983 period at the regional level for northern, central, and southern Illinois, which reflected particularly the coincidence of PDI with the above climate-sensitive crop stages.

While soil moisture and extreme summer temperatures thus have been shown to significantly impact crop production, Growing Degree Days (GDDs) are a measure of seasonal temperature (non-extreme) persistence intended to predict the timing of important crop maturation phases. However, GDDs have been under-utilized in previous agrometeorological research. GDDs are similar to the heating and cooling degree days (HDDs and CDDs) used in energy-climate analyses (e.g., Timmer and Lamb, 2007), but the base temperature for the accumulated totals is tailored to predict the timing of important crop maturation phases. The basic assumption behind GDDs is that appreciable plant growth does not occur below the base temperature (10°C

commonly is used for most crop varieties) or above 30°C, but within this range plant growth rates are linearly related to mean temperature (Cox, 2006). Accordingly, GDDs represent accumulations of daily mean air temperature within this range over a desired time period (monthly to growing season totals in the present study), with daily mean temperatures above (below) this range set to 30°C (10°C) removed before computing the GDD totals. Thus, higher (lower) GDD totals for a given period mean faster (slower) crop growth rates, and so farmers could use season-to-date and seasonal GDD prediction information to anticipate the timing of plant emergence, flowering, and harvest, which is important for more efficient use of farming resources. GDDs also have several other farming strategy applications, such as for fertilizer and insecticide application, since nitrification and mineralization of fertilizer and insect growth are also functions of accumulated heat (Griffin and Honeycutt, 2000).

Surprisingly, meteorological literature exploring the climatology of GDDs is mainly limited to long-term climate change (e.g. Bonsal et al., 2001) and biases associated with daily temperature recording times in the U.S. (e.g., Schaal and Dale, 1977; Byrd, 1985). Research on the relationships between GDDs and crop production on local to national scales is lacking substantially, and studies involving their teleconnections with Pacific Ocean SST patterns are non-existent. This situation prompted inclusion of GDDs in the agrometeorological analyses performed here.

d. Present Objectives and Related Agrometeorological Research

Motivated by the expert systems method Richman and Easterling (1988) applied to Midwest corn farmers, the present study was initiated with input from five

commercial farmer members of the Association of Agriculture Production Executives (AAPEX; www.AssociationofAgriculturalProductionExecutives.org). AAPEX is a program founded in 1994 by Dr. Danny Klinefelter, currently a professor and extension economist in the Department of Agricultural Economics at Texas A&M University, to facilitate education and networking opportunities for commercial farming executives. AAPEX currently has 400 forward-thinking, entrepreneurial, and proactive members who operate large commercial farms scattered across the U.S. and southern Canada, as well as the predominant agricultural countries of Central and South America (e.g., Mexico, Argentina, and Brazil). These members have a strong willingness to participate in interdisciplinary agrometeorological studies such as the present, to help reduce their climate-related risk.

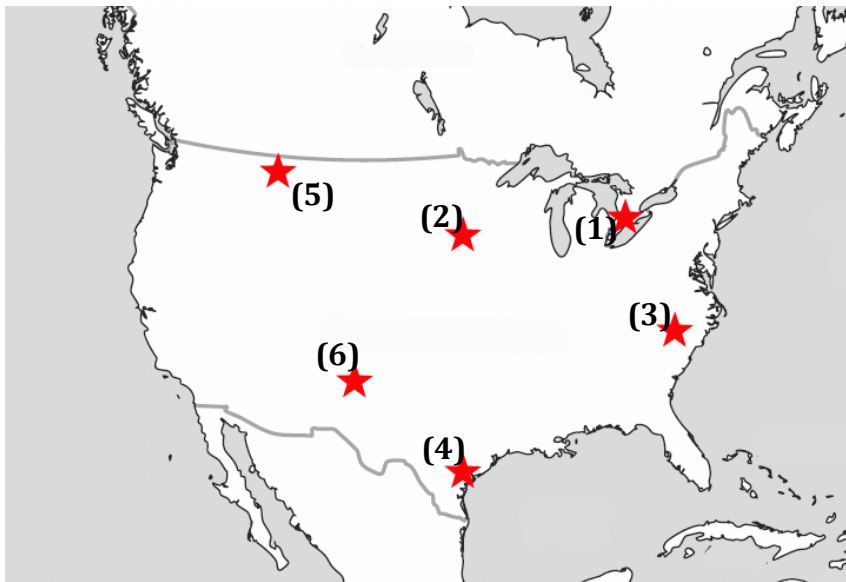


Figure 1. Geographical locations of the commercial farms operated by the five AAPEX members that are included in the present study: (1) AAPEX Farmer #1, Middlesex Co., ON; (2) Farmer #2, Blue Earth Co., MN; (3) Farmer #3, Robeson Co., NC; (4) Farmer #3, Nueces Co., TX; (5) Farmer #4, Liberty Co., MT; (6) Farmer #5, Dallam Co., TX.

While the expert systems method of Richman and Easterling (1988) was limited to Midwest corn farmers, the present study began with interviews of five AAPEX members with farming locations scattered across the U.S. east of the Rocky Mountains and southern Canada (north-central Montana, south-central Minnesota, southern Ontario, southern North Carolina, South Texas, and the Texas Panhandle, Fig. 1). The principal crops of those farms are quite diverse, including soybeans, corn, cotton, spring wheat, and grain sorghum. These AAPEX farmers communicated vital information on the specific climate extremes that negatively and positively impact their crops, the current farming strategies they use to reduce climate-related risk on crop production, and the time windows during their growing seasons that are most weather sensitive. Since climate extremes impact farmers very differently depending on their specific location and crops, this feedback helped to focus the more comprehensive regional to farm-scale agrometeorological analyses of the present study, which broadened the more limited scope of previous research in that area.

The present study builds on the contributions of Richman and Easterling (1988) and Isard and Easterling (1989), who demonstrated strong relationships between Midwest corn production and soil moisture-related climate variables (Palmer Z Index and precipitation) and extreme hot temperatures during mid-summer flowering. Here, we quantify the relative impacts of these agroclimate variables on the range of crops (soybeans, corn, cotton, wheat, and sorghum) at the varied AAPEX farming locations considered (Fig. 1). Motivated by the strong relationships between GDDs and the timing of important crop maturation phases shown in Griffin and Honeycutt (2000) and Cox (2006), and the lack of focus on GDDs in previous agrometeorological research,

the present study quantifies the farm-scale associations between GDDs and crop production for all the above AAPEX farms.

Also assessed in the present farm-scale climate analyses of the present study are the differences and relative importance of soil moisture (Palmer Z Index and precipitation), GDDs, and extreme daily maximum temperatures, as well the exact periods throughout the growing season when these variables have the most significant impact on crop production. These periods are delimited from correlation analyses (March-October) between the above agroclimate variables and de-trended local crop production. Subsequently, the crop yield impacts from monthly extremes during these climate-sensitive growth periods are computed for each AAPEX farming location from historical yield data for the particular focus crop. The impacts of extreme climate also are compared between irrigated and non-irrigated crops for the relevant AAPEX farming locations in the Great Plains, where implementation of large-scale irrigation systems since the 1950s has increased crop production and decreased yield variability dramatically (Kucharik and Ramankutty, 2004).

While most previous agrometeorological studies focus on a single crop and/or region, the inclusion of five diverse commercial farms in the present study allows for comparison of how extreme climate uniquely impacts production for different crops and farming locations. The resulting comprehensive agrometeorological information should be especially useful for the modern commercial farmer, as represented by the five AAPEX members involved in the present study, since they often operate multiple farms separated by vast distances that experience very different prevailing climates. These agricultural executives often share equipment and personnel between their different

farming locations, and thus comprehensive climate information such as developed here can increase the efficiency in managing these multiple commercial farms.

Even though this quantification of local-scale relationships between climate and crop production should help determine the periods during the growing season when extreme climate has the greatest impacts on crop yield, as well as demonstrate the potential importance of agrometeorological research for individual farmers, the usefulness of such information is limited unless periods of relevant extreme climate can be predicted. Accurate prediction of relevant agroclimate would permit farmers to adjust planting dates, fertilizer application, irrigation, management of farming resources, and timing of harvest to reduce the risk posed by extreme climate and maximize the benefit of optimal growing conditions. Thus, the above farm-scale climate information also is investigated for teleconnections with the Pacific Ocean SST patterns described above (El Niño/La Niña, PDO, NPO), the time periods of which are strategically selected to provide at least some predictability of periods of extreme climate for farmers in the U.S. east of the Rocky Mountains and in southern Canada.

Lagged and concurrent teleconnections with Pacific Ocean SST patterns not only are derived for the local climates of the AAPEX farming locations, but they are placed within the context of the larger regional scale (central and eastern U.S. and southern Canada) for GDD and precipitation, which impact farmers more generally in nearly all North American climate regimes for any crop type. Robust and coherent regional teleconnections for warm-season GDD and precipitation are presented for all major modes of Pacific Ocean SST variability. This agroclimate information of larger geographical scope should be useful for the more general pool of North American

farmers. These regional agroclimate teleconnections also help bridge the gap with the more local, farm-scale agroclimate analyses mentioned above.

Several studies have postulated that the effective use of climate information (including seasonal predictions) by the agriculture sector requires predictability, system response, and decision capacity, as well as detailed knowledge of the specific local impacts of climate extremes on crop yield (Lamb, 1981; Hansen et al., 2002; Meza et al. 2008; Lamb et al., 2011). This study is pursued within most of this framework, with emphasis on climatic predictability and system response that are based on teleconnection analyses with Pacific Ocean SST patterns. The goals include bridging the gap between the meteorologist and farmer through extensive farm-scale quantification of local climate-crop yield relationships for a range of crop varieties. The decision capacity aspect is outside the scope of this study, since it depends on the available resources and willingness of the farmers to assume the potential risk associated with inevitable seasonal climate prediction error. The AAPEX farmers considered here utilize the most modern farming equipment and techniques currently available, and thus are ideal candidates to maximize the benefit from the climate information developed in this research.

Chapter 2: Pacific Ocean Sea Surface Temperature Patterns

a. Background

To identify characteristic SST anomaly patterns, Principal Component Analysis (PCA) was performed on seasonal mean Pacific Ocean SST data between 60°N and 20°S for 1949-2005. The PCA was undertaken separately for six 3- and 6-month SST time periods extending from winter through the end of the following growing season (January-March, March-May, June-August, November-April, April-September, January-June). These periods were selected strategically to identify both lagged and concurrent teleconnections with North American agroclimate. For example, advanced knowledge of the lagged associations between winter-spring Pacific SST anomaly patterns and agroclimate extremes during the subsequent growing season could be a valuable tool for farmers seeking to minimize climate-related risk and year-to-year yield variability. The months constituting these 3- and 6-month SST periods thus were selected to extract teleconnections with North American agroclimate before and during critical farming and crop growth time windows – e.g., pre-growing season soil moisture recharge, planting season, crop flowering/reproduction, and fruit/grain development -- for a variety of crop types cultivated in the study region (Fig. 1).

The PCA was performed individually for each of the above 3- and 6-month periods also to capture the time evolution of the extracted Pacific Ocean SST patterns from winter through the growing season. Since the magnitude and location of SST anomaly maxima and minima associated with ENSO, PDO, and NPO have seasonal dependence (Horel and Wallace, 1981; Namias et al., 1988; Ting and Wang, 1997; Barlow et al., 2001), their teleconnections with North American agroclimate also should

be dependent on the seasonal morphology of those SST patterns. While such patterns often persist through multiple seasons and even years once they are established, their development and decay typically transpire over only a few months. Hence, the dominant periodicities of Pacific Ocean SST patterns range from a few months to interannual time-scales, as identified by Rasmusson and Carpenter (1982), Namias et al. (1988), and Chen and Li (2008). Thus, the 3-month periods (January-March, March-May, June-August) are intended to capture the relatively rapid transition phases of ENSO, PDO, and NPO, while the 6-month periods (November-April, April-September, January-June) provide information on the persistence of these patterns from winter through the growing season. For example, El Niño (La Niña) patterns typically reach maturity in winter, with large positive (negative) SST anomalies covering much of the eastern and central tropical Pacific, often after being initiated during the preceding spring into summer as the eastern tropical Pacific anomalies weaken or change sign (Rasmusson and Carpenter, 1982; Ropelewski and Halpert, 1986; Kiladis and van Loon, 1988; Montroy et al., 1998; Barlow et al., 2001; Lamb et al., 2009).

While the evolution of Pacific Ocean SST anomaly patterns from winter to spring is addressed by comparing the above 3- and 6-month PCA loading patterns, PCA also is performed on the annual time-scale to facilitate the ultimate goal here of quantifying the impacts of climate on year-to-year crop yield variability. This comprehensive approach to describing Pacific Ocean SST variability is somewhat unique, being designed not only to benefit the agricultural end-user but also to help overcome inconsistencies and information gaps in previous research. Most of these research inconsistencies are related to the definitions of NPO and PDO, which are a

relatively new focus of Pacific Climate System research, and discrimination between these two closely related but independent North Pacific SST variability modes (e.g., Mantua et al., 1997; Zhang et al., 1997; Salinger and Mullan, 1999; Papineau, 2001; Salinger et al., 2001; Folland et al., 2002; Griffith et al., 2003; Lamb et al., 2009).

b. Pacific Ocean Sea Surface Temperature (SST) Data Set

Monthly SST reanalysis data from the most recent version (Version 2) of the NOAA Extended Reconstructed SST (ERSST) for 1949-2005 (Smith 2003, 2004) provide the basis for deriving the characteristic Pacific Ocean seasonal SST anomaly patterns used in the regional- and farm-scale climate teleconnection analyses below. The ERSST data set is comprised of monthly SST values for the period from 1854 to the present on a 2° latitude by 2° longitude global grid, with no missing data. These ERSST data sets are derived from both the most recent version of the Comprehensive Ocean-Atmosphere Data Set (COADS, Fletcher, et al., 1983), which includes SST observations from ships, buoys, and other platforms, and the combined satellite and in-situ analysis of Reynolds et al. (2002). Version 2 is an improvement over Version 1 of the ERSST data set because of enhanced quality control of the COADS data, inclusion of ice concentration information for high latitude SSTs, and better error estimation techniques (Smith 2003, 2004).

The gridded monthly ERSST data are ideal for the PCA employed here because there are no missing data and due to their uniformly high quality that results from the assimilation of many data sources and improved quality control techniques (Reynolds et al., 2002). The 1949-2005 period was selected for the present study because of the time

overlap with the Richman-Lamb North American daily temperature and precipitation data sets used here, which are described below. Since SST variability in both the tropical Pacific and extratropical North Pacific are of interest, data were used for the domain extending from 60°N to 20°S between 60°W and 120°E (Figs. 2-4). Before applying PCA to establish the characteristic anomaly patterns, the monthly SST data were averaged into the 3- and 6-month discontinuous time series for each 2° latitude/longitude grid cell, and converted into anomalies by subtraction of the 1949-2005 mean for the periods concerned (November-April, April-September, January-June, January-March, March-May, June-August).

c. Principal Component Analysis

S-mode PCA was performed on Pacific Ocean SST anomalies for the above 3- and 6-month periods to extract independent patterns of SST variability, which serve subsequently as the basis for the regional- and farm-scale agroclimate teleconnection analyses below. The S-mode PCA, which was applied to the inter-grid cell SST anomaly correlation matrix, is appropriate for this study because it is intended to isolate groups of grid cells that co-vary similarly, which here represent characteristic Pacific Ocean SST anomaly patterns (Richman, 1986). Since unrotated PCA is merely a data compression method designed to maximize the variance explained over an entire domain, it does not necessarily effectively discriminate between independent modes of the spatial variability of Pacific Ocean SSTs. Thus, “pattern smearing” is inherent in the unrotated PC (UPC) loading patterns (Richman and Lamb 1985), which occurs where multiple coherent, independent modes of Pacific SST variability are captured

within a single PC loading pattern. Such contamination could undermine the present study, for which the desired result is the identification of the unique impacts on North American agroclimate from each of the independent Pacific Ocean SST anomaly patterns.

Richman and Lamb (1985) also showed that unrotated PCA of meteorological parameters (3- and 7-day rainfall in this case) in a domain of rectangular shape can result in predictable loading patterns similar to “Buell Patterns” (Buell, 1975, 1979), which are not physically representative of the input data but a function of the domain shape. Therefore, to eliminate the above concerns and extract physically realistic, independent Pacific SST patterns, the initial UPC loadings were orthogonally rotated under the Varimax criterion (Kaiser 1958). The Varimax rotation generally is accepted as the most accurate analytic algebraic orthogonal PC rotation when applied to “known” data sets (Richman and Lamb, 1985; Richman, 1986).

By definition, the Varimax rotation of UPCs seeks to better capture the “clusters” or patterns of maximum variance in the data, through maximizing the explained variance projected on each resulting Varimax-rotated PC (VPC) (Richman and Lamb, 1985; Richman, 1986). The maintenance of temporal orthogonality also is important here, as it yields independent VPC score time series for the corresponding loading spatial patterns (Richman, 1986). Hence, the unique North American warm-season climate teleconnections for each independent SST loading pattern can be determined using the corresponding score time series. The effectiveness of the rotation especially depends on the sometimes sensitive choice of the optimal number of UPCs to retain and rotate.

Thus, particular diligence was placed on choosing the number of UPCs to rotate to give VPCs. A two-part process was employed, including (1) the objective “point teleconnection pattern” method described in Richman and Lamb (1985) and Richman (1986), as well as (2) a more subjective visual inspection of the spatial VPC loading patterns to assess the extent of “pattern smearing” as defined above in the context of Pacific SST patterns. The goal of this two-part process is to maximize how well the retained VPC loading patterns represent reality, or the SST input data (via the point teleconnection pattern method, described below), while also minimizing pattern smearing between these individual VPC loading patterns. The North et al. (1982) eigenvalue separation criterion method also was considered, with the number of UPCs retained typically matching that indicated by the point teleconnection pattern method for each SST time period.

Application of the point teleconnection pattern method involves correlating the spatial loadings of each VPC with the row/column of the parent correlation matrix that corresponds to the maximum loading, the result of which is expressed as a congruence coefficient (Richman and Lamb, 1985; Richman, 1986). The magnitudes of the congruence coefficients are proportional to how well the VPCs represent the input data, and can be used to identify physically superficial VPC loading patterns that then could be removed from the later agroclimate analyses (Richman and Lamb, 1985; Richman, 1986). A VPC loading pattern is considered sufficiently representative of a “real” Pacific SST pattern and is retained for the agroclimate analyses if the congruence coefficient is $\geq |0.92|$. That value was identified as the lower threshold of the “good” match category by Richman (1986). Generally, if an optimal number of UPCs are

retained and rotated, the congruence coefficients for the resulting VPC loading patterns are maximized, signifying a better representation of their underlying Pacific SST anomaly patterns. However, pattern smearing between the resulting VPCs, as assessed through visual inspection of their loading patterns, still can be significant despite high congruence coefficients and satisfactory representation of the input data. In these cases (all SST periods except March-May), a higher number of UPCs were included in the rotation to minimize further the pattern smearing while still maintaining congruence coefficients above the $|0.92|$ threshold.

The January-March VPCA (Fig. 2) shows a representative example of this two-part process for selection of the ideal numbers of UPCs to retain and rotate. This presents the VPC loading patterns for the four leading modes of Pacific Ocean SST variability that resulted from 6-9 UPCs being retained and rotated. The overlap between VPC loading patterns, or pattern smearing of independent modes of SST variability, was too extensive when less than six UPCs were rotated. Also, when more than nine UPCs were retained and rotated, the congruence coefficient magnitudes for most VPCs (all but VPC1 -- mature El Niño/La Niña) decreased below the above $|0.92|$ threshold. Those VPCs therefore were immediately removed from consideration.

For step 1 above for the January-March period, the congruence coefficients for the VPCs representing the mature El Niño/La Niña mode (Fig. 2, VPC1) and the tropical/subtropical branch of the PDO (defined further below, Fig. 2, VPC3) generally are extremely high ($>|0.97|$) when 6-9 UPCs were retained and rotated. For the January-March VPCs 4 and 5, which represent the NPO and extratropical branch of the PDO, respectively, all except one of the congruence coefficients were greater than the $|0.92|$ threshold.

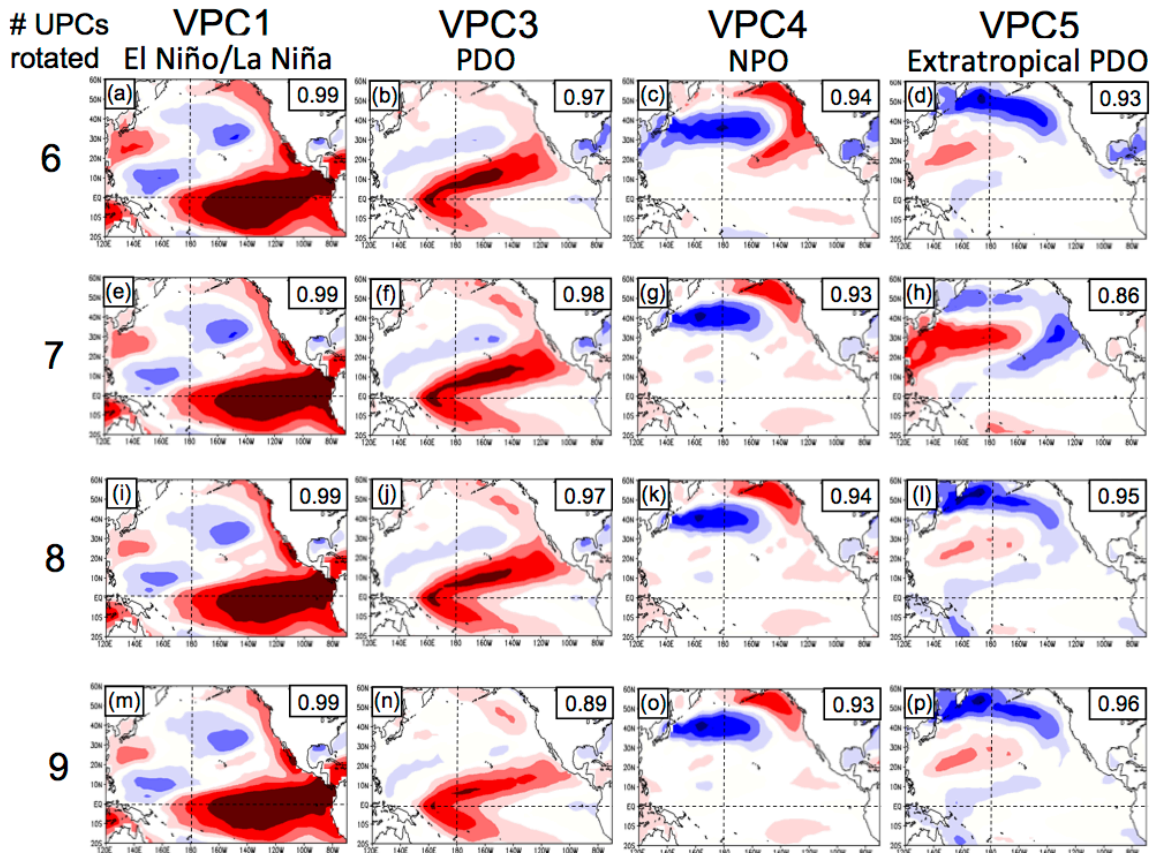


Figure 2. January-March SST VPC loading patterns and congruence coefficient magnitudes (box in upper right) for selected VPCs when 6-9 UPCs were retained for rotation.

Step 2 above narrows the selection process, as visual inspection of the VPC4 (NPO) and VPC5 (extratropical PDO) loading patterns shows decreased pattern

smearing when eight UPCs are retained in the rotation (Fig. 2k, l) compared to when six UPCs are retained (Fig. 2c, d), as well as slightly higher congruence coefficient magnitudes for VPC5 (0.95 versus 0.93). Accordingly, eight was identified as the ideal number of UPCs to retain for the January-March VPCA, and for which the corresponding VPC score time series were used in the subsequent teleconnection analysis for this SST time period. This two-step process was employed similarly for each of the six 3- and 6-month SST periods examined here (Table 1).

Table 1. Optimum number of UPCs retained and rotated to Varimax criterion for each 3- and 6-month period.

Time Period	# UPCs
JAN-JUN	11
APR-SEP	9
NOV-APR	8
JAN-MAR	8
MAR-MAY	6
JUN-AUG	9

d. Characteristic Pacific Ocean SST Anomaly Patterns

Figs. 3 and 4 present the VPC loading patterns for each 3- and 6-month period, arranged down the page in order of decreasing explained variance, except for the few SST time periods when ENSO modes are represented in VPC5 (April-September, Fig. 3m; January-June, Fig. 3n; March-May, Fig. 4n). The VPCA was most effective at extracting and distinguishing between the dominant modes of Pacific SST variability, including the ENSO, PDO, and NPO that are the focus of the Pacific Ocean SST part of

this study. Subsequently, these modes are found to have robust teleconnections with warm-season North American agroclimate, including concerning their seasonal evolution from winter through summer.

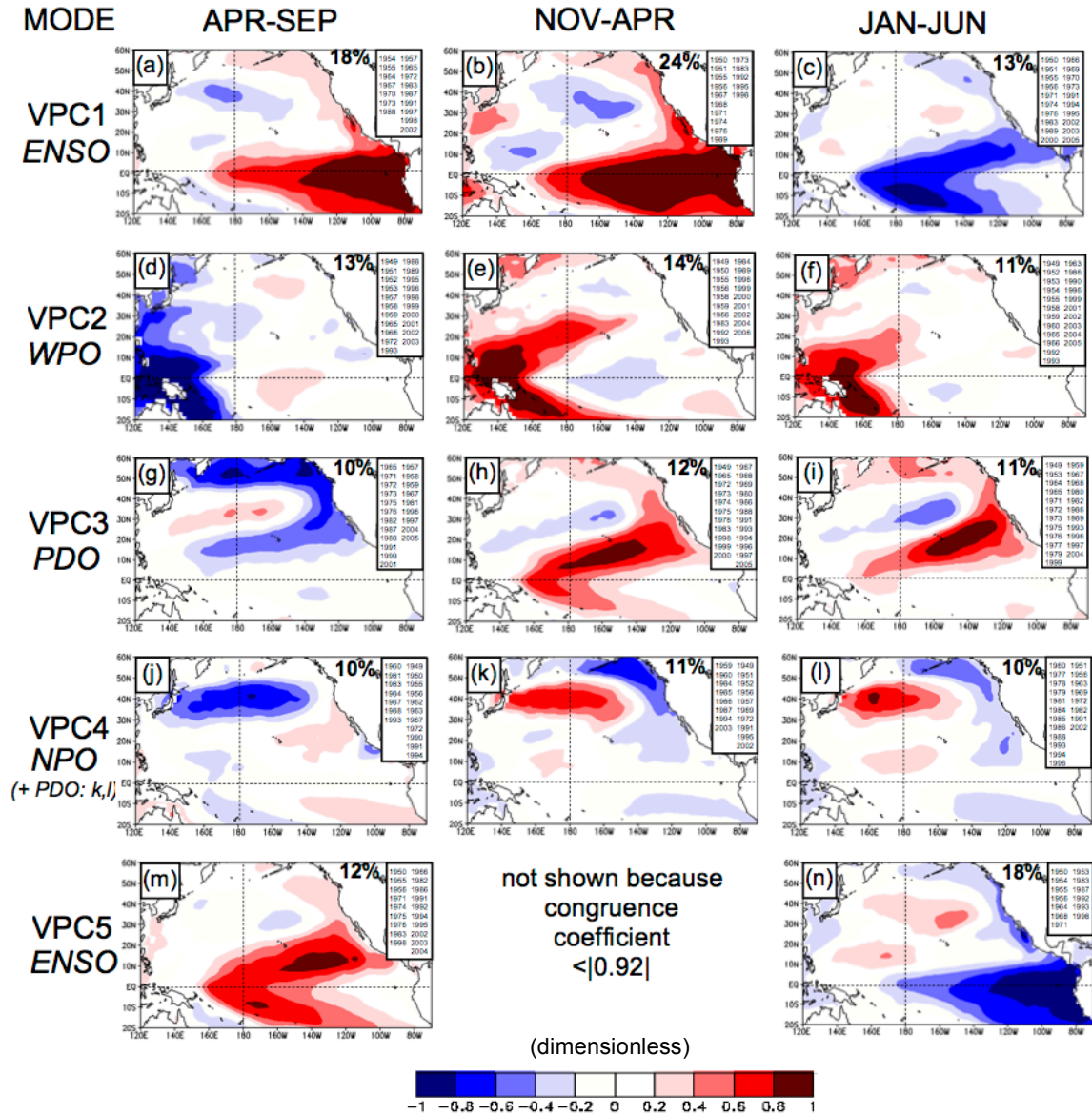


Figure 3. Pacific Ocean SST anomaly patterns extracted by VPCA for 6-month periods. Variance fraction explained by each pattern is given near U.S.-Canada border. Years (November-December for middle column) with score values $\geq |0.97\sigma|$ are listed within the box at upper-right of each panel, with the left (right) column there ranking years of the strongest cold (warm) phases for each pattern. Name of Pacific SST anomaly pattern represented by each VPC is given at right (ENSO: El Niño-Southern Oscillation, WPO: Western Pacific Oscillation, PDO: Pacific Decadal Oscillation, NPO: North Pacific Oscillation).

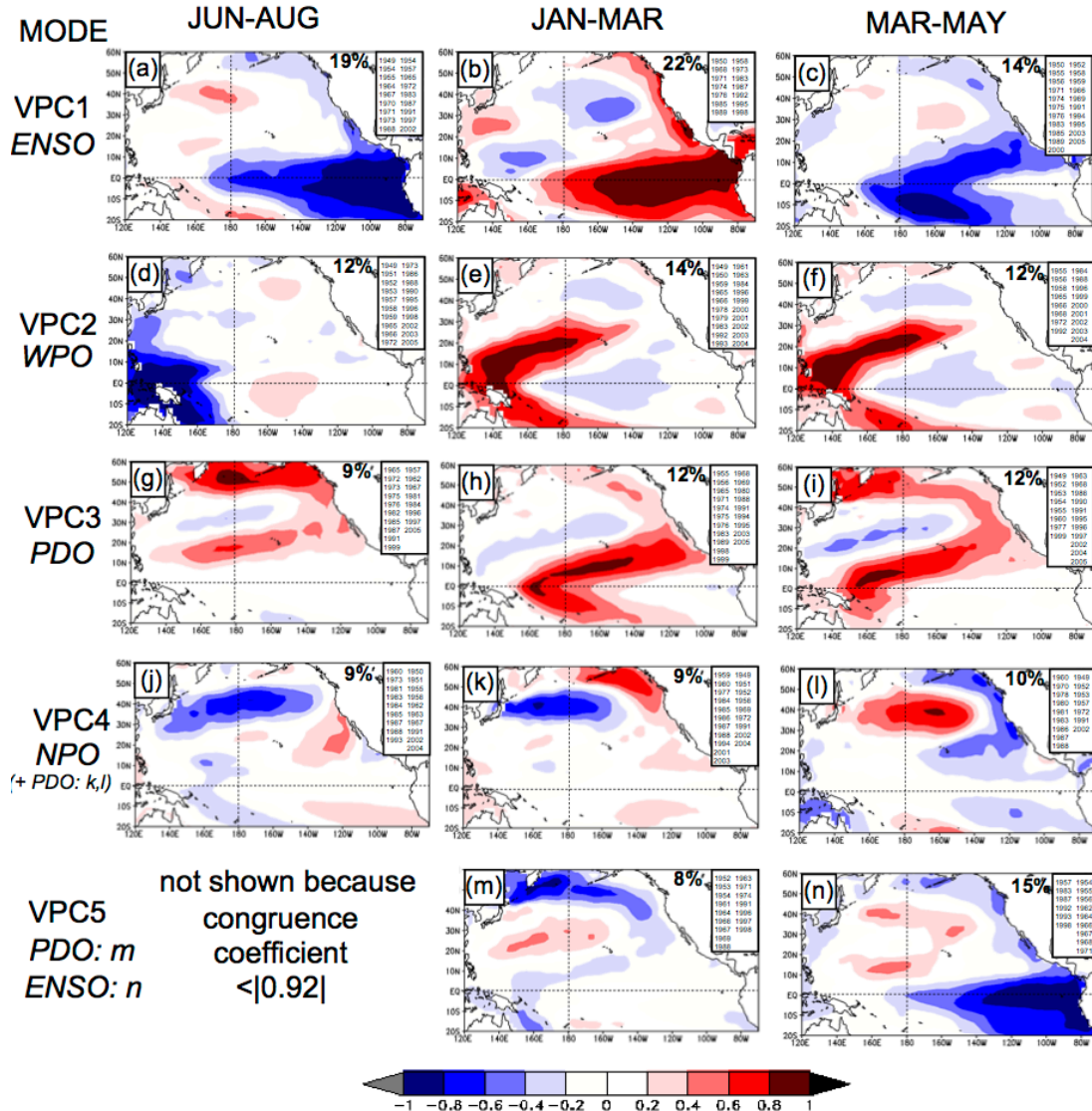


Figure 4. Same as Fig. 3 but for 3-month SST periods.

Another significant Pacific SST anomaly pattern extracted by the VPCA, the Western Pacific Oscillation (WPO; Figs. 3e-f and 4d-f; Mo and Livezey, 1986), explained the second largest percentage of variance for all 3- and 6-month VPCA time periods considered after the ENSO modes. However, this pattern is relatively weakly teleconnected with warm-season North American climate, likely because of the confinement of the associated SST anomalies to the far western Pacific. The WPO of

the present study is very similar to VPC3 of Montroy et al. (1998), which was the first study to identify the characteristic SST pattern of the WPO via PCA, as well as assess its teleconnections with North American climate. Earlier, Mo and Livezey (1986) named this pattern the WPO, but defined it based on atmospheric geopotential height patterns and not SSTs. However, because of its above weak teleconnectivity to North American summer climate, the WPO is not considered further in this study.

In addition to ENSO, PDO, NPO, and WPO, other less robust patterns also were apparent in subsequent VPCs, but they exhibited congruence coefficients below the $|0.92|$ threshold employed here. Also, the spatial loading clusters for these less statistically significant patterns were of such small magnitude and size that their physical representativeness was largely in question, and thus they are not a focus of the present study.

The VPC explaining the largest percentage of total Pacific Ocean SST variance for most 3-month and 6-month periods (VPC1; November-April, 24%; April-September, 18%; January-March, 22%; June-August, 19%) represents mature ENSO events (Figs. 3a, 3b, 4a, 4b), with a large area of strong loading values covering the entire eastern Tropical Pacific stretching to near or west of the dateline. These VPC loading patterns are consistent with the “peak phase” El Niño anomaly composite of Rasmusson and Carpenter (1982) and the leading mode of Pacific SST variability identified in the PCA of Montroy et al. (1998) and Barlow et al. (2001). The VPCA time periods for which VPC1 represent mature or near-mature ENSO events (November-April, April-September, January-March, June-August) are consistent with the typical time of year when ENSO-related SSTAs develop in the eastern tropical

Pacific (summer/fall) and propagate westward to the dateline and reach maturity by the following winter/early spring (Rasmusson and Carpenter 1982). Accordingly, the ENSO-related loadings of VPC1 for the earlier April-September (Fig. 3a) and June-August (Fig. 4a) periods are smaller in geographical size and further east than for the subsequent November-April (Fig. 3b) and January-March (Fig. 4b) periods, because the ENSO events are just beginning to mature during summer into fall, with a majority of the SST anomalies still east of the dateline.

Consistent with ENSO events often weakening or transitioning during late winter into spring, VPC1 for January-June (Fig. 3c) and March-May (Fig. 4c) represents decaying El Niño and La Niña events explaining 13% and 14% of respective SSTA variance. Here, the highest loading values are concentrated in a large horseshoe-shaped region straddling the Equator in the Central Pacific, with slightly weaker loadings extending northeastward to the Baja Peninsula. This horseshoe-shaped region encloses an area of near-zero loading values over much of the eastern Tropical Pacific extending to as far west as 140°W, which is indicative of the typical weakening of ENSO-related Tropical Pacific SST anomalies from east to west beginning just off the coast of Ecuador/Peru (Rasmusson and Carpenter 1982). This same decaying ENSO pattern appears in VPC5 for April-September (Fig. 3m), since this 6-month period encompasses both decaying ENSO events in late winter into spring, and maturing events in late summer into fall (VPC1 here, Fig. 3a). These decaying ENSO patterns are similar to the composite for the spring/summer following an El Niño depicted in Rasmusson and Carpenter (1982) as well as the “west-central Tropical Pacific Horseshoe” of Montroy et al. (1998). However, the Montroy et al. (1998) analyses

were limited to the Tropical Pacific Ocean (between 20°N/S), and thus did not capture the aforementioned northward extension of loadings into the subtropics.

The above unique extraction of both mature and decaying ENSO phases is a desired consequence of performing a separate VPCA for each 3- and 6-month period to provide information on the seasonal evolution of Pacific SST modes. Previous studies that identified modes of Pacific SST variability by incorporating all 12-months into a single PCA, such as Barlow et al. (2001), failed to differentiate between these phases of seasonal SST pattern evolution. This differentiation is important because shifts in the morphology and size of Pacific Ocean SST anomaly patterns can have profound impacts on their teleconnections with North American climate.

For example, Hoskins and Karoly (1981) modeled the atmospheric impacts from isolated low-level thermal forcing in the tropical and subtropical Pacific Ocean (e.g., SST anomaly region) of different geographical shape and latitude, and found substantial differences in the downstream mid-to-upper tropospheric response between tropical, subtropical, and mid-latitude thermal sources. Horel and Wallace (1981) and Hoskins and Karoly (1981) showed that a necessary condition for mid-latitude Rossby wave generation from a tropical Pacific heat source such as El Niño is for the upper tropospheric westerlies to impinge on the tropics over the warm SST anomalies, which is why Northern Hemisphere teleconnections with El Niño are much stronger during winter. However, as the warm SST anomalies expand northward into the subtropical Pacific as an El Niño begins to weaken during late winter into spring (e.g., Fig. 3c, 4c), the thermal source of sufficient magnitude and duration thus should remain closer to the retreating mid-latitude westerlies and sustain the aforementioned teleconnections into

the early part of the North American growing season. Wallace and Gutzler (1981) supported this importance of subtropical Pacific SSTs by linking blocking patterns in western North America with mean sea level pressure and 500 mb geopotential height anomalies in the subtropical Central Pacific Ocean, which largely are driven by the presence of underlying SST anomalies.

Hence, the associated North American climate teleconnections could be very different between the above mature and decaying ENSO phases, given the appearance of SST anomalies in the subtropics with the decaying ENSO, and also the vast differences in size and location of the tropical SST anomalies. This demonstrated importance of an SST anomaly region in the subtropical Pacific during the Northern Hemisphere warm season (North American growing season) supported the inclusion of both tropical and extratropical Pacific SST patterns in the teleconnection analysis below.

VPC3 for all time periods (Figs. 3g-i, 4g-4i) represents SST variability associated with the PDO, which emphasizes SST variability in a horseshoe-shaped region stretching from the Gulf of Alaska, southeast to the U.S. West Coast, and southwest to the central Tropical Pacific between 150°E and 160°W; explaining 8.6% to 12.0% of corresponding SSTA variability. Note that the tropical portion of the PDO is differentiated clearly here from the above decaying ENSO horseshoe pattern -- by the tropical branch of the PDO horseshoe being focused west of the dateline, whereas the decaying ENSO-related horseshoe lies east of the dateline. In six of the VPC patterns, the North Pacific and subtropical/tropical Pacific branches of PDO SST variability either are split between two VPCs (i.e., January-March, Fig. 4h and 4m), or the North

Pacific PDO branch largely appears in VPC4 (January-March, Fig. 4k; March-May, Fig. 4l, November-April, Fig. 3k; January-June, Fig. 3l), which mainly represents SST variability associated with the North Pacific Oscillation (NPO) discussed below. This aggregation of the North Pacific PDO branch and NPO into a single VPC for most 3- and 6-month periods is a consequence of similar timing and seasonal persistence of these North Pacific modes from winter through summer.

As mentioned above, the definition of PDO in previous studies is rather inconsistent. The PDO SST pattern defined here follows that of Lamb et al. (2009), and is similar to the pattern Barlow et al. (2001) obtained in a covariance-based VPCA of year-round monthly SST data. Previous to Barlow et al. (2001), the PDO was defined differently as a combination of the present NPO and PDO patterns into a single mode of North Pacific SST variability (e.g. Mantua et al., 1997; Papineau, 2001; and Gutzler et al., 2002), which also was termed the “North Pacific Mode” in Zhang et al. (1996). These previous studies did not emphasize the substantial subtropical and tropical SST variability shown here for the PDO, the presence of which effects downstream atmospheric teleconnections during the growing season in North America, as will be shown in the present study. Given the basin-wide extent of the VPC3 loadings for all time periods (Figs. 3g-i, 4g-i), this mode will be referred to as the PDO in the present study as in Lamb et al. (2009).

A striking feature of the spring-summer (April-September, June-August) PDO pattern (VPC3, Fig. 3g, 4g) is the pronounced SST variability in a region surrounding the Aleutian Islands southwest of Alaska, and a relative minimum of northern subtropical-tropical PDO SST variability. During the rest of the year, on the other

hand, the northern subtropical/tropical PDO branch is characterized either by VPC3 loading magnitudes that are stronger or approximately equal relative to the extratropical branch in the extreme North Pacific for (Fig. 3h, i; 4h, i). This apparent seasonal shift of maximum PDO SST variability from south-to-north has not been identified in previous research, and plays a role in the evolution and timing of associated North American climate patterns (Chapters 4 and 5).

Another notable feature of the PDO mode is the similarity between the SST patterns of the northern subtropical PDO branch (Figs. 3g-3i, 4h) and the decaying ENSO pattern (Figs. 3c, 3m, 4c), with the subtle difference lying in the central Tropical Pacific as noted above. As defined here, the tropical branch of PDO SST variability is focused west of the dateline, while the decaying ENSO is much more extensive in the central tropical Pacific Ocean east of the dateline, with strong loadings extending as far east as 130°W. These small differences in the location and magnitude of tropical Pacific SST anomaly regions can affect the phase of downstream upper tropospheric waves, as simulated in Hoskins and Karoly (1981) and confirmed in the observational studies of Wallace and Gutzler (1981) and Horel and Wallace (1981). Thus, distinguishing between decaying ENSO and PDO was considered important for identifying regional and local teleconnections in North American agroclimate, depending on the SST time period.

The similarity and timing of these two patterns suggests that a weakening ENSO event likely can be associated with the basin-wide development of a PDO of similar phase. In other words, a weakening El Niño (La Niña) can transition into a positive (negative) PDO, possibly driven by Kelvin Waves that propagate northward from the

eastern tropical Pacific along the western North American coastline (Hurlburt et al., 1976; Yet et al., 2015). Newman et al. (2003) stated that the PDO modulates ENSO, with stronger and more frequent El Niño (La Niña) events during warm (cold) PDO regimes, and also mentioned that ENSO events can precede a same-phase PDO event by only a few months. A transition from ENSO to PDO or lack thereof during late winter into spring affects the evolution of any teleconnections with North American agroclimate, especially given the very different latitudes of the SST anomalies associated with these patterns (DeFlorio et al., 2013; Yeh et al., 2015). Goodrich (2004) established that southwest U.S. summer precipitation teleconnections with El Niño and La Niña are stronger when in-phase with the PDO, supporting further the need for capturing the seasonal evolution of all modes of Pacific SST anomaly evolution.

VPC4 for all time periods (Figs. 3j-1, 4j-1) represents the SST component of the NPO, which explain 9.3% to 10.6% of the corresponding SSTA variance, and is maximized in the central North Pacific along 40°N between 150°E and 150°W. This NPO SST variability (as defined here) was first identified by Davis (1976) using an empirical orthogonal function analysis of North Pacific SST, but he did not refer to this variability as the NPO (or PDO) or any other name. As mentioned above, Mantua et al. (1997), Papineau (2001), DeFlorio et al. (2013), and Gutzler et al. (2002) aggregated the NPO and PDO variability into one single mode of North Pacific SST variability, with Barlow et al. (1999) being the first to distinguish between the NPO and PDO. The present NPO definition follows that of Lamb et al. (2009), which reflected strongly Barlow et al.'s (2001) identification. The similarity in the NPO loading patterns for all 3- and 6-month periods considered here is consistent with the relative persistence of the

NPO from winter into summer mentioned in Barlow et al. (2001). This NPO persistence from winter through the growing season provides substantial opportunity for lagged teleconnections with warm-season North American agroclimate, as investigated in the following regional and farm-scale agroclimate analyses. First, though, the next section describes in detail each agroclimate variable investigated in the present study for teleconnections with the above Pacific Ocean SST variance patterns.

Chapter 3. North American Growing Season Agroclimate Variables

a. Expert Opinion Background

Five AAPEX farmers were interviewed to learn the climate-related challenges and the crop-specific agroclimate sensitivities faced by real-life cultivators of each focus crop considered (soybeans, edible beans, corn, cotton, spring wheat, grain sorghum). Details of their farming operations appear in Table 2. Based on this expert opinion input, as well as previous literature (Hall, 1992; Stewart et al., 1993; Hodges et al., 1993; Wrona et al., 1998; Porter and Gawith, 1999; Armah-Agyeman et al., 2002; Cox, 2006), each of the focus crops are sensitive to three main agroclimate factors -- accumulated heat from planting date to harvest; soil moisture, especially during early growth and from flowering-reproduction to harvest; and abnormally hot temperatures during mid-summer flowering.

While some crops are extremely sensitive to hot temperatures, such as edible beans that thrive in the cooler summer climates of the northern U.S. and southern Canada, other more heat resilient crops such as cotton and the above grains require the hot summers of the southern and interior U.S. to reach maturity (Hodges et al., 1993; Stewart et al., 1993; Wrona et al., 1998; Armah-Agyeman, 2002). Crop sensitivities to soil moisture are even more complex, and are highly dependent on crop type, farming location, and plant development phase (germination, initial growth, flowering-reproduction, maturation). Each crop responds differently to extreme agroclimate, depending not only on the crop variety and location but also on the use of farming methods such as irrigation and fertilization. The present study is intended to quantify

the complex relationships between agroclimate and crop production for a variety of North American crops and farming locations (five AAPEX farms, Fig. 1, Table 2).

Table 2. AAPEX farm and focus crop information. Location includes county, state/province, latitude, and longitude; farm size is given in hectares (ha).

AAPEX Farm and Focus Crop Specifics				
Owner	# in Fig. 1	Location	Size (ha)	Principal Crops
Farmer #1	1	Middlesex, ON, 43.1N, 81.5W	1200	Soybeans
Farmer #2	2	Blue Earth, MN, 43.9N, 94.0W	600	Feed corn
Farmer #3	3	Robeson, NC, 35.0N, 80.4W	2300	Upland cotton
Farmer #3	4	Nueces, TX, 27.9N, 97.4W	NA	Upland cotton
Farmer #4	5	Liberty, MT, 48.4N, 110.6W	2400	Spring wheat
Farmer #5	6	Dallam, TX, 36.0N, 102.9W	NA	Grain sorghum

The variables selected to represent the above agroclimate factors are growing degree days (GDD), precipitation, the Palmer Drought Severity Index (PDSI), and totals of days during crop pollination windows with maximum temperatures above critical crop-specific thresholds. All variables were computed on the monthly time scale using daily precipitation and temperature data. Monthly anomalies of GDD and raw precipitation represent the atmospheric climate extremes most impactful on crop yields, since crop maturation rate and robustness universally depend on accumulated heat and moisture availability. Extreme heat during the mid-summer flowering phase of most crops can slow down or even halt plant reproduction, and the temperature thresholds above which this occurs are highly dependent on crop type.

For example, the soybeans grown by AAPEX Farmer #1 in Ailsa Craig, Ontario (Fig. 1), are highly sensitive to heat during their reproduction phase (late August into

September), with soybean flowering severely hampered by temperatures greater than 80°F. In contrast, similar stress during the crop reproduction phase is experienced by AAPEX Farmer #2's (Blue Earth County, MN) feed corn only when temperatures reach 95°F, despite his farm being at approximately the same latitude that of Farmer #1 (Fig. 1, Table 2). Further, the more hardy crops such as cotton grown by Farmer #3 in South Texas and North Carolina, and grain sorghum produced by Farmer #5 near Dalhart, TX (Fig. 1, Table 2), are far more resilient to extreme heat than both soybeans and corn, and thus can withstand the extreme summer heat of the southern and interior western U.S. (Hodges et al., 1993; Stewart et al., 1993; Wrona et al., 1998; Armah-Agyeman et al., 2002).

The time periods during the growing season when crops are most influenced by accumulated heat (GDD) and soil moisture also vary between crop type and farming location. For example, AAPEX Farmer #1 indicated that damp conditions with high soil moisture just before fall harvesting can be devastating to the soybean yield at his southern Ontario farm because of mold formation and other fungi growth. These adverse conditions also can affect his edible bean crops from flowering season (typically during August, 90-100 days after planting) until fall harvest, because of the beans relative proximity to the ground (Bradley, 2009). In contrast, damp soils just prior to late October harvest are very beneficial to corn production at Farmer #2's location in Blue Earth County, MN, resulting in larger corn kernels at maturity. Additionally, while most farmers prefer dry spring soils before and during planting season for their crops, Farmer #4, who operates a large cereal grains farm in Chester, MT (Fig. 1), emphasized the importance of ample early spring rainfall and top-soil

moisture maintenance for seed germination to occur in the relatively dry climate just east of the Rocky Mountains. Each of these examples shows the complexities in how extreme agroclimate affects crop yields, both beneficial and detrimental, supporting further the need for quantification of local agroclimate-crop production relationships such as are presented below.

These AAPEX farmers helped focus the local climate-crop yield analyses for their individual farms by providing information on the timing of weather-sensitive crop phases, as well as the temperature thresholds above which critical mid-summer flowering and reproduction cease. This vital expert information from “real world” farmers, as well as monthly correlation analyses, then were used to tailor the above agroclimate variables (GDD, precipitation, PDI, and extreme summer heat) for each individual crop of each farmer, and determine which variables have the greatest influence on local crop production. As a representative example, the tailored agroclimate variables with the greatest influence on corn production at AAPEX Farmer #2’s farming location in Blue Earth County, MN (Fig. 1), are wide ranging -- April and July PDI; July-August number of days with maximum temperature above 95°F; August GDD; and October precipitation -- all of which are found to exhibit correlations with annual local (county) corn yield that are statistically significant at the 95% significance level (Chapter 7d).

Each of the agroclimate variables selected for the present study is defined in detail below in terms of their general impact on crop production in the U.S. and southern Ontario, and their relevance to the five AAPEX farming operations considered. Lagged and concurrent teleconnections between tailored agroclimate

variables and the above Pacific Ocean SST patterns also are identified on the regional level (Chapters 4-6, Sections c-f) and for each individual AAPEX farming operation (Chapter 7f), the details of which also are discussed below. Not only is the quantification of agroclimate-crop yield relationships important, but providing predictability for extreme agroclimate conditions enhances substantially the benefit of the present study to North American farmers and motivated the identification of lagged teleconnections with Pacific Ocean SST patterns.

b. Climate Data Sets

The above monthly temperature- and precipitation-based agroclimate variables were quantified using the Richman-Lamb daily temperature and precipitation data sets for North America east of the Rocky Mountains and south of about 56°N. The procedures used to construct the daily maximum and minimum temperature data sets (Skinner et al., 1999; Timmer and Lamb, 2007) followed those employed earlier for the counterpart daily precipitation data set (Richman and Lamb 1985, 1987; Gong and Richman 1995; Montroy et al. 1998). These data sets contain 766 stations or "grid points" that are distributed evenly across the U.S. and southern Canada east of the Rocky Mountains (Fig. 5), for which complete records of daily maximum and minimum temperatures and daily precipitation totals are available from January 1949 through December 2000. The U.S. data were extracted for selected stations from the TD-3200 Cooperative Summary of the Day Data Set of NOAA's National Climatic Data Center (NCDC), while the southern Canadian data were from the counterpart Canadian Daily Climate Data (CDCD) of the Meteorological Service of Canada (Richman and Lamb

1985, 1987; Gong and Richman 1995; Montroy et al. 1998; Skinner et al. 1999; Timmer and Lamb, 2007).



Figure 5. Geographical distribution of the primary stations in the Richman-Lamb daily maximum and minimum temperature data sets used, taken from Skinner et al. (1999) and Timmer and Lamb (2007). The counterpart station distribution for the daily precipitation data set nearly is identical (Gong and Richman, 1995; Montroy et al., 1998). Red dots indicate locations of the six AAPEX farms described in Fig. 1 and Table 2.

In developing these data sets, missing daily temperature and precipitation values at each primary station in Fig. 5 (which totaled ~21% and ~15%, respectively) were replaced by substitutes from nearby secondary or tertiary stations, as described in Richman and Lamb (1985), Gong and Richman (1995), Skinner et al. (1999), and Timmer and Lamb (2007). Despite its intentional grid-like distribution of primary stations, the data set contains actual temperature observations and precipitation

measurements, not objectively analyzed or otherwise interpolated values at formal grid points. These Richman-Lamb daily temperature and precipitation data sets recently were extended from January 2001 through December 2010. These data set extensions will provide independent test data to assess the predictability of the teleconnections for U.S. and southern Canadian agroclimate extremes with the above Pacific Ocean SST patterns (Chapters 4 and 5 for teleconnections and Chapter 6 for predictability assessment, below).

c. Growing Degree Days (GDD)

The maturation of crops from planting to harvest is dependent primarily on accumulated heat and a sufficient water supply, because plants grow in a stepwise manner strongly influenced by ambient temperature (Griffin and Honeycutt, 2000; Cox, 2006; Terando et al., 2012). Even the time between seed planting and emergence is very specific to the amount of accumulated heat, given a sufficiently warm soil temperature, constant planting depth, adequate moisture, and non-freezing air temperatures (Cox 2006). Thus, the use of fixed calendar days to predict the timing of important agricultural windows is largely inaccurate and potentially costly, especially for large commercial farms where such timing inaccuracies can have a negative impact on profit margin.

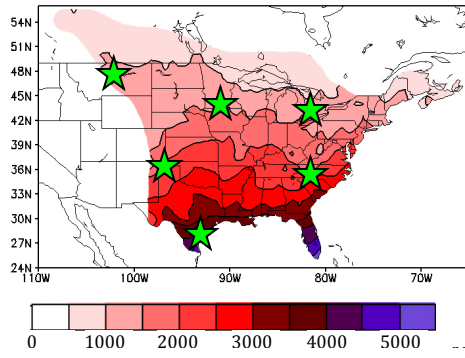
Since a deficient water supply can at least partially be compensated via irrigation practices (where available), accumulated heat probably is considered the most important climate factor for driving crop growth rates and crop resilience, and thus predicting critical crop phases during the growing season. This traditional approach

suggests that anomalously low (high) GDD totals for a particular part of the growing season, where maximal plant growth is critical for full crop maturation, would likely have a negative (positive) impact on eventual harvest yield. However, the farm-scale agroclimate analyses (Chapter 6) will show that GDD totals are not always positively related to crop yield, especially during mid-summer when positive GDD anomalies are often associated with extreme daily maximum temperatures and soil moisture deficiencies.

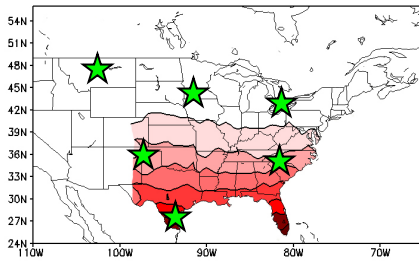
The traditional GDD threshold temperature of 10°C was selected for the present study, because it applies well to growth rates of most crop varieties considered here, including corn, soybeans, grain sorghum, and wheat (Frank and Hofmann, 1989; Zhang et al., 2001; Cox, 2006; Ternando et al., 2012). A base temperature of 10°C also will be used for cotton and cereal grains to maintain uniformity, despite this not being fully consistent with the ideal GDD threshold for these crops (ranging from 10°C to 20°C; Hutmacher et al., 2002; Viator et al., 2005). Following Cox (2006), GDDs are calculated by (1) subtracting the base temperature of 10°C from the daily mean temperature for each day (after setting daily minimum temperatures below 10°C equal to 10°C, and daily maximum temperatures above 30°C equal to 30°C), and then (2) totaling the resulting daily values over a desired time period.

Cox (2006) also has provided the following insight into the use of GDDs. The above computational procedure assumes no appreciable plant growth for an ambient temperature below 10°C and above 30°C. Generally, a higher number of GDDs results in faster plant emergence and an earlier ideal harvesting date, given a sufficient water supply.

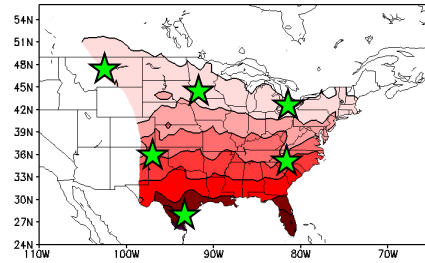
GROWING SEASON



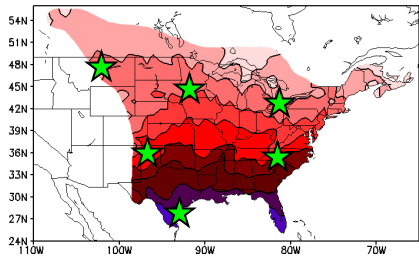
MARCH



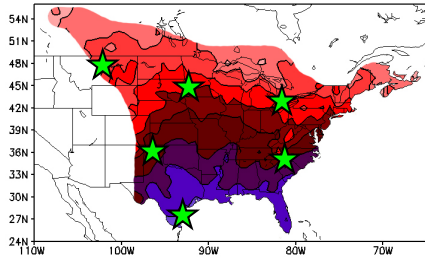
APRIL



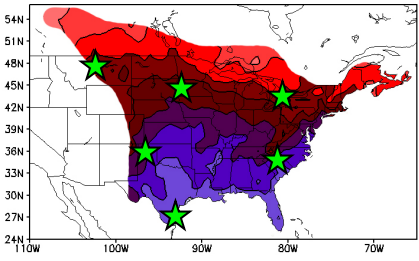
MAY



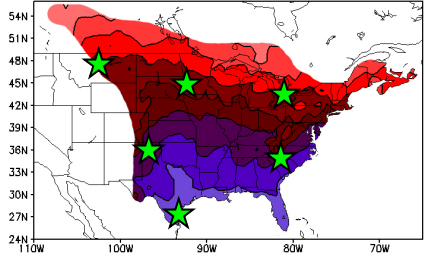
JUNE



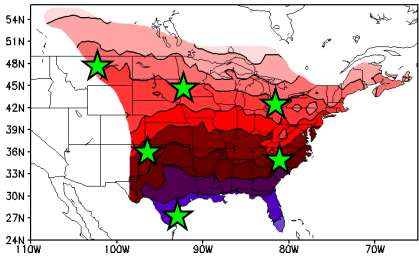
JULY



AUGUST



SEPTEMBER



OCTOBER

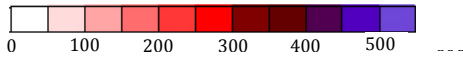
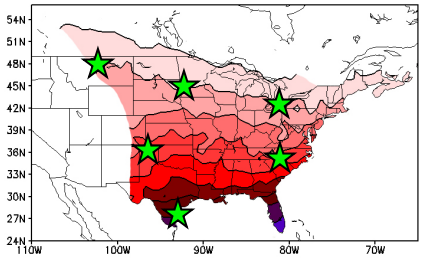


Figure 6. Long-term mean (1949-2000) growing season (March-October) and monthly GDD totals for the central and eastern U.S. and southern Canada. Green stars locate AAPEX farms numbered in Fig. 1. Black contours at 500 (50) GDD intervals for growing season (monthly) totals.

In this regard, Fig. 6 shows a pronounced decrease of monthly and growing season (March-October) total GDDs from south to north across the study region, with growing season totals ranging from 5000+ in the warmest regions of south Florida and Texas to only 500-1000 across southern Canada. Partially offsetting the high GDD totals in the southern U.S., adverse weather extremes such as very high daily maximum temperatures and drought conditions are more common there during the summer than in the northern part of the study region.

Fig. 6 presents long-term average (1949-2000) spatial patterns of GDD totals for the U.S. and southern Canada for the growing season and its constituent months, but the year-to-year extremes that impact yields for native crops are not depicted (see Chapter 4-6 for agroclimate extremes and local crop yield impacts). The locations for the AAPEX farms treated are indicated by the green stars (Fig. 1 and Table 2). The months with the highest overall (mean from 1949-2000 base period) GDD totals are July and August, for which over 500 GDDs accumulate on average for each month along the extreme southern U.S., extending north through the Southern Great Plains and into the Midwest. The areas in the study region with the lowest growing season GDD totals (typically less than 300 during even the warmest months) are across the southern Canadian Prairies into the northern Great Lakes Region and New England. These patterns reinforce the potential for accurate monthly and seasonal predictions of GDD totals for both northern and southern locations in this study region to help farmers better

pinpoint the timing of important crop maturation phases, and more efficiently manage the use of farming equipment and labor.

Because of the aforementioned linear relationship between temperature and crop growth rate, GDD accumulations are a much more useful tool than calendar days to predict the timing of important farming windows, such as crop emergence, flowering, and harvest. Thus, farming resources exploited more efficiently using forecasts of the seasonal accumulation of GDDs to anticipate crop maturation. For example, because the AAPEX members with farms in the northern part of the study region – AAPEX Farmer #2 (southern Minnesota), Farmer #1 (southern Ontario), Farmer #4 (central Montana) -- typically experience zero GDD totals during March (Fig. 6), their planting is delayed until beyond mid-April. Anomalously warm (cold) conditions after emergence then accelerates (delays) key crop growth phases.

The relationships between GDDs and timing of crop growth phases also are specific to crop type. For example, feed corn (as grown by AAPEX Farmer #2) requires around 110-120 GDDs to emerge after planting, around 1300 GDDs before flowering-reproduction occur, and 2000-2150 GDDs between planting in late May and harvest in late September into October (Cox, 2006). In contrast, soybeans hybrids grown in northern part of the study region (as grown on AAPEX Farmer #1's farm in southern Ontario) require only 1200-1300 GDDs between emergence and harvest, showing why these more heat-averse crops are grown in areas that typically escape the extreme June-August heat of locations further south (Zhang et al., 2001).

The grain sorghum and cotton crops of the southern U.S., as grown by AAPEX Farmer #5 in the Texas Panhandle (sorghum) and Farmer #2 in southern Texas/North

Carolina (cotton), are much more heat-resilient compared to corn and soybeans. These sorghum and cotton crops require heat accumulations of 2500-4000 GDD during the growing season (Fig. 6) to reach maturity (Armah-Agyeman et al., 2002; Viator et al., 2005). Typical planting dates in these southern farming locations also are earlier than the aforementioned northern locations, ranging from mid-March to early April, since over 100 GDD are experienced there on average during March, with over 300 for AAPEX Farmer #3's cotton farm in South Texas (Fig. 6)

d. Precipitation

Many complexities characterize the relationships between precipitation and crop maturation, especially when investigated for the variety of crop types, farming locations, and individual crop maturation phases (planting-germination, initial growth, flowering-reproduction, maturity-harvest) considered here. For example, dry conditions during early spring are ideal for the corn and soybean crops of AAPEX farmers #1 and #2 in southern Minnesota and southern Ontario (Fig. 6), since dry soils facilitate planting and encourage the development of deep, vertical root systems that are more resistant to short-term drought conditions later in the growing season (Isard and Easterling, 1989). On the other hand, moist soils during spring are favorable for AAPEX Farmer #3's cotton crops in North Carolina and South Texas, since their water and nutrient requirements during initial growth are remarkably large compared to other crops (Wrona et al., 1998). Based on expert opinion input on spring wheat from Farmer #4 in central Montana, spring precipitation also is vital for top-soil preservation on the

High Plains farms where prolonged periods of dryness accompanied by strong wind are common during the summer.

Even where spring precipitation is welcomed, excessive rainfall can disrupt field planting operations, decrease the effectiveness of fertilizers, and wash away freshly planted seeds for all farmers (Isard and Easterling, 1989). Timely spring planting is especially important for the full-season corn and soybean crops of AAPEX Farmers #1 and #2, since these northern crops must have sufficient time to mature before the onset of sub-freezing temperatures during fall. Given accurate predictions of anomalous spring rainfall, farming operations and planting dates could be adjusted to increase the likelihood of ideal farming conditions and optimum soil moisture for initial crop growth.

Other precipitation-sensitive periods during the growing season include crop flowering-reproduction in mid-summer, when water uptake is maximized and abundant precipitation is beneficial, and just before harvesting when crops are reaching maturity. However, increased rainfall during summer and fall has been linked to white mold formation on soybeans and other low-lying bean crops, especially when the plants are blooming, which causes wilting leaves and shredding of the stem tissue (Bradley, 2009). Late season rains in the southern U.S. also have been found to foster a moisture-loving fungus called Boll Rot that devastates cotton crops (Wrona et al., 1998). By quantifying the relationships between monthly precipitation and crop yield for a variety of crop types and farming locations (Chapter 6d-e), the present study identifies periods such as these where specific crops are uniquely sensitive to periods of anomalous precipitation. The seasonal predictability of anomalous precipitation during these crop-

specific periods also is assessed using lagged teleconnections with Pacific Ocean SST patterns (Chapter 6f).

Complicating further the analysis of precipitation-crop yield relationships is the presence of irrigation systems for particular regions and farms, and inconsistencies in the irrigation practices involved. A vast majority of the irrigated acreage east of the Rocky Mountains is located across the Great Plains west of the Corn Belt, especially the Central Plains (Kansas, Nebraska, South Dakota). Kansas is by far the leading state in terms of large farm (>\$250,000 in crop sales) irrigation, with nearly 30% of these farms utilizing irrigation systems according to the 1998 Farm and Ranch Irrigation Survey of the U.S. Department of Agriculture, followed by Nebraska, South Dakota, and Texas in the 12-16% range. Incredibly, 60% of total U.S. irrigated corn yield occurs in Nebraska (Kucharik and Ramankutty, 2004).

Because of the substantial increase in irrigation practices that began in the 1950s, the Great Plains regional crop yield has increased and yield variability has decreased substantially as farmers are able to better manage soil moisture deficiencies. Kucharik and Ramankutty (2004) compared the trends in overall corn yield and yield variability between irrigated versus non-irrigated crops in Kansas and Nebraska since the 1950s. They found that irrigated corn yield variability was less than non-irrigated variability by a factor of 3, and that irrigated corn yields were consistently double those from unirrigated land. Because of these large yield differences between irrigated and non-irrigated crops revealed by Kucharik and Ramankutty (2004) for the Great Plains, the local climate analyses (Chapter 6d-e) are performed individually for irrigated and

non-irrigated crops for the AAPEX farming locations in the Texas Panhandle and Central Montana (Fig. 1).

Monthly anomalies of precipitation for March-October are included in the agroclimate-crop yield analyses of the present study for each farming location and crop (Fig. 1), and their teleconnections with Pacific Ocean SST patterns also were identified, as described in detail below. Anomalous precipitation was used here to represent the pure meteorological forcing of agricultural drought and wetness, independent of local soil hydrology. However, the impacts on the local soil moisture budgets in this agriculturally diverse study region are accounted for by including monthly PDSI in the present analyses of local and regional agroclimate variability. Monthly lagged and concurrent teleconnections with Pacific Ocean SST patterns also are identified for growing season (March-October) PDI by U.S. Climate Division (Chapter 6c-f, below).

e. Palmer Drought Index (PDI)

(i) Concept of Drought

Drought is a climate-forced natural phenomenon that has plagued North American farmers throughout history, and has the largest negative impact on crop yield of any of the weather variables considered in the present study. Palmer (1965) provided a very generalized definition of drought from the perspective of a farmer as a prolonged shortage of soil moisture in the crop root zone. While this definition may seem simple, the meteorological and hydrological mechanisms that modulate soil moisture availability in a region are very complex. For example, drought or soil moisture surpluses for a specific region are caused not only by anomalous climate for an

extended period of time, but also by soil modulation of the anomalous climate forcing, which is highly dependent on the soil characteristics and topography of the region.

The American Meteorological Society defines drought in four different categories: meteorological, agricultural, hydrological, and socioeconomic (American Meteorological Society, 2000, p. 638; Heim Jr., 2002), where meteorological drought is simply an extended period of anomalously low precipitation, typically defined on the monthly and longer time-scales. For the present study, a meteorological and agricultural definition of drought severity was desired, since the focus here is on the impacts of climate variability on the agricultural production sector. Agricultural drought conditions result from extended periods of anomalously low precipitation, compounded by concurrently high temperatures when evapotranspiration (combination of evaporation from soil and transpiration from vegetation) is maximized. Drought severity is dependent on the duration and magnitude of these anomalies, as well as the amount of stored soil moisture available to respond to the climate forcing. Palmer (1965) developed indices to quantify short- and long-term agricultural and hydrological drought, the background for which is provided below.

(ii) Development of Palmer Drought Indices

Palmer (1965) quantified agricultural drought on the monthly time scale using simple principles of supply and demand applied to a two-layer model of the local soil moisture budget. The upper model layer consists of a “surface layer” roughly equivalent in depth to the plowed layer in an agricultural area, with a constant available water capacity (AWC) of 1 inch for all soil types in arid to humid climates. The

underlying model layer varies in depth depending on the root penetration, and has an AWC that reflects the soil characteristics of the area (Palmer, 1965). Fundamentally, in the Palmer Soil Model, soil moisture is lost to evapotranspiration exclusively from the surface layer until the water capacity of the surface layer is exhausted, and then stored water in the underlying layer is accessed. Conversely, no water recharge occurs in the underlying soil layer until the surface layer is brought to field capacity. By this definition, agricultural drought occurs when the soil moisture supply from precipitation falls short of the moisture demand from evapotranspiration for an extended period of time. This circumstance eliminates available soil moisture for crops from the surface layer first, and the underlying layer subsequently if the period of dryness is sufficiently long.

The components of the soil moisture budget in the two-layer Palmer Soil Model are precipitation (P), “actual” evapotranspiration (ET), runoff (RO), and soil moisture recharge (R) and loss (L), each of which are purely meteorological quantities and/or dependent on the available water capacity of the local soil profile. The long-term average of the monthly soil moisture budget for an agricultural region can be used to quantify the local balance between actual P, ET, RO, R, and L, where

$$\{P\} = \{ET\} + \{R\} + \{RO\} - \{L\} \quad (1)$$

Palmer (1965) computed ET on the monthly time scale as an empirical function of temperature and the dryness of the soil, the latter as a function of the available water content in the local two-layer soil profile. R occurs only when P exceeds ET for a particular month and fills an existing soil moisture deficit, while L occurs only when ET exceeds P and soil moisture is present to be lost.

Each of these “sinks” and “sources” of soil moisture have maximum possible monthly values, termed potential values, that are functions of temperature, precipitation, and/or available soil moisture. However, the observed values hardly ever reach their potential during a warm season month except in very humid climates. Palmer (1965) defined several additional terms in this context -- potential evapotranspiration (PE) as the maximum possible evapotranspiration at a given mean temperature with unlimited soil moisture availability; potential runoff (PRO) as the excess water above the AWC after soil recharge; potential recharge (PR) as the total soil moisture deficit, if any, at the beginning of the month that could be replenished with sufficient precipitation; and potential loss (PL) as the maximum soil moisture remaining in both the surface and underlying soil layer that could be lost to ET given zero precipitation.

Also, Eq. (1) can be used to approximate the “normal” soil moisture requirements for that region for each month by comparing the long-term average monthly ratios of the actual values to their potentials (or maximum possible). ET, RO, R, and L all are functions of the P and available soil moisture content, with the latter being estimated from soil moisture surpluses and deficits of previous months. Thus, the recursive nature of Palmer’s drought indices provides a realistic representation of the persistence of agricultural drought and wetness beyond the initial month when the moisture departure emerged. A monthly departure of an observed moisture variable from its long-term average or “expected” actual value (as opposed to potential) would result in an imbalance in the local soil moisture budget, which can manifest as agricultural drought or wetness given sufficient departure magnitude and duration relative to the prevailing moisture climate of the particular region (Palmer, 1965).

Palmer (1965) computed the actual and potential values for each these components of the local soil moisture budget on the monthly time-scale for two regions with very different soil characteristics -- moist sub-humid central Iowa and semi-arid southwest Kansas -- using long-term monthly temperature (1931-1957) and precipitation (1887-1957) data. The climatologically and soil-topologically different Iowa and Kansas cases were used to demonstrate that drought prevalence and severity are relative terms that depend on the local prevailing climate and available soil moisture capacity. For example, it was shown that a normal soil moisture month during summer for southwest Kansas would be a severe drought in the more humid and wet “corn country” of central Iowa, and that a summer moisture deviation of the same magnitude would be much more agriculturally devastating in southwest Kansas where the prevailing moisture climate already is semi-arid.

Palmer (1965) computed the minimum P threshold required for the soil moisture supply to meet demand for each month and region using Eq. (1) above. Termed Climatically Appropriate For Existing Conditions (CAFEC) by Palmer (1965), the long-term average quantities in Eq. 1 were related to their potential values by

$$\{ET\} = \alpha PE \quad (2) \quad \{R\} = \beta PR \quad (3) \quad \{RO\} = \gamma PRO \quad (4) \quad \{L\} = \delta PL \quad (5),$$

where the coefficients are calculated separately for each calendar month and region.

Palmer (1965) also defined a soil moisture deficit (surplus) for a month to occur when the observed precipitation (P) was below (above) the CAFEC precipitation $\{P\}$, the "displacement" of which is represented by variable d , and weighted by a climate characteristic k to give a “moisture anomaly index” Z as

$$Z = kd = k(P - \{P\}) \quad (6).$$

The climate characteristic weight k is specific to each soil moisture climate, and is intended to standardize the monthly moisture deviations between different locations and months. For example, a given monthly moisture departure will have a much greater (lesser) impact on the agricultural economy in warmer (cooler) locations and months when moisture demand is more (less). Weighting by the characteristic k accounts for these differences. Palmer (1965) computed empirically the characteristic weights for the southwest Kansas and central Iowa regions such that the moisture anomaly indices (Z) representing the driest months on record for both locations were set equal, despite differences in the corresponding displacements (d) from CAFEC precipitation. The Palmer (1965) moisture anomaly index Z , traditionally and henceforth termed the Palmer Z Index, expresses weather of a given month as a departure from the average moisture climate of the calendar month concerned.

The methodology employed by Palmer (1965) in calculating the monthly Z Index for southwest Kansas and central Iowa can be applied similarly to any region with available monthly temperature and precipitation data, as well as an accurate estimate of available soil moisture capacity. Karl (1983) calculated monthly Palmer Z Index values on the state level for the entire U.S. to assess the spatial characteristics of drought duration. Subsequently, Karl (1986) analyzed Z Index data by climate division to determine sensitivities of the index value to calibration period, which is the time period used to calculate the long-term average soil moisture conditions that determine the CAFEC precipitation defined above. Karl (1986) also assigned Palmer Z Index ranges to different z values, ranging from “extremely moist” to “extreme drought”, describing magnitudes of monthly drought or wetness as outlined in Table 2. At present, the

Palmer Drought Indices still are used officially by the U.S. Department of Agriculture (USDA) for policy decisions regarding U.S. drought relief response, and are updated monthly by the National Climatic Data Center (NCDC) for each U.S. climate division. Despite more recent studies proposing alternative measures of agricultural drought and wetness -- such as McKee et al. (1993), Akinremi et al. (1996), and Hayes et al. (1998) which consider purely standardized anomalous precipitation -- the Palmer Z Index is an ideal measure of drought for the present study because it complements raw precipitation by incorporating local soil hydrology, and the moisture categories (Table 2) easily are understood by farmers.

Table 3. Palmer Drought Index ranges for each moisture departure category (Karl 1986).

Moisture Category	Z-Index Range
Extreme drought	-2.75 and below
Severe drought	-2.74 to 2.00
Moderate drought	-1.25 to -1.99
Mid-range	-1.24 to +0.99
Moderately moist	+1.00 to 2.49
Very moist	+2.50 to +3.49
Extremely moist	+3.50 and above

The Palmer Z Index can be aggregated across timescales from weekly to multi-annual to assess the severity of short- and long-term drought using empirical relationships between recent soil moisture departures and available water content during the month of index calculation. The Palmer Drought Severity Index (PDSI), for

example, now known operationally as the Palmer Drought Index (PDI), quantifies drought and pluvial conditions on the monthly-to-seasonal time-scales based on the Z Index (Palmer, 1965; Karl, 1983, 1986; Heim Jr., 2002). The PDI is intended specifically to quantify and monitor drought/pluvial conditions as relevant to local agriculture, and is widely considered as the most representative indicator of the soil moisture conditions experienced directly by local crops (Karl, 1986; Heim Jr., 2002; U.S. Drought Portal, 2014). The Crop Moisture Index (CMI) is another widely used indicator of drought severity and moisture surplus based on the Palmer Z-Index, but is computed on the weekly level for short-term hydrological and general water management purposes, rather than agricultural (Palmer, 1968; U.S. Drought Portal, 2014). On the multi-annual time scales, the Palmer Hydrological Drought Index (PHDI) is the most widely used index of drought severity, but evolves too slowly for the shorter monthly-to-seasonal scope of the present study (Karl, 1983, 1986; Heim et al., 2002; NCDC, 2014). Different than the Palmer Drought Indices, the Standardized Precipitation Index (SPI) is a measure of drought/pluvial severity based entirely on meteorological quantities, or more specifically, on departures of precipitation relative to the prevailing local climate conditions (McKee et al., 1993). While not as representative of soil moisture content as the PDI, seasonal-and-longer SPI is correlated with impacts on groundwater, stream flow, and reservoir/aquifer storage (McKee et al., 1993; U.S. Drought Portal, 2014).

The PDI is an ideal metric of drought for this study that compliments perfectly the purely meteorological agroclimate variables, monthly GDD and precipitation (Chapters 4 and 5, above), and helps to “bridge the gap” between atmospheric and soil

moisture climate as relative to farming in the study region (Fig. 5). Using the two-layer soil model of Palmer (1965), the PDI also captures the striking diversity in soil topology and hydrology found across the central and eastern U.S. and southern Canada (Appendix, Section c), and the moisture categories (Table 3) are in terms easily understandable by farmers. Despite being developed nearly 50 years ago, the weekly CMI, seasonal PDI, and multi-annual PHDI, at present, are still the most widely used operational drought indices most representative of agricultural, hydrological, and even socioeconomic moisture shortages (Palmer 1965, 1968; Karl 1983, 1986; Heim et al., 2002; U.S. Drought Portal, 2014)

A multitude of previous literature has employed the PDI to quantify agricultural drought, including the relationships with local and regional crop yield. Sakamoto (1978) and Isard and Easterling (1989) used the PDI to assess the impacts of monthly-to-seasonal drought on Australian wheat and Illinois corn production, respectively. The latter study related the Z Index to detrended corn yields to produce a linear regression model of Illinois corn production. When only the most extreme cases of dryness or wetness were included in the analyses (Palmer Z Index > 2 and < -2), the highest correlations identified for county-level corn yields (+0.60 and +0.71) occurred for the spring planting-emergence and mid-summer reproduction windows. These results emphasize the Palmer Z Index's utility for crop yield modeling on a local-regional scale and the importance of moisture availability during key crop maturation periods. They encouraged the present use of the Palmer Z Index on the monthly time-scale to capture the moisture conditions during these key periods at each specific AAPEX farming

location in Fig. 1, as a basis for providing important information for farmers to reduce risk from extremes in soil moisture climate.

While such local agroclimate-crop yield analyses are of particular interest for the present study (Chapter 7, below), the PDI also can be used effectively to document the spatial scope and magnitude of drought and pluvial conditions by plotting station values or regional averages. Fig. 7 shows PDI values by U.S. Climate Division for a particularly wet month for soil moisture (October 2009) and a month with extreme drought (August 2000), each of which impacted at least two of the farming locations considered here. For example, ample soil moisture prevailed across the Corn Belt in October 2009, including on AAPEX Farmer #2's farm in southern Minnesota (Fig. 7), which is the moisture-sensitive period around harvest after the corn has matured. On the other hand, August 2000 was a month characterized by widespread extreme drought conditions across the entire High Plains from Montana to the Texas Panhandle, coincident with the moisture-sensitive flowering-reproduction phase of Farmer #4's spring wheat in Montana and Farmer #5's grain sorghum in the Texas Panhandle (Fig. 7). The growing season PDI teleconnections with Pacific Ocean SST patterns identified in Chapter 6 are used here to assess the predictability of these large-scale regional drought and pluvial patterns.

(iii) Present Application of Palmer Drought Index (PDI)

Growing season monthly PDI was incorporated in the present study to expand the agroclimate-crop yield analyses beyond simply atmospheric processes, and to consider also the capability of the local soil profile to recover from anomalous climate

forcing. Since the PDI is computed for the soil layer encompassing the root zone of crops, it is used here as a more direct measure of soil moisture crop stress than raw precipitation, and furthermore better represents moisture departures that take longer than a single month to materialize. Thus, the PDI provides a better measure of the month-to-month persistence of agricultural drought and wetness compared to raw precipitation or the SPI; while available soil moisture values are “carried over” from previous months for each PDI computation, they also respond more quickly to monthly climate forcing compared to the longer-term PDSI and PDHI. Agroclimate analyses on the shorter-term (monthly) time scale are a major focus here, because the goal is to develop agroclimate information for farmers that can be used to optimize farming strategies during specific crop development and maturation phases.

Spring season (planting through initial growth) PDI likely is more important than concurrent spring precipitation for the drier High Plains farming locations considered (Texas Panhandle grain sorghum and central Montana spring wheat; Fig. 1). This is because the PDI reflects the winter recharge and stored pre-spring soil moisture for these semi-arid locations for the prolonged preceding period of low temperatures that result in minimal evapotranspiration. AAPEX Farmers #4 and #5, operating large farms in the semi-arid Texas Panhandle and central Montana, emphasized strongly the importance of late winter into early spring precipitation for top soil recharge, and the spring PDI values are a much better representation of this process than concurrent spring precipitation.

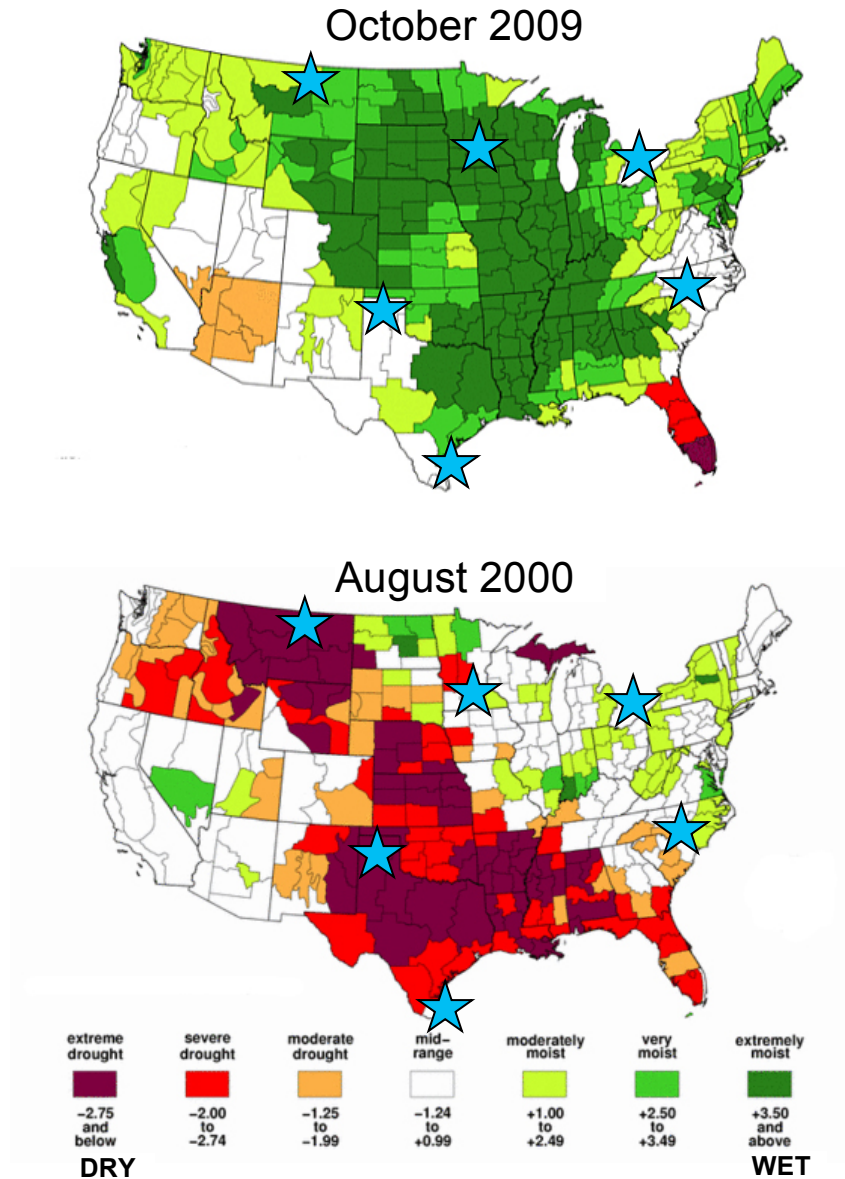


Figure 7. Examples of monthly PDI patterns for the U.S., with a Climate Division spatial resolution (data from the National Climatic Data Center, <http://www.ncdc.noaa.gov/temp-and-precip/drought/historical-palmers.php>). Blue stars indicate AAPEX farm locations.

Extremes in PDI during mid-summer flowering-reproduction also can have significant impacts on crop yield, especially for the farms of more humid climates. Farmer #2 of southern Minnesota (corn), Farmer #1 of southern Ontario (soybeans), and Farmer #3 of North Carolina/South Texas (cotton) -- see farm locations in Figs. 1, 5, 6,

7 -- emphasized the sensitivity of their crops to soil moisture deficiencies during mid-summer flowering. In general throughout the growing season, the corn, soybean, and cotton crops have particularly high soil moisture requirements compared to the more resilient crops of semi-arid farming locations. Thus, drought during soil moisture-sensitive crop maturation phases such as flowering-reproduction can be especially devastating for crop yield (Wrona et al, 1998; Armah-Agyeman et al., 2002; Heim et al., 2003).

Another application of the PDI in the local agroclimate analyses of Chapter 7 below compares the impacts of soil moisture departures between irrigated and unirrigated crops for the semi-arid farming locations where large-scale irrigation systems are commonplace (here, Texas grain sorghum of Farmer #5 and Montana spring wheat of Farmer #4, Figs. 1, 5, 6, 7). The comparison of crop sensitivities to soil moisture between irrigated and unirrigated crops for each month during the growing season indicates the relative importance of irrigation during each crop maturation phase, which can be used to more efficiently manage irrigation resources, especially for those farmers who rent or share irrigation equipment between different farming locations (e.g., Langemeier, 1989).

The present study considers monthly PDI data by U.S. climate division and quantifies soil moisture-crop yield relationships for each farming location, crop type, and month during the growing season. This treatment determines the most important crop maturation phases by month for soil moisture for each AAPEX farm (Fig. 7), such that farmers can better adapt irrigation, fertilization, and the management of farm equipment/labor to offset periods of extreme drought or wetness. Lagged and

concurrent teleconnections with the above Pacific Ocean SST patterns also are used to provide predictability of extremes in the Palmer Drought Index (PDI) during moisture-sensitive crop maturation phases, which will provide farmers more lead-time to adjust farming strategies. For example, advanced knowledge of drought conditions could help farmers overcome potential water shortages during the heart of the growing season by drawing on water storage, as well as increasing early season irrigation. Farmer #2 (southern Minnesota, Figs. 1, 5, 6, 7) and Farmer #1 (southern Ontario) indicated that excess soil moisture during spring and summer decreases the effectiveness of fertilizers, which suggests advanced knowledge of wetness could be used to optimize the frequency and magnitude of fertilizer application. The significance of drought and pluvial periods in modern agriculture cannot be understated, and especially the importance of knowing when these agroclimate extremes are on the horizon.

f. Extreme Mid-Summer Heat

Extreme high daily maximum temperatures have a negative impact on the flowering and reproduction phases of nearly all crops, because it either completely aborts the process or pollen sterilization occurs to impede reproduction and the development of seeds/grain/fruit. Since the flowering-reproduction phase typically occurs during the summer heart of growing season, extreme heat is an endemic problem faced by nearly all farmers and crops across the U.S. and southern Canada. Soybeans and other edible beans are especially sensitive to extreme heat, while higher temperature thresholds abort flowering-reproduction for even more resilient crops such

as cotton and grain sorghum (Hall, 1992; Hodges et al., 1993; Wrona et al., 1998; Armah-Agyeman et al., 2002).

Hall (1992) identified the negative impacts of heat stress on reproductive development from a plant physiological perspective for warm season crop varieties, including soybeans, cotton, wheat, sorghum, and corn. It was found that heat caused damage to early floral bud development such that flowers do not materialize, or resulted in flowers that produce no fruit or seeds. Typically, the lack of fruit or seeds despite the presence of flowers was caused by male plant sterility, given the extreme relative sensitivity to heat of pollen compared to the pistils of female plants. Critical summertime heat thresholds and timing of flowering-reproduction windows were obtained via expert input from the AAPEX farmers for southern Minnesota corn (Farmer #2) and central Montana spring wheat (Farmer #4; supported by Porter and Gawith, 1999), and from previous literature for the remaining AAPEX farming locations and crops (Table 4; southern Ontario soybeans -- Hall, 1992; North Carolina/South Texas cotton -- Stewart et al., 1993; Hodges et al., 1993; Wrona et al., 1998; Texas Panhandle grain sorghum -- Armah-Agyeman et al., 2002).

Table 4. Critical temperature thresholds above which crop reproduction ceases for each AAPEX farm focus crop of the present study (soybeans, corn, cotton, spring wheat, grain sorghum; Armah-Agyeman et al., 2002; Hall, 1992; Hodges et al., 1993; Porter and Gawith, 1999; Wrona et al., 1998).

AAPEX Farmer	Location	Crop	Flowering Window	Sterilization Threshold
Farmer #1	Southern Ontario	soybeans	July-August	90°F
Farmer #2	Southern MN	corn	July-August	95°F
Farmer #3	NC and Southern TX	cotton	June-July	100°F
Farmer #4	Central MT	spring wheat	July	95°F
Farmer #5	TX Panhandle	grain sorghum	June-July	95°F

As a measure of mid-summer heat detrimental to crop production, the total numbers of days with maximum temperatures above the sterilization thresholds in Table 4 were calculated during each specific flowering-reproduction window for each growing season during 1949-2006 (description of crop yield data for each focus crop provided in Chapter 7, Section b). The relative impact of this extreme mid-summer heat on crop yield first was determined for each AAPEX farming location via the local agroclimate analyses described below (Chapter 7, Section c), and then were related to Pacific Ocean SST variability to provide predictive information. Given predictions of a higher probability of extreme heat for flowering-reproduction phases based on teleconnections with Pacific Ocean SST patterns, farmers could adjust planting dates or insurance/futures contracts accordingly to offset the risk posed to crop yields. The next section describes methodologies used for identifying Pacific Ocean SST teleconnections with extreme heat during flowering-reproduction, as well as for the other agroclimate variables considered.

g. Agroclimate Teleconnections with Pacific Ocean SST Patterns

Time series of the above agroclimate variables were computed for each month of the growing season for each AAPEX farming location and crop type, and then were correlated with the local crop yields to determine the relative importance of each variable. Input from the AAPEX farmers provided physical reasoning for the agroclimate variables deemed most important via the correlation analyses. For each SST time period and phase (warm, cold) of each SST pattern, lagged and concurrent teleconnections between the leading agroclimate variables for each AAPEX farming

location and the above Pacific Ocean SST patterns then were evaluated by computing monthly composite anomalies for the above agroclimate variables. Such local teleconnections then are used to assess the predictability of high-impact periods of extreme agroclimate for each AAPEX farm and crop type (Chapter 7). A potential example of such a lagged teleconnection would typically associate a January-March mature El Niño with a higher number of June-July days with maximum temperatures above 95°F at AAPEX Farmer #2 corn farm in southern Minnesota (Chapter 6e). Such predictability would provide sufficient lead-time for adjustment of planting dates to reduce the risk of detrimental midsummer heat.

Regional teleconnections with Pacific Ocean SST patterns are identified below for GDD and precipitation (Chapters 4 and 5) across the entire study region (Fig. 5) via the Lamb Richman Data Set, and for PDI (Chapter 6) by U.S. Climate Division. While merely quantifying the relationships between local agroclimate and crop yield is useful for optimizing farming strategies such as irrigation, fertilization, and determining planting dates, as well as being interesting from an applied climate perspective, the usefulness of these analyses is maximized given strong predictability with sufficient lead-time. Thus, the local and regional teleconnection analyses for the agroclimate variables in this study are very important for enhancing end-user benefits. Their main motivation is to provide farmers with agroclimate information that can not only help optimize farming strategies, but also facilitate more efficiently managing contracts of labor and equipment sharing between farming locations.

Chapter 4. Monthly Growing Degree Day (GDD) Teleconnections

a. Background

GDD composite anomalies were computed for each station in the study region (Fig. 5) for each 3- and 6-month Pacific SSTA mode (Figs. 3 and 4), based on their associated constituent years. Previous studies of warm season North American climate teleconnections with Pacific Ocean SSTA patterns have focused largely on raw temperature or precipitation (e.g., Bunkers et al., 1996; Montroy et al., 1998; Barlow et al., 2001), but monthly-to-growing-season GDD teleconnections have not been explored until the present study. Since the GDDs used here are based solely on aggregates of daily mean temperature ranging from 10°C (50°F) to 30°C (86°F), with temperatures outside of this range excluded from their computation, the monthly GDD anomalies for a particular location or region are often very different from the corresponding raw temperature anomalies. For example, GDD (crop growth rates) are highest during hot, humid periods with warm overnight temperatures and daily maximum temperatures near 30°C; as compared to hot, dry periods with higher daily maximum temperatures but cooler daily minimums overnight. While the temperature anomalies for these two hypothetical cases can be the same, the crop growth rates are much slower during persistent hot, dry conditions with cooler nighttime temperatures, as well as the timing of critical crop growth phases and management of their associated farming practices. Thus, farmers can more effectively adjust planting dates and crop management practices given predictive information on GDDs, as compared to raw temperature anomalies.

The regional GDD teleconnections with Pacific Ocean SSTA patterns for the eastern U.S. and southern Canada (Figs. 8-22) were obtained in the present study to

benefit a myriad of inhabitant farmers and crop types, as well as to build on previous studies of regional North American warm-season climate research tailored for the agribusiness sector. From a purely meteorological perspective, GDD teleconnections with Pacific SSTA patterns also are unique to the already well-documented raw temperature teleconnections, given the dependence of GDDs on atmospheric moisture content. The regional-scale GDD composite anomalies also determine the spatial robustness of the concurrent and lagged teleconnections with Pacific SSTA patterns, thus supplementing the below local analyses of the impacts on crop yield for the five focus crops and six AAPEX farming locations (Chapter 6).

b. Methodology

Warm and cold events were identified for each Pacific sea surface temperature anomaly (SSTA) pattern shown in Figs. 3 and 4 using a threshold of $> |0.97\sigma|$ in the VPC score time series. Because of the normalized nature of the VPC scores, these thresholds delimit the warmest and coldest $\sim 1/6$ of years for each SSTA PC. The same method was employed in the SSTA event selection of Montroy et al. (1998).

Monthly composite anomaly fields (based on 1949-2000 means) then were calculated for GDDs and precipitation for the growing seasons associated with each SSTA extreme, by averaging across the above sets of warmest and coldest years of each SSTA VPC. The resulting GDD and precipitation composite anomalies for each station then were subjected to a local t-test to ascertain the values statistically different from zero at the 95% confidence level. The t-tests employed were two-tailed because of the presence of both negative and positive anomalies (Wilks, 2006, pp. 467, t value = 3.29).

Accordingly, a composite station anomaly was considered statistically significant if it fell outside the local 95% interval, which was calculated from the 1949-2000 anomaly time series for each station. Montroy et al. (1998) similarly determined statistically significant composite station precipitation anomalies on the monthly time scale for central and eastern U.S. associated with concurrent central and eastern tropical Pacific SSTA variability patterns, using the same Richman-Lamb Data Set as the present study.

A unique, supplemental statistical significance test also was developed and employed to assess the “local pattern robustness” for each station and resulting composite anomaly pattern. This test involved first computing local t-tests on the station anomaly value of each constituent year comprising a statistically significant composite anomaly value (Montroy et al., 1998). The local pattern robustness then was defined as the percentage of constituent years also with a statistically significant anomaly (at the 95% confidence level) of the same sign as the composite anomaly. Generally, high robustness was achieved when a large percentage of the constituent years exhibited a statistically significant anomaly of the same sign as the parent, composite anomaly. Statistically significant anomalies with a pattern robustness of 0.70 or higher -- i.e., 70% or more of the constituent years also exhibited statistically significant anomalies of the same sign -- are plotted with green triangles in the composite maps of Figs. 8-27. Composite anomalies that are statistically significant, but with pattern robustness values less than 0.70, are plotted with black triangles in those figures.

This test of local pattern robustness expands on the Montroy et al. (1998) method, which includes only the statistical significance (at the 95% confidence level) of

the composite precipitation anomalies and tables showing percentages of constituent anomalies with the same signs, and not the consistency of "anomaly robustness" within the constituent years. The rationale for enhancing the present composite analyses with information on local pattern robustness is to assess the likelihood of a particular composite anomaly pattern to emerging similarly in the future given development of the associated Pacific Ocean SSTA extreme. This local pattern robustness is especially critical for the composite analyses of the lagged teleconnections, as it provides an assessment of the local predictive confidence for the strong GDD or precipitation anomaly patterns that can have significant impacts on crop yield. A statistical significance test of this kind has not been utilized in previous agroclimate research, and is vital for enhancing the usefulness of these GDD and precipitation composite anomaly analyses for the North American farmer.

The strongest GDD composite anomaly patterns and their associated 3- or 6-month Pacific SSTA modes are introduced below in Figures 8-22, where locations the six AAPEX farms included in the following quantification of local crop yield impacts are in Figs. 1-6. As mentioned, the lagged teleconnections are of greatest value for farms in the study region (Fig. 5) if they can provide ample lead-time to permit adjustment of planting dates or crop management practices during the growing season, such as fertilization, irrigation, application growth inhibitors (cotton), and harvesting. However, given that Pacific Ocean SSTA patterns evolve much more slowly than the overlying atmosphere, even near-concurrent GDD teleconnections can be of use for farmers because the above post-planting farming techniques can be optimized given knowledge of the persistence or robustness of associated GDD anomalies.

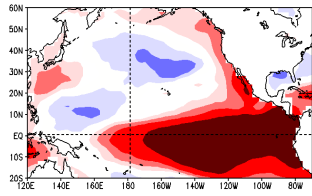
c. Mature ENSO

Four sets of coherent GDD anomaly patterns (Figs. 8 and 9) were found to be associated with the 3- and 6-month VPCs representing mature ENSO events (El Niño, La Niña, Figs. 3a,b,n; Figs. 4a,c,n). The first set of monthly GDD pattern for mature El Niño and La Niña events occurs during spring, and generally is characterized by a robust GDD anomaly regions of one sign in the Central U.S., and a smaller region of opposite GDD anomalies across the southern Canadian Prairies from southern Alberta east to Manitoba that sometimes extends into the northern U.S. (Figs. 8 and 9). The Central U.S. (southern Canadian Prairies) spring GDD anomalies for this teleconnection are positive (negative) for La Niña, and negative (positive) for El Niño. However, the monthly evolution, geographical extent, and magnitude of these monthly GDD anomaly regions during March-June are quite different, or non-linear (Montroy et al., 1998), between the two ENSO phases.

Very characteristic of mature winter-to-spring La Niña/El Niño episodes, this GDD anomaly pattern is one of the most robust and strong teleconnections presented here, and henceforth is termed the ENSO Spring GDD (“ESG”) anomaly pattern. The timing of the ESG anomaly pattern for both ENSO phases is important to farmers, since the associated GDD anomalies occur during planting season through the early part of growing season. This period is a vital window for crop initiation and development, and therefore pivotal in controlling the timing of subsequent important crop windows such as flowering, grain/bean-fill, and harvesting.

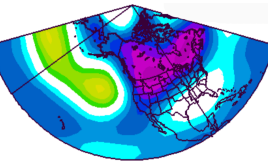
NOV-APR SST MODE

Composite 500 mb Geopotential Height Anomalies

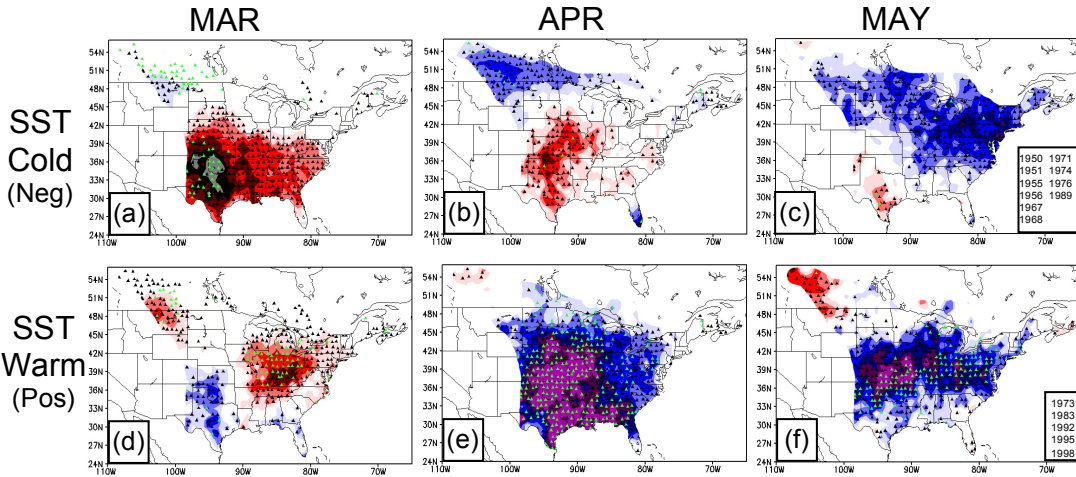
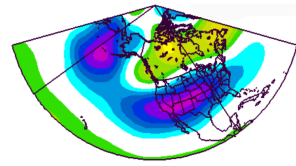


VPC1
Fig. 3b

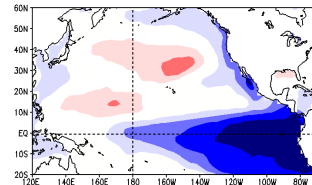
SST Cold



SST Warm

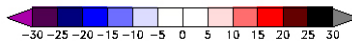
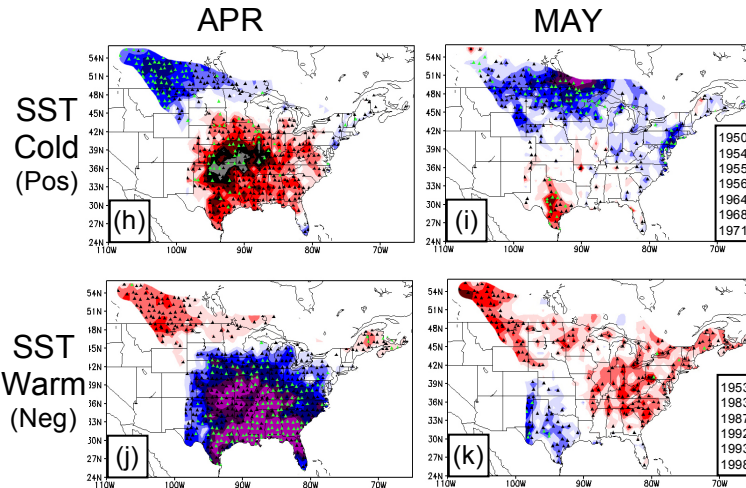
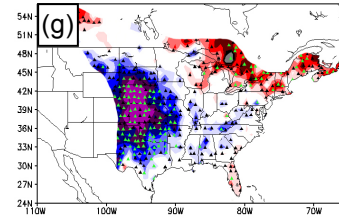


JAN-JUN SST MODE

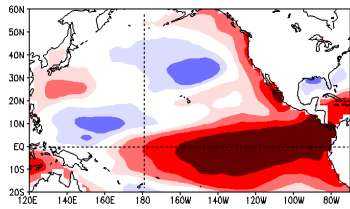


VPC5
Fig. 3n

JUN GDD

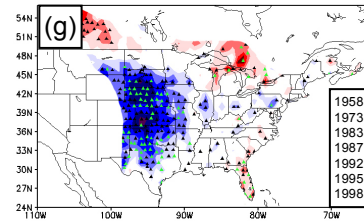


JAN-MAR SST MODE

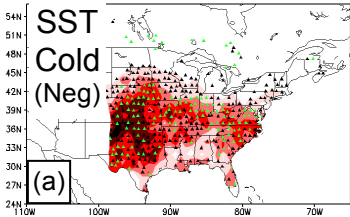


VPC1
Fig. 4b

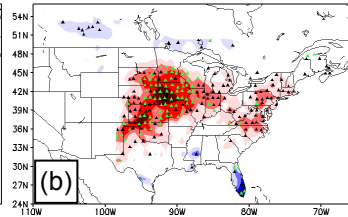
JUN GDD



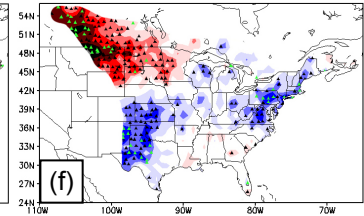
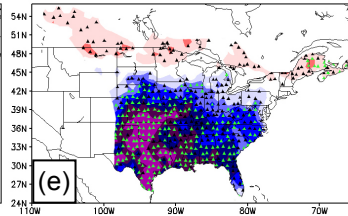
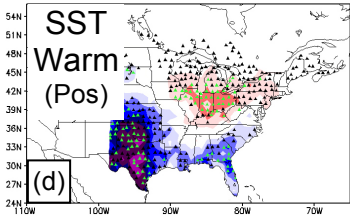
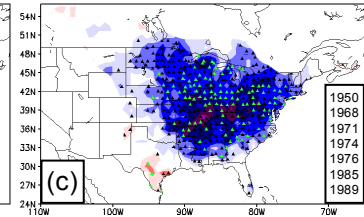
MAR GDD



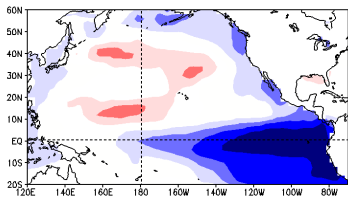
APR GDD



MAY GDD

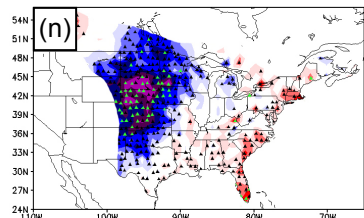


MAR-MAY SST MODE

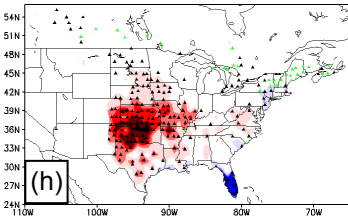


VPC5
Fig. 4n

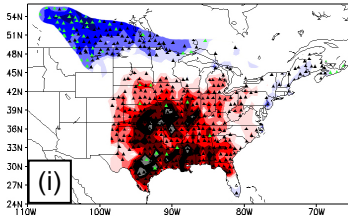
JUN GDD



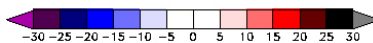
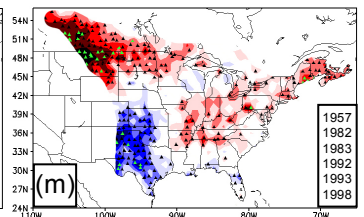
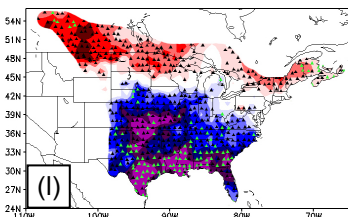
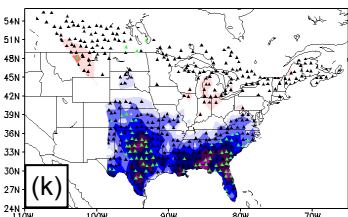
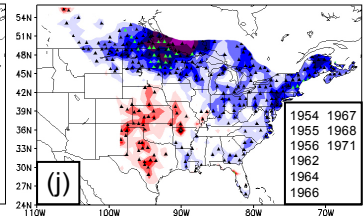
MAR GDD



APR GDD



MAY GDD



Figures 8-9. Monthly spring (March-June) GDD composite anomalies for 6-month (November-April, top; January-June, bottom; Fig. 8) and 3-month (January-March, top; March-May, bottom) representations of mature La Niña (SST Cold) and mature El Niño (SST Warm) phases identified in Chapter 2d. SST modes are repeated at top, with Pos and Neg on left-hand side indicating phase of above SST mode. Scale at bottom gives GDD anomalies for all panels. Green triangles as defined in Section b. Composite member years are in insets of right panels for each mode. Composite 500 mb height anomaly maps are at top right for the composite months shown of each SST phase (scale -50 to 50 m, interval 5 m).

The most palpable non-linearity in the ESG anomaly pattern between mature El Niño and La Niña is in the contrasting geographical extent and robustness of the two aforementioned GDD anomaly regions for the fall/winter into spring/summer 3- and 6-month Pacific SST time periods (January-March, March-May, November-April, January-June). Specifically, the Central U.S. negative GDD anomaly region associated with mature El Niño conditions is of much larger geographical extent than the corresponding positive GDD anomaly region for La Niña during their respective peak months -- April for El Niño (Figs. 8e,j; 9e,l) and March or April for La Niña (Figs. 8a,h; 9a,i). The strong negative GDD anomalies for a mature El Niño reach their maximum spatial extent during April for each SST time period, with anomalies of at least -25 GDDs encompassing most of the Great Plains, extending east through the Southeast U.S.

The counterpart positive GDD anomalies for mature La Niñas of greater than +25 GDDs are largely confined to the Central and Southern Plains during spring, with weaker anomaly magnitudes over surrounding areas. These peak Central U.S. GDD anomaly regions for mature El Niño conditions (Figs. 8e,j; 9e,l) also are characterized by higher local pattern robustness than for La Niñas (Figs. 8a,h; 9a,i). For El Niños, nearly all stations across the Great Plains and Southern U.S. exhibit statistically

significant negative anomalies and greater than 70% local pattern robustness (indicated by green triangles). For La Niñas, on the other hand, the corresponding positive anomaly regions are characterized by lesser pattern robustness, persistence, and geographical size. The location of these ESG GDD anomalies over the Central and Southern Plains, extending east to the Southeastern U.S. (for mature El Niños), enhances their relevance for farmers of cotton, wheat, sorghum, and corn, since the optimum timing of labor-intensive crop growth phases such as sowing, flowering, grain and boll development, and the application of growth inhibitors (cotton), would differ greatly between winter-to-spring mature El Niño and La Niña conditions.

Meanwhile, the Canadian Prairie GDD anomalies associated predominantly with January-June and March-May mature La Niña and El Niño -- opposite in sign to the Central U.S. anomalies for each ENSO phase -- are much stronger and more robust for La Niña (GDD anomalies greater than -20; Figs. 8h,i; 9i,j) than El Niño (GDD anomalies of only +10 to +20; Figs. 8j,k; 9l,m), but peak during April and May for both ENSO phases. This “northern branch” of the ESG anomaly pattern is important for North American agriculture, as it encompasses the vast grain, canola, and soybean farmland between the northern Rocky Mountains and the Great Lakes Region.

The timing and persistence of the above central/southern U.S. and Canadian Prairies/northern U.S. GDD anomalies are also highly non-linear between mature La Niña and El Niño conditions for the fall/winter into spring/summer Pacific SST time periods. The strong negative GDD anomalies across the Central and Southern U.S. associated with mature El Niños exhibit much more month-to-month persistence than the counterpart positive GDD anomalies for La Niñas. The El Niño-related GDD

anomalies emerge as early as March for the January-March (Fig. 9d) and March-May (Fig. 9k) SST periods, maximizing in April for all winter through spring mature El Niño periods (Figs. 8e,i; 9e,l) and even extending through June for all but the January-June mature El Niño (Figs. 8g; 9g,n). These strong negative GDD anomalies (greater than -20) often persist well beyond the associated SST time period for mature El Niños, with a teleconnection lag of up to three months for the January-March El Niño (see April, May, and June GDD patterns; Figs. 9e-g), and of one to two months for the March-May (June GDD, Fig. 9n) and November-April (May and June GDD; Figs. 8f,g) Pacific SST time periods, respectively.

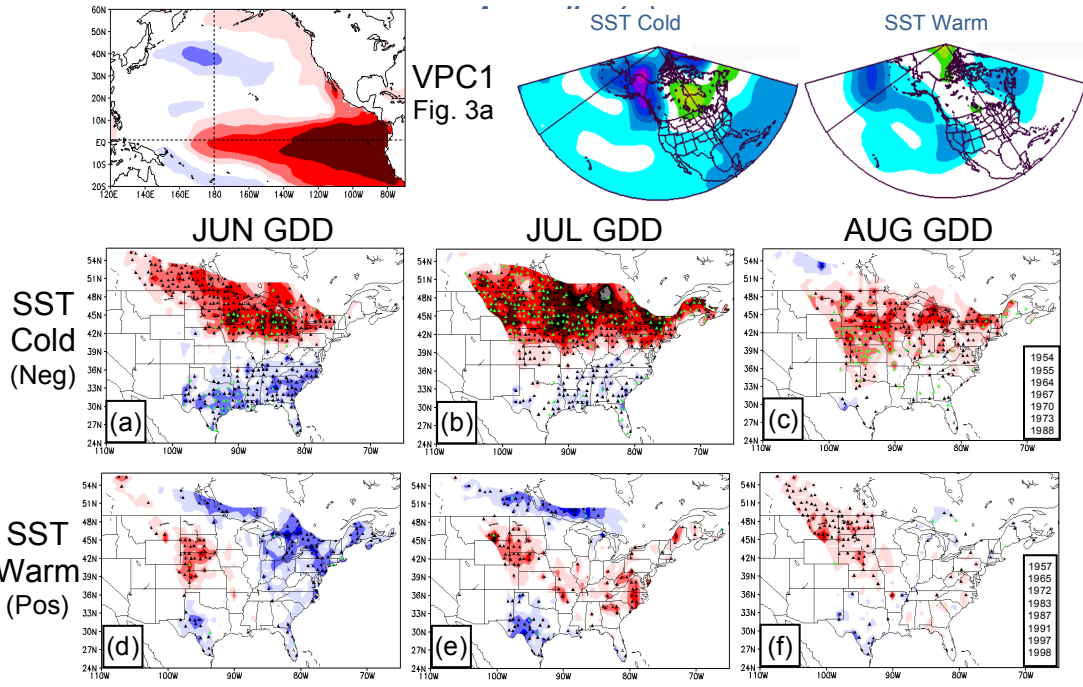
On the other hand, the Central U.S. positive GDD anomalies associated with La Niñas largely are non-existent by May for all fall/winter into spring/summer Pacific SST time periods (Figs. 8c,j; 9c,j). Also, the strength of these patterns peaks during March before weakening by April for November-April and January-March mature La Niñas (Figs. 8a and 9a). Thus, the ESG anomaly pattern is largely a concurrent teleconnection for mature La Niña conditions (except for April GDD with January-March mature La Niñas, Fig. 9b), with the Central U.S. positive GDD anomalies as well as the negative GDD anomalies across the Canadian Prairies highly dependent on the concurrent persistence of mature La Niña conditions through spring.

The second GDD teleconnection identified here for mature ENSO conditions occurs during midsummer (June-August), and is prevalent only for concurrent April-September (Fig. 3b) and June-August (Fig. 4c) La Niña events. This midsummer La Niña teleconnection extends across the northern U.S. and southern Canada, with a large region of strong positive GDD anomalies stretching from the northern High Plains east

to New England during June, July, and August for both spring-to-summer Pacific SST time periods (Figs. 10a-c and 10g-i). The strongest anomalies occur during June and July for June-August and April-September Pacific SST representation of mature La Niña events. A large east-west oriented swath of greater than +20 GDD anomalies prevail from the Dakotas east to the Great Lakes Region during both months (Figs. 10a,b,g,h), before starting to weaken and fragment by the following August (Figs. 10c,i). Especially during June and July, a majority of the stations comprising these strong positive anomalies exhibit greater than 70% local pattern robustness (indicated by green triangles in Fig. 10).

This summer GDD anomaly pattern not only is associated with the persistence of mature La Niña conditions from winter through late summer, but also can emerge given fast maturation of a new La Niña episode by early summer. Because this pattern is absent from all other Pacific SST time periods but April-September and June-August, monthly composite GDD anomalies for aggregate “El Niño and La Niña years” would not necessarily have revealed this important mid-growing season teleconnection. This finding thus supports further the present investigation of multiple discrete 3- and 6-month Pacific SST time periods to assess GDD teleconnections with the SST patterns as they evolve from winter through the growing season. Clearly, emergence of this midsummer GDD teleconnection depends on the persistence of La Niña beyond its typical peak during winter into spring.

APR-SEP SST MODE



JUN-AUG SST MODE

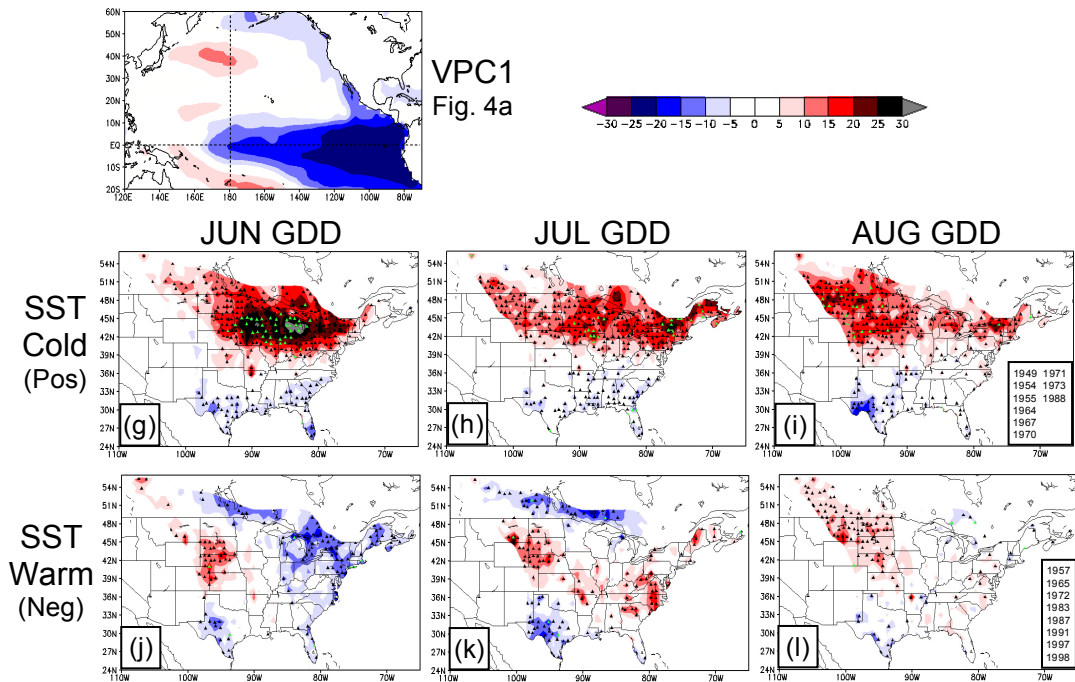


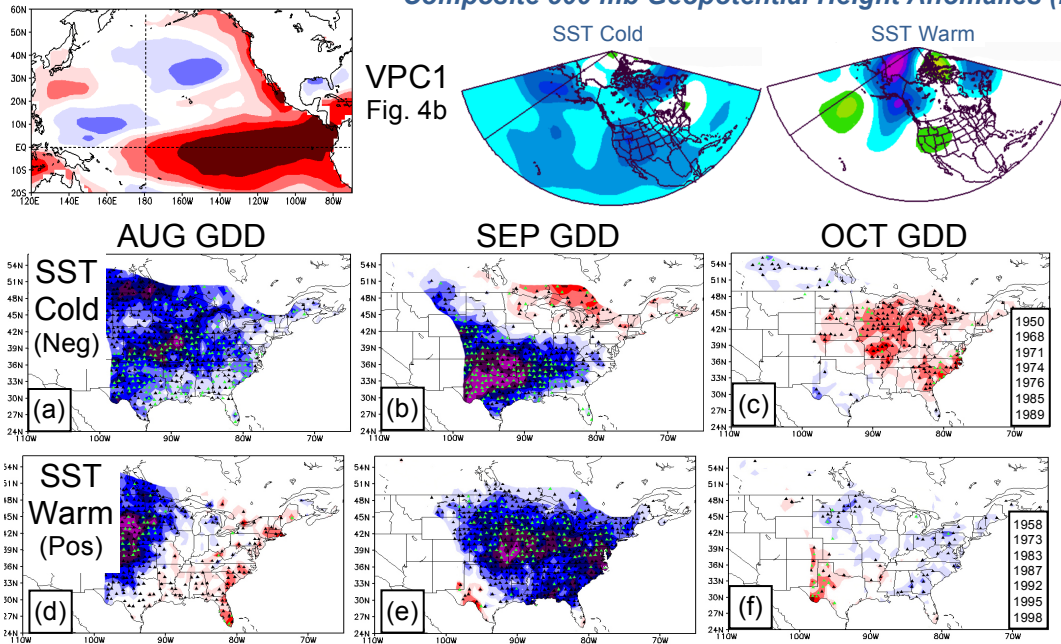
Figure 10. Same as for Fig. 8 except for mid-summer (June-August) monthly GDDs for 6-month (April-September, top) and 3-month (June-August, bottom) representations of mature La Niña (SST Cold) and mature El Niño (SST Warm) phases identified in Chapter 2d. Composite 500 mb height anomaly maps are at top right for the composite months shown of each SST phase (scale -50 to 50 m, interval 5 m).

The third GDD anomaly teleconnection associated with mature ENSO conditions is for August and September following a winter into spring La Niña or El Niño event. It is especially prominent (and linear between the two ENSO phases) for the January-March Pacific SST time period (Figs. 11a,b,d,e). Interestingly, this late summer GDD anomaly pattern for January-March mature ENSO conditions (Figs. 11a,b,d,e) is stronger and more robust than counterparts for the other winter-into-summer Pacific SST time periods, including November-April (Figs. 12a,b,d,e); January-June (Figs. 12g,h,j,k); and March-May (Figs. 11g,h,j,k), despite having a much larger teleconnection lag. The late summer (August and September) GDD teleconnection for January-March mature ENSO exhibits relatively high linearity between the SST extremes, with a large and strong negative GDD anomaly region for August and September over much of the U.S. following January-March La Niñas (Figs. 11a,b), and an equally large GDD anomaly region, opposite in sign, following El Niños (Figs. 11d,e). However, the positive GDD anomalies of El Niño events are centered slightly north of the negative GDD anomalies for La Niñas, and are not as strong during September.

The strong GDD anomaly signal during the subsequent late summer (August, September) of January-March La Niñas (Fig. 4b) features a large region of negative anomalies exceeding -25 stretching from the Southern Plains to the Corn Belt in August (Fig. 11a), and a September focus on the southern Great Plains (Fig. 11b). However, this pattern is not as strong for November-April La Niñas (Fig. 11a,b), which shows that persistence of La Niña conditions beyond December strengthens this negative GDD anomaly during the concurrent/subsequent spring.

JAN-MAR SST MODE

Composite 500 mb Geopotential Height Anomalies (m)



MAR-MAY SST MODE

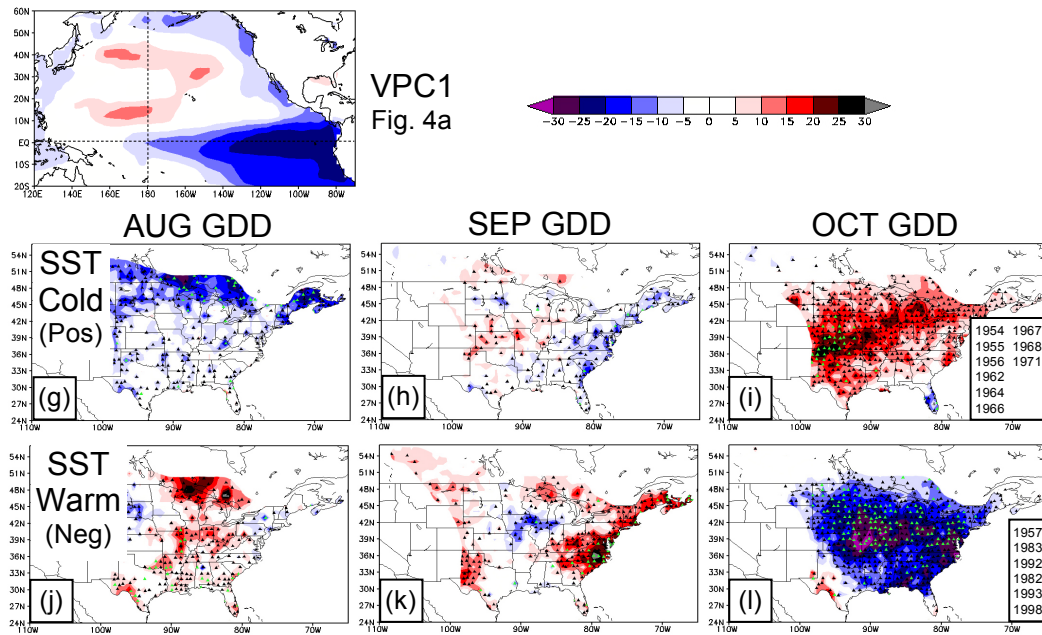
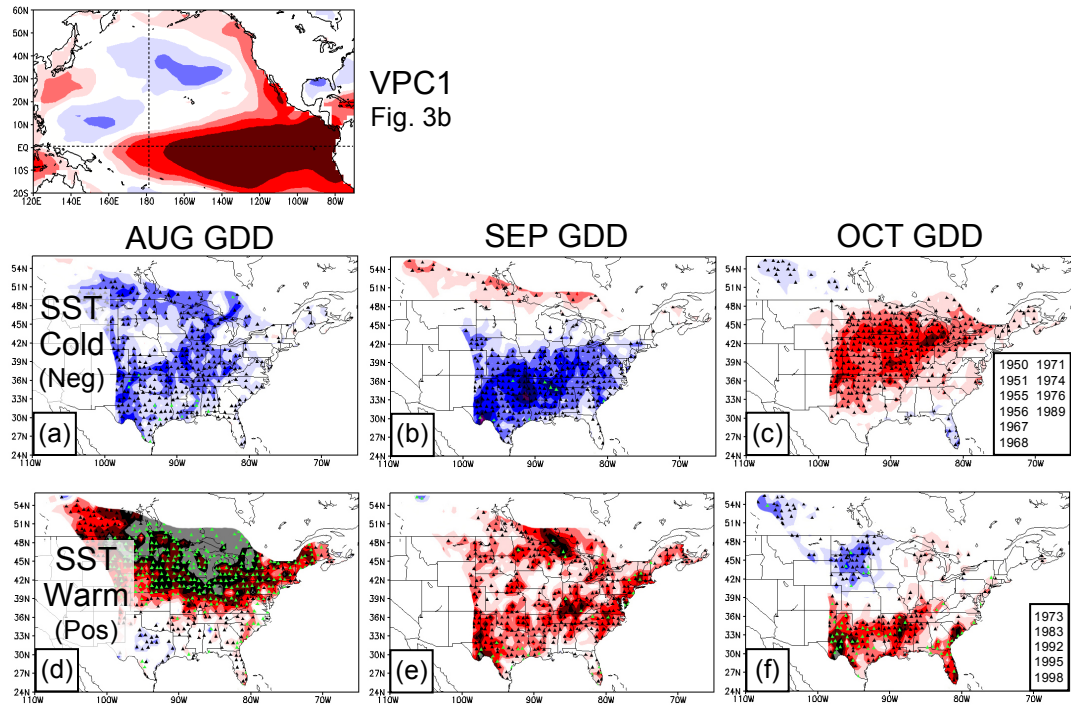


Figure 11. Same as for Fig. 8 except for late summer-to-fall (August-October) monthly GDDs for 3-month (January-March, top; March-May, bottom) representations of mature La Niña (SST Cold) and mature El Niño (SST Warm) phases identified in Chapter 2d. Composite 500 mb height anomaly maps are at top right for the composite months shown of each SST phase (scale -50 to 50 m, interval 5 m).

NOV-APR SST MODE



JAN-JUN SST MODE

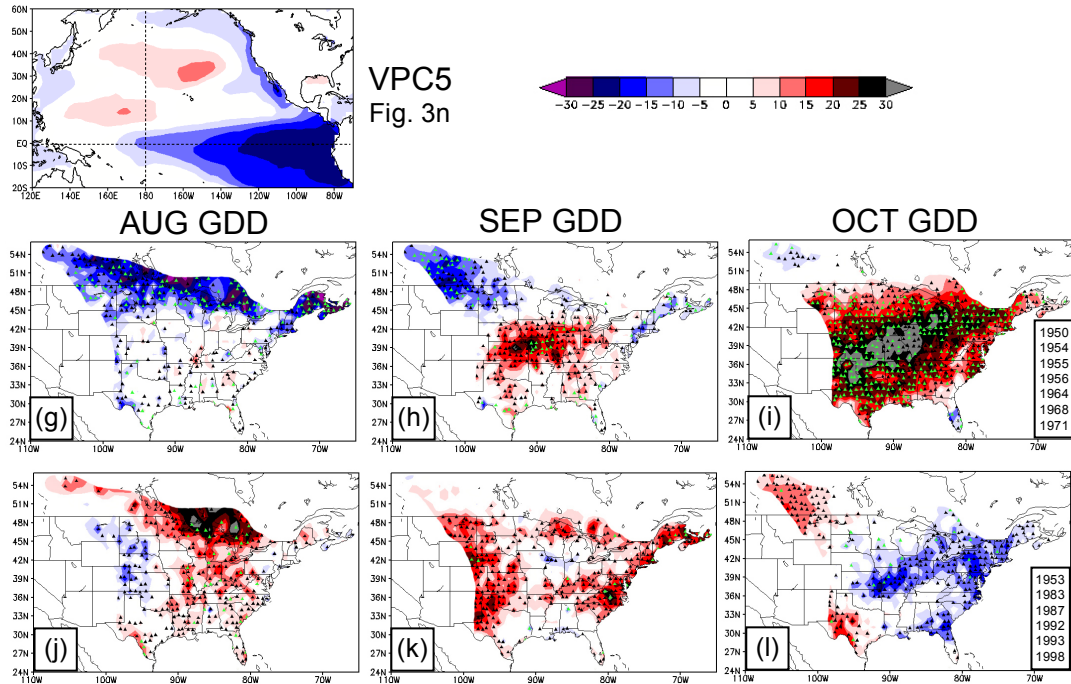


Figure 12. Same as for Fig. 8 except for late summer-to-fall (August-October) monthly GDDs for 6-month (November-April, top; January-June, bottom) representations of mature La Niña (SST Cold) and mature El Niño (SST Warm) phases identified in Chapter 2d.

Conversely, the largely inverse August and September GDD teleconnections with mature El Niños are even stronger for the November-April SST period (Fig. 12d,e) than January-March (Fig. 11d,e), with a very large region of greater than +25 GDD anomalies stretching from the High Plains to New England for August (Fig. 11d), weakening slightly by September (Fig. 11e). Thus, more so than La Niña, the persistence of mature El Niño conditions during the entire winter (November-April as compared to January-March) appears to enhance this GDD teleconnection during the following August and September.

Interestingly, the above August and September GDD anomalies largely are absent from the mature ENSO composites for the January-June and March-May SST time periods (Figs. 12g,h,j,k; 11g,h,j,k), indicating that this late growing season teleconnection does not depend on the persistence of mature El Niño or La Niña conditions into late spring and summer. This stronger relationship between late summer GDD and the preceding winter mature ENSO phase likely stems from one of two factors -- either the effects of winter diabatic heating in the tropical Pacific from ENSO somehow are not “felt” in North America until several months later (August, September), or the ENSO event transitions into a PDO by summer when a more concurrent GDD association prevails. The late summer PDO teleconnections, which are presented in detail in Section e below, are consistent with this lagged ENSO/GDD relationship. Regardless, the four-to-six month lag exhibited between winter mature La Niña/El Niño and late summer GDD in North America could be very beneficial for farmers attempting to optimize production strategies based on climate information, as sufficient lead-time exists to modify contractual arrangements.

The fourth prominent GDD teleconnection identified for mature La Niña/El Niño conditions is for October, which is harvesting time for the Corn Belt and Midwest Soybeans, as well as for the southern U.S. Cotton Belt. Similar to the previous association discussed, this October GDD anomaly region is geographically large with strong magnitudes and forecast confidence, and also occurs at a several month lag from the associated mature ENSO phase. Specifically, strong positive GDD anomalies of greater than +25 cover nearly the entire U.S. from the Great Plains to the Northeast during October following a January-June mature La Niña event (Fig. 12i), with equally strong negative anomalies over the same area during October following a March-May El Niño (Fig. 11i). Thus, persistence of the mature La Niña or El Niño through late spring appears necessary for these GDD anomalies to materialize during October harvesting season

d. Decaying ENSO

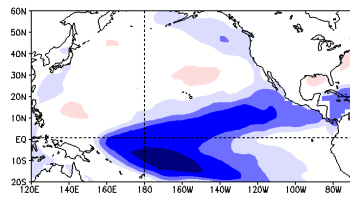
The most prominent GDD teleconnection for decaying ENSO conditions (Figs. 3c,m; 4b,g) is for the late winter-into-spring warm phases (decaying El Niños). This linkage is characterized by strong positive GDD anomalies (greater than +25) that stretch from the western Canadian Prairies across the Northern Plains and Great Lakes Region to as far east as the Northeast U.S. during the following June-September (Figs. 13d-f, j-l; 14d-f, j-m.). These GDD anomalies are also highly non-linear between the cold and warm phases of decaying ENSO -- although more linear for the April-September Pacific SST mode -- with largely non-existent (or weaker) counterpart

negative GDD anomalies during midsummer (June-August) following decaying La Niña events (Figs. 13a-c, g-j; 14a-c, g-j).

The June-August positive GDD anomalies for decaying El Niño are strongest for the January-June and January-March SST time periods (Figs. 13d-f; 14d-f), and maximize during September for the March-May SST time period (Fig. 14m). The relatively weaker midsummer (June-August) GDD anomalies for the April-September and March-May decaying El Niño (Figs. 13j-l; 14j-l), compared to the January-June and January-March Pacific SST time periods, indicates that this GDD teleconnection is dependent primarily on the presence of decaying El Niño during winter, more so than its persistence through spring.

This 2-4 month teleconnection lag, as well as the substantial pattern robustness of the strong positive GDD anomalies for the January-June and January-March SST time periods (indicated by the green triangles in Figs. 13d-f; 14d-f), are significant for farmers of the northern U.S. and southern Canada, since ample lead-time exists to optimize not only planting dates, but also farming practices during the growing season. In addition, the impacts of these GDD anomalies on crop yields are maximized given their timing during June-August, which encompasses the flowering and grain/fruit growth phases of most crop varieties cultivated in this region, including wheat, corn, soybeans, and canola. As shown in Chapter 6e,f, below, however, the impacts from positive GDD anomalies such as associated with decaying El Niño are not always beneficial for crop yields, particularly when associated with extreme hot daily maximum temperatures during the heat-sensitive flowering phases of midsummer.

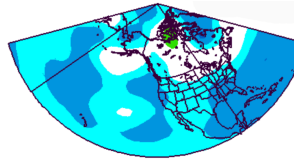
JAN-JUN SST MODE



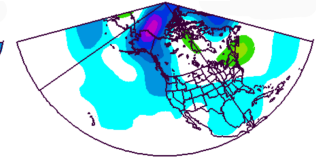
VPC1
Fig. 3c

Composite 500 mb Geopotential Height Anomalies (m)

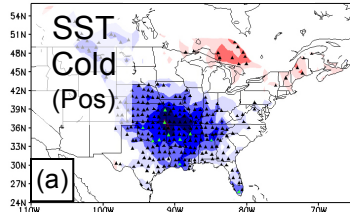
SST Cold



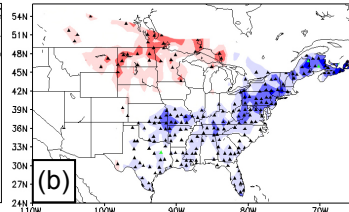
SST Warm



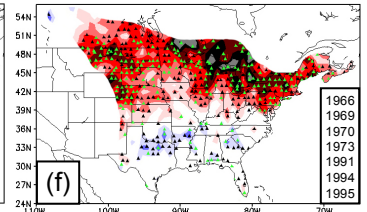
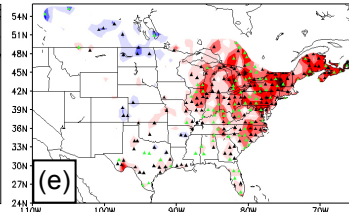
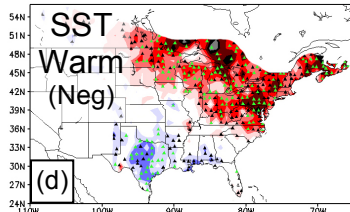
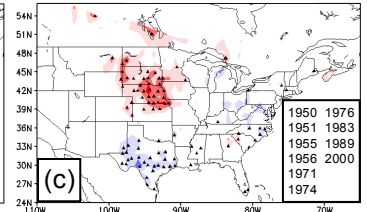
JUN GDD



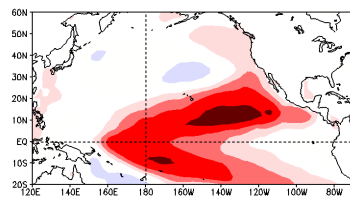
JUL GDD



AUG GDD



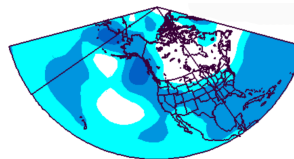
APR-SEP SST MODE



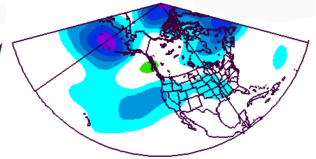
VPC5
Fig. 3m

Composite 500 mb Geopotential Height Anomalies (m)

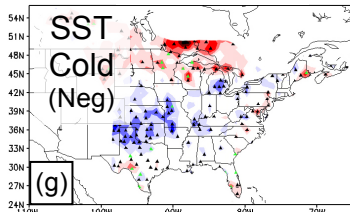
SST Cold



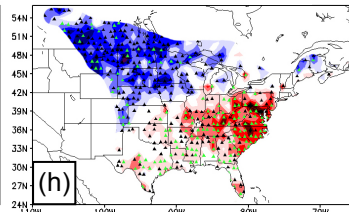
SST Warm



JUN GDD



JUL GDD



AUG GDD

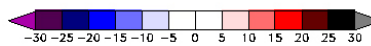
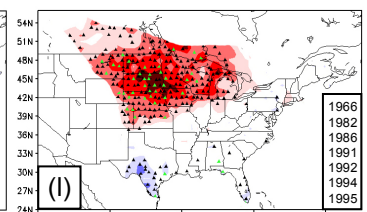
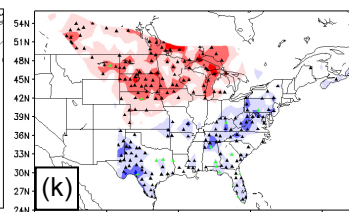
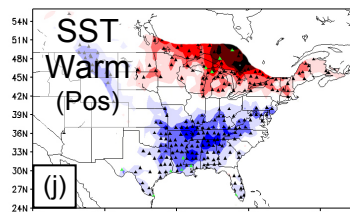
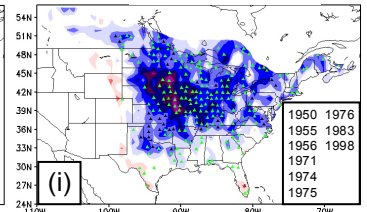
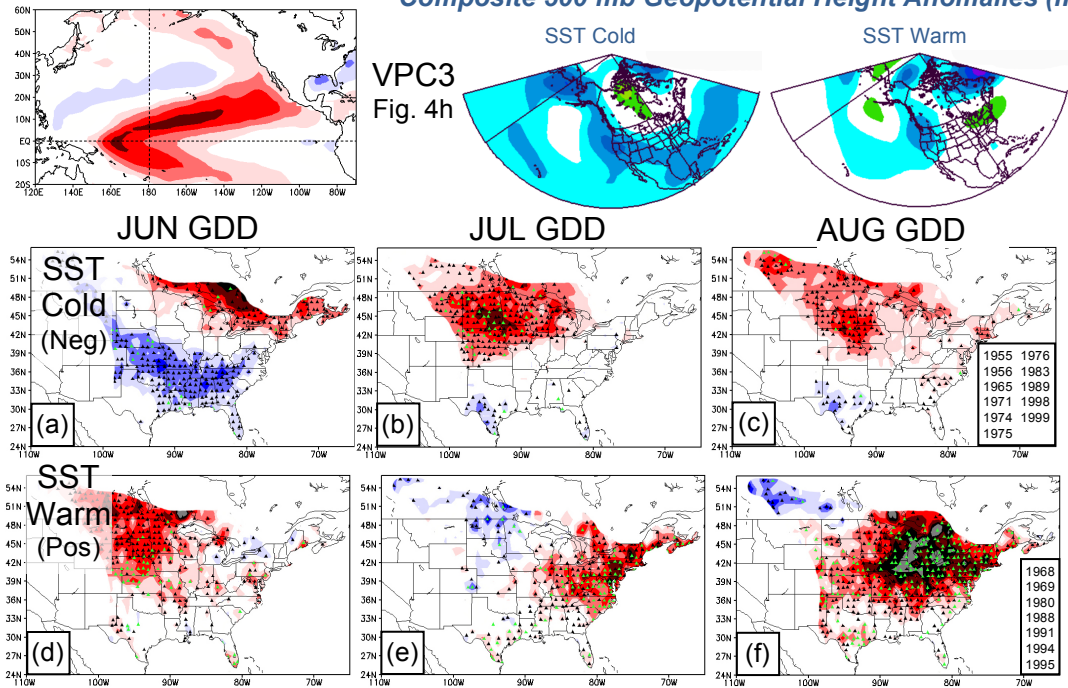


Figure 13. Same as for Fig. 8 except for midsummer (June-August) monthly January-June, bottom) representations of decaying La Niña (SST Cold) and decaying El Niño (SST Warm) phases identified in Chapter 2d.

JAN-MAR SST MODE

Composite 500 mb Geopotential Height Anomalies (m)



MAR-MAY SST MODE

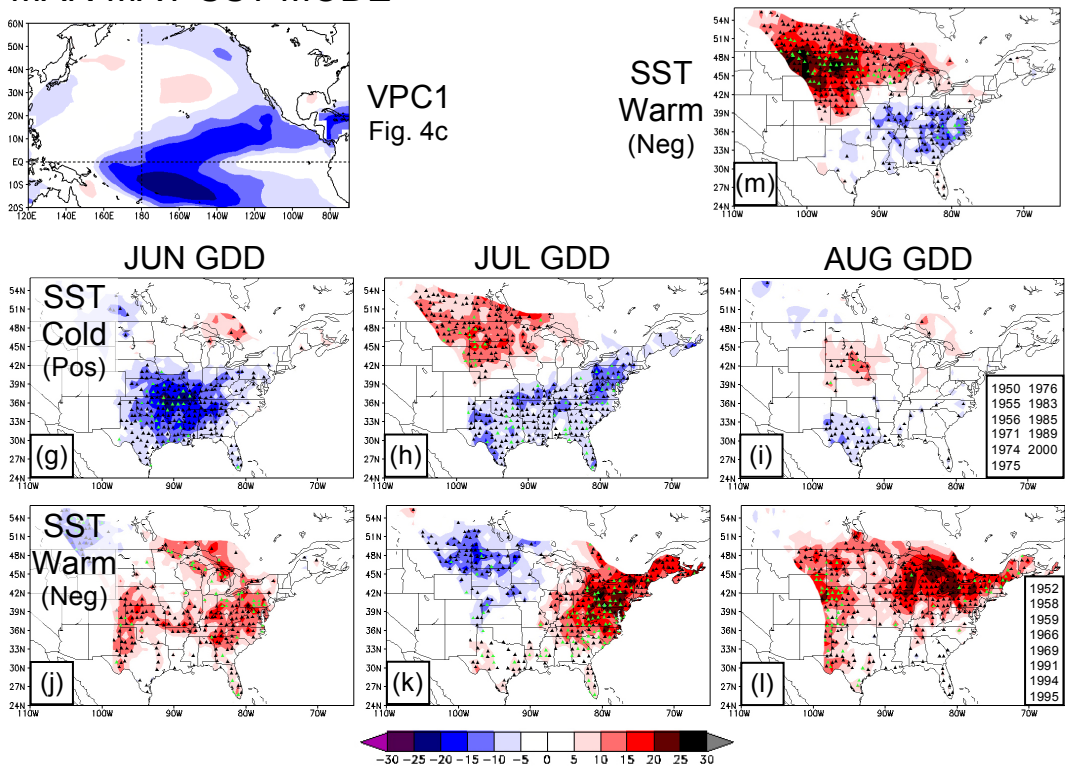


Figure 14. Same as for Fig. 8 except for late summer-to-fall (August-October) monthly January-June, bottom) representations of decaying La Niña (SST Cold) and decaying El Niño (SST Warm) phases identified in Chapter 2d.

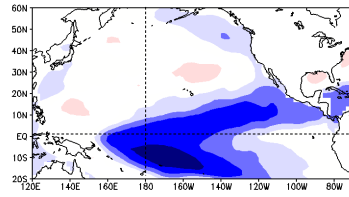
Interestingly, the above positive GDD anomalies, as associated with positive composite anomalies of 500 mb geopotential height as well, emerge first over the western Canadian Prairies during June for the January-March decaying El Niño (Fig. 14d), before strengthening, expanding, and shifting eastward to the Great Lakes Region and Northeast U.S. by August (Fig. 14f). On the other hand, the June positive GDD anomalies over the western Canadian Prairies are largely absent from the March-May SST period composite (Fig. 14j), suggesting that the earlier, northwestern part of this GDD teleconnection hinges on the presence of decaying El Niño from winter into early spring. Since the decaying El Niño pattern during late winter/spring often transitions into a positive PDO by summer, as mentioned above and documented in Section b below, the eastward expansion of these strong positive GDD anomalies during August may be associated with increases in positive SST anomalies over the extreme North Pacific Ocean as warm PDO phases materialize. Conversely, the positive GDD anomalies earlier in the growing season (June) over the western Canadian Prairies likely are linked with the positive SST anomalies in the central tropical Pacific that characterize a decaying El Niño during the preceding late winter into early spring. The similar presence of anomalous GDD warmth during spring over the western Canadian Prairies associated with the ESG anomaly pattern of mature El Niño (Fig. 8f,j,k; 9f,l,m), supports the association of these northwestern GDD anomalies to El Niño-related tropical Pacific SST anomalies.

As mentioned, the above GDD anomaly pattern over the Canadian Prairies and Northern U.S. is highly non-linear during most summer months between decaying El Niño and La Niña events, especially for the winter into spring Pacific SST time periods

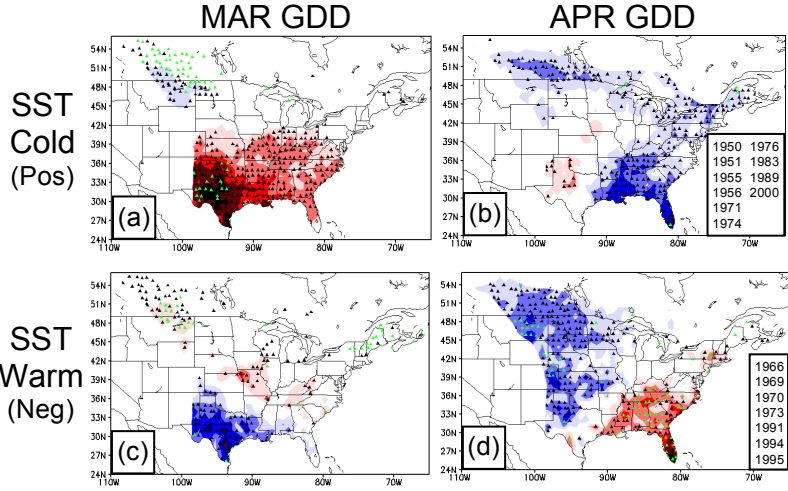
(i.e., January-June and January-March), with a relative absence of counterpart negative GDD anomalies of equal magnitude for decaying La Niñas. However, spring-to-summer decaying La Niñas provide exceptions to the general non-linearity of this midsummer GDD teleconnection. Strong negative GDD anomalies (larger than -20) extend across a large part of the Central U.S., centered over the mid-Mississippi River Valley during June for March-May decaying La Niñas (Fig. 14g), and further north in August for the April-September Pacific SST period (Fig. 13i). The concurrent (or very small lagged) nature of this midsummer teleconnection for decaying La Niña limits its value for relevant farmers compared to the relatively long-lag (2-4 months) GDD associations with decaying El Niños, but still can be used to optimize mid-growing season farming practices that require relatively minimal lead-times.

While non-linearities between El Niño and La Niña teleconnections have been well-documented here, Fig. 15 shows a highly linear association for decaying ENSO conditions that manifests over the Southern Great Plains during early spring. Concurrent with decaying March-May and January-June La Niña (El Niño) conditions, this teleconnection is characterized by particularly strong positive (negative) GDD composite anomalies during March (Figs. 15a,c,e,g) over much of Texas, western Oklahoma, and eastern New Mexico. These positive GDD anomalies also extend into the Southeast U.S. for all above Pacific SST time periods except January-June El Niños (15a,e,g). The relative absence of this Southern Plains GDD teleconnection for the November-April and January-March Pacific SST periods (not shown) confirms the minimal teleconnection lag for this GDD anomaly pattern, at least with regard to decaying El Niño and La Niña events.

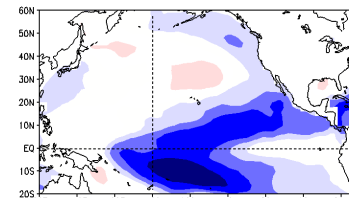
JAN-JUN SST MODE



VPC1
Fig. 3c



MAR-MAY SST MODE



VPC1
Fig. 4c

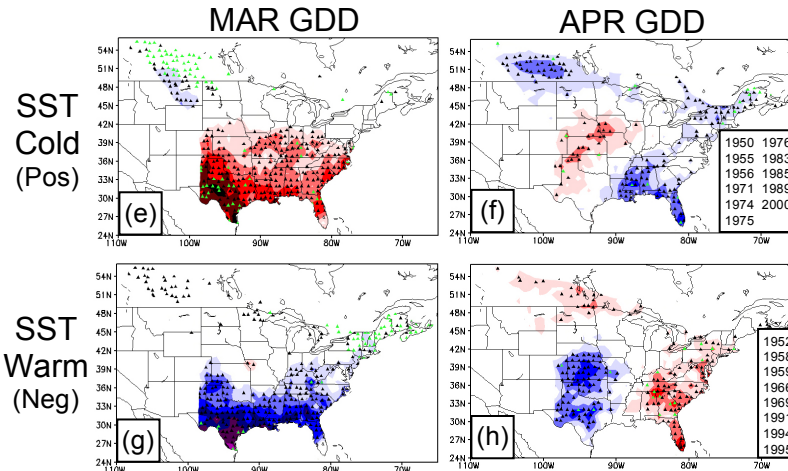


Figure 15. Same as for Fig. 8 except for 6-month (January-June, top) and 3-month (March-May, bottom) representations of decaying La Niña (SST Cold) and decaying El Niño (SST Warm) phases identified in Chapter 2d.

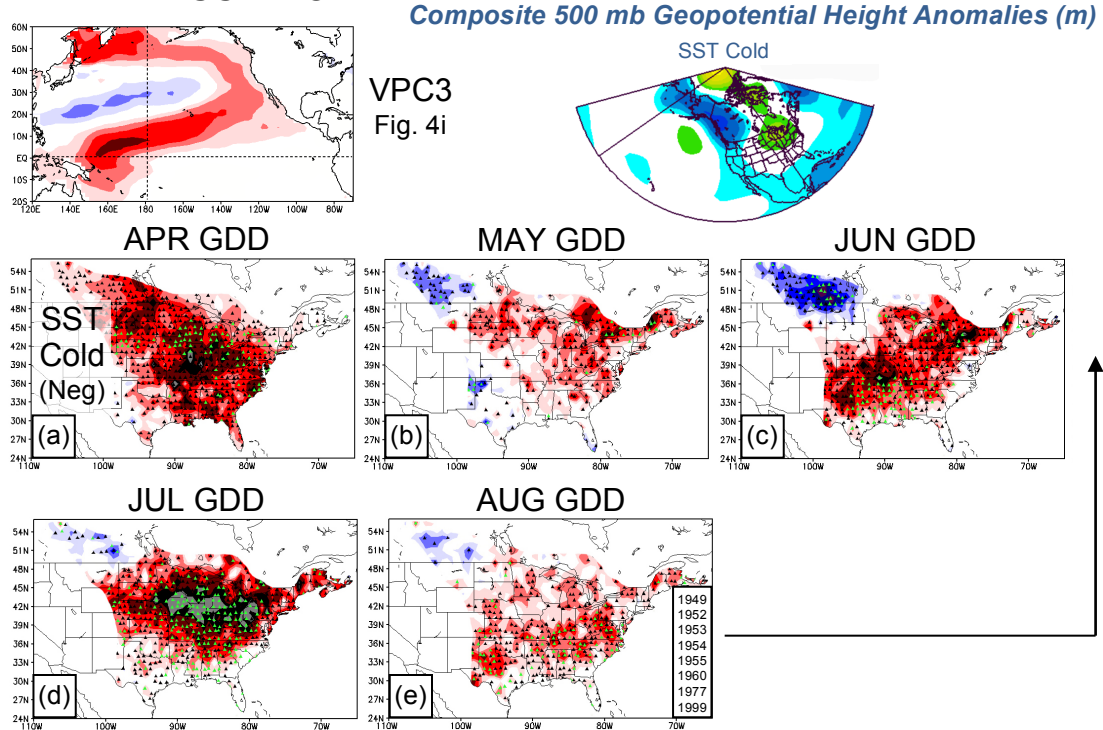
Not surprisingly, however, this concurrent GDD teleconnection with decaying ENSO is similar in timing and scope to the southern branch of the above ESG anomaly pattern during March (also April but much weaker, Fig. 15), which was associated with winter-to-spring mature La Niña and El Niño conditions (Figs. 8a,d; 9a,d). The consistency in emergence and evolution of the southern GDD anomalies of the ESG anomaly pattern between the mature and the “transitional” decaying ENSO modes enhances the robustness of this teleconnection.

e. Pacific Decadal Oscillation (PDO)

Both warm and cold spring-to-summer PDO phases result in one of the most geographically expansive and persistent GDD teleconnections found in the present study, with impactful timing for farmers due to the strongest monthly GDD anomalies encompassing the heart of growing season. This GDD teleconnection is generally quite linear between different PDO phases, with cold (warm) PDO conditions associated with positive (negative) GDD anomalies over large parts of the Central and Northern U.S. during April/May-August and to as late as October for warm PDO (Figs. 16-19). Despite this general linearity -- with the strongest GDD anomalies (of similar magnitudes greater than ± 20) being observed during late spring (April/May) from the Great Plains to the Great Lakes Region for both cold and warm PDO phases (Figs. 16a,f; 17a, 18a,d; 19a,c) -- the constituent GDD anomaly patterns for each phase differ in their summer evolution and persistence, and also in the Pacific SST time periods associated with the strongest spring-to-summer GDD anomalies. Similarly, these

positive GDD anomalies also are associated with positive composite anomalies in 500 mb geopotential height.

MAR-MAY SST MODE



JUN-AUG SST MODE

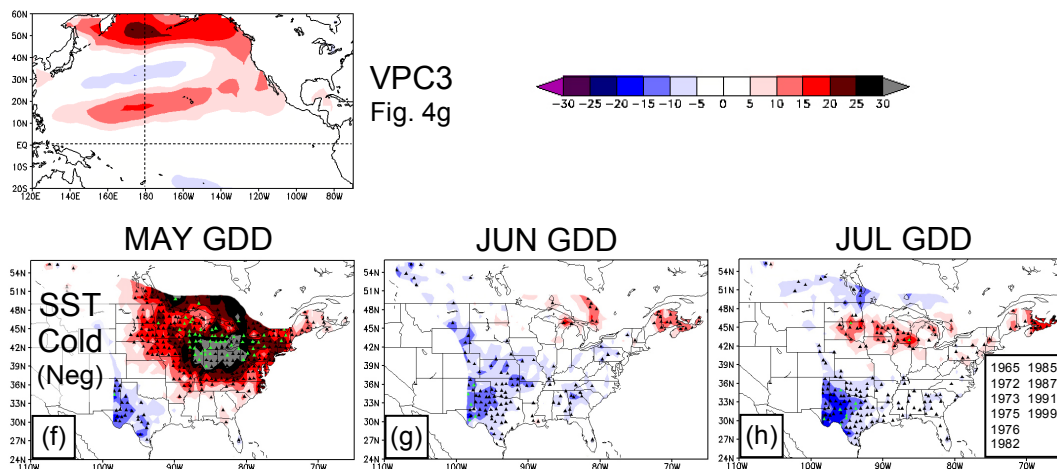


Figure 16. Same as for Fig. 8 except for 3-month (March-May, top; June-August, bottom) representations of decaying La Niña (SST Cold) and decaying El Niño (SST Warm) phases identified in Chapter 2d.

Most notably, the March-May cold PDO phase is associated by April with strong positive GDD anomalies of greater than +15 over most of the study region (Fig. 16a). These GDD anomalies persist through August and are most strong positive during June and July (Figs. 16c,d). Somewhat surprisingly, these strong positive GDD composite anomalies are present only during May for the June-August or April-September PDO SST periods (Figs 16f, 17a), despite prevalence of the PDO mode beyond late spring. Thus, the persistence of these positive GDD anomalies through June-July and even August appears more dependent on cold PDO conditions during the springtime March-May PDO period, rather than the more concurrent June-August and April-September SST periods.

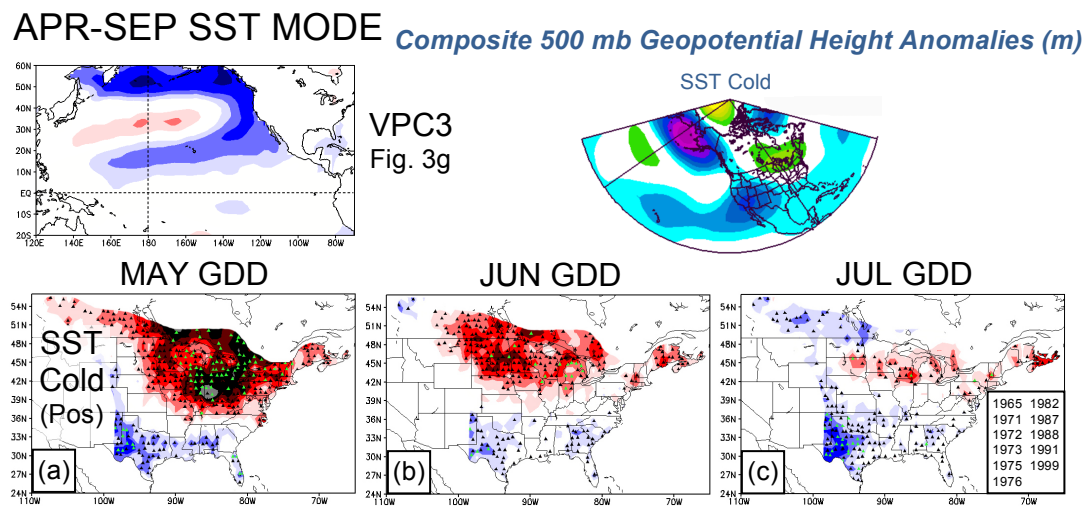


Figure 17. Same as for Fig. 8 except for monthly spring-to-summer (May-July) GDD composite anomalies for 6-month (April-September) representations of cold PDO (SST Cold) phases identified in Chapter 2d. Composite 500 mb height anomaly maps are at top right for the composite months shown of each SST phase (scale -50 to 50 m, interval 5 m).

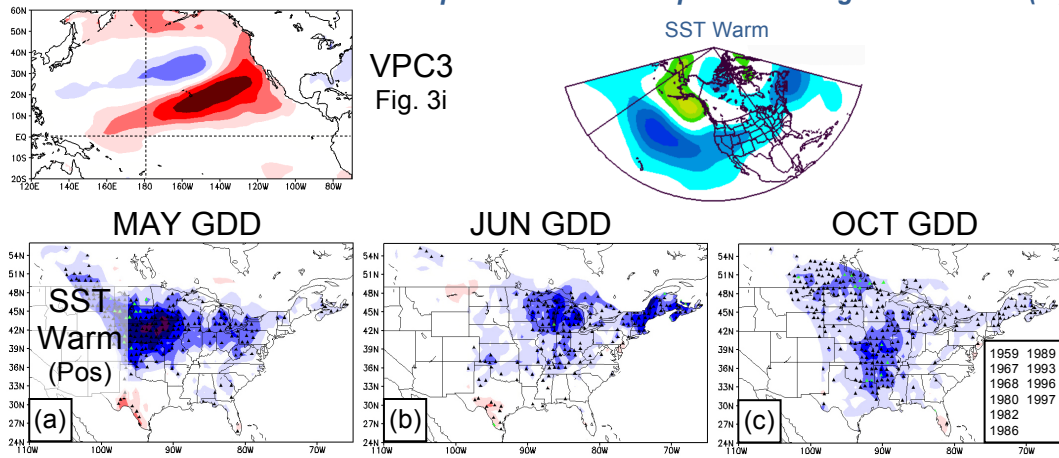
While the strongest and most persistent monthly spring-to-summer GDD composite anomalies for the cold PDO are associated with the March-May SST period - - hence involving a 1-2 month lag with strong positive GDD anomalies associated with

the subsequent summer -- the counterpart negative GDD anomaly patterns associated with warm PDO are less persistent and strongest for the concurrent April-September and June-August SST periods (Figs. 18d-h, 19c-e). Linear to the cold PDO, this negative GDD anomaly pattern peaks during May for the March-May warm PDO events, as well as for the concurrent June-August, January-June, April-September Pacific SST periods (Fig. 18a,d; 19a-c), with GDD anomalies exceeding -25 covering a majority of the North Central U.S. However, different from its cold PDO phase counterpart, the strong negative GDD anomalies during May actually shift completely to strong positive values over the Central U.S. by June for the March-May Pacific SST time period (Fig. 19b). This situation suggests the importance of warm PDO conditions continuing simultaneously through the summer for persistence of these negative GDD anomalies beyond May.

Different from the cold PDO phase, the counterpart negative GDD anomalies for the warm PDO persist coherently beyond May only for the largely concurrent June-August Pacific SST period (Figs. 19e,f). This result would provide very little coherent predictive information, given no teleconnection lag as in the warm March-May PDO conditions. However, also different from the cold PDO phase, these concurrent negative GDD anomalies during the summer of June-August warm PDO events strengthen, expand, and dominate across the entire Eastern U.S. during August and September (Fig. 19f,g), with more than 75% of the statistically significant stations exhibiting strong local pattern robustness.

JAN-JUN SST MODE

Composite 500 mb Geopotential Height Anomalies (m)



APR-SEP SST MODE

Composite 500 mb Geopotential Height Anomalies (m)

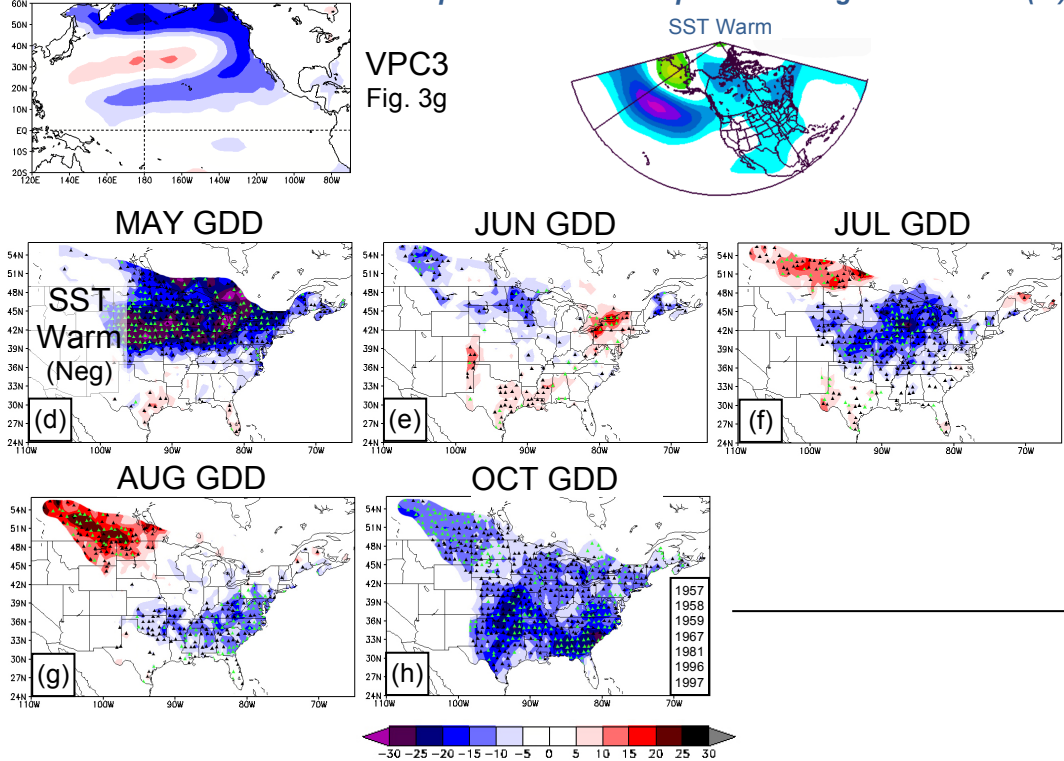
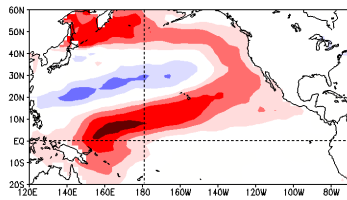
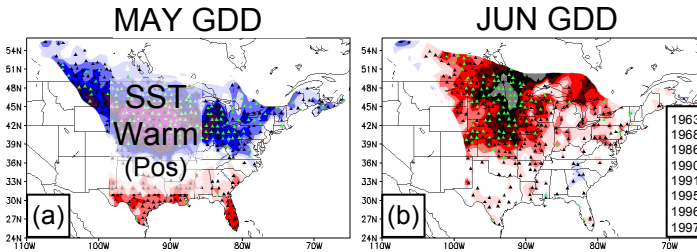


Figure 18. Same as for Fig. 8 except for monthly spring-to-fall (May-October) GDD composite anomalies for 6-month (January-June, top; April-September, bottom) representations of warm PDO (SST Warm) phases identified in Chapter 2d.

MAR-MAY SST MODE

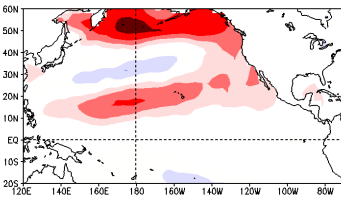


VPC3
Fig. 4i



JUN-AUG SST MODE

Composite 500 mb Geopotential Height Anomalies (m)



VPC3
Fig. 4g

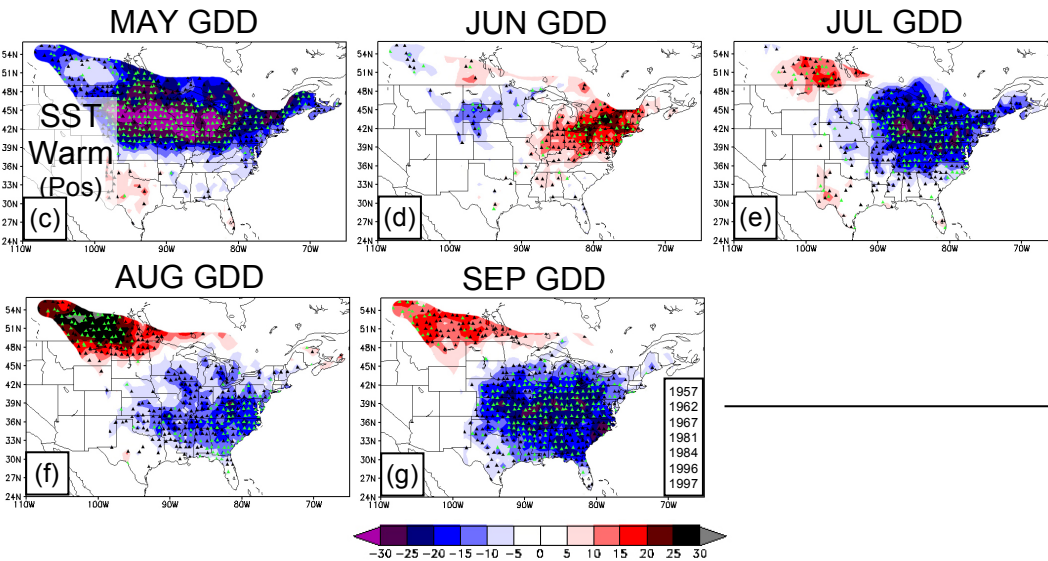
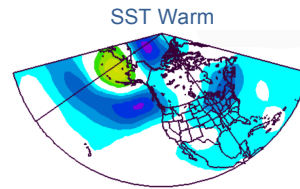


Figure 19. Same as for Fig. 8 except for monthly spring-to-fall (May-September) GDD composite anomalies for 3-month (March-May, top; June-August, bottom) representations of warm PDO (SST Warm) phases identified in Chapter 2d.

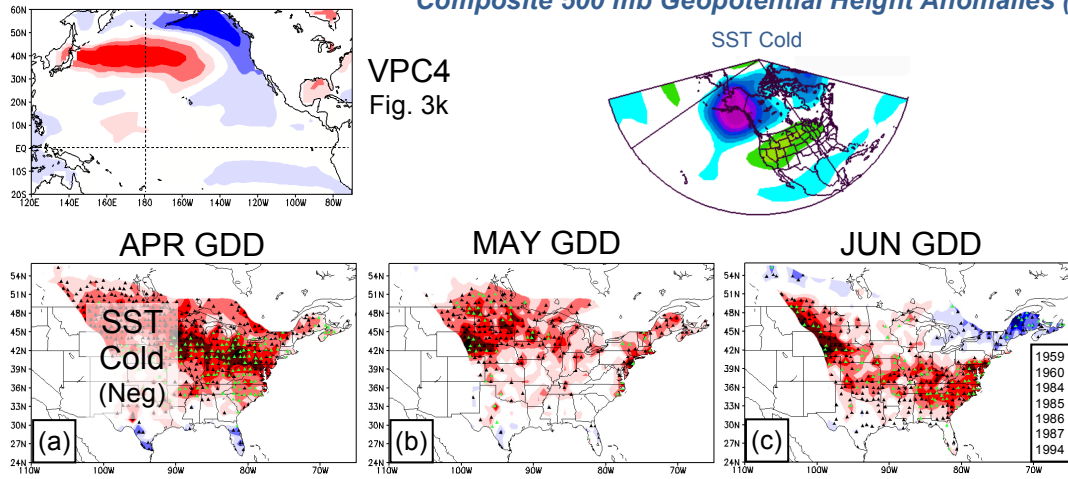
The expansion of these strong negative GDD anomalies (exceeding -25) into the southeastern U.S. during August and September for the June-August warm PDO is particularly important for cotton farmers of this region. Growth inhibitors typically are applied to the cotton crops of the Deep South during late summer into early fall, because post-reproductive cotton is uniquely characterized by rapid, uncontrollable growth that is proportional to GDD. Therefore, the 1-month lagged relationship between June-August warm PDO conditions and the strong negative GDD anomalies during August-September has important management potential for farmers.

f. North Pacific Oscillation (NPO)

A very strong GDD teleconnection associated with the winter-to-spring cold NPO (Figs. 3k,l; 4j,k) is a robust positive GDD anomaly pattern that develops over the far northern part of the study region in southern Canada during April (Figs. 20a, 21a), and expands south to also encompass the northern Great Plains through the Great Lakes Region by summer (Figs. 20c-d, 21c,e-h). This NPO teleconnection is particularly relevant to North American agriculture with strong positive GDD anomalies (greater than +20) of striking geographical coverage dominating primary grain, corn, and soybean growing regions from the Northern Great Plains to the Mid-Atlantic, coinciding with the critical early growth to flowering phases of each. Similar to the PDO, but different than the tropical Pacific Ocean modes (mature and decaying ENSO), the spring-to-summer GDD anomaly patterns for cold NPO conditions for 6-month Pacific SST periods (November-April, April-September; Fig. 20) are much weaker and less-persistent than for the 3-month SST periods (January-March, March-May; Fig. 21).

NOV-APR SST MODE

Composite 500 mb Geopotential Height Anomalies (m)



APR-SEP SST MODE

Composite 500 mb Geopotential Height Anomalies (m)

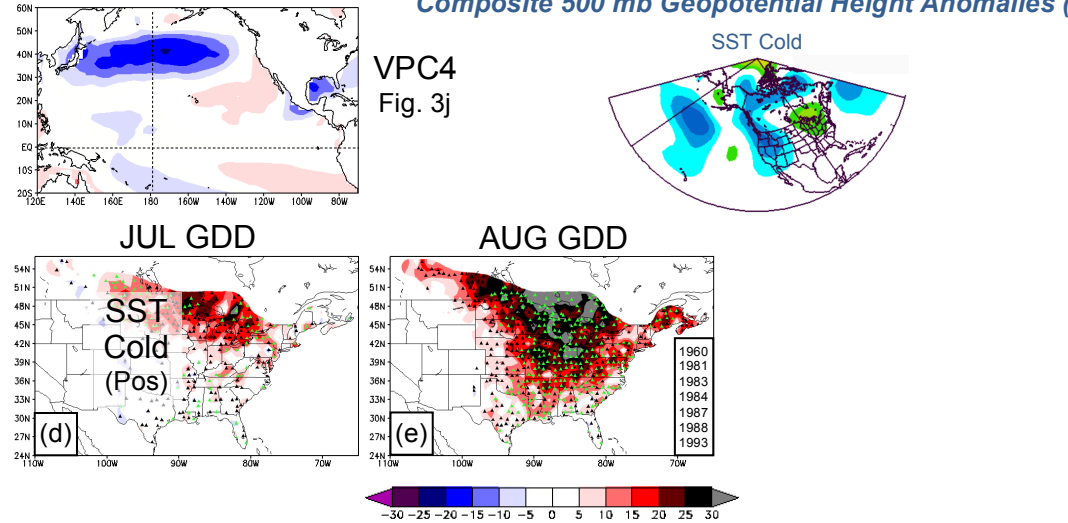
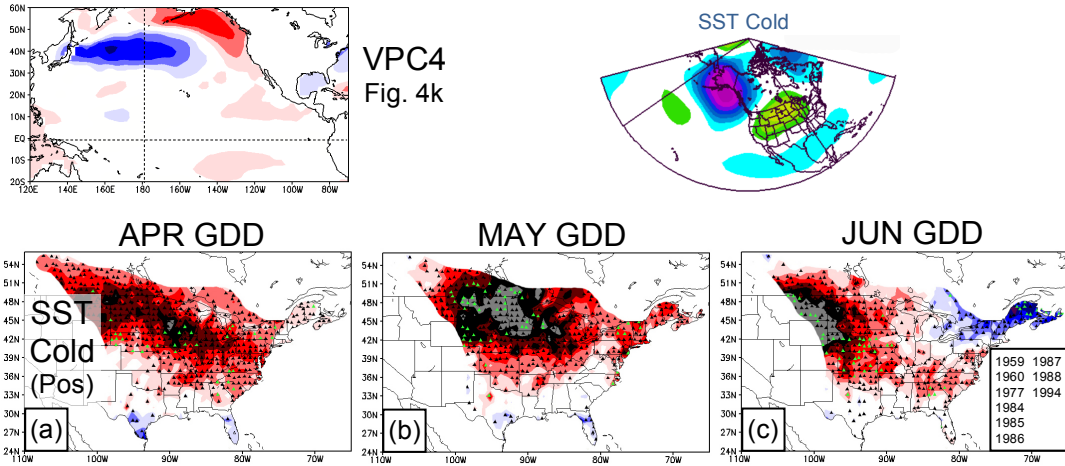


Figure 20. Monthly spring-to-summer (April-August) GDD composite anomalies for 6-month (November-April, top; April-September, bottom) representations of cold NPO (SST Cold) phases identified in Chapter 2d. SST modes are repeated at top, with Pos and Neg on left-hand side indicating phase of above SST mode. Scale at bottom gives GDD anomalies for all panels. Green triangles as defined in Section b. Composite member years are in insets of right panels for each mode. Composite 500 mb height anomaly maps are at top right for the composite months shown of each SST phase (scale -50 to 50 m, interval 5 m).

JAN-MAR SST MODE

Composite 500 mb Geopotential Height Anomalies (m)



MAR-MAY SST MODE

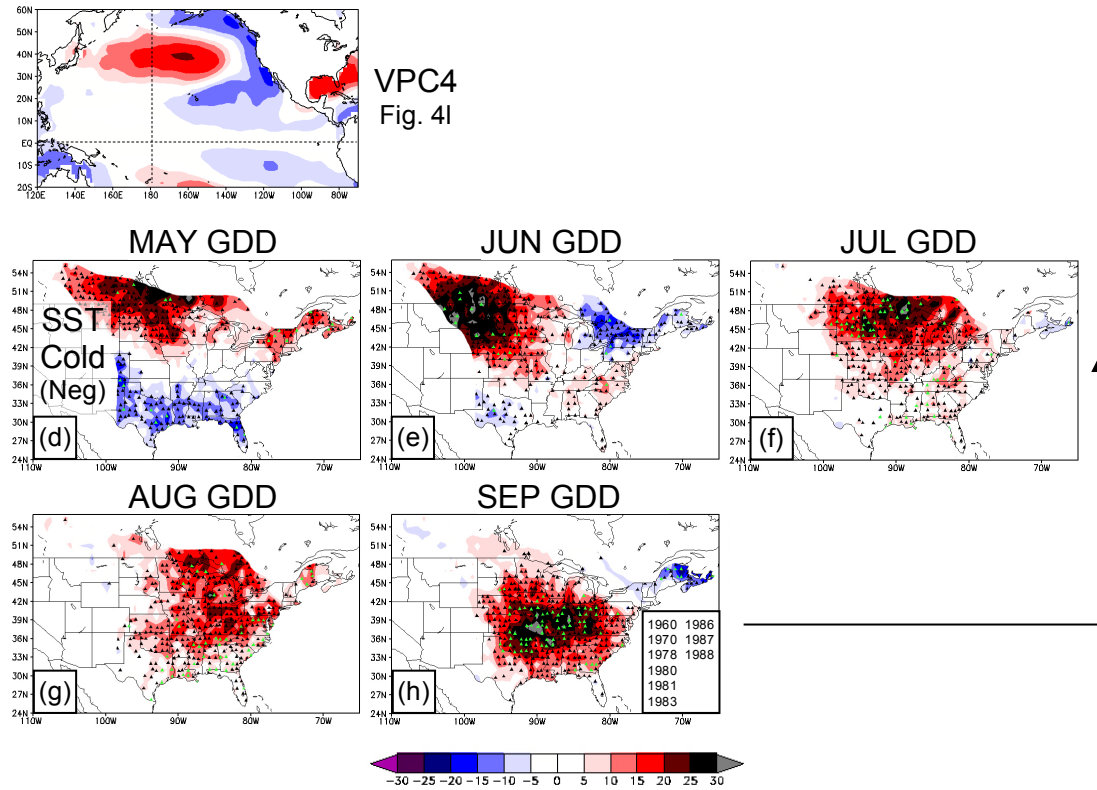


Figure 21. Same as for Fig. 20 except for monthly spring-to-fall (May-September) GDD composite anomalies for 3-month (January-March, top; March-May, bottom) representations of cold NPO (SST Cold) phases identified in Chapter 2d.

The monthly GDD anomaly patterns for the extratropical Pacific SST modes (NPO and PDO) are often strongest for the 3-month SST periods, because of their faster intra-seasonal pattern evolution and more frequent changes in phase from winter to summer (Chapter 2b), and hence, month-to-month GDD teleconnections are more often diluted and under-represented in the composites for 6-month SST periods. Even the subtle eastward expansion of northern Pacific SST anomalies across the Dateline to the Gulf of Alaska that is typically associated with winter-to-summer evolution of NPO can have profound impacts on climate teleconnections downstream. Therefore, composite anomaly analyses for the different 3-month SST periods provide better insight on the evolution and teleconnection lag for this spring-to-summer GDD pattern of cold NPO -- as well as other extratropical NPO/PDO patterns.

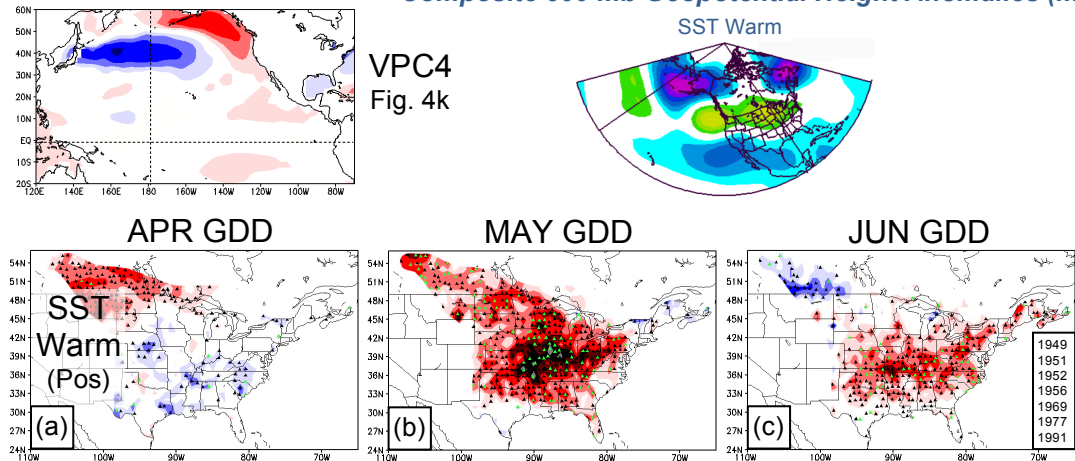
In particular for cold NPO conditions, strong positive GDD anomalies first appear over the Northern High Plains during spring (April for January-March SST, Fig. 21a; May for March-May SST, Fig. 21d), expanding to a maximum coverage and anomaly strength by May (July) for January-March (March-May) cold NPO (Figs. 21b,f), with GDD anomalies greater than +20 GDD encompassing the entire central and northern parts of the study region. Persistence of this expansive pattern of GDD warmth beyond June hinges on the prevalence of cold NPO conditions during the March-May SST period, for which strong positive GDD anomalies (>15) prevail over much of the central/eastern U.S. and southern Canada through September (Fig. 21g,h). The confidence in this strong spring-to-summer GDD warmth materializing as depicted here is relatively high given the prevalence of cold NPO conditions during the January-March or March-May SST period; as supported by the majority (>50%) of stations with

strong GDD composite anomaly values (>15) for these patterns also having greater than 70% local pattern robustness (as indicated by the green triangles in Fig. 21).

Fig. 22 shows the counterpart spring-to-summer (April-July) monthly GDD composite anomalies for January-March and March-May warm NPO. Interestingly, strong and widespread positive GDD anomalies over much of study region are not unique to the cold NPO, but also characterize the May and June GDD anomaly patterns for January-March warm NPO (Fig. 22b,c), and May-July for the March-May SST period (Fig. 22d-f). However, the spatial coverage and evolution of these positive GDD anomalies for warm NPO differ somewhat from those for a cold NPO. Specifically, the positive GDD anomaly region for the January-March and March-May warm NPO first emerges in the Southern U.S. during spring (Figs. 22a,b,d), then expands to the entire Central U.S. by early summer (Figs. 22c,e). The GDD warmth for the March-May positive NPO composite is strongest during June (Fig. 22e), indicating the importance of the warm NPO phase continuing into late spring for the emergence of the Central U.S. GDD anomalies during late spring/early summer. This teleconnection also is prominent during May for the January-March warm NPO composite (Fig. 22b), supporting a consistent two-month teleconnection lag for these positive GDD anomalies. Interestingly, the positive GDD anomalies dissipate in the Central U.S. by July irrespective of whether the NPO warm phase continues through August (not shown).

JAN-MAR SST MODE

Composite 500 mb Geopotential Height Anomalies (m)



MAR-MAY SST MODE

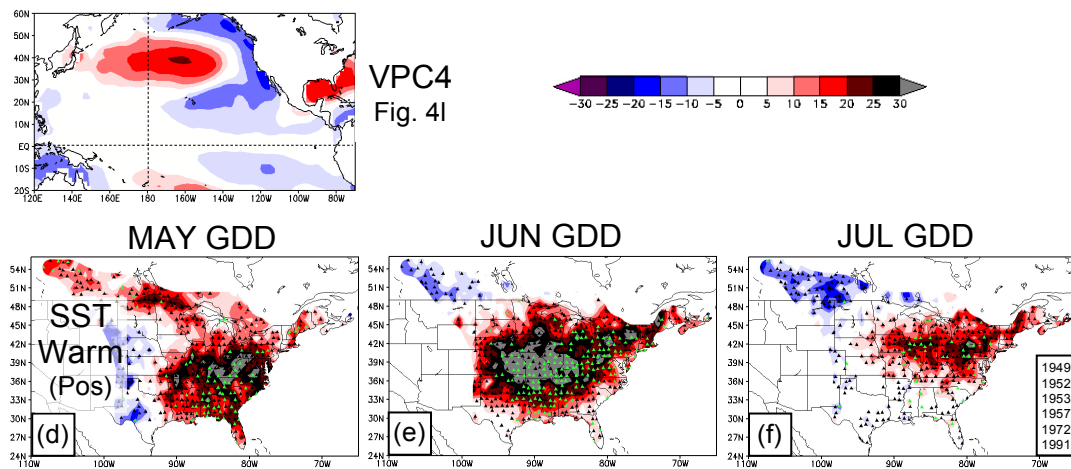


Figure 22. Same as for Fig. 20 except for monthly spring-summer (April-July) GDD composite anomalies for warm NPO (SST Warm) phases identified in Chapter 2d. Composite 500 mb height anomaly maps are at top right for the composite months shown of each SST phase (scale -50 to 50 m, interval 5 m).

The consistent 1-2 month lag associated with the above Central U.S. GDD warmth for both the January-March and March-May NPO warm phase composites (Fig. 22) indicates the high predictive potential of this teleconnection. Supporting further this high predictive potential is the presence of strong positive GDD anomaly stations that also exhibit greater than 70% local pattern robustness, even 1-2 months following the last Pacific SST period month and especially for the June composite of the March-May

NPO warm phase (Fig. 22e). Given this high predictive potential, as well as the fact that the positive GDD anomaly domain encompasses preeminent grain, corn, and soybean growing regions covering most of the Central U.S. from the Great Plains to the Midwest, knowledge of NPO phase can be extremely beneficial for local farmers striving to optimize crop management practices and maximize crop yield.

g. Summary

Fig. 23 provides a visual overview of the most prominent teleconnections identified in the present study between monthly warm-season GDD and four leading modes of tropical and extratropical Pacific Ocean SST variability (Figs. 3, 4). Strong monthly GDD teleconnection patterns were identified for the cold and warm phases of each Pacific SST mode (mature and decaying ENSO, PDO, NPO) and growing season month (March-October), with teleconnection lags ranging from zero (Fig. 23b,e,f,g) to as high as six months for an October GDD anomaly pattern associated with spring decaying ENSO (Fig. 23d). The mature El Niño/La Niña Pacific SST pattern is teleconnected with the largest number of unique monthly GDD teleconnection patterns of relevance (four, Fig. 23a-d), while the most persistent GDD patterns (April-August) were for spring-to-summer PDO (Figs. 3g,i; 4g,i; 23g). In addition to the strong associations identified for mature ENSO and PDO modes, the decaying ENSO and NPO patterns contribute strong teleconnections with monthly GDD during summer, which is a period particularly critical for most North American crops when the temperature and moisture-sensitive crop reproduction takes place.

A majority of the eight main GDD teleconnections identified here for mature and decaying ENSO, PDO, and NPO (Fig. 23a-h), six of them exhibited roughly linear

relationships between the warm and cold phases of each Pacific SST mode (Fig. 23a,c,d,e,f,g); despite the subtle month-to-month differences in strength, morphology, and robustness of the characteristic GDD anomaly patterns as described here in Chapter 4. However, striking non-linearities between warm/cold phases are apparent in the GDD anomaly patterns for summer-to-fall decaying ENSO (Fig. 23b) and winter-to-spring NPO (Fig. 23h) -- both for summer-to-fall monthly GDD. The general linearity exhibited between the warm and cold phases of most Pacific Ocean SST modes studied here, as well as the inherent subtle month-to-month non-linearities that can be identified with more detailed inspections of the individual GDD composite anomaly patterns; are consistent with the findings for North American temperature and precipitation with tropical Pacific SST patterns in Montroy et al. (1998). Each of the strongest teleconnections identified above also are associated with counterpart composite patterns in 500 mb geopotential height to support pattern robustness.

One of the strongest GDD teleconnection patterns identified in the present study is the ESG anomaly pattern (Section c, above), associated primarily with winter-to-spring mature ENSO modes (November-April, January-June, January-March, March-May SST periods) and manifesting during March-May (Fig. 23a). This mature ENSO teleconnection is the only springtime GDD anomaly pattern that materializes at consistent time lags at least 1-2 months from the preceding associated Pacific SST period (e.g., November-April, January-March). Therefore, the ESG anomaly pattern possesses enhanced predictive potential during the critical spring planting periods, particularly for the preeminent cotton- and grain-farming regions of the southern U.S.

and northern Great Plains/Canadian Prairies, where the strongest and most robust GDD anomaly patterns prevail during March-May with the ESG anomaly pattern (Fig. 23a).

Different aspects of the ESG anomaly pattern also appear in other Pacific Ocean SST modes, including both phases of spring decaying ENSO and PDO (i.e., March-May SST period), but at lesser robustness, coverage, and with zero teleconnection lags for spring GDD anomaly patterns. (Fig. 23e,g). More specifically, spring decaying El Niño (La Niña) conditions are associated with what appear to be the southern branch GDD anomalies of the above ESG anomaly pattern, but with the warm (cold) anomalies more concentrated along the extreme southern U.S. from Texas to the Southeast U.S. (Fig. 23e). Both the northern (Northern Plains/Canadian Prairies) and southern branches of the ESG anomaly pattern are present in the spring (and extending through summer) GDD anomaly composites for concurrent PDO SST periods (Fig. 23g), but with a slight shift to the north and expansion east of the southern warm (cold) GDD anomalies with cold (warm) PDO.

Beyond spring, the ESG anomaly pattern persists into summer given spring PDO warm/cold conditions, thus provides additional predictive potential for this ever-critical period in crop maturation -- summer flowering and reproduction -- across much of the prime agricultural-growing regions in North America stretching from the Canadian Prairies to the Mid-Atlantic (including grains, corn, and soybeans). This prominence of the ESG anomaly pattern with not only winter-to-spring mature ENSO, but also spring decaying ENSO and spring-to-summer PDO, is a consequence of the inter-modulation between these Pacific Ocean SST patterns that is also apparent in the materialization of their downstream GDD anomaly patterns during spring and summer.

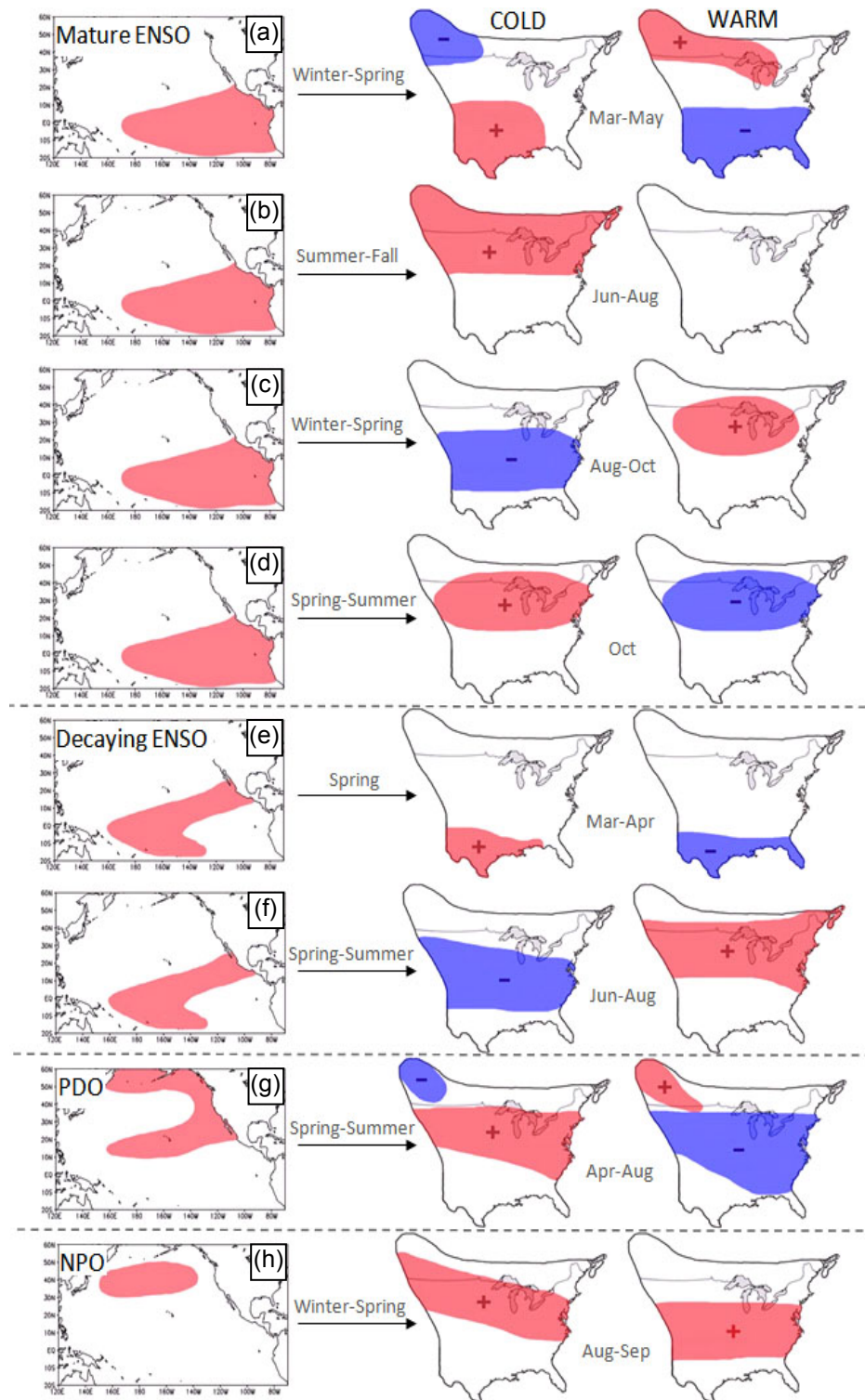


Figure 23. Generalization of the main GDD composite anomaly patterns teleconnected with the cold and warm phases of (a-d) mature ENSO, (e-f) decaying ENSO, (g) PDO, and (h) NPO.

For example, the strong lagged teleconnection between winter-to-spring mature El Niño/La Niña phase and spring-to-summer ESG anomalies (Fig. 23a), and the more concurrent association with spring-to-summer decaying El Niño/La Niña (Fig. 23e) is partly attributed to the tendency of mature ENSO events decaying from east-to-west during spring-to-summer (Chapter 2d). Similarly, the ESG anomaly pattern appears to expand and shift slightly north to encompass the Great Lakes region, hinging on the cold/warm decaying ENSO conditions transitioning into a cold/warm PDO by summer (Fig. 23g). Consequently, the teleconnection patterns presented here for multiple different 3- and 6-month Pacific SST periods for each mode of variability helps to provide insight on the impacts of such seasonal SST pattern evolutions on the morphology of their downstream GDD anomaly patterns.

Separate from the ESG anomaly pattern, most of the GDD composite anomaly patterns identified here manifest in summer-to-fall and are teleconnected with winter-to-spring Pacific SST modes (mature ENSO, Fig. 23d; decaying ENSO, Fig. 23f; NPO, Fig. 23h). Therefore, teleconnection lags of one month to several months provide added predictive potential for these summer-to-fall GDD anomaly patterns, which are of enhanced importance given heightened climate sensitivities of crops between reproduction and fall harvest. The spatial coverage of these summer-to-fall GDD patterns are very similar between the above winter-to-spring Pacific SST modes, and roughly linear between the warm and cold SST phases, with strong composite anomalies stretching across the entire central and northern parts of the study region (Fig. 23d,f,h). Similar to the ESG anomaly pattern, the consistent morphology of this summer-to-fall GDD anomaly pattern between the mature ENSO, decaying ENSO, and

NPO of different SST time periods shows the inter-modulation within this GDD teleconnection between these different Pacific SST modes (i.e., winter-to-spring mature El Niño/La Niña often transitioning into a decaying El Niño/La Niña of similar phase by summer). The present study provides insight on how this seasonal evolution of four main Pacific SST modes impacts the morphology of monthly GDD anomaly patterns downstream, and explores in more detail (Chapter 6e, below) the potential predictability of each teleconnection summarized in Fig. 23.

Chapter 5. Monthly Precipitation Teleconnections

a. Background

Similar to the GDD teleconnection pattern analyses of Chapter 4, monthly precipitation composite anomalies were computed for each station in the study region (Fig. 5) for each 3- and 6-month Pacific SSTA mode (Figs. 3 and 4), based on their associated constituent years. Several previous studies have indicated the linkage between El Niño/La Niña and spring-to-summer anomalous precipitation in North America (Ropelewski, 1988; Trenberth et al., 1988; Trenberth and Branstator, 1992; Kunkel et al., 1995; Montroy et al., 1998; Barlow et al., 2001; Bates et al., 2001; Fye et al., 2004). Bates et al. (2001) even identified associations between ENSO and individual monthly anomalous precipitation events in North America, including the devastating floods of summer 1993 that ravaged the Corn Belt and other parts of the Central U.S. during the prevalence of a mature El Niño in the eastern Tropical Pacific.

While the association between ENSO and warm-season North American precipitation has been well-documented in previous literature, the month-to-month composite anomaly analyses presented below for March-October precipitation provide unique insight on the teleconnection lags and evolution of coherent precipitation anomaly patterns associated with ENSO, PDO, and NPO. These Pacific Ocean SST variability patterns and SST time periods (January-March, March-May, June-August, November-April, January-June, April-September) considered in the present study also provides the level of comprehensiveness necessary to understand the complex relationships between the Pacific Climate System and North American warm season climate. Hence, the following March-October precipitation patterns identified for

ENSO (mature and decaying), PDO, and NPO using the same composite analysis methodology as for GDD (Chapter 4b), not only supplement previous research on this subject, but in particular enhance the usefulness of this climate information for the North American farmer.

b. Methodology

The same delineation of warm and cold Pacific Ocean SSTA modes as the monthly GDD composite analyses (Chapter 4) was used to derive the characteristic precipitation anomaly patterns (Sections c-g, below). Similarly, the monthly March-October precipitation anomaly fields associated with each Pacific SST pattern (Figs. 3-4) were based on 1949-2000 means computed by averaging across the constitute years for the warmest and coldest phases of each SSTA mode. Inches/month (25.4 mm/month) was retained as the dimension for the precipitation anomalies since inches are more easily understood and conceptualized by North American farmers. Two-tailed t-tests also were employed to identify the composite anomalies that are statistically different from zero at the 95% confidence level (t value = 3.29; Wilks, 2006, pp. 467; Montroy et al., 1998).

Also like the GDD composite analyses, local pattern robustness was computed for each station contributing the strongest monthly precipitation anomaly patterns. To reiterate, a monthly composite anomaly that is statistically significant at the 95% confidence level is deemed “robust” when 70% or more of the constituent years also exhibit statistically significant anomalies of the same sign (“local pattern robustness” of ≥ 0.70). Like for the above GDD analyses, computation of local pattern robustness is

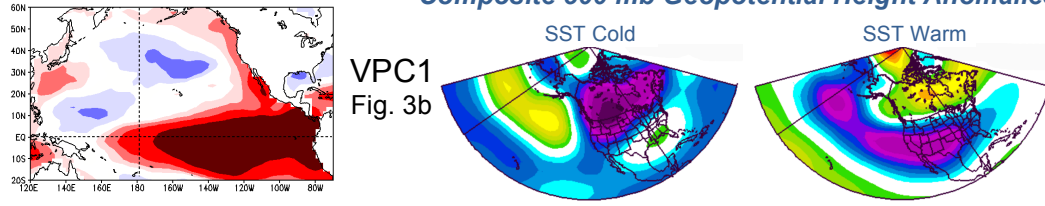
intended to provide predictability information for the strongest monthly precipitation anomaly patterns, since this station-level metric reveals how consistently the wetness or dryness materialized for the same historical month and Pacific Ocean SSTA conditions at particular location. The geographical coverage of stations with high local pattern robustness (location, density, scope) also is a measure of monthly precipitation anomaly pattern strength, and reveals the specific regions within a pattern where the wetness/dryness is most likely to materialize given similar evolution of the associated Pacific SST regime. The locally robust stations within the monthly precipitation anomaly composites (Figs. 24-35, below) are denoted with a yellow triangle instead of the green triangles used for GDD (Figs. 8-22, above). Precipitation composite anomalies that are statistically significant at the 95% confidence level, but with local pattern robustness values less than 0.70 are plotted with black triangles.

c. Mature ENSO

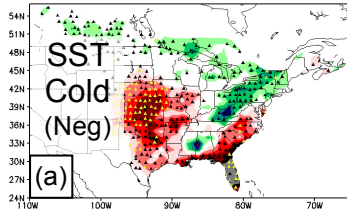
The strongest and most widespread monthly precipitation anomaly patterns occur during early spring (March-April) and are associated with mature El Niño and La Niña for the winter-to-spring Pacific SST periods (November-April, January-June, January-March, March-May; Figs. 3b,n; 4b,n). Characterized by strong and robust precipitation anomalies across much of the central/southern study region during March-April (Figs. 24, 25), this precipitation pattern has striking similarities in geographic coverage and seasonal timing to the southern branch of the ENSO Spring GDD (“ESG”) anomaly pattern (Chapter 4c). This early spring teleconnection will henceforth be termed the ENSO Spring Precipitation (“ESP”) anomaly pattern.

NOV-APR SST MODE

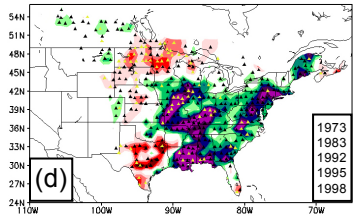
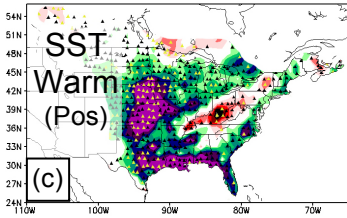
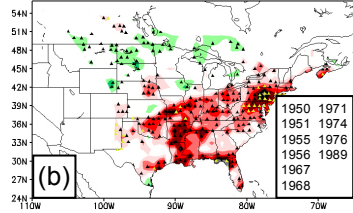
Composite 500 mb Geopotential Height Anomalies (m)



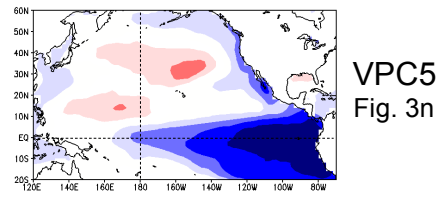
MAR PRECIP



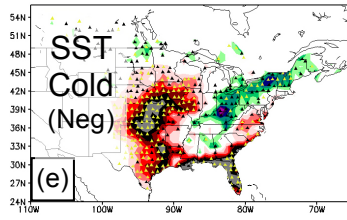
APR PRECIP



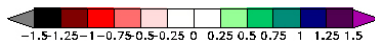
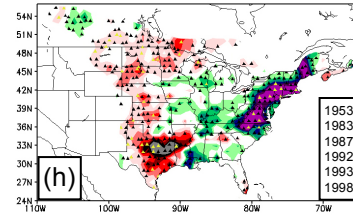
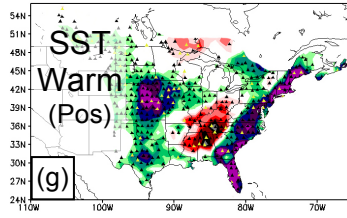
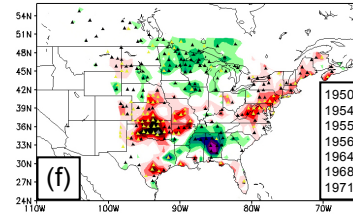
JAN-JUN SST MODE



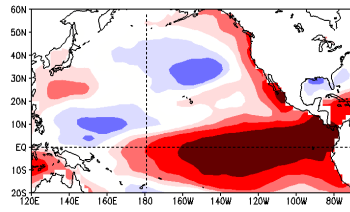
MAR PRECIP



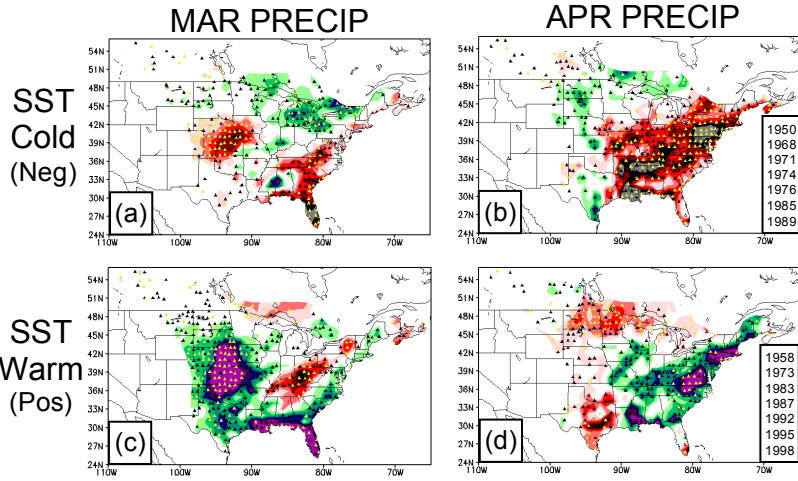
APR PRECIP



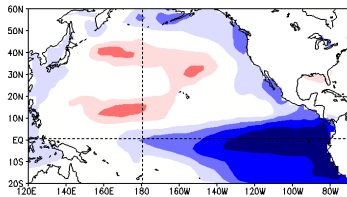
JAN-MAR SST MODE



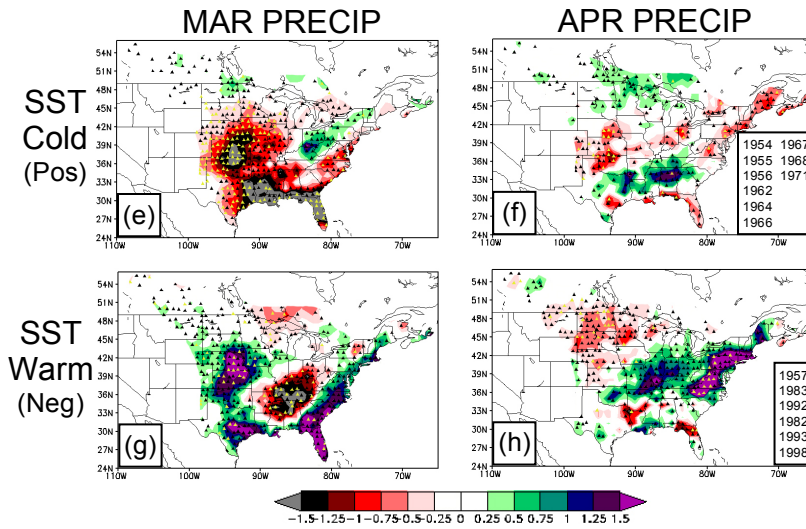
VPC1
Fig. 4b



MAR-MAY SST MODE



VPC5
Fig. 4n



Figures 24-25. Monthly spring (March-April) GDD precipitation anomalies for 6-month (November-April, top; January-June, bottom; Fig. 24) and 3-month (January-March, top; March-May, bottom; Fig. 25) representations of mature La Niña (SST Cold) and mature El Niño (SST Warm) phases identified in Chapter 2d. SST modes are repeated at top, with Pos and Neg on left-hand side indicating phase of above SST mode. Scale at bottom gives GDD anomalies for all panels. Green triangles as defined in Section b. Composite member years are in insets of right panels for each mode. Composite 500 mb height anomaly maps are at top right for the composite months shown of each SST phase (scale -50 to 50 m, interval 5 m).

Similar to the ESG anomaly pattern, the strongest composite precipitation anomalies of the ESP pattern first develop by March over the central and southern Great Plains and stretch east across the Gulf Coast Region to the Florida Peninsula. Strong positive monthly anomalies of greater than +1.25 inches (extreme wetness) are prevalent in these regions for winter-to-spring mature El Niño, and strong negative anomalies of equivalent magnitude (extreme dryness) and geographic coverage accompany La Niñas (Figs. 24a,c,e,g; 25a,c,e,g). This large-scale, relatively linear (between warm and cold SST phases) March precipitation pattern covering much of the central/southern U.S. is strong and robust (see yellow triangles in Figs. 24a,c; 25a,c) for the November-April and January-March ENSO SST periods (especially El Niño), and thus possesses enhanced predictive potential. Also similar to the ESG anomaly pattern, negative (positive) 500 mb geopotential height composite anomalies over the northwest Pacific Ocean are associated with winter-to-spring mature El Niño (La Niña; Fig. 25, upper-right panels).

However, different from EL Niño, the negative composite anomalies over the central/southern Great Plains with mature La Niña are weaker (-0.50 to -1.0 central, absent southern) for these early SST time periods, especially January-March SST (Fig. 25a), than for January-June and March-May which exhibit widespread dryness of -1.50

inches and greater across the southern Great Plains and Gulf Coast regions (Figs. 24e, 25e; respectively). This suggests that the La Niña pattern must typically persist into spring for the ESP anomaly pattern, or dryness across the Great Plains, to materialize, but still shows teleconnection lags of 1-2 months with predictive potential given the weaker but statistically significant/locally robust (see yellow triangles in Figs. 24e, 25e) dryness over the central Great Plains and far Southeast U.S.

The Great Plains/southern U.S. spring wetness with the ESP anomaly pattern for El Niño (Figs. 24c,d,g,h; 25c,d,g,h) is attributed to a stronger Subtropical Jet Stream emanating from the Tropical Pacific during winter into spring, and an increased frequency and intensity of embedded vorticity maxima that yield abundant precipitation (Montroy et al., 1998; Barlow et al., 2001; Fye et al., 2004). These vorticity maxima with the stronger, El Niño-fueled Sub-Tropical Jet Stream also have a more southern track along the Gulf Coast Region to the Southeast U.S. during winter to spring, resulting in much above normal precipitation there as well (Figs. 24c,g; 25c,g). Conversely, La Niña results in dryness over these areas (Figs. 24a,b,e,f; 25a,b,e,f) with an associated weaker Sub-Tropical Jet Stream, since much of the spring precipitation over the central/southern Great Plains is from a more westward phasing of troughs in the Subtropical and Polar Front Jet Stream just east of the Rocky Mountains, and upper-level cyclonic systems tend to have a more northerly track.

The above dry (wet) spring pattern over much of the Central U.S following winter-to-spring La Niña (El Niño) events is consistent with the longer-term findings of Fye et al. (2004), who performed composite analyses for periods of extended wetness and drought during 20th century warm seasons. As mentioned above (Chapter 1a), Fye

et al. (2004) showed that persistent El Niño conditions prevailed in the Tropical Pacific Ocean during the pluvial of 1905-1917, with La Niña prevalent during the Dust Bowl of 1929-1940 and Central U.S. drought of 1946-1956. The shorter-term, monthly ESP anomaly pattern also is consistent with the monthly spring precipitation composites identified by Montroy et al. (1998) and Barlow et al. (2001) for mature El Niño/La Niña.

While this large-scale March precipitation pattern that encompasses much of the central/southern U.S. exhibits striking linearity between the warm and cold mature ENSO phases, a relatively small precipitation anomaly region of equivalent strength but opposite sign (dryness) materializes concurrently from the northern Gulf Coast states to the Ohio River Valley for winter-to-spring El Niño (Figs. 24c,g; 25c,g). Interestingly, counterpart patterns of wetness over the same region are largely absent in the winter-to-spring La Niña precipitation anomaly composites for March (Figs. 24a,e; 25a,e). This relatively subtle, non-linear pattern of March dryness is much stronger for the January-June and March-May mature El Niño, with both associated March composites having precipitation anomalies greater than -1.5 inches over much of Kentucky/Tennessee (Figs. 24g; 25g); suggesting a dependence of this precipitation pattern on the persistence of El Niño through spring. This El Niño-related dryness surrounded by the strong wetness of the ESP anomaly pattern can be attributed to intense anticyclones north and west of the stronger and more frequent storm systems embedded in the Sub-Tropical Jet Stream (Montroy et al., 1998; Barlow et al., 2001; Fye et al., 2004).

Different from March, the most striking precipitation anomaly feature of the April ESP anomaly pattern that also is highly linear between SST phases is a drastic

weakening of the Great Plains dryness/wetness in March for both mature El Niño and La Niña phases of all four winter-to-spring SST periods (Figs. 24b,d,f,h; 25b,d,f,h). Meanwhile, a strengthening and expansion of positive precipitation anomalies ($\geq +1.25$ inches) across the East Coast from the Carolinas north to the Canadian Maritimes characterizes the April composites for mature El Niño for all winter-to-spring SST periods (Figs. 24d,h; 25d,h). In contrast, strong April dryness (monthly anomalies of -1.0 inches and greater) predominates in the same area for only the November-April and January-March SST periods (Figs. 24b, 25b). The April wetness (dryness) is most expansive for the earlier winter-to-spring SST time periods of November-April (January-March) mature El Niño (La Niña), with widespread anomalies of greater than $+1.25$ (-1.25) inches extending from the East Coast to the eastern fringe of the Great Plains. A majority ($> 80\%$) of these statistically significant anomalies have greater than 0.70 local pattern robustness (Figs. 24b,d; 25b,d). However, the El Niño-related April wetness is focused along the East Coast for the later winter-to-spring SST time periods (January-June, March-May), while the April dryness with mature La Niña is near completely absent (Figs. 24f,h; 25f,h). This suggests that materialization of the April ESP anomaly pattern across much of the central and eastern parts of the study region has little dependence on the persistence of the mature ENSO phase beyond March, but has enhanced predictive potential given the strength and robustness of this teleconnection with the earlier SST time periods.

All facets of the above ESP anomaly pattern disappear by May for each SST time period (not shown), which is different than the more persistent ESG anomaly pattern for March-June GDD identified in Chapter 4c (Figs. 8, 9). However, the lack of

persistence beyond April for the ESP anomaly pattern should not lessen its importance for North American farmers, because the associated widespread wetness/dryness in March-April coincides with spring planting (i.e., North Carolina/South Texas cotton, March 1-April 1; Texas Panhandle grain sorghum, April 15-June 7) and subsequent early crop growth phases of the central/southern study region. Each of the five AAPEX farmers (Table 2, above) interviewed in the present study emphasized the importance of sufficient rainfall during spring for optimum crop maturation, but also stressed that too much rainfall during spring planting substantially disrupts field operations.

Beyond spring into the heart of summer, monthly teleconnections of wetness generally are not as strong or robust as the patterns of dryness, especially across the southern part of the study region because warm season precipitation there largely is attributed to random air-mass thunderstorm development and not the passage of synoptic-scale mid-latitude cyclones (e.g., Fig. 26b,c,f,g,h). By June, the Polar Front Jet Stream is typically located across the northern U.S./southern Canada and predominantly north of the international border by July-August. Since teleconnections between North American precipitation and Pacific Ocean SST patterns are modulated largely by Rossby Wave-related jet stream displacements (Horel and Wallace, 1981; Hoskins and Karoly, 1981), any associated patterns of summer-to-early fall wetness are more prevalent in the northern U.S. and southern Canada where the Polar Front Jet Stream typically resides. However, patterns of summer monthly dryness are more common in the southern U.S., since anomalously low mid-summer precipitation most often is attributed to strong, persistent anticyclones and suppression of air mass thunderstorm development to the south of the Polar Front Jet Stream.

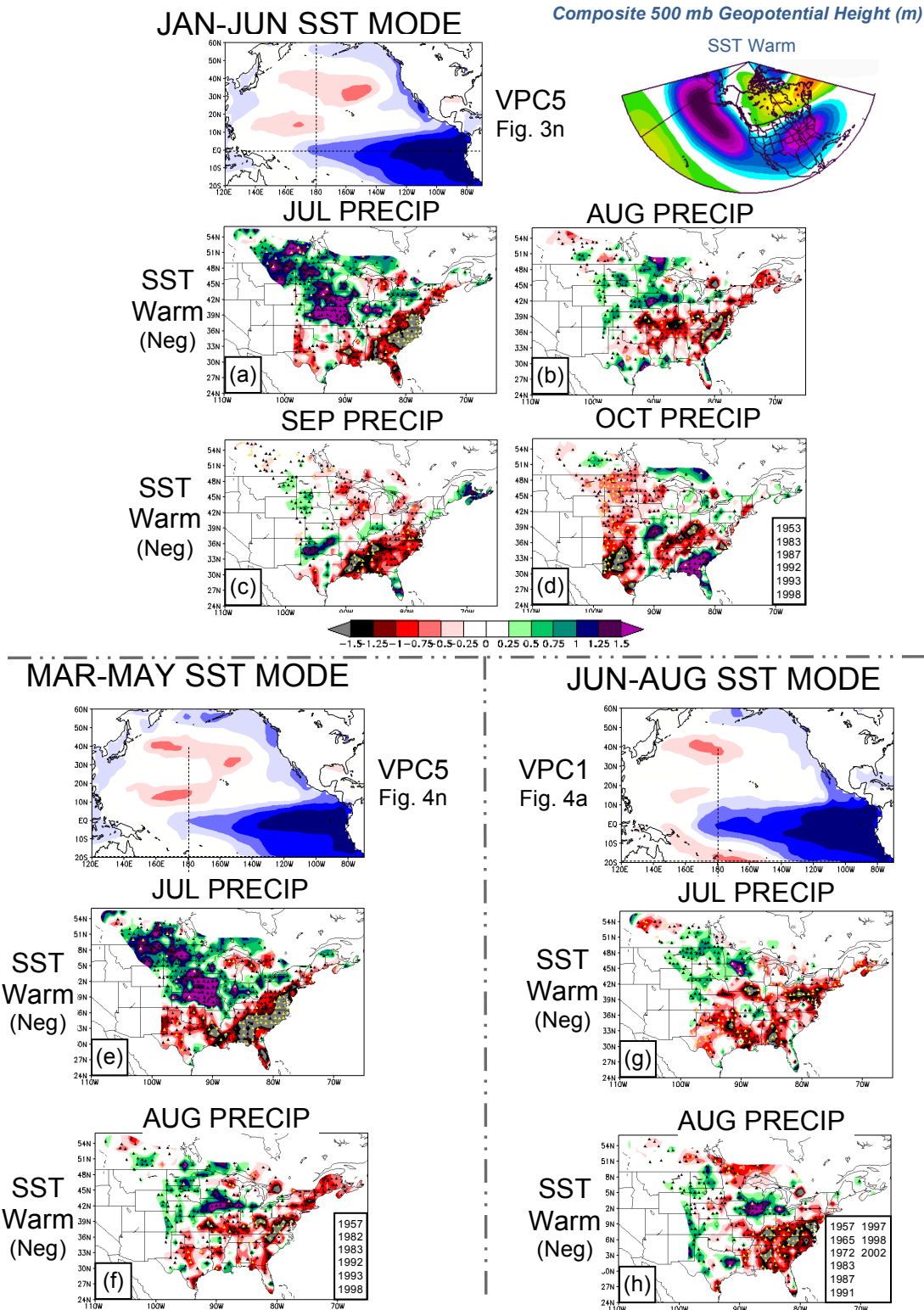


Figure 26. Same as for Fig. 24 except for summer-to-fall (June-October) monthly precipitation for 6-month (January-June, top) and 3-month (March-May, bottom-left; June-August, bottom-right) representations of mature La Niña (SST Cold) and mature El Niño (SST Warm) phases identified in Chapter 2d.

This 4-5 month period of dryness in the central/southern U.S. is accompanied by less-persistent wetness (July-August for January-June and March-May SST; Fig. 26a,b,e,f) of smaller spatial coverage in the northern Great Plains to southern Canada (Fig. 26). Dissimilar to the ESP anomaly pattern (Fig. 24, 25 above), this summer-fall precipitation pattern only is associated with the warm phase of mature ENSO (El Niño) and lacks a La Niña counterpart pattern. This summer-fall precipitation pattern is overall strongest in July for the January-June and March-May Pacific SST periods (Fig. 26a,e). Greater than +1.25 inch anomalies prevail from Kansas and Missouri to southern Alberta for both SST time periods, and larger than -1.25 inch anomalies occur across the entire Southeast U.S. to as far northeast as New England. The consistency in the evolution of this July precipitation pattern for both January-June and March-May SST periods, but an absence from the January-March and November-April SST periods (not shown), indicates that the northern Great Plains July wetness ($> +1.25$ inch anomalies) and strong Southeast U.S. dryness (> -1.25 inches) are dependent on a mature El Niño phase persisting into the spring.

This July precipitation anomaly pattern weakens substantially for the June-August mature El Niño (Fig. 26g), especially for the northern Great Plains wetness, which signifies that persistence of the El Niño beyond May is not a necessary condition for this teleconnection to materialize. The positive precipitation anomalies from the central Great Plains to southern Canada completely disappear by August for all Pacific SST time periods, except January-June (albeit weaker), where +0.75 to +1.25 inch August anomalies persist over a smaller region in the central Canadian Prairies and northern Great Plains (Fig. 26b). The confinement of the July wetness to the northern

Great Plains and southern Canada is consistent with the more northern track of the Polar Front Jet Stream by midsummer, as explained above.

Also consistent with the more northern jet stream track in midsummer, the strong dryness of this precipitation pattern is confined to the southern U.S. (especially the southeast) in July and August for all El Niño SST periods (Fig. 26a-b,e-h), and persists there through October for January-June El Niño conditions (Fig. 26c,d). By August, this southern dryness is strongest and most expansive for the June-August SST period, with large pockets of greater than -1.50 inch anomalies persisting from the central Gulf Coast Region to the Carolinas. Strong negative precipitation anomalies are also present in August for the January-June and March-May mature El Niño composites (Fig. 26b,f), but with the strongest anomalies (> -1.25 inches) confined to the East Coast from the Carolinas to the Mid-Atlantic. This robust southern U.S. dryness persists with similar strength and coverage into September (Fig. 26c) and October (Fig. 26d) for the 6-month January-June El Niño, but disappear in the composites for the 3-month SST periods (March-May, June-August; not shown). Therefore, the persistence of drought conditions into fall (September, October) in the southern U.S. hinges on a more persistent mature El Niño event from the previous winter to spring (i.e., January-June; 6 months).

Even for the less persistent and robust pattern of July wetness in the northern Great Plains/southern Canada, the SST time periods for which this pattern is strongest (January-June, March-May; Fig. 26a,e) precede the July composite month by one-to-two months. Additionally, the above more widespread and persistent southern U.S. dryness associated with mature El Niño conditions has an even greater teleconnection

lag of up to 3 months (i.e., fall of January-June mature El Niño, Fig. 26c,d). Therefore, this summer-to-fall precipitation anomaly pattern of mature El Niño, which lacks a La Niña counterpart precipitation pattern, possesses enhanced predictive potential. This predictive potential is supported by the relatively high fraction of statistically significant station anomalies that also have local pattern robustness values greater than 0.70 -- for the above peak composite months of northern wetness (~50%, July, January-June SST; Fig. 26a) and southern dryness (>70%, July-September, January-June SST; Fig. 26a-c). However, the absence of linearity between ENSO phases reduces the frequency of precipitation pattern occurrence when this predictive information could be utilized.

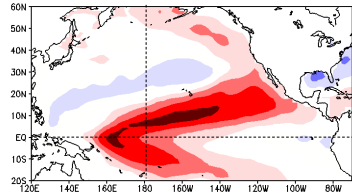
Despite only being associated with mature El Niño conditions, the predictive potential of this summer-fall precipitation pattern, and the coincidence of the associated regions of wetness/dryness with critical flowering/reproductive windows for all five focus crops (Chapter 3d, Table 3), enhances substantially the utility of this agroclimate information for North American farmers from the Great Plains to the Southeast U.S. The persistent precipitation shortages across the entire Southeast U.S. from July to as late as October are especially critical for the extensive cotton crops grown there, because sufficient moisture and nutrient uptake is vital during summer-fall for cotton bolls to reach full maturity (Hodges et al., 1993; Stewart et al., 1993; Wrona et al., 1998; Armah-Agyeman, 2002). Meanwhile, the above normal July precipitation over the vast grain farming country from the U.S. Great Plains to southern Canada can be very beneficial for spring wheat and grain sorghum crops, which also have heightened moisture uptake during midsummer flowering.

d. Decaying ENSO

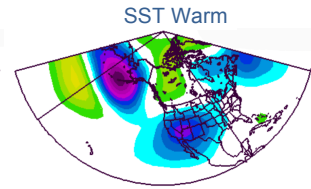
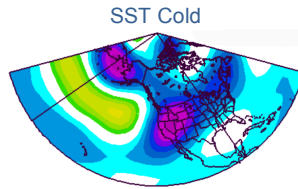
The main SST characteristic that differentiates between a decaying and mature La Niña (El Niño) pattern, as defined in the present study, is the relative absence of cold (warm) SST anomalies in the tropical Pacific Ocean east of 160-140°W longitude, following a northward displacement of these SST anomalies to the subtropical Pacific Ocean (Chapter 2d, above). Despite previous research emphasizing that the strongest North American climate teleconnections with the Pacific Climate System stem from SST anomalies residing in the subtropics (Karoly and Hoskins, 1981; Horel and Wallace, 1981), the overall strength and coverage of the spring precipitation anomaly patterns for winter-to-spring decaying La Niña/El Niño are weaker than for the above ESP anomaly pattern of mature ENSO. The most striking example of these relative weaknesses in the spring precipitation patterns for decaying ENSO is a complete absence of the strong March precipitation anomalies over the central/southern Great Plains (not shown), which is a predominant ESP anomaly pattern feature of both phases for mature ENSO (La Niña, dryness; El Niño wetness; Figs. 24a,c,e,g; 25a,c,e,g). The relative weaknesses of the spring precipitation anomaly patterns here likely are attributed to the absence of SST anomalies in the eastern Tropical Pacific. These overall weaker precipitation teleconnections for decaying El Niño/La Niña are consistent with Karoly and Hoskins (1981) and Horel and Wallace (1981), which demonstrate the importance of diabatic heating minima/maxima over subtropical Pacific Ocean for enhancement of North American monthly-to-seasonal climate teleconnections. This situation is consistent with subtropical Pacific SST variability being stronger for the decaying ENSO pattern than mature ENSO (Figs. 2, 3).

JAN-MAR SST MODE

Composite 500 mb Geopotential Height Anomalies (m)



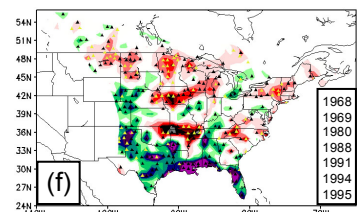
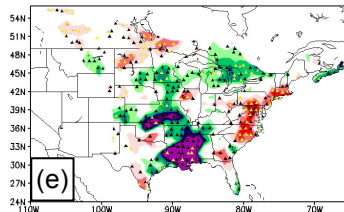
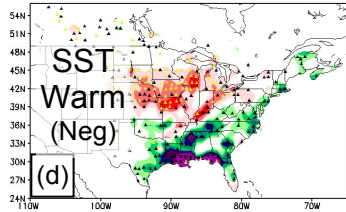
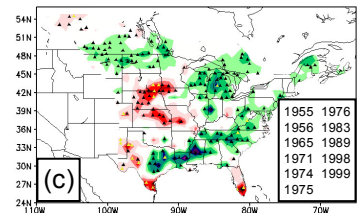
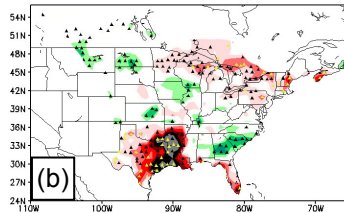
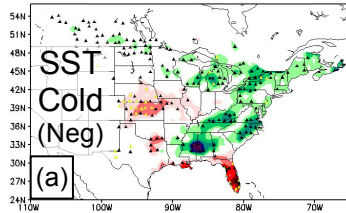
VPC3
Fig. 4h



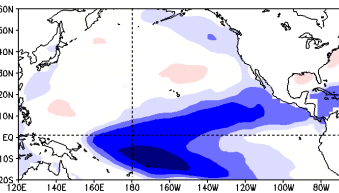
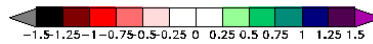
MAR PRECIP

APR PRECIP

MAY PRECIP



JAN-JUN SST MODE



VPC1
Fig. 3c

APR PRECIP

MAY PRECIP

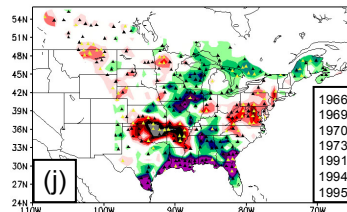
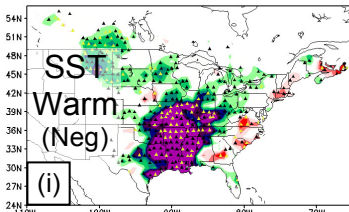
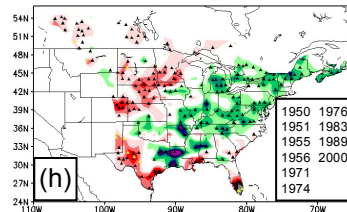
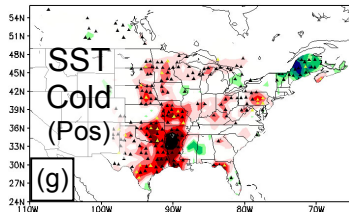


Figure 27. Same as for Fig. 24 except for spring (April-May) monthly precipitation for 3-month (January-March, top) and 6-month (January-June, bottom) representations of mature La Niña (SST Cold) and mature El Niño (SST Warm) phases of Chapter 2d.

Compared to the strong precipitation teleconnections of the ESP anomaly pattern for mature La Niña -- including not only the Great Plains March dryness (Figs. 24a,e; 25a,e) but also the vast eastward expansion of strong negative anomalies by April for the January-March SST period (Fig. 25b) -- spring composite anomaly patterns for winter-to-spring decaying La Niña are strikingly weak (Fig. 27a-c,g,h). The April composite for January-March decaying La Niña shows the only relevant precipitation pattern for the cold phase of this ENSO pattern, albeit comparatively small in geographic coverage, with a small region of strong and predominantly robust anomalies (greater than -1.5 inches) concentrated southward from Arkansas/southeast Oklahoma to the Gulf of Mexico.

Different from La Niña, strong spring precipitation patterns are teleconnected with winter-to-spring decaying El Niño, although not nearly as widespread as the ESP anomaly pattern for mature El Niño. However, similar to the ESP anomaly pattern, the spring monthly composites for decaying El Niño are characterized by wetness over much of the extreme southern U.S. (March-May precipitation, Fig. 27d-f,i,j). This shared southern wetness between mature and decaying El Niño is associated with the stronger than normal Subtropical Jet Streams that emanate from the anomalously warm central Tropical Pacific Ocean, which is typical of both ENSO patterns (Ropelewski, 1988; Trenberth et al., 1988; Trenberth and Branstator, 1992; Montroy et al., 1998; Barlow et al., 2001; Fye et al., 2004).

Interestingly, while spring precipitation anomaly patterns generally are stronger and more widespread for mature ENSO conditions of both warm and cold phases, the El Niño-related patterns of spring southern wetness are most persistent for the decaying El

Niño patterns. More specifically, strong positive monthly anomalies (greater than +1.0 inches) are prevalent across much of the Gulf Coast Region in each monthly composite during March-May for both January-March and January-June SST periods (Fig. 27d-f, i-j). Despite the January-June SST period having the strongest and most widespread April-May monthly anomaly patterns for decaying El Niño (Fig. 27i,j), the similar persistence of the southern wetness through May for the January-March SST period (Fig. 27e,f) is most relevant to the farming industry in the study region (Fig. 5) because of the 1-2 month teleconnection lag (i.e., robust April, May precipitation patterns following January-March SST period). Thus, equal emphasis is placed on both the strength/robustness of the agroclimate teleconnections identified and the time lag between the composite month and associated SST period, as motivated by our dual-perspective, agro-meteorological approach in shaping the methodologies and analyses of the present study.

As a more specific example, the strongest and most widespread spring precipitation pattern associated with decaying El Niño is for April of the January-June SST period, with greater than +1.25 inch anomalies covering a majority of the central U.S. from Illinois to the Gulf of Mexico and the eastern Great Plains to the Ohio River Valley (Fig. 27i). Despite its geographical expansiveness, this April precipitation pattern also is characterized by the highest fraction ($> 2/3$) of statistically significant anomalies with local pattern robustness values greater than 0.70. Still though, while intriguing and informative from a meteorological perspective, the concurrent timing of this April composite pattern and associated January-June SST time period limits the predictive potential for this teleconnection, as with other concurrent agroclimate

teleconnections. However, these concurrent patterns can be used to support the coherency of lagged relationships such as the April-May southern U.S. wetness for January-March decaying El Niño. Given the greater agricultural relevance of possible lagged spring teleconnections for the January-March SST period, a more detailed month-by-month inspection of these March-May precipitation composite anomaly patterns (Fig. 27d-f) follows below.

For January-March El Niño conditions, March precipitation anomalies in excess of +1.5 inches are concentrated along the immediate Gulf of Mexico coastline from southeast Louisiana to the Florida Panhandle (Fig. 27d). However, despite this overlap with the January-March SST period, a negligible percentage of even the strongest March precipitation anomalies have greater than 0.70 local pattern robustness values (Fig. 27d). Similarly in April, strong positive precipitation anomalies of greater than +1.25 inches attain much greater northward extent than March, stretching from southeastern Texas to western Alabama, north through the lower Mississippi River Valley to the Ohio River (Fig. 27e). Also different than March, greater than 50% of these strong April precipitation anomalies show local pattern robustness values greater than 0.70, despite a one month time lag from the January-March SST period (yellow triangles, Fig. 27e).

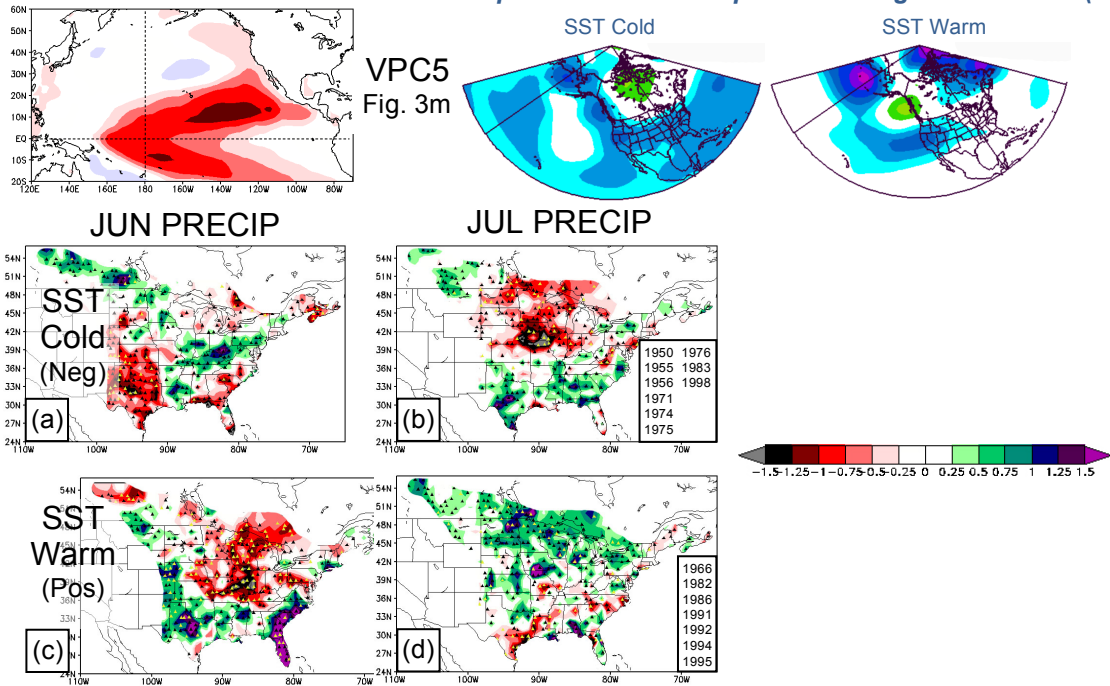
The May precipitation pattern for the January-March decaying El Niño (Fig. 27f) has positive precipitation anomalies of similar geographic coverage and strength as March (Fig. 27d) along the Gulf Coast Region, but +0.25 to +0.75 inch anomalies stretching west across all of Texas to the southwestern Great Plains. Embedded within this southern Great Plains wetness are widely scattered pockets of strong positive

anomalies of +1.25 inches and greater in Texas and eastern New Mexico, with a majority of these stronger western anomalies also having pattern robustness values over 0.70. Interestingly, a relatively small but strong pattern of dryness (> -1.50 inch anomalies) develops in May with decaying El Niño conditions for both January-March (Fig. 27f) and January-June (Fig. 27j) SST periods, from across the Ozark Mountain Region of northern Arkansas east to the Mississippi River. A vast majority of these strong negative anomalies also have greater than 0.70 local pattern robustness, even at two-month time lags.

The enhanced persistence of these spring (March-May) positive precipitation anomalies in the southern U.S. for decaying El Niño conditions compared to the ESP anomaly pattern of mature El Niño, is consistent with the enhanced importance of subtropical Pacific Ocean SST anomalies in modulating North American climate shown in Hoskins and Karoly (1981) and Horel and Wallace (1981). Since decaying El Niño (and La Niña) is distinguished from mature El Niño here by the northward displacement of warm SST anomalies from the eastern tropical Pacific Ocean (160°W to Peruvian Coast) to the subtropics, the northerly migrating Polar Front Jet Stream by late winter into spring can impinge on these subtropical diabatic heating maxima later in the seasonal cycle. As the Polar Front Jet Stream continues to migrate farther north and traverses the far northern Pacific Ocean by summer, the mid-latitude modes of Pacific SST variability such as NPO and PDO become increasingly important modulators of North American climate (Wallace and Gutzler, 1981; Namias et al., 1988; Barlow et al., 2001).

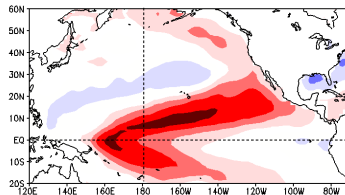
APR-SEP SST MODE

Composite 500 mb Geopotential Height Anomalies (m)



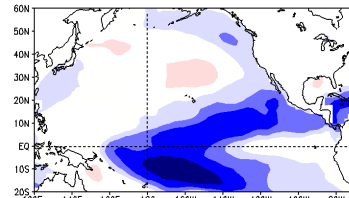
JAN-MAR SST MODE

VPC3
Fig. 4h



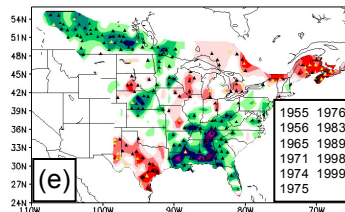
MAR-MAY SST MODE

VPC1
Fig. 4c



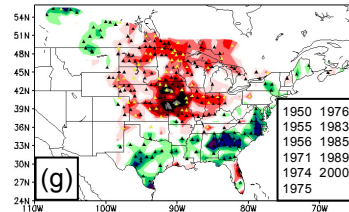
JUN PRECIP

SST
Cold
(Neg)

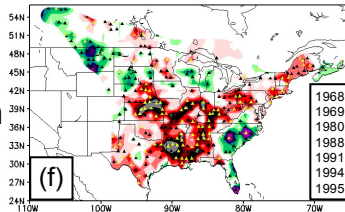


JUL PRECIP

SST
Cold
(Pos)



SST
Warm
(Pos)



SST
Warm
(Neg)

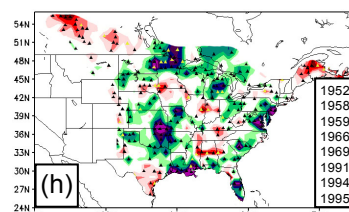


Figure 28. Same as for Fig. 24 except for early summer (June-July) monthly precipitation for 6-month (April-September, top) and 3-month (January-March, bottom-left; March-May, bottom-right) representations of decaying La Niña (SST Cold) and decaying El Niño (SST Warm) phases of Chapter 2d.

Contrary to spring, equally strong and robust precipitation patterns are prevalent for both decaying La Niña and El Niño for the mid-summer (June, July), particularly for the January-March, March-May, and April-September SST time periods (Fig. 28). Also different from spring, the June and July composites for decaying ENSO have vastly contrasting precipitation anomaly patterns for the above agriculturally relevant Pacific SST time periods, despite the striking month-to-month persistence in the spring patterns associated with this SST mode (March-May) evident in Fig. 27. June-July monthly precipitation composites are shown for the April-September (Fig. 27a-d; June, July), January-March (Fig. 27e,f, June), and March-May (Fig. 27 g,h, July) SST periods for decaying La Niña and El Niño conditions, which include all teleconnections of any relevance. For example, July composite patterns for the January-March SST period were not shown in Fig. 27 because of a complete absence of coherent precipitation anomaly regions for both decaying ENSO phases. June precipitation composites for the March-May SST time period were excluded here for the same reason.

Overall, the June-July composite patterns associated with decaying La Niña and El Niño are strongest for the 6-month April-September SST modes, but any predictive information that can be inferred from these concurrent teleconnections is limited by the overlap between precipitation composite month and SST time period. However, the strongest June-July precipitation patterns for the 3-month SST time periods (January-March, June precipitation; March-May, July; Fig. 28e-h) can be used to evaluate the sensitivity of these June-July precipitation anomaly patterns to the persistence of the decaying ENSO conditions (i.e., by comparing 3-month with 6-month SST teleconnections), as well as identify predictive potential via teleconnection lags. For

June of April-September decaying La Niña, a pattern of dryness encompasses the central and southern Great Plains, with -0.50 inch and greater anomalies from Kansas southward, and a region of stronger dryness (-1.0 to -1.5 inch anomalies) from eastern New Mexico to western Texas (Fig. 28a).

Strong negative precipitation anomalies (greater than -1.5 inches) also develop across extreme southern Mississippi to the Florida Panhandle as part of June pattern, but weaker positive anomalies (no stations with local pattern robustness values greater than 0.70) encompass the Ohio River Valley northwest to the Canadian Prairies. The June dryness in the southern U.S. for April-September decaying La Niña is then replaced by positive precipitation anomalies for July across the southern Great Plains to eastern Gulf Coast Region (Fig. 28b).

This July southern wetness is characterized by widespread relatively weak positive anomalies (+0.25 to +0.75 inches), with localized regions of stronger wetness in central Texas and southern Georgia/extreme northern Florida (+1.0 inch anomalies and greater). Even for these stronger July positive anomalies in the Deep South, none of the constituent station anomalies exhibit local pattern robustness values greater than 0.70. This indicates that given April-September decaying La Niña conditions, the June to July “flip-flop” from dryness to wetness across the southern U.S. has relatively low predictive potential. Only ~56% of the composite years (1950, 1955, 1971, 1975, 1976) show positive precipitation anomalies in July across any of the southern U.S from Texas eastward. The strongest and most robust July precipitation pattern for April-September decaying La Niña, is a localized region of -1.5 and greater precipitation anomalies centered over eastern Nebraska, northern Missouri, southern Iowa, and extreme western

Illinois (Fig. 28b). This feature also is inconsistent with the June composite. Nearly all of these -1.25 inch and greater anomalies in July over the central Missouri River Valley show local pattern robustness values greater than 0.70, with widespread statistically significant positive anomalies (~50% locally robust) extending as far north as southwest Ontario (Fig. 28b).

The June and July monthly composites for April-September decaying El Niño also show substantial month-to-month disparities in the associated precipitation anomaly patterns, with June having the strongest teleconnection patterns (Fig. 28c). Similar to April-September decaying La Niña, a general flip-flopping in precipitation anomaly sign is apparent between the June and July composite patterns. Specifically, the June precipitation anomaly pattern shows strong dryness (-1.0 inch anomalies and greater) across most of the Corn Belt from the central Missouri River Valley to the southwest Great Lakes Region, with concurrent strong wetness (+1.5 inch and greater June anomalies) to the south across the Florida Peninsula/eastern Carolinas and Northwest Texas (Fig. 28c). More than 75% of the strongest negative and positive June anomalies (± 1.0 inches and greater) for the April-September warm SST phase also show local pattern robustness values of at least 0.70. The strong Midwest dryness in June associated with this decaying El Niño pattern is replaced in July by widespread modest positive precipitation anomalies covering nearly the entire northern half of the U.S. to southern Canada (Fig. 28d). Only a few small, isolated areas of stronger wetness (+1.5 inch anomalies and greater) are embedded within (Fig. 28d). Even the strong and particularly robust positive anomalies in June across parts of the southern

U.S. are replaced by negative, albeit very weak, precipitation anomalies by July for April-September decaying El Niño.

Analyses of the June and July precipitation anomaly patterns for the 3-month SST periods (January-March, March-May) for both decaying La Niña and El Niño provide insight into these June-to-July disparities (Fig. 28e-h). For La Niña, the above southern Great Plains June dryness prevalent with the April-September SST period weakens and shrinks in geographical coverage for June following the January-March SST period, with only +0.25 to +0.50 inch anomalies limited to central and southeast Texas (Fig. 28e). Meanwhile for July of decaying La Niña modes, the composite precipitation patterns associated with the April-September (above) and March-May SST periods are nearly identical (Fig. 28b,g). This suggests that the central and northern U.S. dryness is associated most strongly with the early part of the April-September SST period for decaying La Niña.

The differences in the June precipitation composites are more substantial between April-September and January-March decaying El Niño than La Niña, with the above strong central U.S. dryness emerging in June for the April-September SST mode much stronger and more widespread (Fig. 28f). Specifically, the June composite for January-March decaying El Niño has precipitation anomalies of greater than -1.25 inches not only focused across the Corn Belt (April-September SST period, Fig. 28c), but prevalent over a much larger region stretching from Kansas east to the Ohio River Valley and to as far south as the central Gulf Coast Region (Fig. 28f). Additionally, despite the time lag between this stronger central and southern U.S. June dryness and January-March SST period, over 90% of these strong composite anomaly values (-1.25

inches and greater) exhibit local pattern robustness values of 0.70 and greater. Consequently, the above strong June wetness across parts of the southern U.S. for April-September decaying El Niño conditions is completely absent (e.g., Texas) or substantially weakened (southeast U.S.) for the January-March SST mode.

These June precipitation pattern differences between April-September and January-March SST modes of decaying El Niño can be attributed to the sustenance of a stronger Subtropical Jet Stream and attendant southern U.S. wetness through spring with the former SST period, as associated with more persistent decaying El Niño conditions. The positive precipitation anomalies covering much of the study region in July for the April-September and March-May El Niño SST periods (Fig. 28d,h) support further that continuation of decaying El Niño to summer preempts the strengthening and expansion of the June negative precipitation anomalies associated with the January-March SST period (Fig. 28f).

In summary, the above analyses of the June-July precipitation anomaly patterns for the 3- and 6-month SST modes of decaying El Niño suggest that emergence of the southern U.S. wetness in June (April-September SST period, Fig. 28c), and subsequent study-region-wide expansion in July (April-September and March-May SST periods, Fig. 28d,h) hinge on the concurrent prevalence of this SST pattern. Accordingly, once decaying El Niño conditions in the central Tropical Pacific and enhancement of the Subtropical Jet Stream dissipate, the summer positive precipitation anomalies downstream over the study region wane simultaneously. Not only does a minimal teleconnection lag characterize this precipitation pattern, but it also is consistent for El Niño-related wetness in all spring-to-summer composites for both decaying and mature

SST modes (Figs. 25-28). The strongest of these teleconnections typically are concurrent with the SST period. Spring and summer wetness related to enhancement of the Subtropical Jet Stream thus has limited predictive potential compared to other precipitation teleconnections identified in the present study, such as the widespread June dryness for January-March decaying El Niño, which largely stem from Rossby Wave generation as the Polar Front Jet Stream impinges on subtropical and extratropical Pacific Ocean SST anomalies (Horel and Wallace, 1981; Hoskins and Karoly, 1981).

The above July pattern of dryness for March-May decaying La Niña -- also prevalent for the April-September decaying La Niña -- is an example of a robust precipitation anomaly pattern with substantial time lag (2 months) from the associated SST time period, likely attributed to Rossby Wave generation from the cold subtropical Pacific SST anomalies in the preceding spring (Fig. 4c). Different from the contrasting June and July precipitation patterns, this late summer/early fall teleconnection with decaying La Niña is persistent with remarkably similar month-to-month morphology. Beginning with July precipitation (April-September and March-May SST time periods), the pattern of dryness continues into August with slightly weaker negative composite anomalies, but similar geographic coverage (not shown). This dryness reaches a peak in September for both April-September and March-May La Niña conditions (Fig. 29a,c), and is most prominent for the April-September SST period showing that the continuance of decaying La Niña conditions beyond May helps to strengthen this negative precipitation anomaly pattern with time. While the September patterns for both SST time periods are characterized by precipitation anomalies of at least -0.50

inches stretching from the southeastern Great Plains to upper Mississippi River Valley, for the 6-month April-September SST time period (Fig. 29a) much larger and more robust areas of -1.5 inch and greater anomalies occur over the central Missouri River Valley (northeast Kansas, northwest Missouri, southwest Iowa, southeast NE) and southwestern Great Lakes Region (central/southern Wisconsin, northern Illinois, southwestern Michigan). These areas of stronger negative precipitation anomalies are not as prominent for the March-May decaying La Niña, but still are centered over same regions (Fig. 29b).

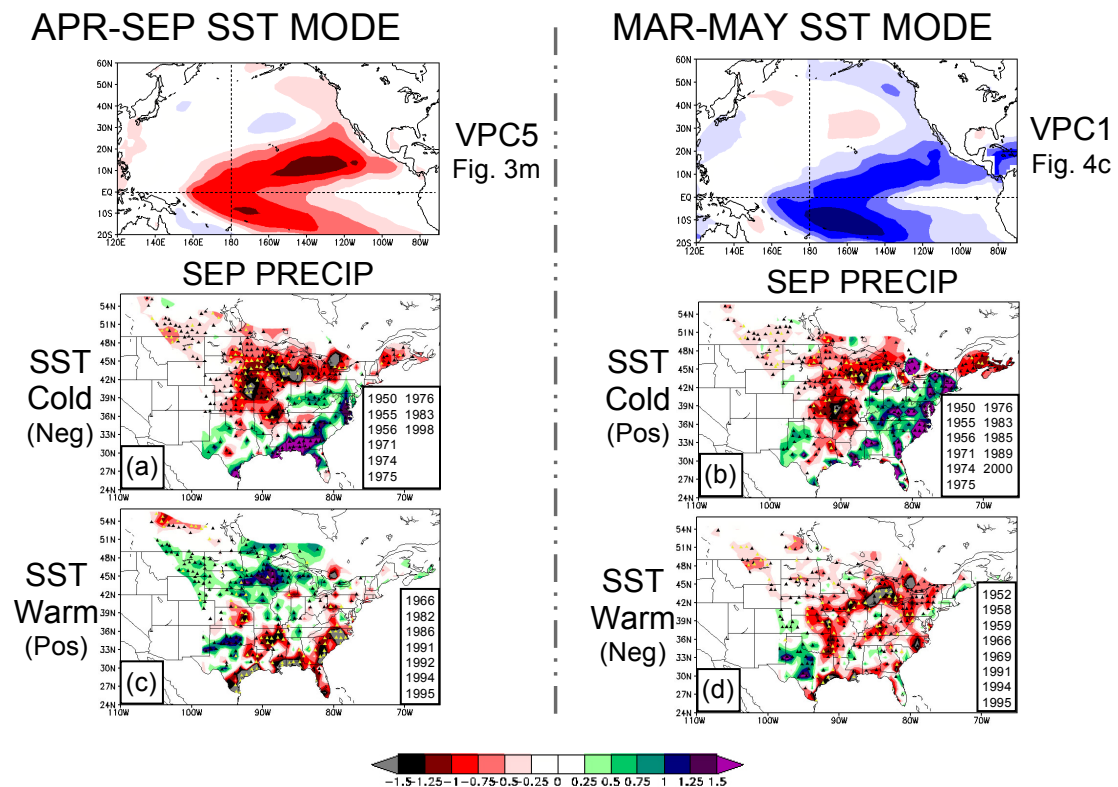


Figure 29. Same as for Fig. 24 except for September precipitation composite anomalies for 6-month (April-September, left) and 3-month (March-May, right) representations of decaying La Niña (SST Cold) and decaying El Niño (SST Warm) phases identified in Chapter 2d.

The stronger negative precipitation anomalies in September for the April-September decaying La Niña, compared to the March-May SST period, also reveal a

more direct, exclusive association between this composite pattern and cold phases of this specific Pacific SST mode. The opposite is true for the above June precipitation patterns for April-September and January-March El Niño (Fig. 28c,f), suggesting that the stronger, more expansive dryness for the latter 3-month SST period is more likely attributed to different but related SST modes. For example, this June dry pattern associated with decaying El Niño could be an artifact of concurrent cold PDO conditions, which stem from prior La Niña events that have since transitioned, as stronger, large-scale dryness is identified below (Section e) for May-July with the January-March and March-May cold PDO modes (Figs. 30c,d; 31a,b). This teleconnection exclusivity for decaying La Niña as exhibited with the above persistent, large-scale central/northern U.S. dryness in July-September, enhances even further the predictive potential along with a 2-3 month teleconnection time-lag. For September precipitation during April-September decaying La Niña conditions, over 80% of the stations with greater than -0.75 inch anomalies also have local pattern robustness values exceeding 0.70, with greater than 50% for the March-May SST period (Fig. 29a,c). Both September precipitation composites also show positive anomalies in the Southeast U.S. to as far northeast as New England (March-May La Niña), but not a single station with a positive precipitation anomaly has local pattern robustness greater than 0.70.

The September precipitation patterns associated with decaying El Niño conditions also are strongest for the March-May and April-September SST modes (Fig. 29b,d). However, different from decaying La Niña, they lack the month-to-month teleconnection persistence and precipitation anomaly pattern coherence between the two SST time periods. The August and October precipitation composite analyses for all

decaying El Niño modes show a complete absence of any coherent precipitation anomaly pattern (not shown), and the September precipitation composites for both April-September and March-May SST modes also are very inconsistent with the preceding June-July patterns (Fig. 28a,g; above). Interestingly, the positive precipitation anomalies associated with El Niño in all March-July composite analyses, especially in the southern U.S., are replaced with strong dryness by September associated with April-September decaying El Niño conditions (Fig 29c,d). This shows that despite warm SST anomalies persisting concurrently in the central tropical Pacific Ocean with El Niño, the positive precipitation anomalies so prominent in March-July from Subtropical Jet Stream enhancement cease by August.

While a disappearance of positive September precipitation anomalies in the southern U.S. is consistent for both April-September and March-May decaying El Niño conditions, these composite analyses are otherwise very dissimilar. The September pattern for the April-September SST period is highlighted by strong, robust dryness (-1.5 inch anomalies, 0.70 local pattern robustness values, and greater) across most of the Gulf Coast Region and southeast U.S., with weaker precipitation anomalies of opposite in sign over the north-central U.S. (Fig. 29b). Meanwhile, these non-robust positive precipitation anomalies disappear in the September composite analysis for March-May decaying El Niño, and negative precipitation anomalies expand across most of the study region with the strongest magnitudes (-1.50 inch anomalies and greater) over the Great Lakes Region instead of the Deep South (Fig. 29d). This lack of September precipitation pattern coherency between the April-September and March-May decaying

El Niño modes reduces the predictive potential of this pattern compared to the above La Niña counterpart.

e. Pacific Decadal Oscillation (PDO)

The PDO is a very unique Pacific Ocean SST pattern that emphasizes two distinct basin-wide regions of tropical/subtropical (Equator to 30°N) and northern mid-latitude (45°N to 60°N) SST variability that stretch across the entire Pacific Basin, and merge just off the West Coast of North America (Chapter 2d). These southern and northern branches of SST variability vary as one collective pattern on time scales longer than seasonal, hence the term “PDO horseshoe” used in some previous literature to describe the SST anomaly pattern for the warm/cold PDO phases (i.e., Barlow et al., 2001; Lamb et al., 2009). However, this aggregate treatment of PDO-related SST variability is an oversimplification in the context of the present study, since any differences in seasonal evolution between the tropical/subtropical and mid-latitude SST anomaly branches of cold/warm PDO events, or “PDO horseshoe asymmetries”, can have profound impacts on the teleconnections with North American warm season precipitation (Horel and Wallace, 1981; Namias et al., 1976, 1988; Ting and Wang, 1997; Barlow et al., 2001).

The comprehensive seasonal-level treatment of Pacific Ocean SST variability of the present study that includes six 3- and 6-month SST time periods is ideal for isolating these PDO horseshoe asymmetries within the seasonal cycle, such that their unique teleconnections with March-October monthly precipitation in the study region (Fig. 5) can be quantified. The seasonal-level incoherencies between the tropical/subtropical

and mid-latitude branches of SST variability of the PDO have not been comprehensively explored in previous literature (i.e., Mantua et al., 1997; Papineau, 2001; Barlow et al., 2001; Gutzler et al., 2002), but are strikingly evident in the six 3- and 6-month representations of the PDO identified here. Four of six PDO modes emphasize exclusively the tropical/subtropical (November-April, January-June SST periods; Fig. 3h,i) or mid-latitude (January-March, June-Aug; Fig. 4g,m) branches of SST variability, with both PDO branches concurrently prevalent in the March-May and April-September SST modes (Figs. 3g, 4i, respectively). Hence, the monthly composite patterns for March-October precipitation associated with the single-branch and aggregate cold/warm PDO modes (Figs. 30-32) are used as a comprehensive assessment of the complex PDO-related teleconnections with growing season anomalous precipitation.

The multi-faceted teleconnections with growing season precipitation from PDO variability are complex not only because of seasonal incoherencies between the tropical/subtropical and mid-latitude Pacific SST anomaly patterns, but also from the two very different primary mechanisms of ocean-atmosphere coupling that contribute to the teleconnections from these respective latitude zones. For the mid-latitude SST anomaly branch of cold/warm PDO conditions, excitation/modulation of high-amplitude Rossby Waves in the Polar Front Jet Stream (7-12 km above sea-level) is the primary initiating mechanism here for teleconnections with North American warm-season rainfall (Whitney, 1969; Horel and Wallace, 1981; Hoskins and Karoly, 1981, Wallace and Gutzler, 1981). Meanwhile, teleconnections with March-October monthly precipitation from the southern SST anomaly branch of PDO are attributed primarily to

the modulation of Subtropical Jet Stream strength and moisture content from the tropical/subtropical Pacific SST anomalies (Krishnamurti, 1961; Rasmusson and Carpenter, 1982; Ropelewski and Halpert, 1986; Montroy et al., 1998; Fye et al., 2004).

For the northern PDO branch, atmospheric positive feedbacks specific to the Polar Front Jet Stream facilitate a non-linear growth of initially subtle perturbations in the jet stream and rapid development of high-amplitude, semi-permanent Rossby Waves (Horel and Wallace, 1981; Hoskins and Karoly, 1981, Wallace and Gutzler, 1981). The sign and spatial coverage of the northern branch PDO anomalies determine the phase of these Rossby Waves as they propagate slowly toward North America, and along with SST pattern timing transmogrify their impacts (if any) on study region March-October monthly precipitation. In general, positive PDO conditions with northern SST branch emphases are associated with semi-permanent, high amplitude ridges over most of western/central North America, while the negative PDO phase is associated with the opposite “trough-ridge pattern” (Namias et al., 1976, 1988; Barlow et al., 2001). Negative (positive) PDO conditions with northern SST branch emphases thus should favor anomalously wet (dry) conditions over the western/central study region during spring-to-summer, independent of other teleconnection factors.

These Rossby Wave-related teleconnections between the mid-latitude SST anomaly branch of cold/warm PDO and growing season precipitation in the study region have enhanced predictive potential, because the semi-permanent trough-ridge configurations in the Polar Front Jet Stream can persist up to months beyond dissipation of the source SST pattern (Namias et al., 1976, 1988). This is supported by the strength in the corresponding composite anomaly patterns in 500 mb geopotential height for the

January-March and March-May midsummer teleconnections (Fig. 30-31, upper-right panels). However, even with the very comprehensive treatment of PDO in the present study, these time-lagged teleconnections are particularly difficult to independently quantify from other subsequent precipitation anomaly patterns concurrent with SST modes (i.e., warm-phase southern PDO branch and spring wetness, Fig. 30e,f, above).

The southern SST anomaly branch of the PDO impacts March-October precipitation in the study region (Fig. 5) through completely different meteorological processes than the northern PDO branch, as the Subtropical Jet Stream does not exhibit the propensity for Rossby Wave development as in mid-latitudes. Rather than driven by atmospheric temperature gradients like the Polar Front Jet Stream, the Subtropical Jet Stream forms in the upper tropospheric branches (10-16 km) of the Hadley Cell in both hemispheres, where warm/moist air from the equatorial Pacific Ocean is transported poleward and eastward at rate proportional to tropical/subtropical Pacific warmth (Krishnamurti, 1961). Thus, similar to decaying and mature El Niño SST modes (Sections c and d, above), Subtropical Jet Stream enhancement with positive PDO events is associated with warm SST anomalies in the tropical/subtropical SST anomaly branch, as coincident with a strengthened Hadley Circulation. Conversely, and consistent with La Niña modes, negative PDO conditions in the tropical/subtropical Pacific Ocean typically are associated with a weaker-than-normal or even non-existent Subtropical Jet Stream (Krishnamurti, 1961; Rasmusson and Carpenter, 1982; Ropelewski and Halpert, 1986; Montroy et al., 1998; Fye et al., 2004).

MAR-MAY SST MODE

Composite 500 mb Geopotential Height Anomalies (m)

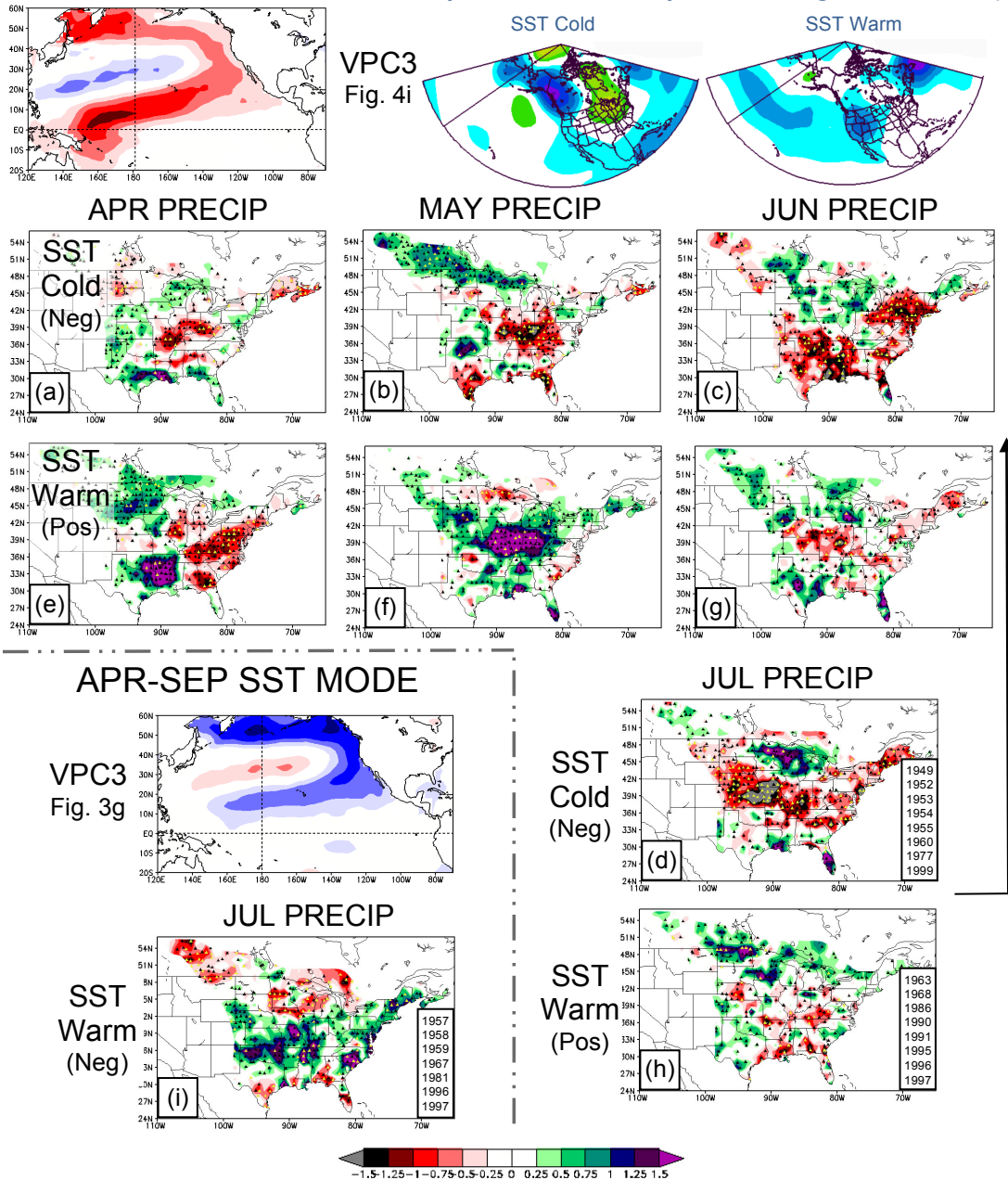


Figure 30. Same as for Fig. 24 except for spring-summer (April-July) precipitation composite anomalies for 3-month (March-May, top) and 6-month (April-September, bottom) representations of negative PDO (SST Cold) and positive PDO (SST Warm) phases identified in Chapter 2d.

Different from Rossby Wave-related teleconnections, spring precipitation anomaly patterns associated with Subtropical Jet Stream strength as modulated by the

southern branch of the PDO hinge on the concurrent presence of these tropical/subtropical SST anomalies. This relative absence in teleconnection time lag is because Subtropical Jet Stream enhancement ceases as soon as the underlying positive SST anomalies in the Pacific Ocean weaken, with the complete absence of an identifiable jet stream in the upper troposphere Hadley Cell given negative SST anomalies in the Tropics/Subtropics. Teleconnection time lags are relatively minimal even for the above spring-to-summer monthly precipitation anomaly patterns associated with decaying and mature ENSO modes (Figs. 24-28), which are characterized by stronger, more robust SST anomalies in the tropical/subtropical Pacific Ocean than the PDO modes of southern branch emphasis (i.e., November-April, January-June SST time periods; Fig. 3h,i); likely because of increased SST anomaly pattern transience during the warm seasons outside of the Mid-latitudes. With regard to teleconnections of spring-to-summer precipitation, while the tropical/subtropical SST branch of the PDO lacks the increased predictive potential of SST anomaly modes with mid-latitude branch emphasis, the intermodulation between the two branches of the PDO horseshoe is shown here to be particularly important during the first half of the North American growing season.

The SST anomalies of the southern PDO branch alone (i.e., November-April, January-June SST modes; Fig. 3h,i), accordingly, do not result in strong, persistent monthly precipitation anomalies during spring-to-summer (March-July). Instead, coherent teleconnections from the southern SST branch of the PDO (especially the positive phase) depend strongly on the simultaneous presence of SST anomalies in the mid-latitude PDO branch (i.e., March-May, April-September modes; Figs. 3g, 4i).

Additionally, the Rossby Wave patterns over North America stemming from the mid-latitude SST branch of the PDO are modulated predominantly during spring-to-summer (July and earlier) with warm PDO conditions, when a stronger-than-normal Subtropical Jet Stream coincides with a tendency for high-amplitude troughs in the Polar Front Jet Stream over western North America. The uniquely complex intermodulation between northern and southern SST branches of the PDO in terms of their teleconnections with March-July monthly precipitation (both strengthening and dampening effects) can be identified most explicitly via comparison of monthly composite analyses between the January-March (northern branch emphasis, Fig. 31) and March-May (northern and southern branch emphases, Fig. 30) PDO modes.

The March-May SST period is the most symmetric between mid-latitude and tropical/subtropical branches of SST variability of all 3- and 6-month PDO modes, indicative of the narrow time window (i.e., spring) in the PDO seasonal cycle when the SST anomaly branches align, and the above teleconnective intermodulation is most relevant. Consequently, the April and May monthly precipitation composites (Fig. 30e,f) for March-May warm PDO conditions are characterized by strong, widespread patterns of above-normal precipitation in the central/southern U.S., but are absent from the spring composite patterns of all other PDO SST modes with southern branch representation (November-April, January-June, April-September SST periods). A large region of +1.5 inch and greater precipitation anomalies is prevalent across the southeastern Great Plains to southern Mississippi River Valley in April for March-May warm PDO events (Fig. 30e), becoming more widespread in May (Fig. 30f) with equally strong anomalies (greater than +1.5 inches) stretching from the central Missouri

through Ohio River Valleys. The relative expanse and coherence of this positive precipitation anomaly pattern is consistent with the aforementioned strengthening of the trough-ridge pattern in the Polar Front Jet Stream across North America by an enhanced Subtropical Jet Stream, as teleconnected with the northern and southern SST branches of warm PDO conditions, respectively. The weaker but very robust region of negative precipitation anomalies in the same April composite (Fig. 30e) across the east-central U.S. also are consistent with this warm PDO-induced trough-ridge pattern.

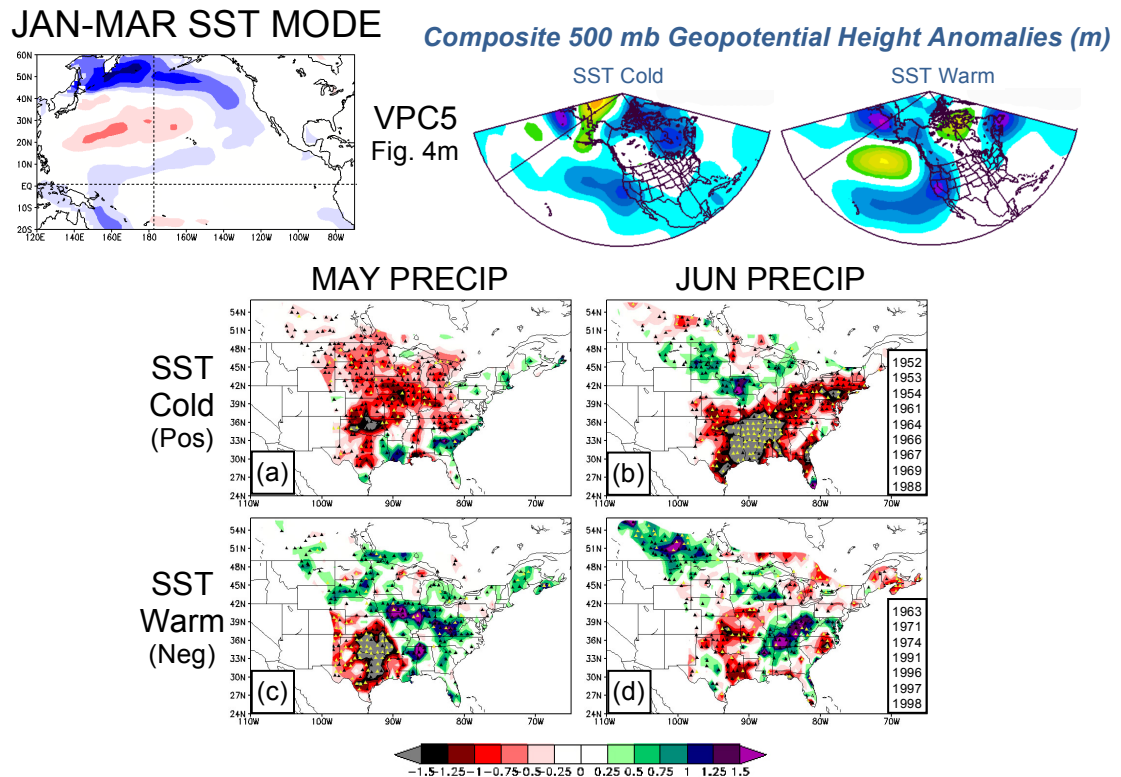


Figure 31. Same as for Fig. 24 except for May-June precipitation composite anomalies for 3-month (January-March) representations of negative PDO (SST Cold) and positive PDO (SST Warm) phases identified in Chapter 2d.

The complete dissipation of these strong positive precipitation anomalies by June (Fig. 30 g) for the March-May warm PDO mode supports further the minimal teleconnection time lag for precipitation anomaly patterns associated with Subtropical Jet Stream enhancement, even when coupled with the mid-latitude PDO branch. The transient nature of the tropical/subtropical SST anomaly branch during spring-to-summer, as represented by a shift to mid-latitude SST branch emphasis in the June-August PDO pattern, also attributes to the relative lack of predictive potential for this fickle yet strong association of spring wetness. Weaker and less coherent (single month) central/southern U.S. positive precipitation anomalies do materialize in July for the April-September SST period (Fig. 30i), also hinging on SST pattern-composite month concurrence and dual presence of northern/southern SST anomaly branches (dependence on PDO pattern intermodulation), with much of the central U.S. from Oklahoma to the Carolinas showing greater than +0.75 inch precipitation anomalies.

However, this July pattern of above normal precipitation is statistically not a continuance of the more coherent April-May pattern with the March-May warm PDO mode, as merely two analogue years (1996, 1997; Figs. 3g, 4i) exhibited positive PDO conditions for both March-May and April-September SST periods in the same year. This lack of temporal overlap for the warm phases of the two closest representations of a PDO horseshoe pattern is largely a consequence of the aforementioned high spring-to-summer transience of the tropical/subtropical SST anomaly branch.

The spring precipitation anomaly patterns (Fig. 31c,d) for January-March warm PDO conditions, which emphasize exclusively the mid-latitude SST branch (Fig. 4m), confirm the pivotal role of a concurrently enhanced Subtropical Jet Stream for the

above spring wetness to first materialize west of the lower Mississippi River Valley in April and maximize in strength/coverage by May. As such, predominantly neutral precipitation anomalies characterize the April composite for the January-March warm PDO mode (not shown). Extreme dryness then dominates the entire southern Great Plains Region by May of the January-March SST mode, with -1.50 and greater monthly precipitation anomalies all showing at least 0.70 local pattern robustness (yellow triangles in Fig. 31c), despite the 1-month teleconnection lag. Meanwhile in the same monthly composite for May, this Great Plains extreme dryness is adjacent to above-normal precipitation (greater than $+0.50$) covering most of the central U.S. east of the Missouri River, with pockets of $+1.5$ inches and greater in southeast Iowa, central Illinois, and northwest Alabama/northeast Mississippi. These positive May precipitation anomalies for the January-March warm PDO are strong and robust even with only four of the analog years (1963, 1991, 1996, 1997; Fig. 4i,m) exhibiting a symmetrically warm PDO horseshoe pattern for the concurrent March-May SST period, supporting an equal importance of the semi-permanent Rossby Wave pattern (i.e., aforementioned trough-ridge phase) that subsequently persists downstream over the study region. The continuance of this southern Great Plains dryness and central U.S. wetness in June (albeit weaker in magnitude) with the January-March positive PDO mode (Fig. 31l) also supports the increased teleconnection time lags with mid-latitude SST anomaly patterns.

While the April-June composite precipitation anomaly patterns for the warm phase of the January-March PDO mode show the importance of intermodulation between northern and southern SST branches in the development of strong, expansive

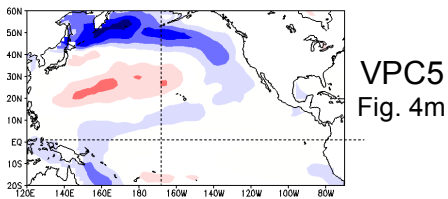
patterns of above-normal precipitation in April and May (Fig. 30e,f), the counterpart composite analyses for cold phase PDO conditions show quite the contrary. For example, the striking pattern of June dryness (Fig. 31b) associated with January-March cold PDO events is much stronger, more robust and widespread than any of the April-July monthly composite patterns associated with March-May cold PDO modes (Fig. 30a-d), despite a 2-month teleconnection lag. This June teleconnection of below-normal precipitation is not only stronger than the any March-May cold PDO teleconnections, but is more robust and widespread than any composite precipitation pattern identified here for both phases of all 3- and 6-month SST modes; as a majority of the south-central U.S. is encompassed by -1.5 inch and greater precipitation anomalies with local robustness values of at least 0.70, stretching to as far northeast as the Mid-Atlantic Region. The preceding May pattern of dryness (Fig. 31i) also is more widespread than its March-May cold PDO counterpart even without the teleconnection concurrence and symmetry between northern and southern SST anomaly branches.

Hence, these coherent May and June negative precipitation anomaly patterns associated with January-March SST mode support the drastically reduced relevance of a weakened/non-existent Subtropical Jet Stream from cold PDO conditions, with even a dampening effect on this teleconnection from any intermodulation between the tropical/subtropical and mid-latitude cold SST anomaly branches of the March-May PDO mode. Accordingly, the July pattern of strong, robust dryness over the central Great Plains to Ohio River Valley for the March-May cold PDO horseshoe (Fig. 30d) stems primarily from the mid-latitude cold SST anomalies represented, or their

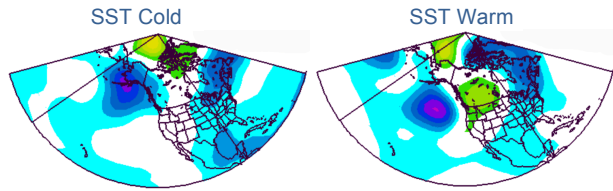
persistence beyond the January-March SST period as needed for this July precipitation pattern to realize.

This discrepancy between the warm and cold PDO phases in the impacts of the tropical/subtropical SST anomaly branch on spring/early summer precipitation patterns not only stems from differences in Subtropical Jet Stream strength and position, but most importantly from phasing of Rossby Wave patterns downstream over North America (Krishnamurti, 1961; Reiter and Whitney, 1969). The strongest patterns of above-normal spring/early summer monthly precipitation transpire during the warm PDO modes that emphasize both southern and northern branch SST anomalies, because a stronger-than-normal Subtropical Jet Stream acts to increase the amplitude and persistence of trough-ridge patterns in the Polar Front Jet Stream over North America, as associated with anomalously warm SST anomalies in the northern mid-latitude Pacific Ocean. This enhancement of Rossby Wave amplitudes occurs as the strong, moisture-laden Subtropical Jet Stream very high in the troposphere (10-16 km) impinges on or “overruns” the base of a trough within the lower-level (7-12 km) Polar Front Jet Stream at 7-12 km over southwestern North America (Reiter and Whitney, 1969). This interaction between the Polar and Subtropical Jet Streams generates greater cyclonic vorticity at the base of the trough axis, thus increasing its amplitude at the expense of eastward translation, which leads to above normal precipitation from the southern Great Plains through much of the central/southern U.S. during the first half of the growing season (July and earlier). Conversely for cold PDO conditions, a “ridge-trough pattern” over North America minimizes the intermodulation between southern and northern SST anomaly branches.

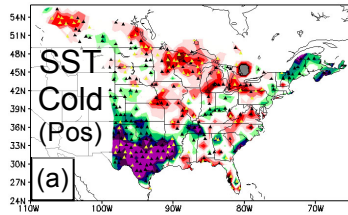
JAN-MAR SST MODE



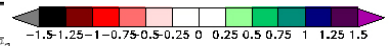
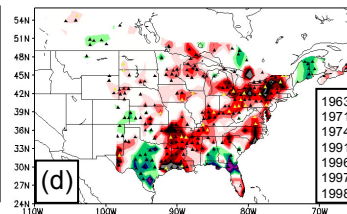
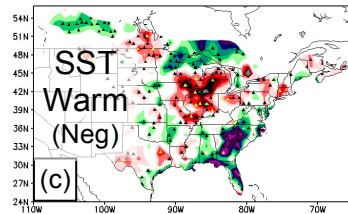
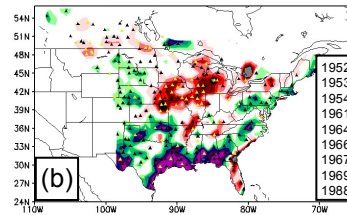
Composite 500 mb Geopotential Height Anomalies (m)



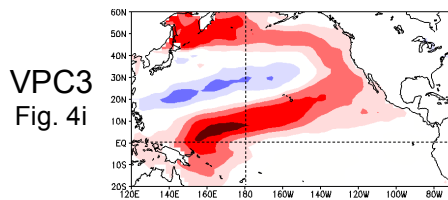
AUG PRECIP



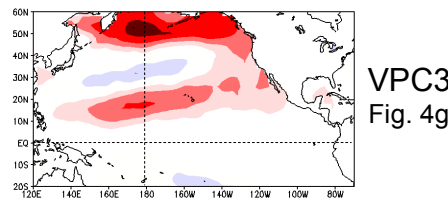
SEP PRECIP



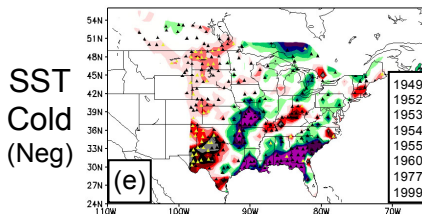
MAR-MAY SST MODE



JUN-AUG SST MODE



SEP PRECIP



OCT PRECIP

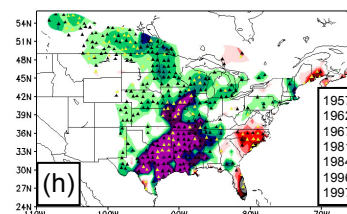
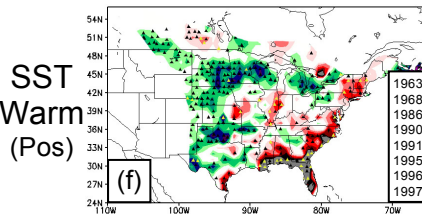
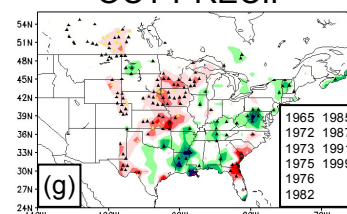


Figure 32. Same as for Fig. 24 except for August-October precipitation composite anomalies for 3-month (January-March, top; March-May, bottom-left; June-August, bottom-right) representations of negative PDO (SST Cold) and positive PDO (SST Warm) phases identified in Chapter 2d.

Similar to decaying and mature El Niño modes, the direct impacts from an enhanced Subtropical Jet Stream on the study region's precipitation cease by mid- to late-summer (i.e., August-September) for warm PDO modes, as strong anti-cyclonic regimes climatologically prevail in the central/southern U.S. at this point in the growing season. With minimal teleconnective "forcing" from the Polar or Subtropical Jet Streams in the heart of summer over the southern half of the study region (Fig. 5), anomalous precipitation is very localized and dependent on the random development/persistence of small-scale air mass thunderstorms. Hence, the robust patterns of August and September wetness (dryness) beginning in Texas and stretching along the Gulf Coast Region to western Florida with cold (warm) January-March and March-May PDO events (Fig. 32) likely stem from climate system factors related indirectly to earlier jet stream patterns.

The concentration of +1.5 inch and greater monthly precipitation anomalies around the entire immediate Gulf of Mexico Coastline by September for both January-March and March-May cold PDO modes (Fig. 32b, e), with the warm PDO phase of the latter SST period associated with strong negative precipitation anomalies (-1.5 inches and greater, Fig. 32f) in the same region and extending up the Atlantic Coastline; this highly linear teleconnection very likely is attributed to the frequency of land-falling tropical cyclones. The relatively low pattern robustness (less than a third showing at least 0.70) of this September teleconnection for the cold PDO modes (positive precipitation anomalies) also is consistent with this tropical cyclone rationale, as such strong positive composite anomalies can easily be generated by a single slow-moving tropical cyclone making landfall in that Gulf of Mexico region.

This particularly extensive overview of the teleconnections between cold/warm PDO conditions and growing season (March-October) monthly precipitation, and the physical reasoning that base them, was motivated by the unique complexities with this Pacific Ocean SST mode in discriminating between tropical/subtropical and mid-latitude SST anomaly patterns. The seasonal cycle incoherencies between the southern and northern PDO branches that complicated further this analysis would not have been identified if not for uniquely comprehensive treatment of Pacific Ocean patterns of SST variability as employed in the present study. Fittingly, this extensive teleconnection analysis is concluded with the description of a seemingly very simple precipitation anomaly pattern for October, which coincides with fall harvesting season for many crops grown in the study region. This October teleconnection is prevalent only for June-August warm PDO conditions, and is characterized by strong and very robust positive precipitation anomalies from Texas to southern Wisconsin east to the central/lower Mississippi River Valley (Fig. 32h). Interestingly, this late growing season pattern is similar to the Subtropical Jet Stream-related wetness in spring, but is associated with a warm PDO mode of northern SST branch emphasis but weak representation of the tropical/subtropical SST anomalies. Consistent with the mid-latitude SST branch teleconnections identified above, however, this October above-normal precipitation in the southwest and south-central portion of the study region maximizes at a 1-month teleconnection lag; indicating enhanced predictive potential.

f. North Pacific Oscillation

Compared with the PDO, the NPO teleconnections with growing season (March-October) monthly precipitation are much simpler to isolate and identify relative to the seasonal cycle, since all SST variability is focused in the mid-latitude Pacific Ocean (Figs. 3k-l, 4k-l). Hence, Rossby Wave generation in the Polar Front Jet Stream is the predominant source of warm-season precipitation teleconnections from cold/warm NPO modes of all 3- and 6-month SST time periods, with negligible modulation from the Subtropical Jet Stream given the absence of any SST anomaly emphasis south of 30°N. In addition to the oval-shaped characteristic SST anomaly pattern representing pure NPO variability, henceforth termed the “NPO oval”, the northern half of the PDO horseshoe pattern is apparent in four of the NPO modes (i.e., “pattern smearing” between VPCA loading patterns for NPO and PDO; November-April, January-June, January-March, March-May SST modes); implying some covariance between NPO and northern branch PDO during winter and spring. Aside from teleconnection lags, any other discrepancies between NPO modes will stem from the relative emphases on the northern part of the PDO horseshoe (i.e., level of pattern smearing), or the west-to-east seasonal migration of the NPO oval across the Dateline from winter to spring as depicted by the January-March and March-May SST time periods (Fig. 4k,l; respectively).

Comparison of the spring-to-summer composite precipitation anomalies between the January-March and March-May NPO modes (Fig. 33) shows a strong sensitivity of these teleconnections to the west-to-east migration of the NPO oval, particularly with the warm phases. The March-May NPO mode, for example, is

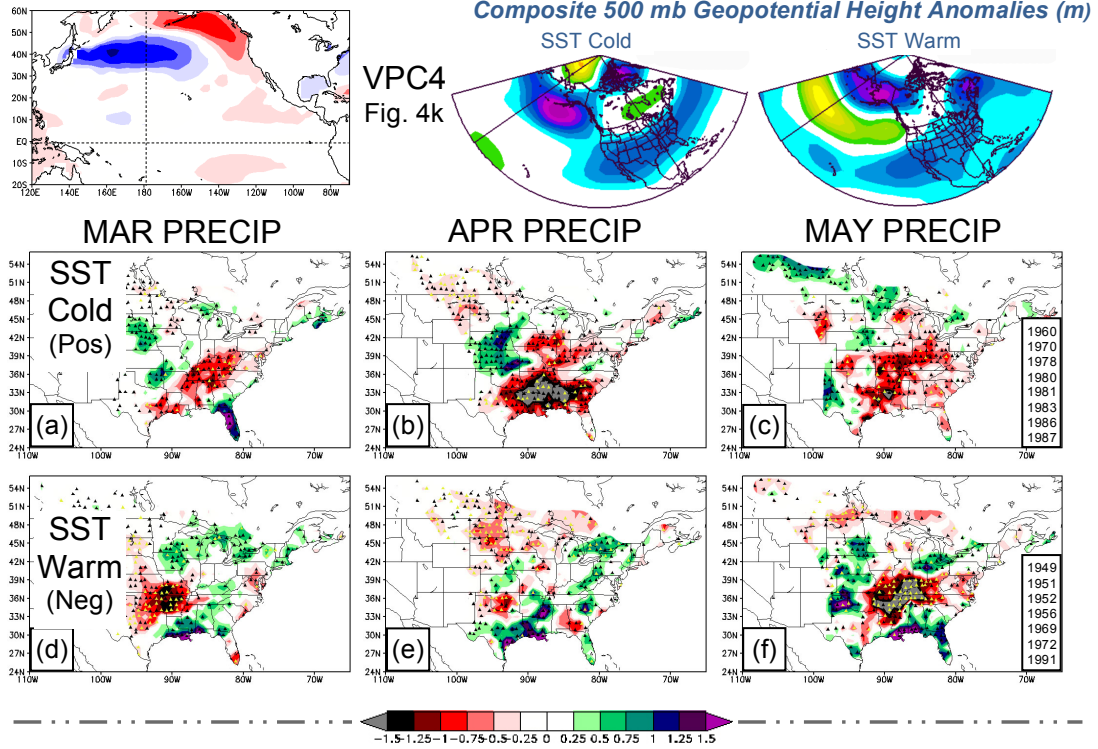
associated with strong above-normal precipitation anomalies over much of the south-central U.S. in April; with greater than +1.5 inch anomalies stretching from Texas to southern Missouri south to the lower Mississippi River Valley (Fig. 33j). Strong positive anomalies (greater than +1.5 inches) persist in the southern U.S. for May of March-May warm NPO events, but shift south and east along the Gulf Coast Region (Fig. 33k), before dissipating completely by June (not shown), thus suggesting limited predictive potential.

Meanwhile, for January-March warm NPO, this spring wetness is drastically dissipated in magnitude and coverage in all March-May composite precipitation analyses (Fig. 33d-f). Even strong negative precipitation anomalies (greater than -1.25 inches) are prevalent over eastern Oklahoma through the Ozark Mountains Region in March for January-March warm NPO (Fig. 33d), with stronger dryness (greater than -1.5 inch anomalies) over this same area but expanding to the Ohio River Valley in May (Fig. 33f); with 100% of these stations showing at least 0.70 local pattern robustness. This discrepancy in the prevalence of positive precipitation anomalies between the January-March and March-May NPO can be attributed to the NPO oval being focused east of the Dateline during spring, with a more typical westward displacement of the warm SST anomalies during the January-March period. Since upper-level anticyclones tend to form over large warm SST anomaly regions as associated with positive NPO conditions, the climatological trough induced downstream from the January-March SST mode too far west in phase to yield the substantial patterns of spring wetness as March-May warm NPO events. The prominent Gulf of Alaska SST variability emphasis with the January-March warm phase, opposite in sign as the NPO oval (cold SST anomalies)

and from representation of the northern PDO branch, encourages development of semi-permanent troughs west of North America instead of over the Rocky Mountain Region.

Interestingly, for NPO cold phases, the spring/summer composite precipitation patterns are much more similar between the January-March and March-May SST modes (Fig. 33a-c,g-i) despite the longitudinal difference in the NPO oval. Both NPO modes have strikingly similar patterns of strong, robust dryness in April (large areas of -1.5 inch and greater anomalies; Fig. 33b,g) focused from eastern Texas to the lower Mississippi River Valley, and persisting here in a weaker state through May for just the January-March cold NPO. The absence of a teleconnection time lag contributes higher pattern robustness for the April dryness of the March-May cold NPO mode, with nearly 100% of these strongest anomalies (-1.0 and greater) showing also at least 0.70 local robustness values (Fig. 33g); however, the coherence of the spring dryness (first appears in March, Fig. 33a) with the January-March SST period indicates enhanced predictive potential. The re-emergence of this negative precipitation anomaly pattern in July across most of the southern U.S. for the March-May cold NPO phase supports this 1-month teleconnection lag.

JAN-MAR SST MODE



MAR-MAY SST MODE

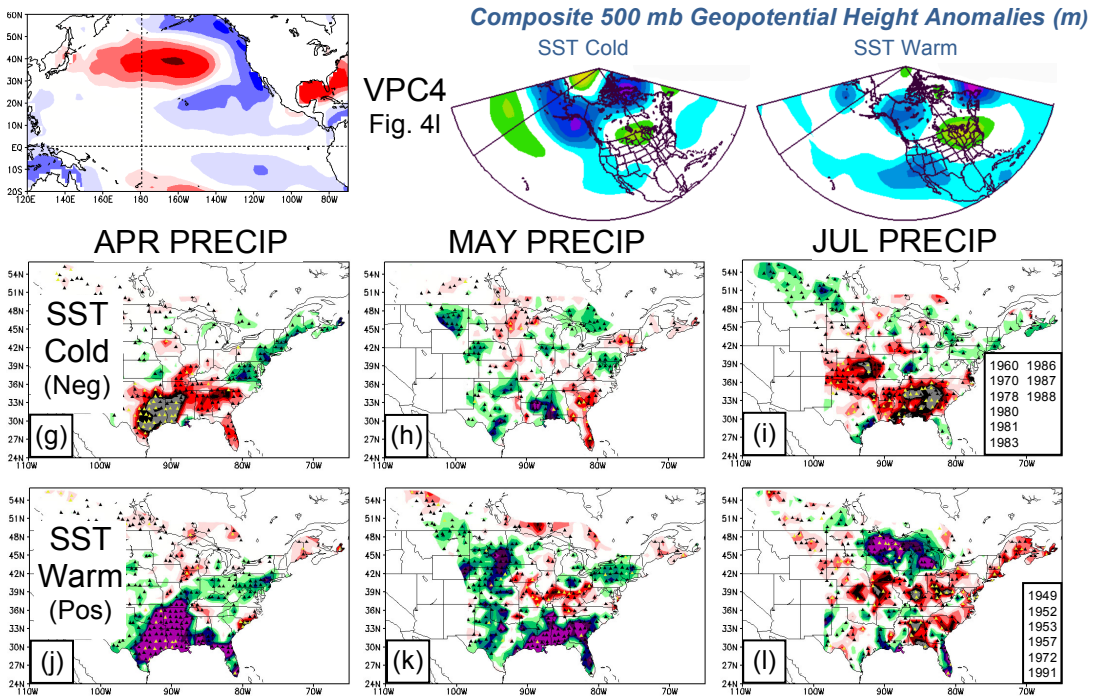
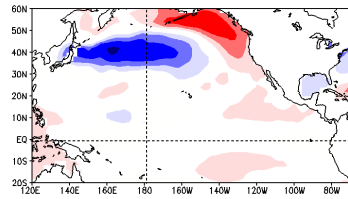


Figure 33. Same as for Fig. 24 except for April-July precipitation composite anomalies for 3-month (January-March, top; March-May, bottom) representations of negative NPO (SST Cold) and positive NPO (SST Warm) phases identified in Chapter 2d.

The dominant monthly precipitation patterns during late summer/early fall (August-September) for the NPO change in sign for both cold and warm phases (Fig. 34), with mainly positive and negative precipitation anomalies, respectively, over parts of the central/northern U.S. and southern Canada. This teleconnection is apparent in the January-March, March-May, and January-June cold/warm NPO modes with subtle differences in the precipitation composites between SST periods, particularly for the cold phases (Fig.34a,c,d,g,h; above normal precipitation). These late summer anomalies are more “spotty” than the spring precipitation patterns likely because of the typical more northern track of the Polar Front Jet Stream at this point of the seasonal cycle, with most rainfall events attributed to air mass thunderstorm development, tropical cyclone landfalls, and more inherently sporadic northwesterly flow events east of strong upper-level anticyclones.

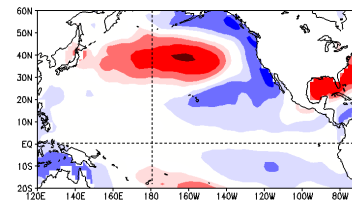
Despite the maximum teleconnection time lag (5 months), the strongest September teleconnections for anomalous precipitation are with both cold and warm phases of January-March NPO (cold phase, Fig. 34a; warm phase, Fig. 34b). Strong positive precipitation anomalies (+1.5 inches and greater) in September for January-March cold NPO are focused across the northwest Great Lakes Region, with widespread +0.25 to +1.0 inch anomalies extending northwest into the Canadian Prairies. Concurrent dryness to the south in the western Gulf Coast Region is consistent with this northern September wetness being associated with large upper-level anticyclones parked over the western half of North America, as initiated by the January-March cold NPO oval.

JAN-MAR SST MODE



VPC4
Fig. 4k

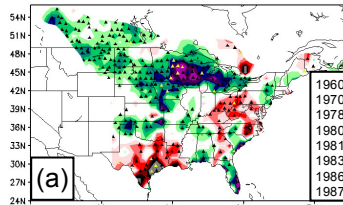
MAR-MAY SST MODE



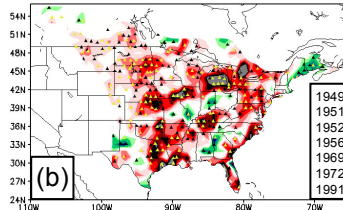
VPC4
Fig. 4l

SEP PRECIP

SST
Cold
(Pos)

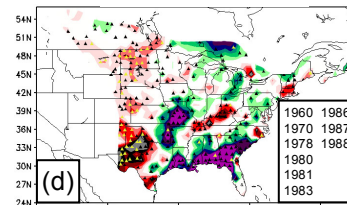


SST
Warm
(Neg)

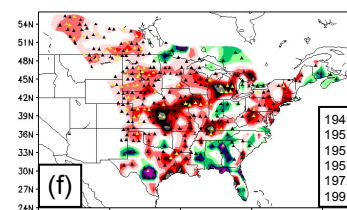


SEP PRECIP

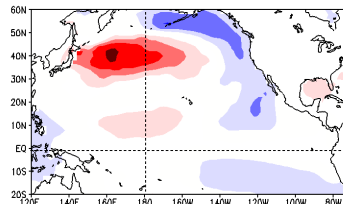
SST
Cold
(Pos)



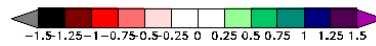
SST
Warm
(Pos)



JAN-JUN SST MODE

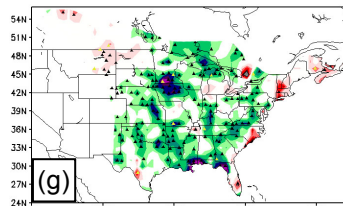


VPC4
Fig. 3l

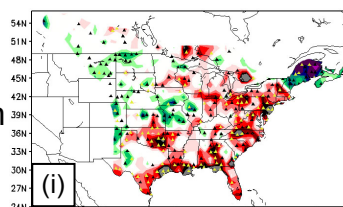


AUG PRECIP

SST
Cold
(Neg)

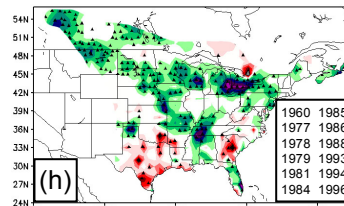


SST
Warm
(Pos)



SEP PRECIP

SST
Cold
(Pos)



SST
Warm
(Pos)

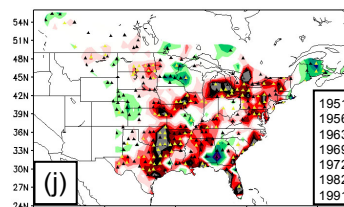


Figure 34. Same as for Fig. 24 except for April-July precipitation composite anomalies for 3-month (January-March, top; March-May, bottom) representations of negative NPO (SST Cold) and positive NPO (SST Warm) phases identified in Chapter 2d.

This above-normal precipitation during late summer also is present for the January-June cold NPO phase with weaker composite anomalies, but is much more widespread across a majority of the study region (Fig. 5) and persists during both August (Fig. 34g) and September (Fig. 34h). The August and September patterns of dryness for the January-June warm PDO phase (Fig. 34i,j; respectively), on the other hand, are equivalently as strong and robust as the September composite for January-March warm PDO. The August/September patterns of negative precipitation anomalies evolve similarly for March-May warm NPO phases (Fig. 34e,f) as for January-March and January-June SST periods, but the composite positive anomalies of the March-May cold NPO mode (Fig. 34c,d) are much weaker in the central and northern parts of the study region, suggesting that this teleconnection overall is much more sensitive to SST pattern persistence with the cold NPO phase. The strong positive precipitation anomalies (+1.5 inches and greater) confined to the Gulf Coast Region during September of March-May cold NPO phases is likely due to the associated anomalously warm Gulf of Mexico and increased frequency of tropical cyclones making landfall here.

g. Summary

Growing season (March-October) precipitation across North America can be attributed to a wide range of diverse atmospheric mechanisms ranging from expansive mid-latitude cyclones on the synoptic-scale, to the random development of diurnal air mass thunderstorms that frequent the central/southern U.S. during midsummer (i.e., July-August), the daily evolution of which are driven by storm-scale processes. On

spatial scales larger than the storm-scale but smaller than synoptic, meteorological phenomena such as tropical cyclones and slow-moving mesoscale convective systems have contributed exclusively or in part to the most prolific heavy rainfall events in modern U.S./Canadian history, with devastating impacts on regional-to-national farming industries. Hurricane Floyd in September 1999, for example, made landfall in North Carolina right on the heels of Hurricanes Dennis and Irene, producing historic rainfall totals (up to 50 cm in eastern NC, widespread 20 cm from NC to southeastern NY) in the Mid-Atlantic region over a period of less than a week that would be typical here for an entire season (Lawrence et al., 2001; Atallah and Bosart, 2003; Smith et al., 2007). Nearly every river basin in eastern North Carolina and Virginia broke 500-year records, with flooding that crippled local cotton and tobacco yields with national-level impacts. Crop losses from Hurricane Floyd over 44 counties under disaster declaration in eastern North Carolina alone totaled \$432 million (NOAA).

The extensive precipitation and flooding associated with Hurricane Floyd from North Carolina through New England materialized on such a large geographic scale, because a mesoscale tropical cyclone interacted with a synoptic-scale midlatitude trough centered over the Ohio River Valley, inducing a prolific rain-producing baroclinic zone along the Atlantic Coast from North Carolina through New England (Atallah and Bosart, 2003). This interaction between mesoscale and the synoptic-scale features can complicate monthly-to-seasonal climatological analyses of North American precipitation during the warm season, such as the present study, since teleconnections with Pacific Ocean SST modes are attributed predominantly to the evolution of synoptic-scale precipitation patterns. Another example are the Floods of 1993 across

the Upper Mississippi River Basin to the U.S. Corn Belt, which were caused primarily by repeated, slow-moving mesoscale convective systems (MCS) over the same areas, contributing to anomalous rainfall amounts and \$15-20 billion in agricultural losses over a geographical region comparable in size to the atmospheric synoptic-scale (Kunkel et al., 1994, 1995). However, since the formation and evolution of these repeated MCSs responsible for the Floods of 1993 are modulated by the overall synoptic pattern, there is predictive potential using teleconnections with Pacific Ocean SST patterns for such a culmination of warm-season mesoscale events.

Even the frequency and geographical coverage of the isolated diurnal air mass thunderstorms that dominate midsummer (July-August) climate in the central and southern U.S. are dictated at least in part by the overall synoptic pattern, and more specifically, the strength and corresponding large-scale subsidence of the semi-permanent anticyclones that often encompass the regions where these air mass thunderstorms evolve on a daily basis. Despite being very isolated in nature, these air mass thunderstorms can produce very high precipitation rates over the same location given their slow storm motions with weak upper-level flow under broad midsummer anticyclones. Even though large-scale anticyclones are typically associated with dry conditions regardless of season, the aggregate precipitation-impacts from these midsummer air mass thunderstorms in the central/southern U.S. and from tropical systems during the latter part of the growing season (i.e., August-October) that can make landfall on the Gulf of Mexico and Atlantic Coastlines of the study region, and thrive in these anticyclonic synoptic-scale environments.

Different from the cold season, monthly precipitation during the growing season (March-October) is a complicated aggregate of storm-scale, mesoscale, and synoptic scale meteorological features. The interaction between and culmination of atmospheric phenomena of such a wide range of spatial scales can complicate the ability to extract statistically and comprehensively the large-scale precipitation teleconnections with Pacific Ocean SST modes for the March-October growing season. During winter, when most of North America is characterized largely by environments of high atmospheric static stability, monthly precipitation is determined primarily by synoptic-scale features such as Rossby Waves embedded within the Polar Front Jet Stream and the strength/positioning of the Subtropical Jet Stream, with substantially less contribution from mesoscale and storm-scale precipitation features as during the warm season. Since the Polar Jet Stream also traverses lower latitudes on average during winter, teleconnections between North American precipitation and Pacific Ocean SST variability are most coherent and definitive during the cold-season, as has been documented extensively in previous literature (i.e., Horel and Wallace, 1981; Hoskins and Karoly, 1981; Rasmusson and Carpenter, 1981; Ropelewski and Halpert, 1986; Livezey, 1997; Montroy et al., 1998; Gershunov and Barnett, 1998; Goodrich, 2004).

Although not as coherent as for the winter season, strong and robust composite precipitation anomaly patterns with predictive potential as teleconnected with Pacific Ocean modes of SST variability, have been identified here for each growing season month (March-October, Sections c-f); building on prior research emphasizing warm-season teleconnections (Ting and Wang, 1977; Namias et al., 1988; Trenberth, 1988; Barlow et al., 2001; Fye et al., 2004). Overall, the evolution of storm-scale air mass

thunderstorms, mesoscale tropical cyclones and MCSs, and synoptic-scale warm season midlatitude cyclones that contribute to a majority of growing season monthly accumulated precipitation throughout the study region are modulated by Rossby Wave patterns in the Polar Front Jet Stream, the strength of the Subtropical Jet Stream, or a combination of these teleconnective mechanisms. These three factors also are the main drivers of North American teleconnections for winter precipitation, but during the March-October growing season, the aggregate effects from air mass thunderstorms and mesoscale precipitation-producing systems can have subtle dampening or strengthening effects on composite anomaly patterns when superimposed on more coherent, definitive synoptic-scale teleconnections. The treatments of these storm-scale to mesoscale subtleties base many of the physical interpretations for the monthly composite precipitation analyses here, given their association with the Pacific Ocean SST modes considered.

The significance of Rossby Waves in the Polar Front Jet Stream in generating teleconnections downstream with North American cold and warm season monthly-to-seasonal precipitation has been emphasized in previous research (i.e., Horel and Wallace, 1981; Hoskins and Karoly, 1981; Namias et al., 1988; Ting and Wang, 1997; Barlow et al., 2001; Oakley and Redmond, 2014), as related to both subtropical and midlatitude diabatic heating minima or maxima (e.g., Pacific Ocean SST anomaly patterns; El Niño/La Niña, PDO, NPO). The role of a stronger-than-normal Subtropical Jet Stream, which often are associated with El Niño conditions during winter-to-spring/early summer and above-normal precipitation over the central/southern U.S. also has been well-documented in previous literature, focusing predominantly on the cold

season (Rasmusson and Carpenter, 1981; Ropelewski and Halpert, 1986; Montroy et al., 1998; Fye et al., 2004; DeFlorio et al., 2013). The intermodulation of the Polar Front and Subtropical Jet Streams and its impact on growing season (March-October) monthly precipitation relative to the seasonal cycle of the respective jet streams, as explored in the present study, have not been a focus of previous related research.

Overall, in terms of teleconnections with synoptic-scale precipitation patterns, the NPO which emphasizes midlatitude Pacific Ocean SST variability, is teleconnected with growing season monthly precipitation in the study region primarily through upstream Rossby Wave generation in the Polar Front Jet Stream (Fig. 35d); while teleconnections with mature and decaying ENSO modes predominantly are based on the direct strengthening and weakening of the Subtropical Jet Stream with El Niño/La Niña cycles (Fye et al., 2004; Oakley and Redmond, 2014). The most complex Pacific Ocean SST mode of the analysis of monthly precipitation teleconnections is the PDO, for which interaction between the Polar Front and Subtropical Jet Streams is inherent in the characteristic “PDO horse shoe” that includes both subtropical and midlatitude SST variability, often concurrently.

Distinguishing objectively between those precipitation teleconnections associated with the respective subtropical and midlatitude SST anomaly branches of the PDO, and any intermodulation between these teleconnection factors, is key for a comprehensive and representative depiction of the physical reasoning behind the composite anomaly patterns identified here (Section e). Conveniently, the present study’s method for extracting separately 3- and 6-month Pacific Ocean SST patterns of variability yields PDO modes that emphasize individually the subtropical (November-

April, January-June, January-March SST) and midlatitude (June-August SST) branches, as well as the aggregate PDO horseshoe (March-May, April-September SST) to facilitate a better understanding of the respective roles of Rossby Waves and Subtropical Jet strength (PDO spatial patterns: Figs. 3g-i, 4g,h)

Similar to the growing season (March-October) composite anomaly patterns for temperature-based GDD (Chapter 4c-d), but not quite as coherent or robust, the teleconnections with monthly precipitation are overall strongest during spring-to-early summer (March-June) and to a lesser extent, late summer-to-fall (September-October). These stronger teleconnections (Figs. 24, 25, 27, 30, 31) stem from the Polar Front Jet Stream and embedded Rossby Waves more typically traversing the heart of the study region during these “transitional” seasons, and also when El Niño-induced enhancement of the Subtropical Jet Stream is most likely (Rasmusson and Carpenter, 1981; Ropelewski and Halpert, 1986; Montroy et al., 1998).

The physical interaction of the Subtropical and Polar Front Jet Streams does not seem to be a dominant factor for ENSO modes (particularly mature and decaying El Niño/La Niña) in driving teleconnections with growing season precipitation. Accordingly, the stronger-than-normal Subtropical Jet Streams as associated with El Niño conditions often lead to anomalously wet conditions in the central/southern U.S. during spring-to-early summer (i.e., ESP anomaly pattern; Figs. 24c,d,g,h; 25c,d,g,h; 27d-f,i,j), regardless of midlatitude cold or warm Pacific Ocean SST anomalies. This suggests an independence of the ESP anomaly pattern from the Polar Front Jet Stream, and any Rossby Wave patterns excited by negative or positive-phase NPO and PDO conditions upstream in the North Pacific Ocean. The strong positive composite

precipitation anomalies of the ESP anomaly pattern during March-June, for both mature and decaying El Niño modes, are hence attributed primarily to the greater atmospheric moisture content and more frequent embedded jet streaks within an enhanced Subtropical Jet Stream.

For La Niña conditions, and a typically weaker-than-normal Subtropical Jet Stream, on the other hand, the anomalously dry conditions of the cold-phase ESP anomaly pattern are much weaker and less persistent (1-2 months) than the counterpart El Niño wetness -- materializing only in March-April (Figs. 24a,b,e; 25b,e; 27b,g). These teleconnection non-linearities between the cold and warm SST phases can likely be attributed to spring-to-early summer precipitation from Rossby Waves in the Polar Front Jet Stream that is prevalent despite a La Niña-weakened Subtropical Jet Stream. These non-linearities are most apparent in the composite precipitation anomaly magnitudes (Figs. 24, 25, 27), but also to a lesser extent in spatial coverage of the composite anomalies between El Niño and La Niña modes, as generalized in Fig. 35a, below.

The strongest growing season precipitation teleconnections identified in the present study were for PDO, also during spring (and to a lesser extent, fall), with a broad resemblance to the ESP anomaly pattern of ENSO modes (Fig. 35c, top maps). These particularly strong and robust spring-to-early summer (April-July) monthly precipitation anomalies associated with cold- and warm-phase PDO modes (Figs. 30, 31, above) are more geographically widespread and of greater month-to-month persistence than the ESP anomaly pattern of El Niño/La Niña. Hence, these PDO spring-summer teleconnections possess greater predictive potential for spring-summer

anomalous precipitation based on preceding 3- and 6-month SST periods. The enhanced persistence and robustness of the April-July composite precipitation anomalies for both negative and positive PDO, compared to the ENSO modes, can be attributed to the inherent intermodulation between Subtropical and Polar Front Jet Stream anomalies induced concurrently by the northern and southern SST branches of the PDO horseshoe (Section e, above).

Warm PDO conditions during winter-to-summer are characterized by a anomalously strong Subtropical Jet Stream during the first half of the growing season (April-June), which facilitates the development of a high-amplitude, semi-permanent Rossby Wave trough over the Pacific Ocean just west of North America, and moisture-laden southwesterly upper-level flow (i.e., “the Pineapple Express”) overspreading Great Plains Region. This typically results in above-normal precipitation from the southern to northern Great Plains, with dry conditions in the southeast U.S. under mean anticyclonic flow east of the enhanced trough (Fig. 35c, upper-right map). This southeast dryness is different than the strong wetness across the entire Gulf Coast Region during spring-to-early summer with the ESP anomaly pattern. Also different than the ESP anomaly pattern, the negative-phase PDO modes are teleconnected with stronger and more widespread dryness than the positive-phase PDO counterparts, with negative composite precipitation anomalies covering a majority of the study region (Fig. 35c, upper-left map). During fall (September-October), interestingly, this striking PDO-precipitation teleconnection flip-flops in sign between the negative and positive SST phases.

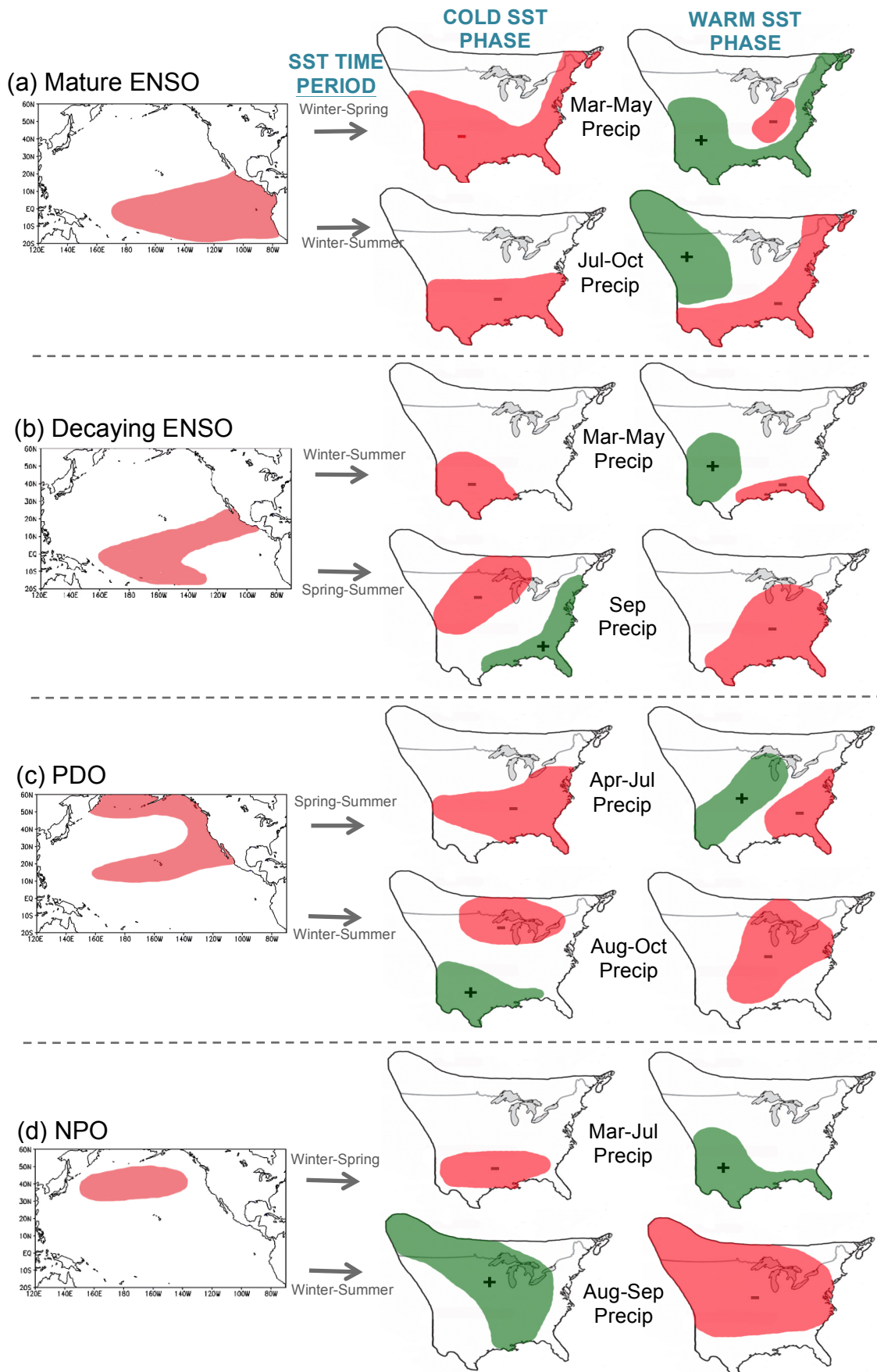


Figure 35. Generalization of the main precipitation composite anomaly patterns teleconnected with the cold and warm phases of (a) mature ENSO, (b) decaying ENSO, (c) PDO, and (d) NPO.

The ESP anomaly pattern of mature and decaying ENSO modes, and the even more robust and widespread precipitation anomaly patterns associated with PDO during spring to at least early summer, are agriculturally significant because they coincide with the critical planting, early growth, and reproductive phases of many crops grown in the study region. In the present context, the cotton farms in extreme southern Texas and North Carolina Piedmont operated by AAPEX farmer #3; the grain sorghum crops of AAPEX Farmer #5 farmed in the Texas Panhandle; the large commercial feed corn farm of AAPEX Farmer #2 in southern Minnesota; to as far northeast as AAPEX Farmer #1's soybean farm in southern Ontario (for negative-phase PDO conditions, Fig. 35c, upper-level map) all would be impacted by these spring-summer precipitation anomalies from planting season through crop maturity (Chapter 3a, Table 2). These ENSO- and PDO-related composite precipitation anomaly patterns can encompass the entire life-cycle of AAPEX Farmer #4's spring wheat crop in central Montana, since that variety (Red Spring Wheat) is planted in the fall before germinating in early spring and reaching maturity/harvesting by early- to mid-summer. Fall precipitation anomalies also have impacts on harvesting logistics and fungal growth on the full-growing season AAPEX crops considered here (i.e., corn, cotton, soybeans).

As the Polar Front Jet Stream lifts north to the northern U.S. and Canada, and the Subtropical Jet Stream weakens during midsummer (July-September), overall teleconnections with monthly precipitation become weaker and less robust, as a majority of monthly accumulated precipitation across the central/southern study region

is from a culmination of daily air mass thunderstorms, long-lived mesoscale convective systems, and tropical cyclones. However, the prominence of these storm-scale to mesoscale features in the central and southern U.S. are indirectly associated with the strength of the semi-permanent anticyclone that frequently resides over this region during summer. The strength of attendant large-scale, deep-layer subsidence beneath this mean anticyclonic regime can suppress this daily air mass thunderstorm development, which often is the only source of precipitation during summer south of the summer-mean Polar Front Jet Stream track. Conversely, an anomalously weak anticyclone can lead to a relative abundance in air mass thunderstorms over the central/southern U.S. and above normal July-September precipitation. Hence, in addition to tropical cyclone frequency (Section e, above) the randomness of precipitation related to air mass thunderstorms contribute primarily to the less spatially coherent and robust positive and negative precipitation anomaly regions from summer-to-early fall (July-September).

More robust July-September monthly precipitation anomaly patterns materialize in the northern third of the study region, across the northern U.S. and southern Canada, as associated with semi-permanent Rossby Wave patterns in the Polar Front Jet Stream at its northern most position in the seasonal cycle. Not surprisingly, the entirely midlatitudinal cold and warm NPO conditions yield the strongest composite precipitation anomaly patterns for the midsummer-early fall months of the growing season (July-September; Figs. 33i,l; 34, above), which largely are linear between the SST phases, with cold (warm) NPO events associated with above-normal (below-normal) anomalies over the entire northern U.S. and Canada (Fig. 35d, bottom maps).

These July-September precipitation anomalies impact the crop yields of particularly the northern AAPEX farming locations of the present study (except for AAPEX Farmer #4, central Montana, spring wheat; since harvesting window is June), including AAPEX Farmer #2's southern Minnesota corn crop and AAPEX Farmer #1's Great Lakes Region soybeans (Chapter 3a, Table 2), since midsummer is the high-moisture demand flowering/reproduction window of these crops. Soil moisture deficiencies also can hinder substantially the subsequent grain fill stages when the kernels/beans grow to maturity, thus decreasing directly the crop yields at fall harvest (Chapter 3a,d).

The above teleconnections between monthly growing season precipitation and mature and decaying ENSO, PDO, and NPO modes are of maximum benefit to any farmer in the study region given time lags between the composite months and associated Pacific Ocean SST periods, which infers predictive potential within the context of the present study. The teleconnections summarized here in Section g are those that not only are robust, but also possess predictive potential (at least 1-month teleconnection time lags). A more objective treatment of the physical reasoning behind the strongest monthly GDD and precipitation teleconnections from Chapters 4c-f and 5c-f is included below in Chapter 6b, along with analyses of local crop yield impacts at each of the six AAPEX farming locations (Chapter 3a, Table 2).

Chapter 6. Monthly Palmer Drought Index (PDI) Teleconnections

a. Background

Growing season (March-October) monthly composites of Palmer Drought Index (PDI) were computed for each 3- and 6-month Pacific SSTA mode (Figs. 3 and 4), based on their associated constituent years, similar to the teleconnection patterns identified for GDD and precipitation (Chapters 4 and 5, above). The relationships between North American Drought and Pacific Ocean SST variability generally are well documented in previous literature (Barlow et al., 2001; Fye et al., 2004; Shin et al., 2010; Dettinger, 2013), but a majority of these earlier studies are hyper-focused on El Niño/La Niña patterns and/or lack a concerted qualitative analysis of monthly-to-seasonal drought predictability. Barlow et al. (2001), for example, identified concurrent linkages between warm-season monthly PDI and modes of basin-wide Pacific SST variability that are relatively similar to the present study (Figs. 3 and 4), but includes only a subjective discussion on agricultural drought predictability. The present study's unique and very comprehensive treatment of time-lagged monthly PDI teleconnections is intended specifically to assess the relative monthly-to-seasonal predictability of North American agricultural drought for the dominant modes of Pacific Ocean SST variability. (e.g., mature/decaying ENSO, PDO, and NPO).

Severe drought has plagued North American agriculture for generations as the most feared aspect of climate variability since the Dust Bowl of the 1930s, and still today is widely known amongst modern farmers as the “silent killer” or “creeping disaster”, with the devastating crop impacts are often not realized until its too late (Ludlum, 1971; Fye et al., 2004; Andreadis, 2005). The socioeconomic significance of

agricultural drought even during the present modern era of farming cannot be understated, especially with the recent severe drought of 2012-14 surpassing the infamous 1988 drought/heat wave as the costliest natural disaster in U.S. history (Fye et al., 2004; Dettinger, 2013). The dependence of the global food supply on U.S. agricultural production has also grown to astounding levels, with over 80% of the world's annual corn supply and 50% of soybeans grown in the U.S. (EPA, 2000; U.S. Grains Council, 2010; American Soybean Association, 2014), such that widespread severe drought in the study region (Fig. 5) is really a global natural disaster with devastating economic and human ramifications felt around the world. Hence, the need for accurate predictive information on the timing and severity of agricultural drought is clearly growing stronger despite the advent of modern farming in the U.S.

Similar to the above teleconnection analyses for GDD and precipitation (Chapters 4 and 5), the strongest and most persistent monthly PDI composite patterns are assumed to have enhanced predictability only if the composite months are time-lagged from their corresponding SST periods. Overall, the strongest composite anomaly patterns for PDI (Section b, below) have much higher overall month-to-month persistence within the growing season compared to GDD and precipitation, thus monthly agricultural drought and pluvial should be characterized overall by greater predictability. This teleconnective persistence of the PDI is likely attributed to the cumulative relationship between stored soil moisture and the precipitation anomalies of preceding months, as well as the longer time lags required for soil moisture budgets to achieve equilibrium following prolonged periods of meteorological drought or pluvial.

The inclusion of the monthly PDI composite analyses compliments perfectly the monthly GDD and precipitation teleconnections (Chapters 4 and 5, above), and effectively and uniformly bridges the gap between climate forcing and the moisture climate experienced directly by the root zones of crops, which is vital for such an agriculturally and soil topologically diverse study region as the central/eastern U.S. and southern Canada (Palmer, 1965; Karl, 1983; 1986; Kucharik and Ramankutty, 2004; Appendix, Sections b-c, below). The Pacific SST patterns with the strongest, most coherent growing season (March-October) teleconnections with monthly PDI are identified below, including the cold/warm phases of mature ENSO, PDO, and NPO (Sections c-f). The value of the PDI composite patterns for applications on monthly-to-seasonal prediction of agricultural drought/pluvial in the study region also is determined based on the presence of these teleconnection time lags. Hopefully, monthly PDI composite analyses below will at least make this “creeping disaster” just a little more conspicuous.

b. Methodology

The same delineation of warm and cold Pacific Ocean SSTA modes as the GDD and precipitation composite anomaly analyses (Chapters 4 and 5, respectively) was used to derive the monthly characteristic patterns for PDI (Sections c-f, below), with the strongest teleconnections for the cold and warm phases of each Pacific mode (mature ENSO, decaying ENSO, PDO, and NPO) compared with its precipitation composite anomaly counterpart (Figs. 36-46). Two-tailed t-tests also were employed to identify the PDI composite values that are statistically different from zero, which represents “Mid-

range” or normal soil moisture conditions at a U.S. Climate Division for a particular month, at the 95% confidence level (t value = 3.29; Wilks, 2006, pp. 467; Montroy et al., 1998).

Growing season monthly (March-October) PDI data by U.S. Climate Division (Karl et al., 1986; Heddighaus and Sabol, 1991; NCDC, 2014) were used for this composite analysis, different from the purely meteorological GDD and precipitation data that is based on the Lamb-Richman Data Set (Chapter 3, Section b). The Climate Division level is the highest resolution available for monthly PDI across the study region, which is important given the climatological, agricultural, and soil topological diversity prevalent in the central/eastern U.S. and southern Canada (Appendix). The monthly PDI composite patterns below are defined in terms of the Karl (1986) moisture categories (Table 3), ranging from “extremely moist” for monthly PDI values of +3.50 and higher, to “extreme drought” for values of -2.75 and below. The “mid-range” category is reserved for normal soil moisture conditions relative to long-term averages, and includes monthly PDI composites between -1.24 and +0.99.

c. Mature ENSO

Not surprisingly, the strongest and most persistent teleconnections with Pacific SST patterns of all agroclimate variables considered in this study, including those for monthly GDD and precipitation (Chapters 4 and 5, Sections c-g), were discovered between growing season monthly (March-October) PDI and mature ENSO modes, especially for the warm phase (El Niño) of the January-March SST period. While the most robust teleconnection patterns for GDD and precipitation persist up to four

consecutive months during the growing season (e.g., mature ENSO and monthly precipitation; Fig. 35a), the strongest PDI composite patterns for both cold and warm phases of January-March mature ENSO persist through the entire 8-month growing season (Figs. 36c-j and 37c-j). Interestingly, this strongest and most coherent of all the monthly PDI teleconnections happens to be associated with the 3-month SST period (i.e., January-March, La Niña, Fig. 37m-t) with the largest teleconnective lag relative to the composite pattern months of March-October, and thus, is characterized by enhanced monthly-to-seasonal predictive potential.

While the growing season-long PDI teleconnections with January-March ENSO are of equivalent persistence between the cold and warm SST phases, the composite patterns associated with January-March El Niño are much stronger in magnitude and more expansive in coverage for all months (March-October) compared with those with La Niña of the same SST period. The spring and summer (March-July) composite patterns for January-March El Niño show a massive pluvial across much of the central and southern U.S., peaking in March with monthly PDI composite values in the extremely moist category (+3.50 and above) across most of the Southwest U.S., Great Plains Region, and Southeast U.S. (Fig. 37m). These El Niño-fueled strong pluvial conditions show striking persistence in the southwest U.S. and Great Plains through July (Fig. 37q), with PDI values of at least the moderately moist category (+1.00 to +2.49) even lasting through October (Fig. 37t) over much of the central/southern Plains. This strong pluvial persistence associated with January-March El Niño prevails even though the counterpart composite patterns for monthly precipitation show strong positive anomalies over these regions only during early spring (Fig. 37a-b).

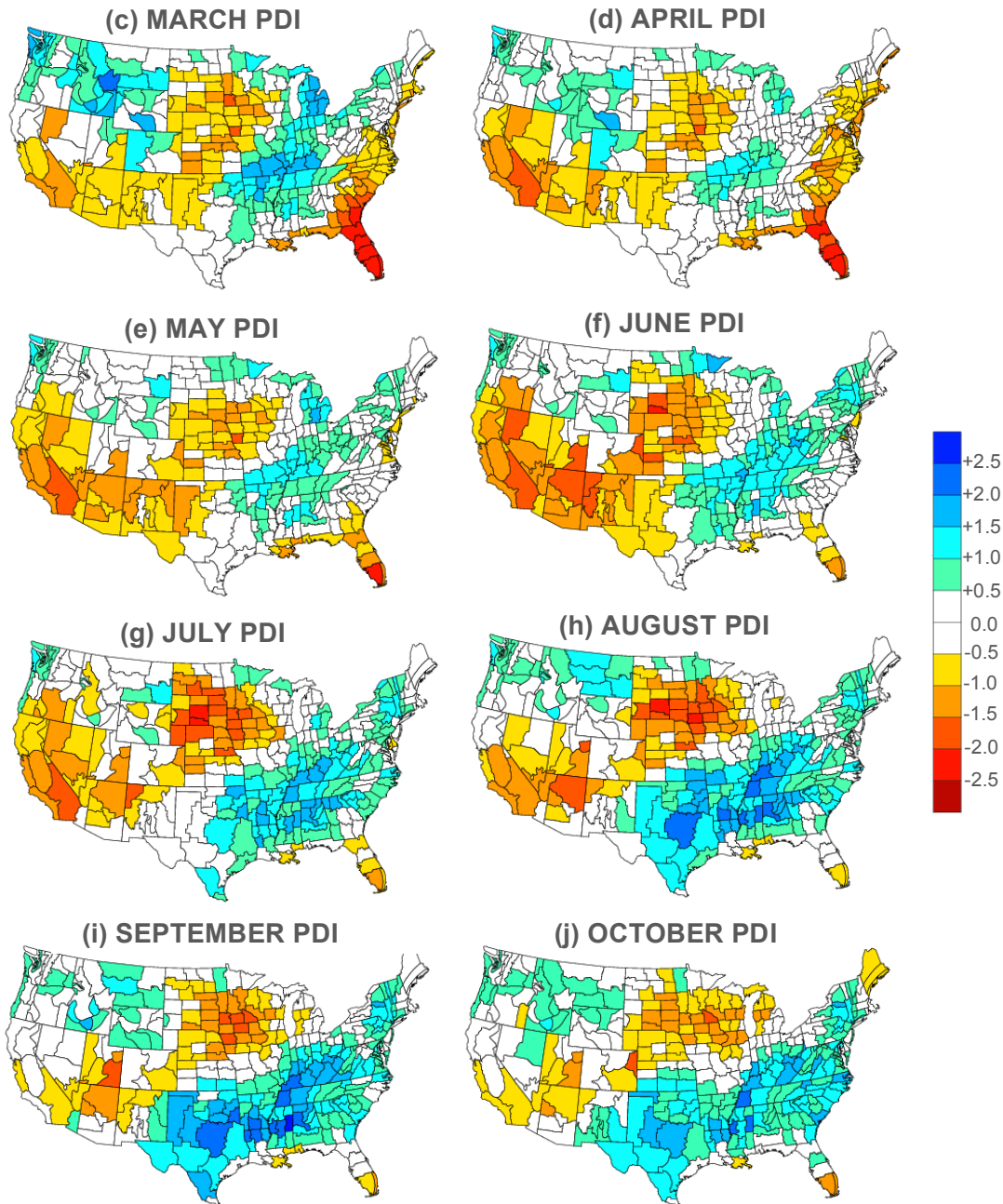
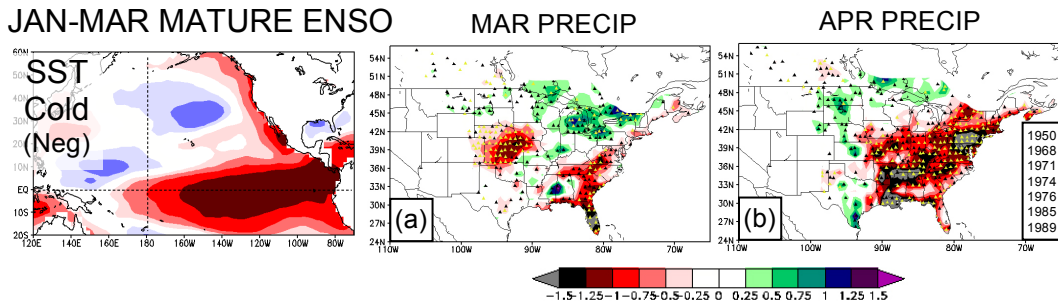


Figure 36. March-October monthly composite PDI by U.S. Climate Division for mature La Niña of January-March SST period (top left panel, Fig. 4b) for same analogue years listed in b. Counterpart March-April monthly composite anomalies of precipitation included in panels a and b.

JAN-MAR MATURE ENSO

MAR PRECIP

APR PRECIP

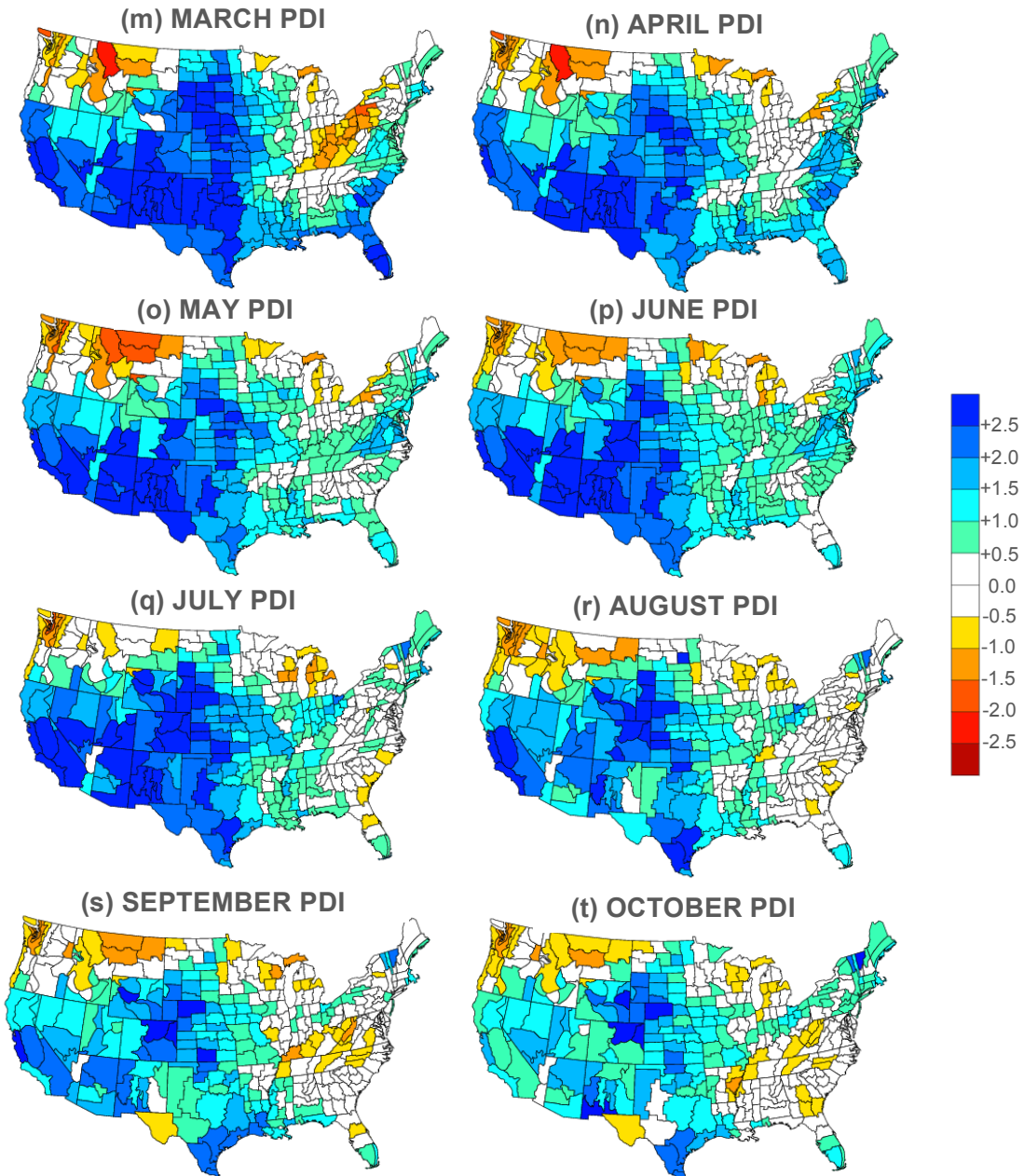
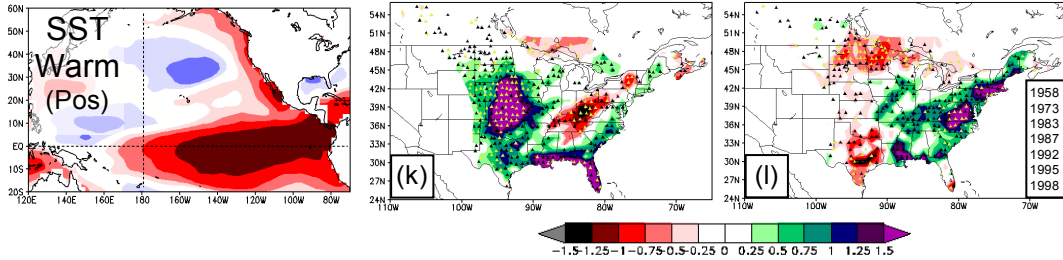


Figure 37. March-October monthly composite PDI by U.S. Climate Division for mature El Niño of January-March SST period (top left panel, Fig. 4b) for same analogue years listed in b. Counterpart March-April monthly composite anomalies of precipitation included in panels k and l.

The March-October PDI composite patterns for January-March La Niña show a corresponding pattern of agricultural drought that is weaker and smaller in coverage compared with the massive pluvial with El Niño, with monthly PDI composite values of at least the moderate drought category (-1.25 to -1.99), more focused over the northern Great Plains Region and far southwest U.S. but also persisting through the entire growing season (Fig. 36c-j). These agricultural drought conditions with January-March La Niña peak later in the growing season as compared with the El Niño pluvial, however, with strong negative PDI composites of at least the severe drought category (-2.74 to -2.00) expanding across a large part of the northern Great Plains Region into the Corn Belt (Fig. 36f-h). Also teleconnected with January-March La Niña is a large weak-to-moderate pluvial that emerges during the second half of the growing season from Texas to the Mid-Atlantic Region to the south/southeast of the aforementioned Northern Plains drought.

Interestingly, the composite anomaly patterns for monthly precipitation associated with January-March ENSO overall are much more similar in terms of spatial coverage and magnitude between the cold and warm SST phases (Figs. 36a-b, 37a-b), with strong positive (negative) anomalies during spring (March-April) of January-March El Niño (La Niña) particularly across the Great Plains Region and extending to the East Coast. These discrepancies are likely attributed to differences in prevailing climate and soil topology from west to east across the study region, with the sandy porous soils of the semi-arid western Great Plains much more drought-prone than the fertile loams and humid growing seasons of the eastern U.S. (Palmer, 1965; Rathjen, 1973; Kucharik and Ramankutty, 2004; Appendix, Sections b-c).

d. Pacific Decadal Oscillation

Different than the mature ENSO teleconnections, the PDI composite patterns associated with PDO variability are much stronger and more widespread with the cold SST phase, especially for the January-March and March-May SST periods, with moderate to even extreme drought conditions dominating most of the U.S. in the spring-summer composite maps, from the northern Rockies through all of the Great Plains, to as far northeast as western New England (Figs. 38c-h, 39c-h). Widespread weak-to-moderate drought conditions first emerge in the April composites of January-March and March-May cold PDO (Figs. 38a, 40a) and strengthen throughout the growing season before dissipating completely after September. These June-September PDI composites for the January-March and March-May cold PDO modes (Figs. 38c-h, 39c-h) actually represent the strongest, most expansive teleconnections of agricultural drought identified in the present study, surpassing even the La Niña modes here as the new infamous Pacific culprit of North American drought. These findings for the PDO are unique to prior related research mostly on La Niña teleconnections (i.e., Ropelewski, 1988; Trenberth et al., 1988; Trenberth and Branstator, 1992; Montroy et al., 1998; Fye et al., 2004).

The monthly precipitation composite patterns for the January-March and March-May SST periods of cold-phase PDO also exhibit strong dryness over much of the central/southern U.S., but manifest only in the May-July composites (Figs. 38a-b, 39a-b), while the monthly PDI patterns continue to strengthen for a few months thereafter even as the corresponding August-September precipitation composites return to normal in that region. The longer persistence of the growing season PDI teleconnections with

cold PDO compared with monthly anomalies of precipitation is attributed to not only the slower evolution of soil moisture climate compared with the overlying atmosphere, summer when the Polar Front Jet Stream is typically farther south.

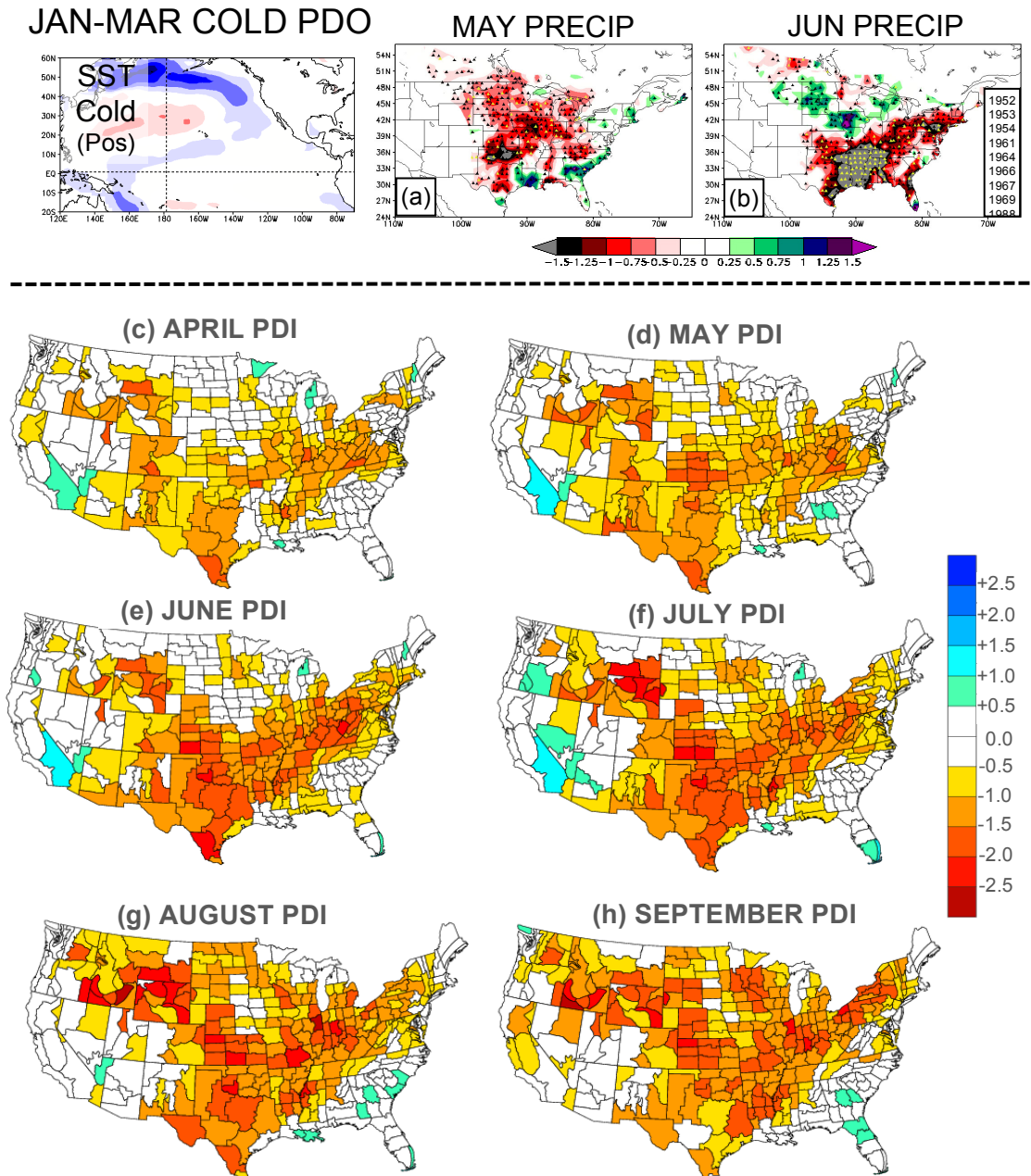


Figure 38. April-September monthly composite PDI by U.S. Climate Division for cold PDO of January-March SST period (top left panel, Fig. 4m) for same analogue years listed in b. Counterpart May-June monthly composite anomalies of precipitation included in panels a and b.

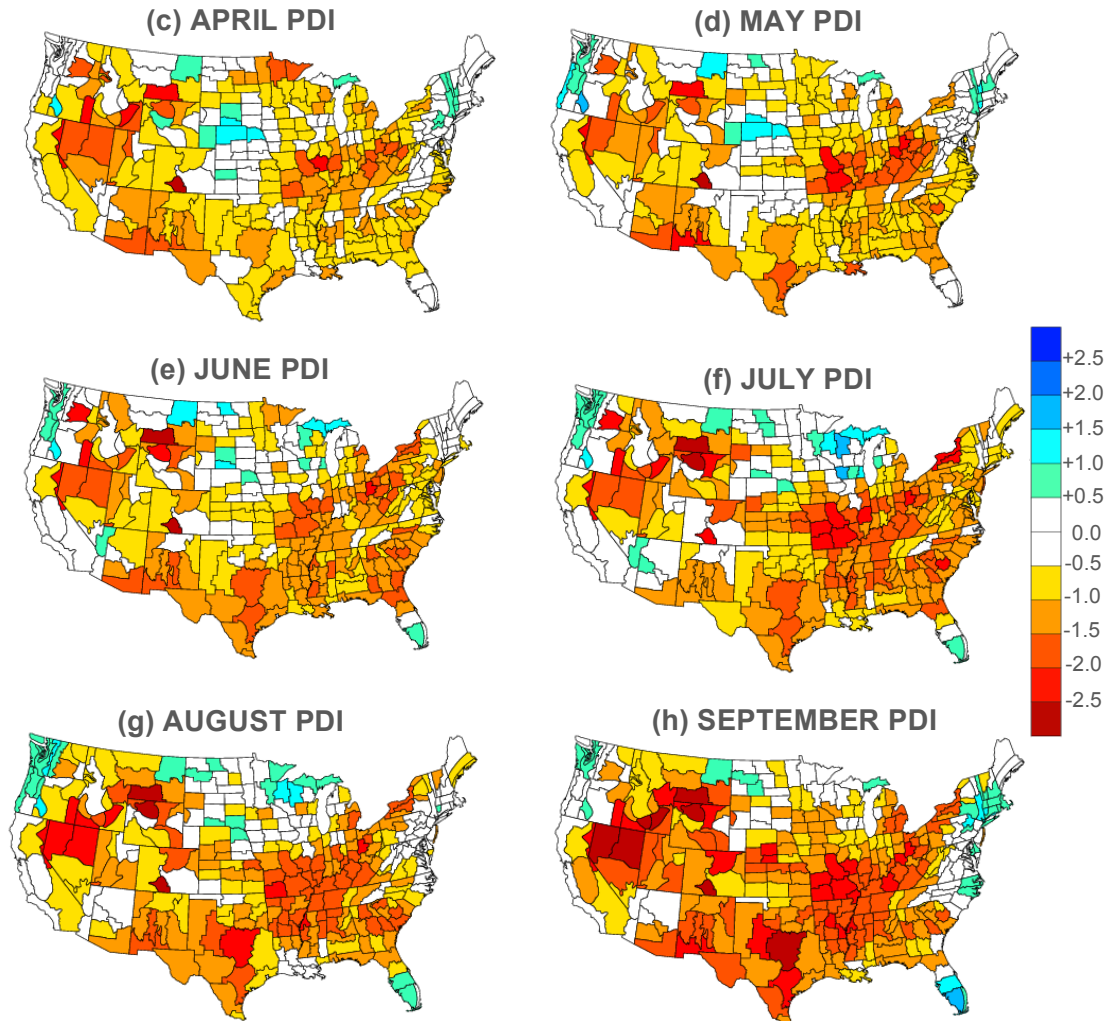
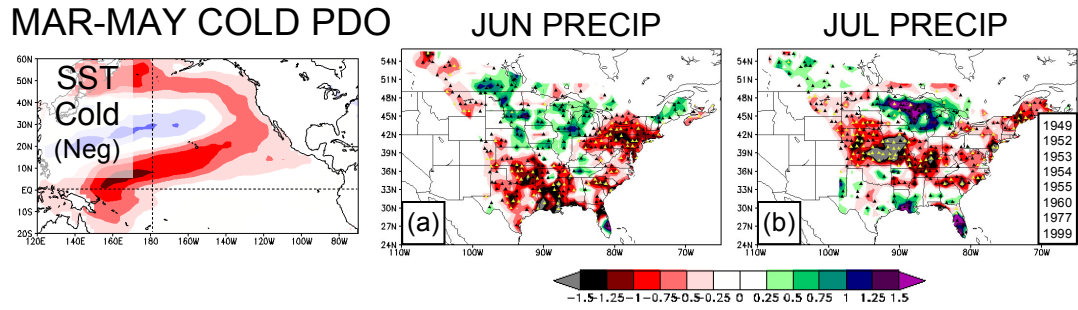


Figure 39. April-September monthly composite PDI by U.S. Climate Division for cold PDO of March-May SST period (top left panel, Fig. 4i) for same analogue years listed in b. Counterpart June-July monthly composite anomalies of precipitation included in panels a and b.

Despite close similarities in the spring-summer PDI composite patterns between the January-March and March-May SST modes of cold/warm PDO (Figs. 38-41c-f), the characteristic loading patterns of these PDO modes are quite different. More specifically, the January-March SST mode emphasizes only the mid-latitude branch of the “PDO horseshoe”, while the March-May SST mode represents equally the northern and southern PDO branches (Figs. 38-41, upper-left panels). This discrepancy indicates that the subtropical branch of the PDO likely is not a necessary condition for this particular PDI teleconnection pattern to materialize during spring-summer. This result is consistent with the monthly precipitation teleconnections of the 3-month PDO modes, which also exhibit a much diminished importance of the subtropical PDO branch during summer, attributed largely to the pole-ward seasonal migration of the Polar Front Jet Stream during summer while the Subtropical Jet weakens (Krishnamurti, 1961; Chapter 5f-g).

Different from large-scale drought teleconnections with January-March and March-May cold PDO modes, growing season (March-October) monthly PDI composite anomalies for warm PDO are confined primarily to west of the Mississippi River, with a consistent pattern of moderate to severe drought across the Desert Southwest in the May-August composites for both SST periods (i.e., PDI -2.0 and below; Figs. 40d-h, 41d-h); extending east into the southern Great Plains in the April-July PDI composites for the January-March SST mode (Fig. 40c-f). A less coherent region of wetness, with PDI composite values mainly in the “moderately moist” and occasionally “very moist” categories (PDI of +1.00 to +3.49, Table 3), especially across

the Pacific Northwest and in a compact area of the central High Plains centered over South Dakota (Figs. 40-41).

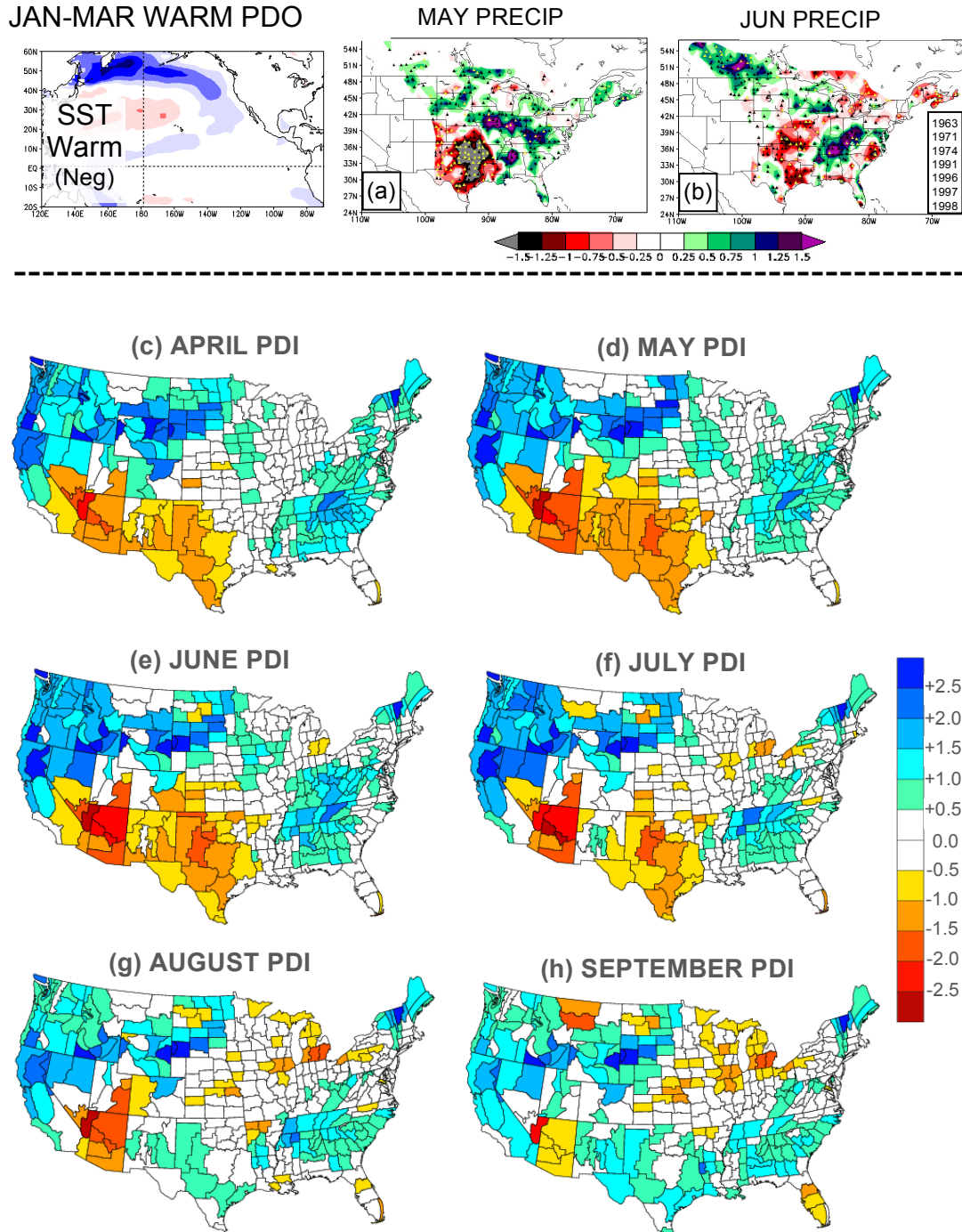


Figure 40. April-September monthly composite PDI by U.S. Climate Division for warm PDO of January-March SST period (top left panel, Fig. 4m) for same analogue years listed in b. Counterpart May-June monthly composite anomalies of precipitation included in panels a and b.

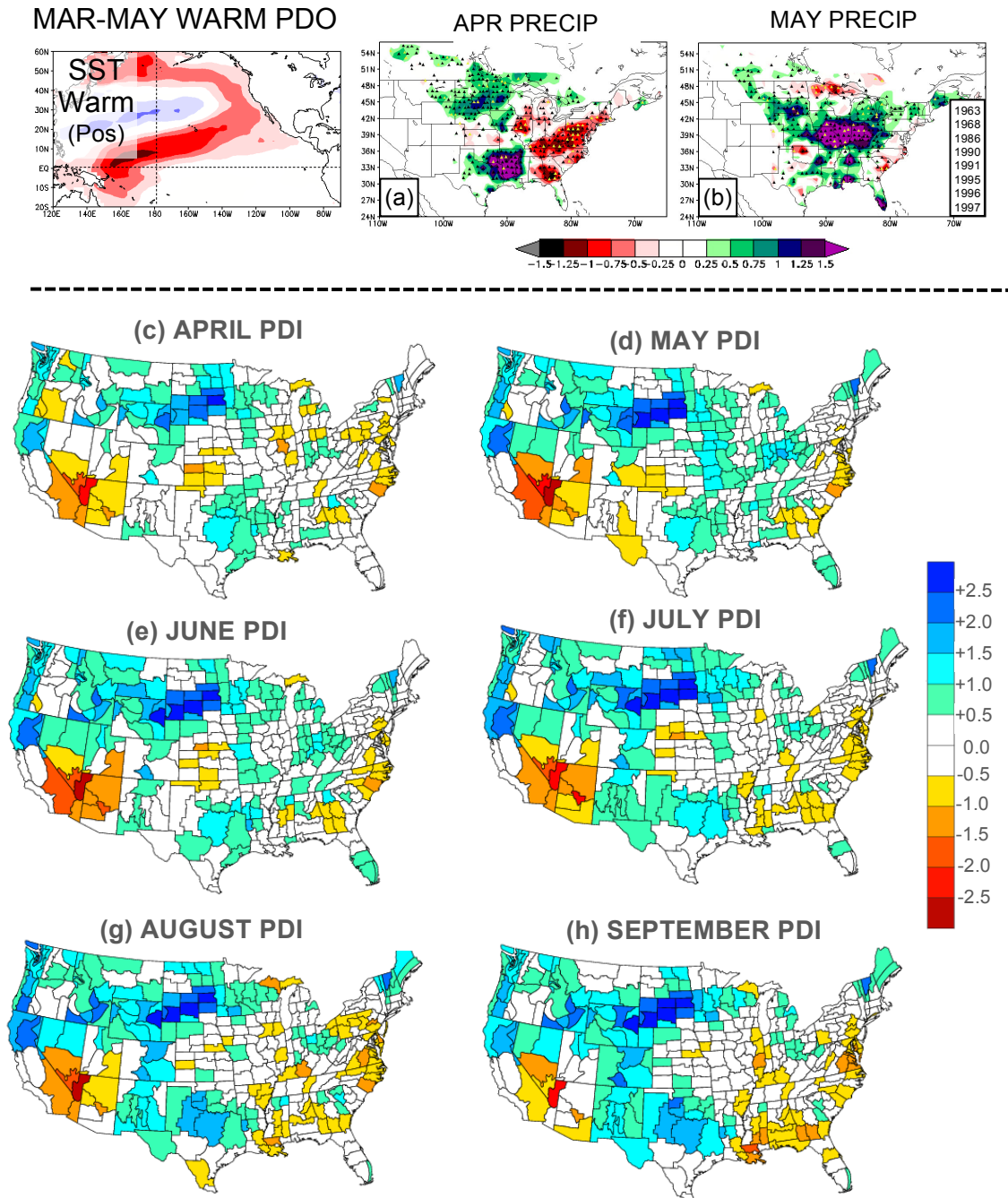


Figure 41. April-September monthly composite PDI by U.S. Climate Division for warm PDO of March-May SST period (top left panel, Fig. 4i) for same analogue years listed in b. Counterpart April-May monthly composite anomalies of precipitation included in panels a and b.

The eastward expansion of negative PDI composite values of at least the “moderate drought” moisture category from the Desert Southwest through the southern Great Plains is apparent only in the April-July composites for January-March warm PDO (Fig. 40c-f), with PDI composite values flip-flopped in sign across southern Plains for the March-May SST mode to even the weak pluvial category, especially in New Mexico and Texas (Fig. 41c-f). The corresponding monthly precipitation composites also show this discrepancy in southern Plains moisture between the January-March and March-May SST modes for warm PDO, with strong positive composite anomalies of greater than +1.5 inches across most of Texas in the April precipitation composite for the March-May SST mode (Figs. 41a). Since the March-May PDO mode emphasizes the subtropical SST branch, while the January-March mode includes only mid-latitude SST variability, the eastward expansion of negative PDI composite values into Texas during spring/summer with warm PDO hinges on the absence of a subtropical SST branch of my favorite horseshoe, and the resultant weaker-than-normal Subtropical Jet Stream (Krishnamurti, 1961; Dettenger, 2013).

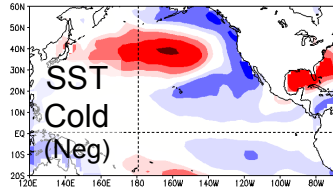
e. North Pacific Oscillation

Growing season monthly PDI teleconnections with cold and warm phases of the NPO are not nearly as coherent and widespread in coverage as those for mature ENSO and PDO modes, likely attributed in part to the more transient nature of the NPO on the seasonal level compared with Pacific Ocean modes of prominent subtropical or tropical SST variability (i.e., mature ENSO, PDO subtropical branch; Chapter 2d; Namias, 1988; Barlow et al., 2001). The strongest PDI teleconnection identified here for the cold

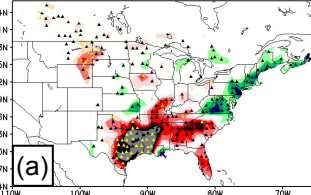
NPO mode is a relatively focused pattern of strong dryness across the interior Southeast U.S. north of Florida that first appear in April and persist through the end of the growing season, peaking during June-July with PDI values well within the “severe drought” moisture category across the southern Appalachian Mountain Region and western Carolina Piedmont (-2.74 to -2.00, Table 3, above). This dryness actually extends as far west as East Texas earlier in spring (i.e., only April PDI composite; Fig. 42c), as triggered by strong negative precipitation composite anomalies of at least -1.5 inches in that region in April (Fig. 42a), and then are replaced to weak positive PDI values by the May composite, as the strong moisture deficits refocus over the southern Appalachian Mountain Region (Fig. 42b).

These same April-October composite maps for March-May cold NPO also exhibit mild moisture surplus across the Southwest U.S. through West Texas, with PDI values of at least the moderately moist category in Arizona and New Mexico in spring before expanding east to the southern High Plains “grain sorghum country” by August (i.e., August-October PDI composite months, Fig. 42j-l). Since the Desert Southwest is outside of the Lamb-Richman data set domain, which includes the central/eastern U.S. and southern Canada east of the Rocky Mountains, it is unclear when during the growing season this mild moisture surplus is triggered. However, this cold NPO-related moisture pluvial in the Desert Southwest as highlighted in the April-October monthly PDI composites (Fig. 42c-l) likely is attributed to the mean “trough-ridge” pattern in the Polar Front Jet Stream, as forced by cold North Pacific SSTAs with the May-March cold NPO mode (Chapter 2, Section e, above),

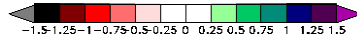
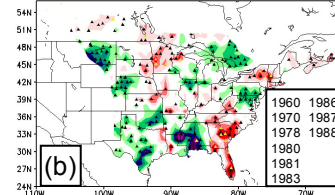
MAR-MAY COLD NPO



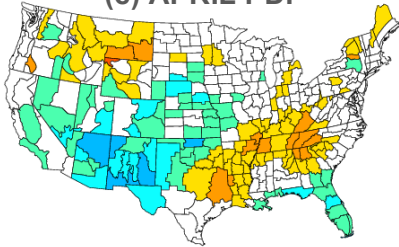
APR PRECIP



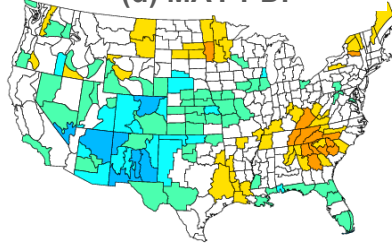
MAY PRECIP



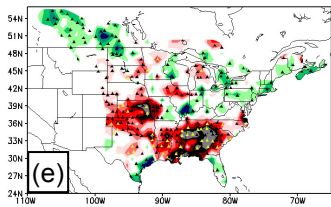
(c) APRIL PDI



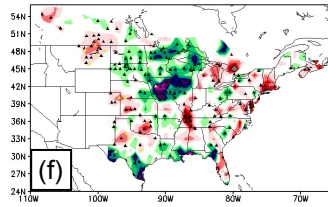
(d) MAY PDI



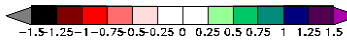
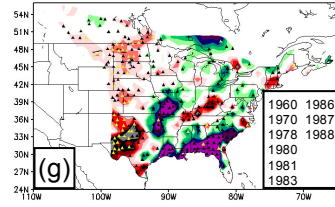
JUL PRECIP



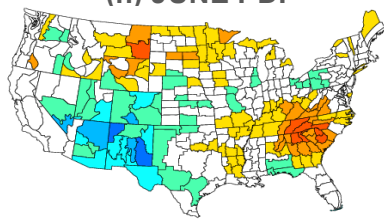
AUG PRECIP



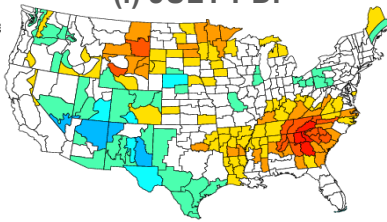
SEP PRECIP



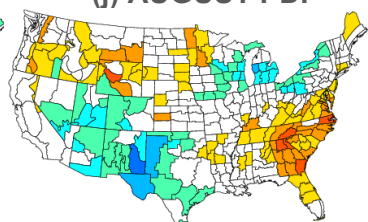
(h) JUNE PDI



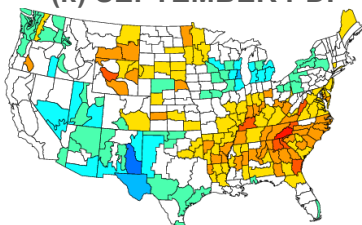
(i) JULY PDI



(j) AUGUST PDI



(k) SEPTEMBER PDI



(l) OCTOBER PDI

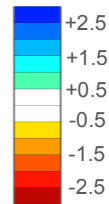
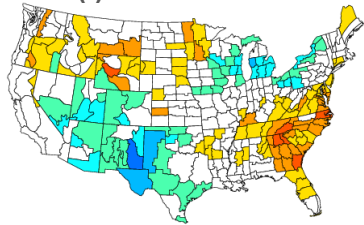
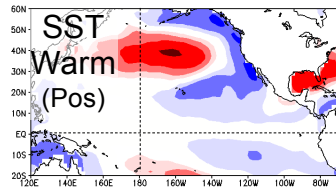
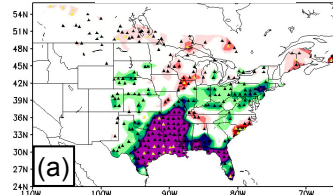


Figure 42. April-October monthly composite PDI by U.S. Climate Division for cold NPO of March-May SST period (top left panel, Fig. 41) for same analogue years listed in b. Counterpart April-September monthly composite anomalies of precipitation included in panels a and g.

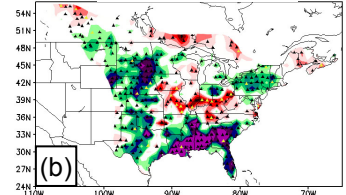
MAR-MAY WARM NPO



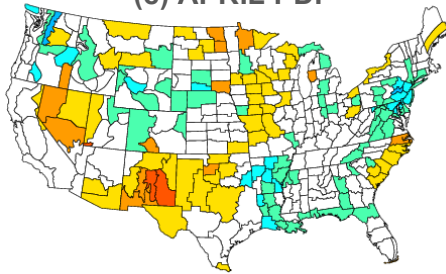
APR PRECIP



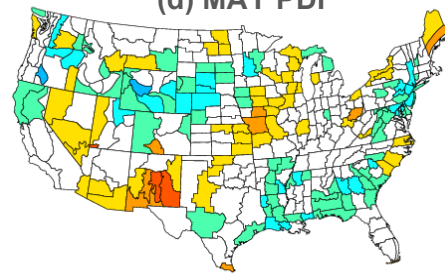
MAY PRECIP



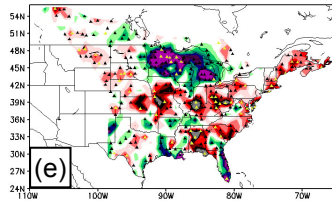
(c) APRIL PDI



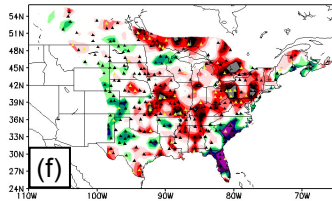
(d) MAY PDI



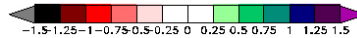
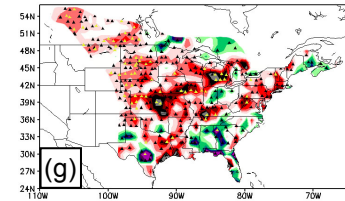
JUL PRECIP



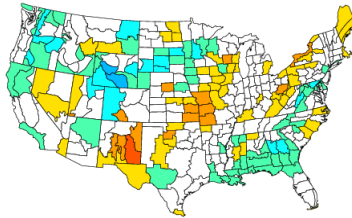
AUG PRECIP



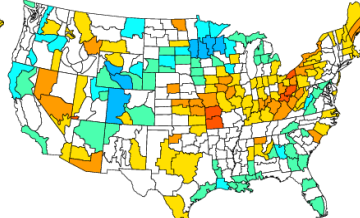
SEP PRECIP



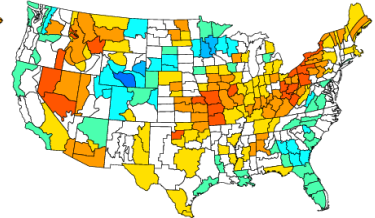
(h) JUNE PDI



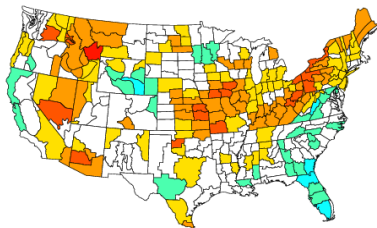
(i) JULY PDI



(j) AUGUST PDI



(k) SEPTEMBER PDI



(l) OCTOBER PDI

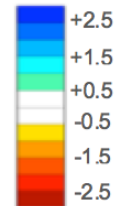
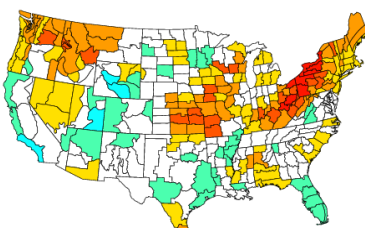


Figure 43. April-October monthly composite PDI by U.S. Climate Division for warm NPO of March-May SST period (top left panel, Fig. 41) for same analogue years listed in b. Counterpart April-September monthly composite anomalies of precipitation included in panels a and g.

Aside from the January-March and March-May SST modes of the cold PDO (Figs. 38-39), the warm NPO mode is the only other SST pattern that shows strong, relatively widespread PDI teleconnections in the Northeast U.S., with August-October composite months for the March-May SST period showing a solid pattern of “severe drought” from the eastern Ohio River Valley to western New England (i.e., monthly PDI of -2.00 to -2.74 Fig. 43j-l). This agricultural drought signal for warm NPO also extends as far west as Kansas and Missouri in the late summer months, but with weaker PDI composite values than the Northeast U.S. pattern.

f. Summary

The monthly composite analyses for growing season (March-October) PDI show teleconnections with Pacific Ocean SST variability of comparable strength as the purely atmospheric climate extremes of monthly anomalous GDD and precipitation (Chapters 4, 5), but with much greater month-to-month persistence and longer teleconnection time-lags. This is because the PDI teleconnection patterns in spring-summer often persist or even grow stronger for several months beyond the period of initial atmospheric climate forcing. While these enhanced PDI teleconnection time lags infer greater predictability overall for monthly-to-seasonal agricultural drought and pluvial, this teleconnective persistence of the PDI is attributed to the cumulative relationship between stored soil moisture and the precipitation anomalies of preceding months, as well as the longer time lags required for soil moisture budgets to achieve equilibrium following prolonged periods of meteorological drought or pluvial.

In addition to this enhanced month-to-month persistence, the most striking characteristic of the growing season PDI teleconnections is the immense geographical coverage of the strongest monthly composite patterns, especially those for mature El Niño and cold PDO modes (i.e., January-March and March-May SST periods). The massive drought signal as associated with winter-spring cold PDO phase in the Pacific, with coherent negative PDI composite values covering a majority (>70% of Climate Divisions) of the U.S. during six months (April-September) of the growing season (Fig. 38c-f, 39c-f), would strike fear into the heart of any North American farmer at first glance. If there exists a Pacific Climate System harbinger for these well-documented “mega-droughts” that are capable of crippling modern North American agricultural production for seasons and even years, such as the more recently infamous Droughts of 1988 and 2012, then the mid-latitude SST branch of the cold PDO mode is at least part of the solution.

On the other hand, the monster pluvial patterns dominating the Great Plains Region and adjacent southern U.S. in the spring-summer (March-July) monthly PDI composites for El Niño, represent overall growing conditions for thriving North American agricultural production (Anderson et al., 1985; Ostlie, 2002; Fye et al., 2004; Dettenger, 2013). However, as initiated by winter-to-spring patterns of abundant rainfall in the Great Plains and southern U.S., strong pluvials and abundant soil moisture can also be associated with elevated potential for outbreaks of crop fungus and insect pests (Ostlie, 2002; Appendix, Section b), thus predictive information on these El Niño-fueled pluvials during spring and summer also can be used to take full advantage of periods of favorable growing conditions.

The value to the North American farmer of even the strongest teleconnection patterns identified for growing season PDI (Figs. 38-41c-f), including monthly GDD and precipitation or any agroclimate extreme, cannot fully be realized without a comprehensive quantitative understanding of their specific impacts on local crop yield. The following analyses quantify the local crop yield impacts at each of the AAPEX farming locations from growing season agroclimate extremes that are deemed impactful for these specific AAPEX crops, which include the main dominant varieties farmed in the study region - corn, soybeans, cotton, grain sorghum, spring wheat (Appendix, Section a).

Chapter 7. Local Crop Yield Impacts from Agroclimate Extremes

a. Background

Climate is defined not only as the average of weather for a particular location or region over a period of time, but also by the extremes in weather behavior observed over the same period (AMS, 2012). The term agroclimate is defined here as the meteorological, geological, hydrological, and biological climate factors that influence collectively local and regional agriculture, defined similarly in recent research by Terando et al. (2012). The monthly-to-growing season extremes in agroclimate are most impactful on crop yield when coincident with critical crop maturation phases of heightened moisture demand and sensitivity to environmental temperature; such as midsummer crop reproduction, grain fill, and fruit/kernel development (Pohl and Durland, 2002; Cox, 2006; Pitts, 2008; Rankin, 2009; Appendix, Section b).

The above composite anomaly patterns for monthly Growing Degree Days (GDD) and precipitation (Chapters 4c-f, 5c-f) represent the meteorological aspects of agroclimate variability, shown visually in the below flowchart (Fig. 44). Meanwhile, the teleconnection patterns of monthly Palmer Drought Index (PDI, Chapter 6c-f), or agricultural drought and pluvial severity, represent meteorological, geological and hydrological aspects of agroclimate variability (Fig. 44, below). Collectively, these monthly extremes in GDD, precipitation and PDI account for the temperature and moisture conditions that universally modulate crop maturation, robustness, and most importantly, crop yields throughout the study region. While Chapters 4-6 above discuss the predictability of these meteorological and non-meteorological agroclimate extremes using Pacific Ocean SST variability (Fig. 44), the following analyses of local crop yield

impacts determine which are specifically most relevant at each of the six AAPEX farms described in Section b. Overall, the present chapter focuses on the base of the flowchart of agroclimate variability in Figure 44 – quantifying the impacts on local crop yield in the study region from growing season (March-October) extremes in monthly agroclimate.

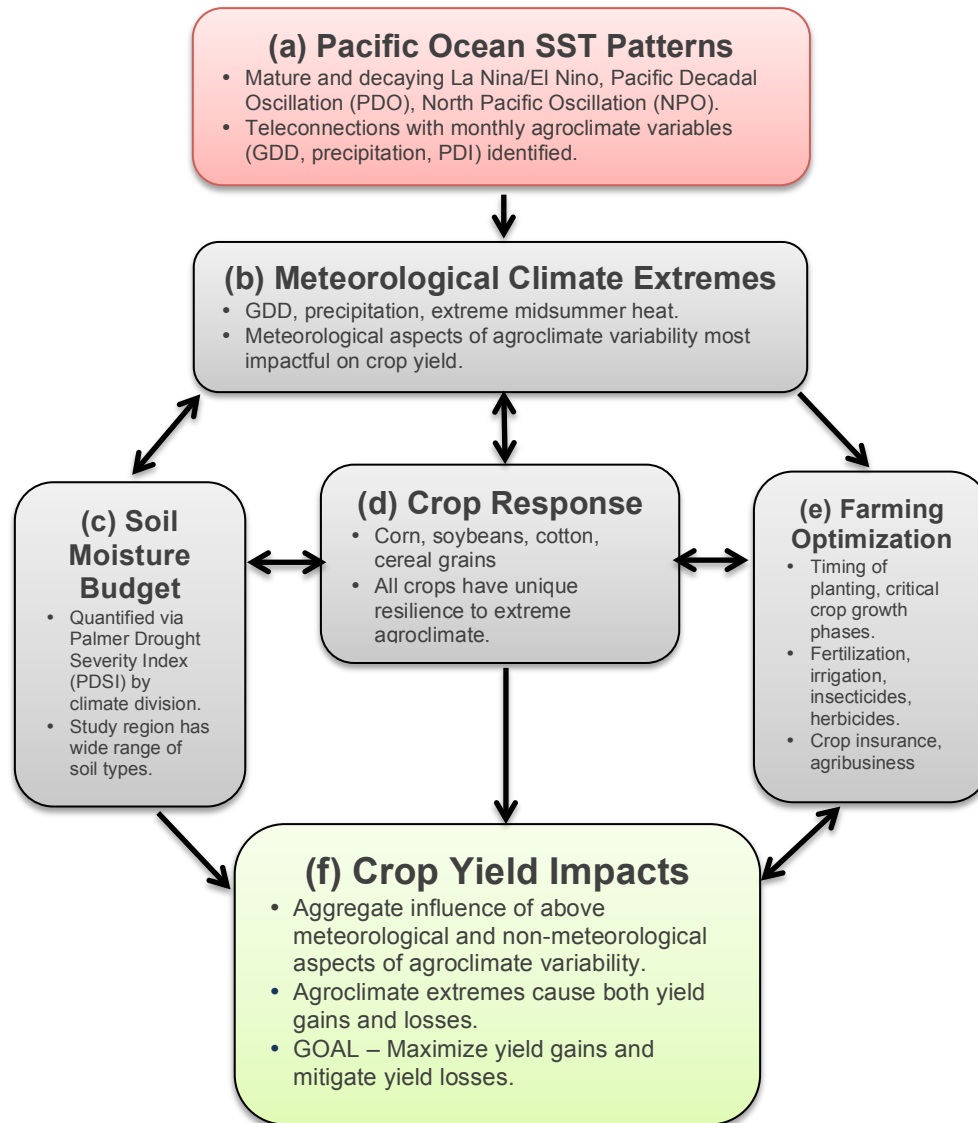


Figure 44. Flow chart of the meteorological and non-meteorological aspects of agroclimate variability (b-e) that are most impactful to crop yield.

Once the most impactful aspects of local agroclimate variability are determined via the correlation and composite analyses (Sections b and c, below) at each AAPEX farm (Fig. 45), the predictability of these specific agroclimate extremes is discussed relative to the Pacific Ocean teleconnections identified in Chapters 4-6. These analyses of local crop yield versus agroclimate variability are intended to “bridge the gap” in understanding between that of the meteorologist or climatologist, and the North American farmer – which is one of the primary end users intended to benefit from the present research. These specific crop yield impacts computed below for specific monthly-to-seasonal extremes in agroclimate (i.e., GDD, precipitation, PDI) at the six AAPEX farm locations also are discussed in terms of timing within the crop maturation cycle, the local farming practices employed, and specific physiological responses of the crops cultivated there (Fig. 44d-e; Appendix, Sections b and c).

Agroclimate extremes can also indirectly hinder crop production through disruption of farming practices and encouragement of pest infestations. For example, excessive rainfall can be absolutely devastating to crop yield when vital field operations like spring planting, fertilizer/insecticide application, and fall harvesting are disrupted. Newly planted seeds, fertilizer and insecticide/fungicide applications that are timed strategically to promote healthy crops and plant populations can easily be washed away by excessive rainfall, with residual impacts felt by crops throughout the remainder of the growing season. If not washed away immediately following application, insecticides, herbicides, and fertilizers, as applied to a vast majority of crops farmed in the study region (Fig. 1), are relatively ineffective in cool, damp soils, as emphasized by all AAPEX members contributing to the present study (Section c, below). Specifically

for nitrogen-based fertilizers, the mathematical dependence of de-nitrification rates on GDD is well documented in previous literature (Isard and Easterling, 1989; Conley et al., 2005). Given accurate predictive information on growing season climate, farmers can use fertilizers of different known de-nitrification rates to manage soil nitrogen content and control the timing of crop maturation periods to coincide with appropriate growing conditions.

For example, farmers of cereal grains such as sorghum and wheat will use fertilizer application techniques to control the length of tiller development, the growth phase preceding grain crop flowering, such that the timing of subsequent crop maturation phases is ideal relative to the growing season climate (Prasad et al., 2004; Conley et al., 2005; Fokar et al., 2006). Selection of plant density at planting and the visual inspection of new growth panicles for visual inspection are other cultural farming practices employed by grain farmers to optimize tiller development, also based on anticipated temperature and crop moisture conditions. However, in order to most effectively employ these farming practices and not only limit crop losses from agroclimate extremes, but also maximize crop yields during periods of favorable growing conditions, accurate predictive information on growing season (March-October) agroclimate variability is needed, such as derived in the present study.

Irrigation and hybridization are two of the most widely used modern farming techniques that have evolved over time to hedge the detrimental impacts from growing season climate extremes. These same cultural farming practices that have evolved for decades can be further optimized and refined based on the local and crop-specific climate information developed in the present study. The prolific expansion of modern

large-scale irrigation systems across the Great Plains starting in the 1950s have already doubled regional crop yields and decreased drastically their year-to-year variance compared with non-irrigated crops (Kucharik and Ramankutty, 2004), and this was based on very limited forecasts of agroclimate beyond the Farmer's Almanac. This benefit to crops from large-scale irrigation is supported in the below local agroclimate variability-crop yield analyses for the AAPEX member farms producing grain sorghum and spring wheat (Texas Panhandle, AAPEX Farmer #5; northern Montana, AAPEX Farmer #4; Table 2, above; Section c, below). The below comparisons of non-irrigated and irrigated yields alone are agriculturally useful for cost justification and water management purposes, especially for these AAPEX member farms and others in the "Wheat Belt" of the semiarid Great Plains. However, the analyses of local crop yields of grain sorghum and spring wheat for these respective AAPEX farms (i.e., Figs. 46d,e; 47d,f; 48e,f; 49e,f; Tables 5 and 8, below) would be particularly useful in fine-tuning growing season irrigation schedules to maximize study region cereal grain yields.

Hybridization is yet another modern farming technique that gives farmers additional options for reducing climate-related risk, and has exploded on the worldwide agricultural scene over the last half century. Widespread and effective hybridization of crops did not appear until the 1930s, even in the U.S., but was mainly limited to the corn industry before extending to other main crops a few decades later (Economic Research Service, 2004). By 2003, 73% of the 68 million hectares of crops worldwide benefitted from the use of genetically modified subspecies tailored to maximize production and minimize the negative impacts from temperature/moisture extremes in each specific climate regime (Gray, 2005). Even non-irrigated U.S. corn production has

doubled since the 1940 as attributed largely by expansion and refinement of crop hybridization, with sorghum, wheat, cotton, and soybean yield experiencing similar systematic increases since 1950 (Gray, 2005). Every crop variety is associated with a multitude of hybrid subspecies that have been genetically engineered to thrive in specific growing climates with desired crop sensitivities to agroclimate extremes. Like irrigation and other modern farming strategies, the benefits of hybridization techniques can also be maximized with the appropriate predictive information on monthly-to-seasonal agroclimate variability (e.g., Section c, below), but for an even wider variety of crop types and growing climates.

Even though crop production is driven predominantly by environmental temperature and moisture availability during the growing season, the impacts on crop yield from climate extremes are determined ultimately by the effectiveness of these modern crop management strategies like irrigation, hybridization, and fertilization. This expansive study region encompasses a wide variety of growing climates, soil topologies, crop varieties, and cultural farming practices adapted uniquely (and often subjectively) for each growing climate and crop type (Palmer, 1965; Karl, 1986; Heim Jr., 2002; Kucharik and Ramankutty, 2004; Appendix, Sections b and c). The AAPEX members provided expert opinion input vital to understanding the specific farming challenges posed by agroclimate variability, as well as the techniques adapted to overcome them, for six farming locations and five different crop varieties (i.e., corn, soybeans, cotton, grain sorghum, spring wheat), henceforth termed “focus crops” (Fig. 45, Table 5, below).

The AAPEX member farms include crop types of striking physiological diversity, including the cereal grains (grain sorghum, spring wheat) characterized by rigid protective seed husks and deep penetrating root systems custom evolved for the semiarid, extreme growing climates and Kastanozems (sandy) soils of the western Great Plains; the leafy, low-lying soybean crops that thrive in the fertile loam soils of the temperate and moisture-abundant Midwest to eastern U.S.; corn which represents plant physiological characteristics of both cereal grains and soybeans, from a region that produces annually more than 90% of the world's corn supply (known as the U.S. Corn Belt); and Upland Cotton as cultivated in two widely separated locales across the Deep South, a very unique crop in terms of farm management that often requires growth inhibitors after harvest as well as incredible soil moisture intake (Reddy and Reddy, 1998; EPA, 2000; U.S. Grains Council, 2010). These AAPEX farm locations and focus crops (corn, soybeans, cotton, sorghum, wheat; Fig. 45, Table 5) were selected to represent the wide variety of agroclimates found across the central and eastern U.S. and southern Canada.

While the strongest composite patterns of growing season (March-October) monthly GDD, precipitation, and PDI (Chapters 4-6, above) are relatively coherent spatially within the study region, the local crop yield impacts from these agroclimate extremes are highly specific to each crop variety. For example, during anomalously wet periods within the growing season, fungus development is much more common with the low-lying, leafy crop types such as soybeans and cotton, as compared to the hearty, drought-resistant cereal grains. White mold can be crippling to these crops if fungicide application is ineffective as a preventative measure (Bradley, 2009). The moisture-

loving “Boll Rot” is another fungus that often plagues specifically cotton crops in the southern U.S. during rainy growing seasons. Even though not as common as for the more-leafy crop types (i.e., soybeans, corn, cotton), cereal grain yields can be decimated completely by fungal and bacterial pests, such as *Rhizoctonia* Root Rot, Sorghum Ergot (*Claviceps Africana*), and “Black Chaff”, which are related to excessive irrigation during periods of extreme heat (Ashley et al., 2001; Workneh and Rush, 2006). A detailed, comprehensive description of the insect and fungal pests that frequent the crop types and local growing climates of each AAPEX member farm (soybeans, corn, cotton, grain sorghum, wheat; Table 2) is included in the Appendix, Section c. As is universally the case with any agroclimate extreme, the most severe crop yield losses from insect and fungal pest outbreaks transpire when they overlap with pivotal crop growth phases such as flowering/reproduction and grain fill (Section b, Table 5).

The prevailing agroclimates across this expansive study region (Fig. 1) are of striking diversity, ranging from the semiarid western Great Plains where agricultural impacts from any moisture shortages are exacerbated by the relative inefficacy of the calcareous, sandy soils at storing water, to the fertile Corn Belt and Midwest, regions renowned for optimum loam soils, prime growing conditions, and unparalleled agricultural production (Rathjen, 1973; Neild and Smith, 1983; Cox, 2006). Agricultural soil morphologies include sandy, clay, silty, sandy-clay, and silty-clay loams, each with unique moisture storage potential, available water content, and organic/humus content depending on the relative concentrations of sand, silt, and clay (Palmer, 1965; Rathjen, 1973; Karl, 1986; Heim Jr., 2002; USDA, 2008; Kucharik and

Ramankutty, 2004). The six AAPEX farming locations represent each of these agricultural biomes found in this vast study region as summarized below in Section b.

b. AAPEX Farm Specifics and Local Crop Yield Histories

The Association of Agricultural Production Executives (AAPEX) includes over 1,000 owner-managed farms and ranches across virtually every geographic growing region and agricultural commodity in the U.S. and southern Canada, including also Mexico, Argentina, and Brazil (AAPEX, 2015). The five AAPEX members participating in the present study (i.e., AAPEX Farmer #1-5; Chapter 3, Section a, above) manage six large commercial farms at widely scattered locations from the western Great Plains through the Great Lakes Region and across the southern U.S., selected to represent the immense agroclimatological diversity found across the study region (Table 2, Fig. 45). The five focus crops cultivated at these six AAPEX farms (i.e., corn, soybeans, cotton, grain sorghum, spring wheat; Fig. 45) also were selected to represent overall a majority of North American agricultural production and a wide variety of crop resiliencies to growing season climate extremes, as discussed in great detail in the Appendix, Sections a-c).

These five AAPEX farmers provided the expert opinion input (Chapter 3a) that shaped the present analyses of local and regional agroclimate variability-crop yield relationships, and thus, were selected also based on their immense collective experience as North American farmers dealing with “Mother Nature” every single growing season for decades, each with over over thirty years of farm management experience. These AAPEX farmers are deeply familiar with impacts of local climate extremes on crop

yield, especially having endured such extremes as the catastrophic summer drought and the heat wave of 1988 and the deadly floods of 1993. For example, AAPEX Farmer #1 operates a large commercial soybean farm near Ailsa Craig, Ontario, incorporated as “Twilight Acres Farms, Ltd.”, has more than 40 years of experience cultivating soybeans in the complex prevailing climate of the Great Lakes Region, and is also involved substantially with the U.S. and Canadian bean trading market. AAPEX Farmer #1 founded Great Canadian Bean Company in 1978 by first brokering beans from his own farm to local markets in southern Ontario, and shortly thereafter expanded to other markets throughout Canada and the United States (Phair, 2010). Farmer #1’s extensive knowledge of the intricate interrelating factors that drive local bean price was integral in shaping the local analyses of soybean agroclimate in the Great Lakes Region.

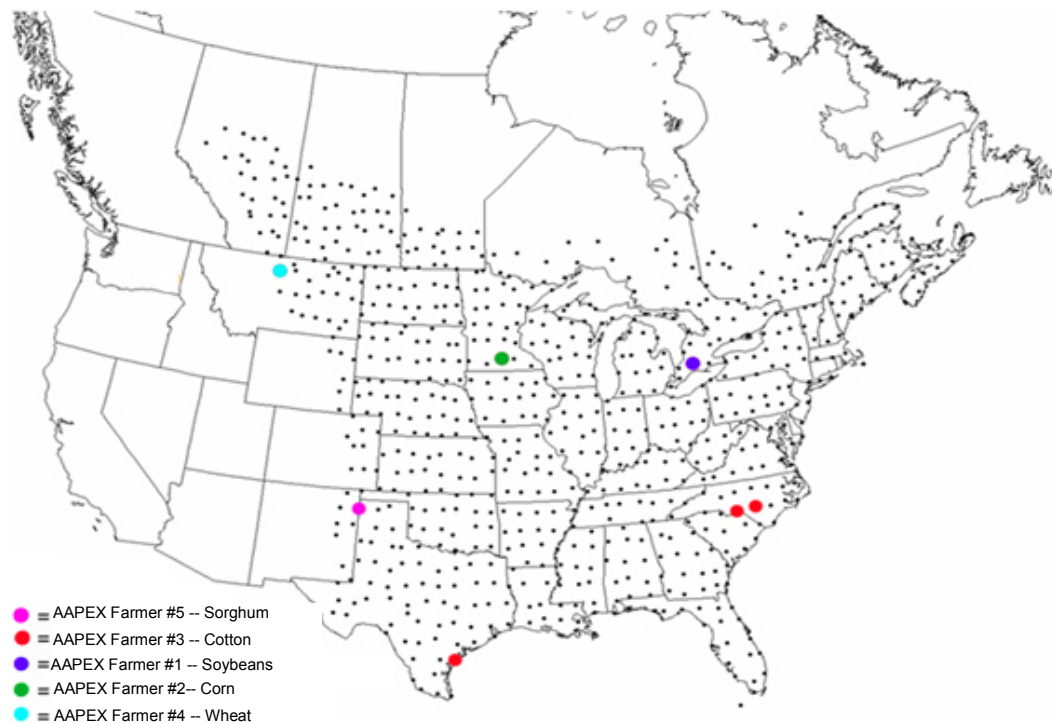


Figure 45. Geographical locations of the six AAPEX member farms including in the below analyses of local crop yield versus monthly extremes in GDD, precipitation, and PDI.

AAPEX Farmers #2-5, similarly helped shape the analyses of local agroclimate for the corn, cotton, spring wheat, and grain sorghum farming locations. The cultural farming practices for each of these focus crops and study locations are outlined in Table 6. The reproductive windows below for each focus crop were not only based on information provided by the AAPEX farmers, but also selected to include all flowering-related processes with heightened sensitivity to extreme agroclimate that also proceed the actual pollination and seed/fruit development stages, discussed in detail above for each crop variety of interest.

AAPEX Farmer #3 has a particularly vested interest in this study, given his sharing of large farm equipment and labor between the two cotton farming locations studied here -- Robeson Co., NC and Nueces Co., TX (Table 6). The use of this farm equipment, such as the massive combine-like cotton harvesters, requires substantial rental fees and operating costs. Consequently, increasing the efficiency of this sharing between widely separated farming locations, which is largely dependent on growing season agroclimate, has substantial implications for crop profitability. For example, following the harvesting of cotton 150 to 170 days from the sowing date, “defoliant” must be applied to cotton crops to abort unmanageable growth, since cotton uniquely continues vegetative growth during and after reproduction (Reddy and Reddy, 1998; Ritchie et al., 2004). This difference of twenty days is substantial in terms of farm management when sharing equipment between distant locales, especially given the substantial equipment and manpower required for the harvesting and defoliation of cotton. Hence, detailed knowledge of local agroclimate-crop yield relationships and

especially predictive information for anomalous seasonal climate, are of particular value for farming executives like AAPEX Farmers #1-5

As learned via expert opinion input from the AAPEX farmers as well as supplementary independent research, Table 5 shows the time windows of planting, flowering and harvesting for each of the six AAPEX farming locations and focus crops. These crops varieties are uniquely susceptible to specific agroclimate extremes during these critical crop maturation windows, and also particularly impactful on crop yields by the harvesting window. A detailed breakdown of the specific climate sensitivities throughout the growing season for each of the five focus crops of corn, soybeans, Upland Cotton, grain sorghum, and spring wheat, are included in the Appendix, Section c, summarized in Tables 10-14.

Table 5. Typical date ranges for critical farming phases specific to each crop and location, as provided by the five AAPEX farmers and associated farming locations (Table 5) and/or previous literature (Anderson et al., 1985; Fehr and Caviness, 1977; Hicks, 2006; Prasad et al., 2004; Reddy and Reddy, 1998)

Critical Growing Season Specifics					
AAPEX Farm	Sowing	# Days to flowering	Reproduction window	Harvesting Window	Irrigation
ST	May 01 ::: May 15	90-100	Aug 1-Sep 1	Oct 1-Oct 15	N
PD	May 01 ::: May 15	50-60	July 1-Sep 1	Sep 20-Nov 1	N
AB1	April 1 ::: May 1	50-65	June 1-Aug 1	Oct 1-Nov 10	N
AB2	March 1 ::: April 1	50-65	May 1-Jul 1	Aug 20 - Oct 1	N
CM	May 1 ::: May 15	50-60	July 1-Aug 1	Aug 15-Sep 15	Y
ML	April 15 ::: June 1	50-60	June 1-Aug 1	Sep 1-Oct 1	Y

Table 6 summarizes the specific challenges faced by crops at the six AAPEX locations during these critical farming windows, as learned through interviews of the five AAPEX members at the *apex* of the present study (Chapter 3, Section a). The specific local crop yield impacts from agroclimate extremes (i.e., monthly anomalies of

GDD, precipitation, PDI), as coincident with these critical farming windows and throughout the March-October growing season, are quantified below in Sections c and d (Figs. 47-51, Table 8).

Table 6. Brief descriptions of weather-sensitive phenomena/operations for each farming location and critical crop maturation window (Table 5) as provided by the five AAPEX members.

Weather-sensitive Phenomena/Operations	
Farm	Description
AAPEX Farmer #1	<ol style="list-style-type: none"> 1. <i>All windows</i>: Excess precip. may disrupt field operations. 2. <i>Growing season</i>: Summer droughts are detrimental to all crops. 3. <i>Edible bean flowering</i>: Flowering aborts when the temperature reaches 27-30°C. Flowering occurs 90-100 days after planting. 4. <i>Bean harvesting</i>: Damp conditions result in poor bean quality 5. <i>Combine operation</i>: Ideal conditions are very cold nights with Tmin<15°C. Combine sieves freeze up in temperatures around freezing.
AAPEX Farmer #2	<ol style="list-style-type: none"> 1. <i>All windows</i>: Excess precip. may disrupt field operations. 2. <i>Growing season</i>: Summer droughts are detrimental to all crops. 3. <i>Fertilization</i>: Warm, saturated soils during May and June result in denitrification rates that are too rapid. Cool spring and summer soils result in inefficient “manure N” to “nitrate N” conversion.
AAPEX Farmer #3	<ol style="list-style-type: none"> 1. <i>All windows</i>: Excess precip. may disrupt field operations. 2. <i>Growing season</i>: Summer droughts are detrimental to all crops. 3. <i>Equipment/labor transfer</i>: Excess precip. can lead to unplanned delays and disruption of sharing.
AAPEX Farmer #4	<ol style="list-style-type: none"> 1. <i>All windows</i>: Excess precip. may disrupt field operations. 2. <i>Growing season</i>: Summer droughts are detrimental to all crops. 3. <i>Early spring rainfall</i>: Sufficient precip. is vital to restoring topsoil moisture to ensure germination. 4. <i>Cereal grain flowering</i>: Insufficient precip. and extreme hot temperatures lead to aborted flowering and pollination.
AAPEX Farmer #5	<ol style="list-style-type: none"> 1. <i>All windows</i>: Excess precip. may disrupt field operations. 2. <i>Growing season</i>: Summer droughts are detrimental to all crops.

County-level crop yield data was used to quantify the impacts of agroclimate extremes for each focus crop and corresponding study location. This annual data was obtained from the National Agriculture Statistics Service (NASS) of the United States Department of Agriculture (<http://www.nass.usda.gov>). Table 8 shows the growing season average crop yield and production for each study location, as well as for the encompassing state and U.S. for each focus crop, to shed light on the relative importance and field efficiencies of the particular crop varieties in each respective local agroclimate. Table 8 also highlights the agroclimatological diversity in the growing

climates of the six AAPEX farming locations, and across this vast study region (Fig. 45), with growing season averages of daily maximum (minimum) temperature ranging from 73.8°F (42.4°F) for the cool northern wheat country of Montana near the Canadian Border, to 86.5°F (68.3°F) for the coastal plain cotton country in extreme southern Texas just north of the Mexico Border. Growing season precipitation ranged from only 1.4 inches in the semiarid Montana location, to 4.3 inches in southern North Carolina one of the cotton-growing locales of AAPEX Farmer #3 (Table 8, Appendix, Sections b-c). However, these growing season average temperature and precipitation values mask the true severity of the local weather and short-term climate variability exposed to the crops between planting and harvest, especially for the High Plains locations (Liberty Co., MT and Dallam Co., TX), as well as the month-to-month impacts of relevant agroclimate extremes on local crop efficiencies – which are shown more specifically below in Section d, Figures 48-51.

The growing season average crop yield values in Table 8 also show the benefit of irrigation for spring wheat and grain sorghum crops in their semiarid growing climates, with substantially higher field efficiencies for irrigated compared to non-irrigated crops at the county and state levels (separate data not available on the national level), with nearly 100% improvements for both varieties. Interestingly though, despite these similarly higher crop yields for irrigated crops, spring wheat acreage is largely un-irrigated at the county through national levels as indicated by their respective production values (Table 8). Irrigation of sorghum in the Texas Panhandle is quite extensive, on the other hand, as fed from the Ogallala Aquifer -- a massive reserve of ground water that is the region's most valuable resource, supporting agriculture there

for decades (Guerrero et al., 2010). The local agroclimate impact analyses for irrigated and non-irrigated spring wheat and sorghum crops below could at least be used to justify the expenses of implementing large-scale irrigation systems on presently non-irrigated acreage, in addition to optimizing watering strategies for those that do irrigate.

Table 7. Annual crop yield and production averages based on 1990-present for province, states, and counties of each AAPEX farm location. Irrigated (red) versus non-irrigated (blue) are included where possible. Mean daily maximum and minimum temperatures and precipitation values are 1949-2000-averaged, growing season-aggregate for the typical planting and harvesting dates of each focus crop and study location (Table 6). Units for cotton production are in bushels per 480 pound bale; all other production values are in bushels. Units for cotton yield are pounds/acre; all other yield values are bushels/acre (National Agricultural Statistics Service, U.S. Department of Agriculture).

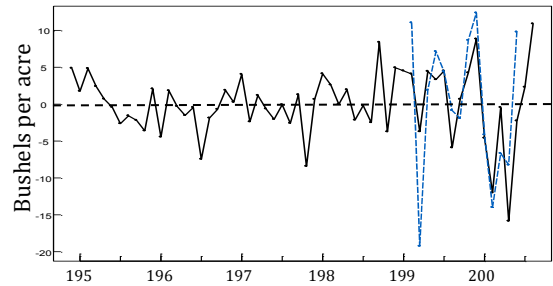
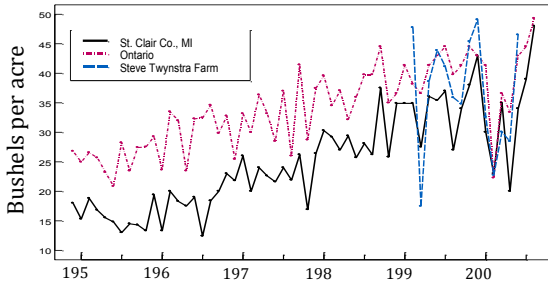
Focus Crop Yield and Production							
1990- present Averages							
AAPEX Farm Location	Southwest Ontario	Southern Minnesota	North Carolina	Southern Texas	Northern Montana	Texas Panhandle	
Crop	Soybeans	Corn	Cotton	Cotton	Spring Wheat	Sorghum	
U.S. yield	38.8	136.7	706.1	706.1	36.6 (total)		64.0 (total)
State yield	37.4	142.0	699.2	552.1	62.0	36.0	78.1 50.2
County yield	34.6	148.0	614.4	558.3	53.6	26.8	79.9 35.5
U.S. production	2.7B	10.1B	17.54M	17.54M	506M (total)		504M (total)
State production	67.1M	950.6M	0.92M	1.78M	72M	9M	108M 40M
County production	2.1M	26.8M	32.2k	124.0k	4M	0.1M	694k 719k
G.S. mean T max	75.8°F	77.6°F	84.3°F	86.5°F	73.8°F		82.2°F
G.S. mean T min	56.0°F	53.8°F	62.5°F	68.3°F	42.4°F		67.8°F
G.S. total precip.	23.4"	21.1"	25.8"	16.3"	7.1"		15.3"

Figure 46 shows the annual county crop yields since 1949 (1968 for Nueces County, TX cotton; 1979 for Liberty County, MT irrigated spring wheat; and 1972 for Dallam County, TX non-irrigated and irrigated sorghum) for each crop variety and

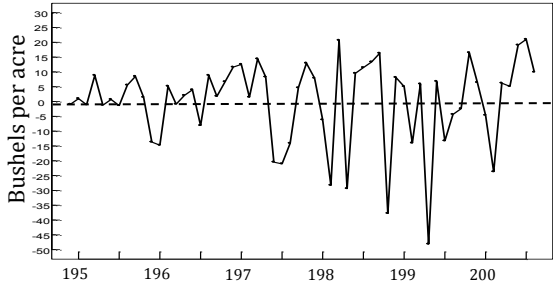
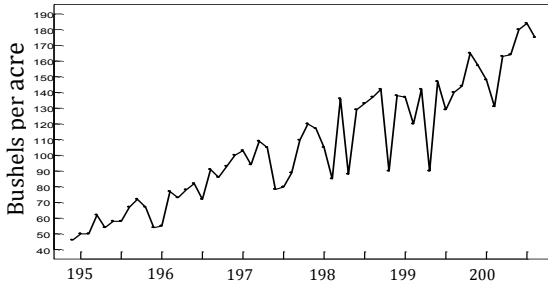
farming location studied here. For the southwest Ontario/St. Clair County, MI AAPEX farm, soybean yields are used for the local agroclimate analyses, as supported via Ontario total and farm-scale data provided by AAPEX Farmer #1 (Fig. 46a). More specifically, Farmer #1 was able to supply soybean yield data for his farm since 1991, and exhibited a correlation of +0.70 with Ontario total soybean yield over 1991-2004, and +0.76 for St. Clair County, MI soybean yield over the same period. Thus, the St. Clair County yield is more locally representative of soybeans in southwest Ontario and the rest of the southern Great Lakes Region, likely because of the large range of summer climate from north to south across Ontario.

The strongest positive trends in crop yield of the five focus crops over their respective study periods (1949-2006) are for St. Clair County, MI/Ontario soybeans and Blue Earth County, MN corn, both relatively heat-sensitive crop varieties and cultivated in northern parts of the study region (Fig. 45). The cotton farming locations studied here experienced lesser linear increases in raw crop yield since 1949, but similar slopes between the trend-lines or lines of best fit for Robeson County, NC and Nueces County, TX (cotton yield data for latter county is only available since 1968). Since this study focuses on agroclimate variability on monthly-to-seasonal time scales, these time series were de-trended by subtracting the linear best fit line (in a least squares sense) from the original data, resulting in time series of residuals from the lines of best fit. This focuses the agroclimate analyses on fluctuations in the data about the trend, independent of systematic increases in crop yield. Malone (2009) used similar linear de-trending of Iowa corn yield for investigating associations with ENSO, as did Kucharik and Serbin (2008) in studies of the impact of climate change on Wisconsin county corn yield.

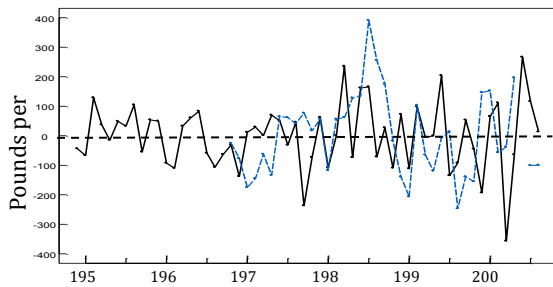
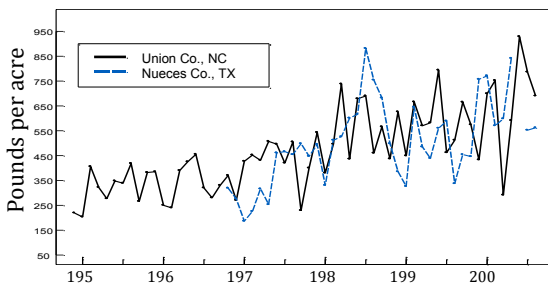
(a) SOUTHERN ONTARIO SOYBEAN YIELD



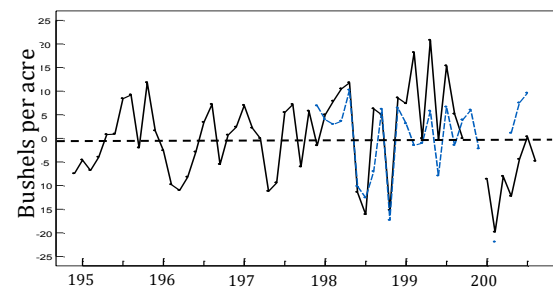
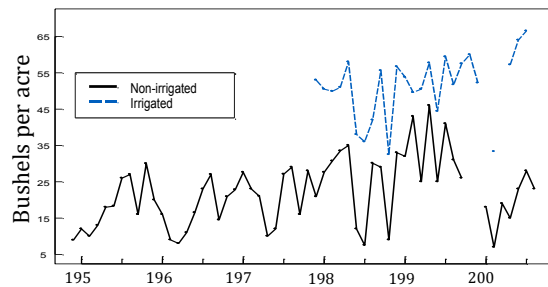
(b) BLUE EARTH CO, MN CORN YIELD



(c) ROBESON CO, NC & NUECES CO, TX COTTON YIELD



(d) LIBERTY CO, MT SPRING WHEAT YIELD



(e) DALLAM CO, TX SORGHUM YIELD

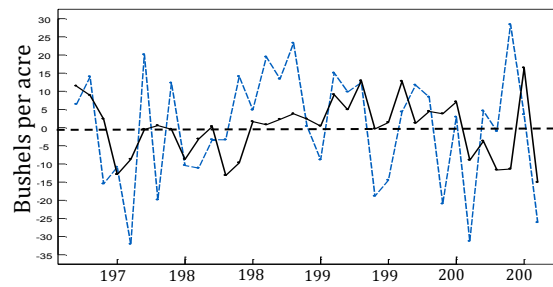
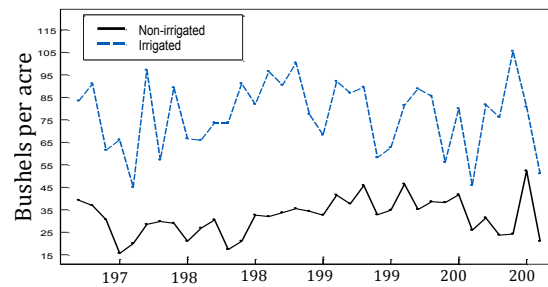


Figure 46. Annual raw (left) and de-trended (right) county crop yields for the five focus crops for the longest period possible during 1949-2006.

Time series of raw crop yields are shown in the left panels of Figure 46a-e, and the residuals from the linear lines of best fit are shown to their right, for each AAPEX farming location and focus crop. Cotton yields for Robeson County, NC and Nueces County, TX are overlaid to show their relative variability, given the sharing of farming resources between these locations by AAPEX Farmer #3. Annual crop yields for non-irrigated and irrigated fields are superimposed in the plots for Liberty County, MT spring wheat (Fig. 46d) and Dallam County, TX grain sorghum (Fig. 46e). Interestingly, crop yields for non-irrigated and irrigated spring wheat (Liberty County, MT) and sorghum (Dallam County, TX) show very little systematic increase in yield over their local data records, although the crop yields are substantially higher for irrigated than non-irrigated crops as mentioned above. As expected, the spring wheat yield residuals (Fig. 46d) during the favorable years are higher for non-irrigated crops than irrigated crops, since the purpose of irrigation is to provide sufficient soil moisture even during climatological periods within the growing season with dry soil moisture conditions.

However, the yield deficits are unexpectedly similar for both irrigated and non-irrigated crops for Liberty County, MT spring wheat, indicating that irrigation is not limiting the variability in yield from unfavorable to favorable growing seasons as much as intuition would suggest. In fact, the negative crop yield residuals for irrigated sorghum are stronger than the corresponding residuals for non-irrigated sorghum (Fig. 46e), as attributed possibly to an over-exacerbation of drought impacts from

inappropriate irrigation practices, which can also lead to increased severity of fungal and pest outbreaks especially when coincident with heat waves. Irrigation strategies in the Great Plains, as well as other modern farming practices employed throughout North America, can easily be optimized and used more proactively to minimize such crop losses from agricultural drought, given accurate predictive information on agroclimate extremes as derived in the present study.

c. Agroclimate and Local Crop Yield Co-variability

Figure 47 shows time series of the growing season GDD and precipitation anomalies and crop yield residuals for each AAPLEX farm/focus crop for 1949-2000, along with the associated growing season correlation values (Table 8). The strongest statistically significant correlations for these growing season aggregate measures are for southern Ontario soybeans and GDD (+0.43), Nueces Co., TX cotton and GDD (+0.31), Liberty Co., MT non-irrigated spring wheat and precipitation (+0.33), and Dallam Co., TX non-irrigated and irrigated precipitation (+0.50 and +0.38, respectively). Clearly, the crops cultivated in growing climates of more ample precipitation (soybeans and cotton) are more dependent on sufficient accumulated heat than precipitation, while the opposite is true for the High Plains crops of semiarid growing climates. The strong correlation between soybeans and GDD is likely attributed to the northern growing location, with undesirable late harvests resulting from cool summers and insufficient accumulated heat.

While not statistically significant, the still relatively strong negative correlations between GDD and yield for spring wheat (-0.23 irrigated and non-irrigated) and grain

sorghum (-0.29 and -0.18 irrigated and non-irrigated, respectively) are attributed primarily to the extreme hot midsummer temperatures that are often associated with seasons of positive growing season GDD anomalies, thus hindering crop reproduction as discussed in detail above. The relatively lesser dependence on precipitation for the irrigated grain crops, especially spring wheat, shows its relative effectiveness at least at these AAPEX farming locations (Fig. 47e,f). However, the season-to-season variability of especially the irrigated sorghum crop yield seems to have remained consistently high over the study period (1972-2000), but with variability in anomalous growing GDD and precipitation decreasing since 1985. The subsequent month-to-month analyses of agroclimate-crop yield relationships between irrigated and non-irrigated crops will shed light on such inconsistencies in the benefit of irrigation.

Another interesting feature apparent in the Dallam County, TX sorghum time series is a striking mode of variability on the inter-annual time scale for both non-irrigated and irrigated crops, with negative yield residuals more frequent during the 1972-1985 period, and positive yield residuals more frequent during the 1985-2000 period. A shift back to negative residuals also appears to have taken shape since the 2000 growing season. Since the growing season soil moisture in the High Plains is highly dependent on winter into spring recharge, as mentioned above, the ample rainfall over the Southern Plains that accompanies El Niño winters likely plays a role in this inter-annual variability. This teleconnection for ENSO could have significant implications for predictability of impactful agroclimate extremes relative to the sorghum crops of the southern Great Plains (Section e, below).

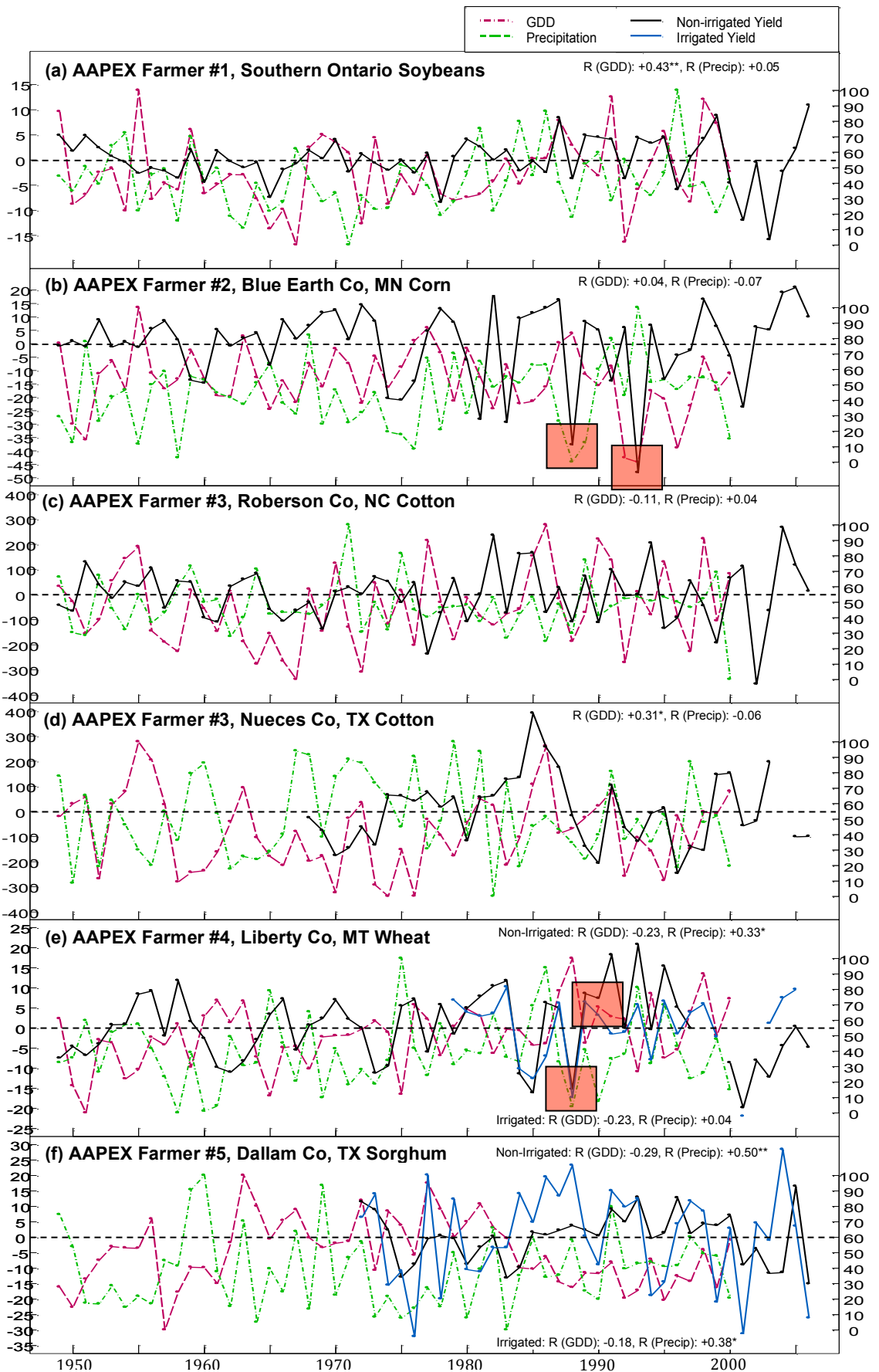


Figure 47. Growing season GDD and precipitation anomalies based on 1949-2000 averages and crop yield residuals for each study location. Irrigated crops are displayed in blue for (e) Liberty Co., MT spring wheat and (f) Dallam Co., TX grain sorghum.

Table 8 below shows the growing season (March-October) monthly correlations between local crop yield and GDD, precipitation, and PDI, for each AAPEX farm/focus crop, to identify the specific monthly agroclimate extremes for which to compute crop yield impacts in Section d, below. Generally, the strongest correlations are for GDD for soybeans, corn, and cotton during specific spring and summer months, and all three mid- to late-summer agroclimate extremes for the Great Plains AAPEX farms (Table 8). However, no months with statistically significant correlations exist for the irrigated sorghum crops in Dallam Co., TX, indicating the relative effectiveness of irrigation for this particularly heat resilient, soil moisture-independent cereal grain.

Each of the statistically significant monthly correlation values for GDD, precipitation and PDI above can be attributed to one of the crop-specific climate sensitivities discussed in Section b, above, or in greater detail in the Appendix, Sections b-c. Specifically, the highest monthly GDD correlations include July GDD and southern Ontario soybeans (+0.55); late summer (August-September) GDD and Robeson County, NC cotton (-0.30 each month); early spring (March-April) GDD and Nueces County, TX cotton (+0.34 and +0.42, respectively); and late spring-summer (May-July) GDD and Liberty County, MT spring wheat (as low as -0.58 for July, non-irrigated; -0.50 for June, irrigated). The strong positive July GDD correlation for soybeans can be attributed to the importance of faster plant growth rates during the mid-summer flowering phase and subsequent bean growth, while the positive early spring

GDD correlations for Nueces County, TX show the importance of sufficient accumulated heat coincident with the much needed spring rainfall that characterizes that growing climate. As indicated above, the negative GDD correlations during mid-summer show the heightened sensitivity and susceptibility of those crops to extreme heat during their respective flowering/reproduction time windows.

Mid-summer (June-August) precipitation and PDI are particularly important for the cereal grains, except for the irrigated sorghum crops. Since the data record for the irrigated yield is shorter than the non-irrigated data record for Liberty Co. MT spring wheat (i.e., 1979-2000), Table 13 also shows the correlations for the non-irrigated yield for the 1979-2000 period as well as 1949-2000 for comparative purposes. Accordingly, irrigation of spring wheat seems to help in the negative dependence of crop yield on July GDD, with a July correlation of -0.58 for non-irrigated crops during 1979-2000, and -0.28 for irrigated crops. During June, however, there is no difference between the irrigated and non-irrigated GDD correlations for spring wheat, with both cases having a -0.50 correlation. Since these negative GDD correlations during mid-summer for spring wheat are attributed to extreme summer heat, as will be shown in the impact analyses of anomalous daily maximum temperature below, typical irrigation practices seem ineffective at mitigating these negative impacts during June, but not during July. As mentioned above, this disparity could be caused by the increased likelihood for wheat fungi from unnecessary, excessive irrigation during periods of extreme heat. Knowledge such as this could be of significant value for not only farmers of Hard Red Spring wheat in Liberty County, MT, but for wheat farmers across the High Plains whose crops are similarly impacted by midsummer extreme heat.

(a) AAPEX Farmer #1
Southern Ontario Soybeans, 1949-2000

Month	GDD	Precip	Z Index
Mar	+0.23	-0.14	+0.02
Apr	+0.14	-0.03	+0.14
May	+0.21	+0.03	+0.01
Jun	+0.26	-0.07	+0.10
Jul	+0.55**	+0.20	+0.10
Aug	+0.17	+0.03	+0.23
Sep	+0.03	-0.06	-0.02
Oct	+0.03	+0.14	+0.13
All	+0.43**	+0.05	+0.19

**|R| ≥ 0.27 (0.35) significant at 5% (1%) confidence level

(b) AAPEX Farmer #2
Blue Earth Co, MN Corn, 1949-2000

Month	GDD	Precip	Z Index
Mar	+0.03	+0.09	-0.01
Apr	+0.15	-0.19	-0.32*
May	+0.13	-0.19	-0.06
Jun	-0.05	-0.19	-0.01
Jul	-0.11	+0.15	+0.28*
Aug	-0.29*	-0.20	+0.05
Sep	+0.25	+0.02	-0.10
Oct	+0.07	+0.32*	-0.13
All	+0.04	-0.07	-0.08

**|R| ≥ 0.27 (0.35) significant at 5% (1%) confidence level

(c) AAPEX Farmer #3
Robeson Co, NC Cotton, 1949-2000

Month	GDD	Precip	Z Index
Mar	+0.18	-0.15	-0.19
Apr	-0.11	+0.14	+0.28*
May	-0.06	+0.15	-0.07
Jun	+0.10	+0.02	-0.02
Jul	-0.21	+0.20	+0.05
Aug	-0.30*	-0.05	+0.23
Sep	-0.30*	-0.18	+0.06
Oct	+0.15	+0.01	-0.14
All	-0.11	+0.04	+0.09

**|R| ≥ 0.27 (0.35) significant at 5% (1%) confidence level

(d) AAPEX Farmer #3
Nueces Co, TX Cotton, 1968-2000

Month	GDD	Precip	Z Index
Mar	+0.34*	+0.03	-0.23
Apr	+0.42**	-0.02	-0.23
May	+0.16	+0.05	+0.02
Jun	-0.03	+0.11	+0.06
Jul	-0.14	+0.16	+0.21
Aug	+0.18	-0.21	-0.12
Sep	+0.10	-0.18	-0.20
Oct	+0.14	-0.12	-0.02
All	+0.31*	-0.06	-0.12

**|R| ≥ 0.34 (0.44) significant at 5% (1%) confidence level

(e) AAPEX Farmer #4
Liberty Co, MT Wheat, Non-irrigated (N1):1949-2000, (N2): 1979-2000; Irrigated (I): 1979-2000

Month	GDD(N1)	GDD(N2)	GDD(I)	Precip(N1)	Precip(N2)	Precip(I)	Z (N1)	Z (I)
Mar	+0.01	0.00	-0.15	+0.05	+0.07	+0.13	+0.23	+0.41
Apr	-0.21	-0.34	-0.26	+0.11	+0.09	+0.14	+0.24	+0.28
May	-0.10	-0.45*	-0.32	+0.18	+0.21	0.00	+0.24	+0.28
Jun	-0.23	-0.50*	-0.50**	+0.33*	+0.55**	+0.24	+0.52**	+0.47*
Jul	-0.43**	-0.58**	-0.28	+0.41**	+0.59**	+0.49*	+0.64**	+0.66**
Aug	+0.02	-0.05	-0.05	+0.03	+0.11	-0.04	+0.21	+0.26
Sep	+0.14	+0.24	+0.49*	-0.04	-0.17	-0.46*	-0.09	-0.50*
Oct	-0.13	-0.04	-0.09	-0.14	-0.23	-0.19	+0.03	-0.40
All	-0.23	-0.49*	-0.23	+0.33*	+0.39	+0.04	+0.51**	+0.42

**|R| ≥ 0.27 (0.35) and 0.43 (0.54) significant at 5% (1%) confidence level for 1949-2000 and 1979-2000, respectively

(f) AAPEX Farmer #5
Dallam Co, TX Sorghum, Irrigated (I) and Non-irrigated (N): 1972-2000

Month	GDD (N)	GDD (I)	Precip (N)	Precip (I)	Z Index (N)	Z Index (I)
Mar	-0.01	-0.14	+0.20	+0.18	+0.11	+0.15
Apr	-0.09	-0.35	-0.14	+0.16	-0.10	+0.02
May	+0.12	+0.20	+0.13	-0.01	-0.21	-0.19
Jun	-0.19	-0.13	+0.24	+0.11	+0.20	+0.28
Jul	-0.33	-0.03	+0.47**	+0.18	-0.02	+0.20
Aug	-0.49**	-0.19	+0.10	+0.18	+0.22	+0.11
Sep	-0.34					-0.15
Oct	-0.16					-0.08
All	-0.29	-0.18	+0.50**	+0.38*	+0.04	+0.10

**|R| ≥ 0.37 (0.46) significant at 5% (1%) confidence level

Table 8. Correlations between monthly and total growing season weather variables and corn crop yield for Blue Earth County, MN. According to two-tailed *t* tests, correlation magnitudes exceeding 0.27 (0.35) are significant at the 5% (1%) confidence level

[Wilks, 2006, pp. 117-118; Holland and Webster, 2008]. One (two) asterisks indicate correlation coefficients significant at 5% (1%) confidence level.

d. Crop Yield Impacts from Agroclimate Extremes

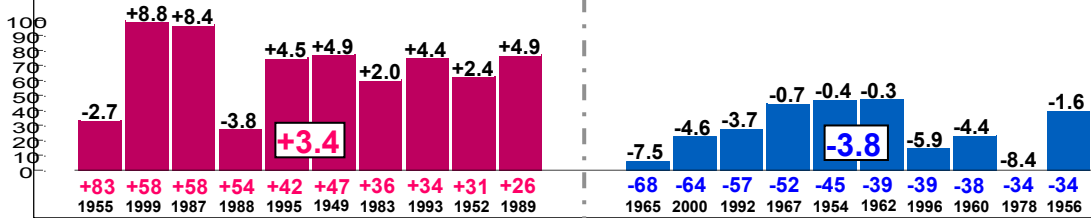
Figure 48 shows the crop yield residuals for years with the ten highest and lowest monthly GDD totals over time periods with the strongest correlations between GDD and county-level crop yield at each of the six AAPEX farming locations. The crop yield residuals are also scaled from 0 to 100 for comparative purposes, with the ordinates of the plots being scaled crop yield residual, as 0 representing the lowest residual and 100 the highest residual for each time series (Heim et al., 2003). Hence, visual inspection of the bar plots in Figure 48 provides insight on the relative impacts of the GDD monthly extremes for each particular AAPEX farm/focus crop, including comparisons between irrigated and non-irrigated crops for the Great Plains cereal grains (Fig. 48e,f). The disparities in the mean crop yield residuals between the ten highest and lowest GDD totals are greatest for southern Ontario soybeans and Nueces County, TX cotton (Fig. 48a,d), for which the respective GDD months compared (i.e., July and March-April, respectively) correspond with critical growth windows (Table 6, above).

The predictive potential of monthly agroclimate extremes with enhanced influence on crop yield, such as these identified for GDD at each AAPEX farm, can be assessed based on the strength and time-lags of their associated Pacific Ocean SST teleconnections (Chapters 4-6, Sections c-f, above). Given this predictive agroclimate information, farming practices could be optimized to maximize crop yields.

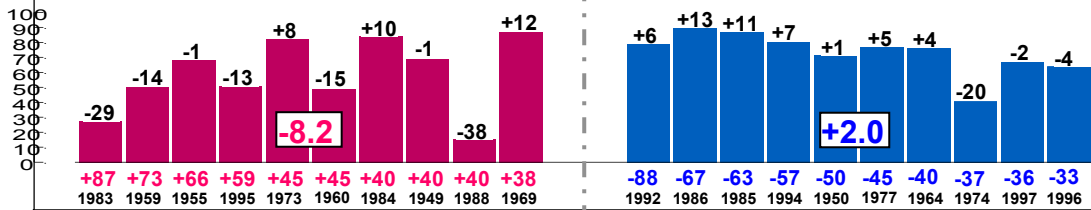
HIGHEST GDD ANOMALIES

HIGHEST GDD ANOMALIES

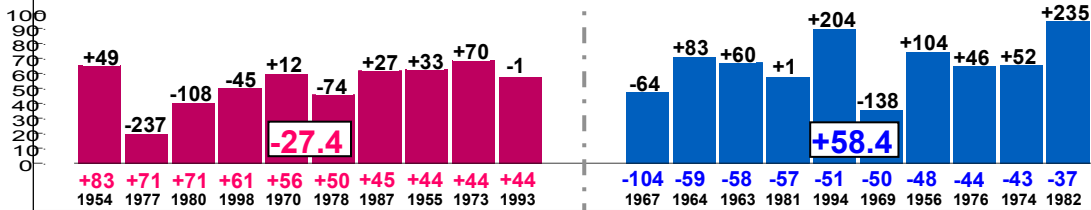
(a) AAPEX Farmer #1, Southern Ontario Soybean Yield Residuals, July GDD



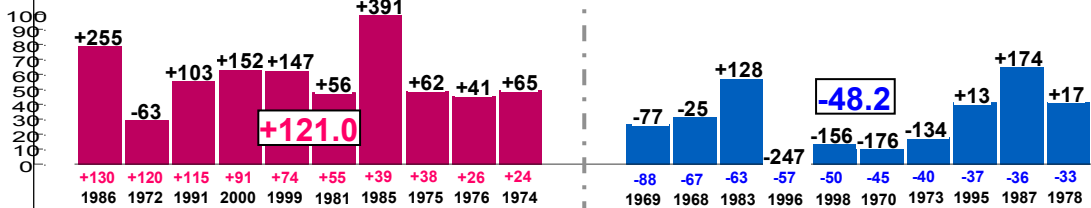
(b) AAPEX Farmer #2, Blue Earth Co, MN Corn Yield Residuals, August GDD



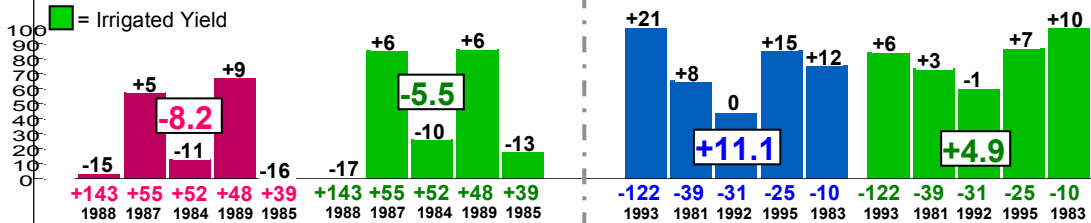
(c) AAPEX Farmer #3, Robeson Co, NC Cotton Yield Residuals, Jul-Aug GDD



(d) AAPEX Farmer #3, Nueces Co, TX Cotton Yield Residuals, Mar-Apr GDD



(e) AAPEX Farmer #4, Liberty Co, MT Wheat, June-July GDD



(f) AAPEX Farmer #5, Dallam Co, TX Sorghum, August GDD

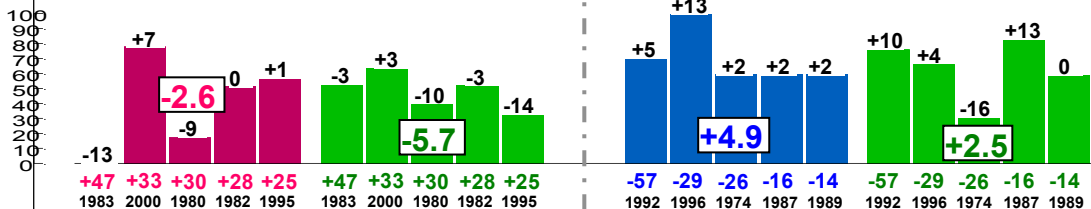


Figure 48. Raw and average crop yield residuals for the ten highest and ten lowest GDD anomalies for relevant months for each focus crop, with ordinates representing scaled (0-100) crop yield residual for comparative purposes (Heim et al., 2003). Years of each GDD anomaly are listed below the associated bar.

The disparity in mean yield residuals between the early spring GDD extremes (March-April) is particularly substantial for Nueces Co., TX, with a +121.0 bushels/acre (-48.2 bushels/acre) mean residual for the ten highest (lowest) March-April GDD totals for the reasons mentioned above. On the other hand, the disparities are not as consistent between the GDD extremes representing the aforementioned negative GDD relationships with crop yield from extreme midsummer heat for the non-cereal grain varieties (Blue Earth County, MN corn -- Fig. 48b and Robeson Co., NC -- Fig. 48c), because of the less direct representation of extreme midsummer heat detrimental to crop yields. Accordingly, the more northern soybean crops in southern Ontario (St. Clair Co., MI) with the opposite relationship with midsummer GDDs (i.e., July), with yields directly dependent on sufficient accumulated heat during flowering and bean growth, show consistent and substantial disparities in the mean yield residuals for the ten highest/lowest July totals (Fig. 48a).

The sorghum yield impacts from August GDD extremes for non-irrigated and irrigated fields show an especially interesting result for the five highest GDD anomalies in Dallam Co., TX (five highest/lowest GDD years were included for data segregated by irrigation use -- Fig. 48e,f), that was suggested above. The negative mean crop yield residual is stronger for the irrigated sorghum crops (-5.7 bushels/acre) than the non-irrigated crops during the five highest August GDD anomalies, indicating the relative ineffectiveness of local cultural irrigation practices at mitigating the detrimental crop

yield impacts from extreme heat during flowering and grain fill of sorghum. As mentioned above, this could be attributed to the increased likelihood of grain fungi outbreaks and pest infestations given excessive irrigation coincident with hot temperatures, or because the heat tolerance of crops decreases when the humidity immediately surrounding the plants increases as stomata aperture increases. Similarly, the positive mean crop yield residual is lower for irrigated crops than non-irrigated during the five lowest August GDD anomalies, suggesting a relative ineffectiveness of irrigation in helping crops take full advantage of ideal growing conditions (Fig. 48f).

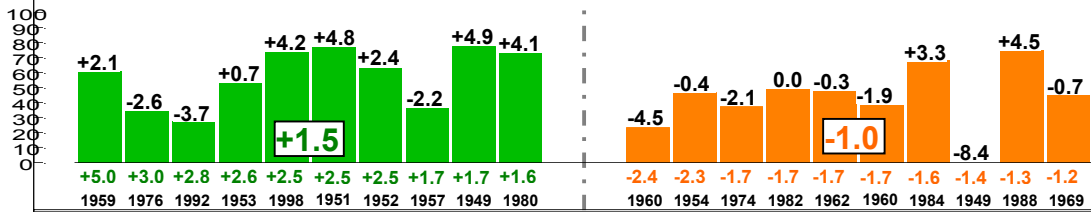
Knowledge of the specific impacts of extreme agroclimate during critical crop growth phases within the growing season, such as that provided above for GDD for a variety of crop types and farming locations, could clearly be used to optimize farming strategies such as irrigation and fertilization. Since substantial lead-time is often required to adjust these practices, especially for farmers like AAPEX Farmer #3 who share equipment and labor between farming locations, the above GDD impacts (as well as for the other agroclimate variables below -- monthly precipitation, PDI, and extreme midsummer heat) are investigated for teleconnections with the above Pacific Ocean SST patterns to assess their predictability.

Similarly, Figure 49 shows the crop yield impacts from monthly precipitation extremes during the relevant months within the growing seasons of each focus crop and farming location. Discrepancies between the ten highest and ten lowest historical monthly precipitation anomalies are again largest for the semiarid growing climates of the cereal grains.

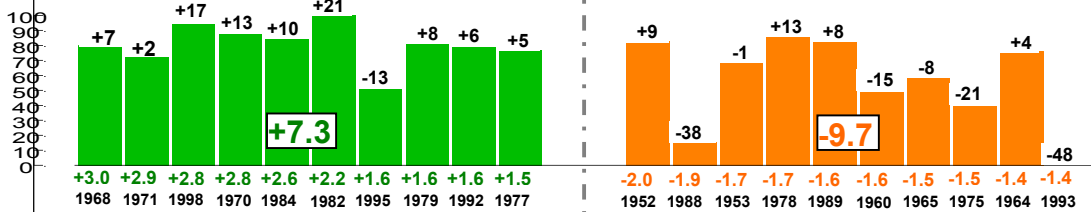
HIGHEST PRECIP. ANOMALIES

LOWEST PRECIP. ANOMALIES

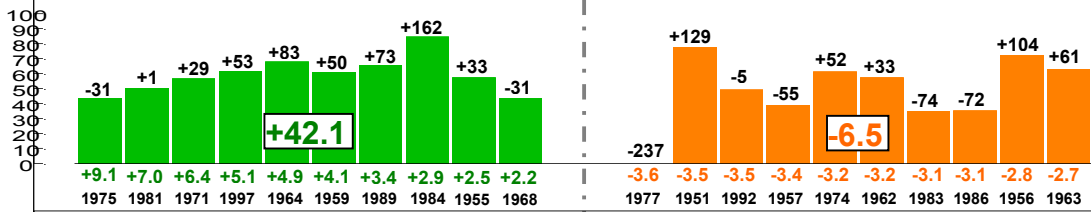
(a) AAPEX Farmer #1, Southern Ontario Soybean Yield Residuals, July Precip.



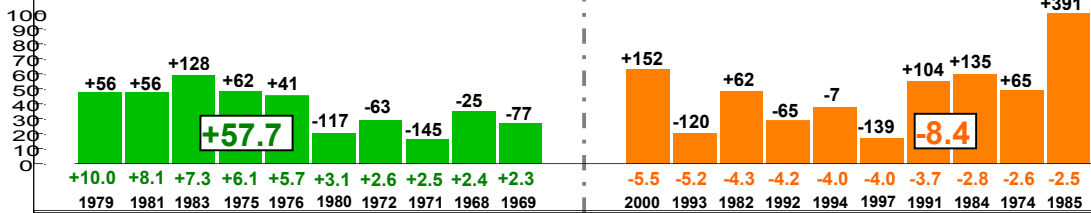
(b) AAPEX Farmer #2, Blue Earth Co, MN Corn Yield Residuals, October Precip.



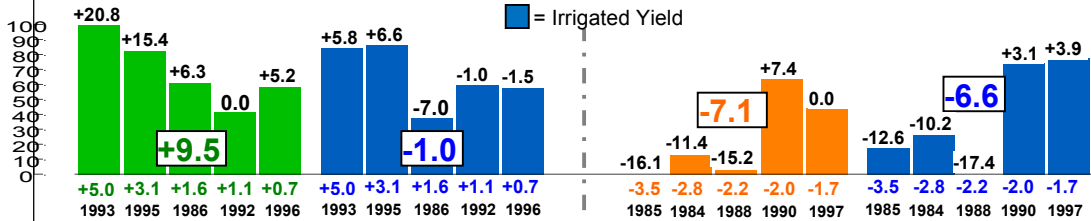
(c) AAPEX Farmer #3, Robeson Co, NC Cotton Yield Residuals, July Precip.



(d) AAPEX Farmer #3, Nueces Co, TX Cotton Yield Residuals, Jul-Aug Precip.



(e) AAPEX Farmer #4, Liberty Co, MT Wheat Yield Residuals, June-July Precip



(f) AAPEX Farmer #5, Dallam Co, TX Sorghum Yield Residuals, Mar-Oct (GS) Precip

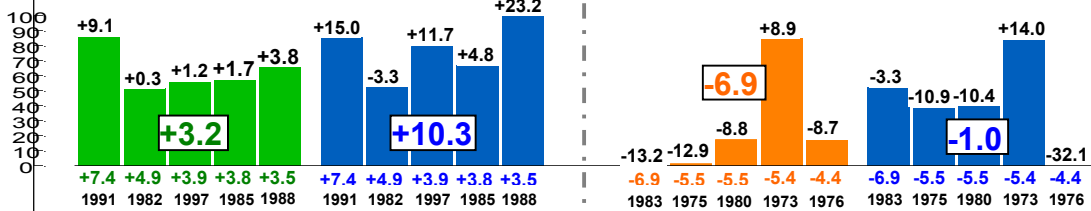


Figure 49. Raw and average crop yield residuals for the ten highest and ten lowest monthly precipitation anomalies for relevant months for each focus crop, with ordinates representing scaled (0-100) crop yield residual for comparative purposes (Heim et al., 2003). Years of each GDD anomaly are listed below the associated bar.

In general, crop yield residuals are consistently higher for the ten highest precipitation monthly anomalies at the respective AAPEX farm locations, except for the dry subset of years for soybeans, corn, and cotton (Fig. 49 a-d). The positive crop yield residuals occurring despite strong negative precipitation anomalies can be attributed to two factors: the ability of the local soil profile to store moisture following isolated rainfall events associated with summer air mass thunderstorms, as well as the specific ability of the crops to recover from isolated monthly precipitation deficiencies given ample rainfall during the remaining months. Consequently, the disparities in the crop yield residuals between the five highest and lowest precipitation anomalies are maximized for the grain crops in the High Plains (Fig. 36e,f), where the porous, sandy local soil profiles have relatively low available water capacities, and soil moisture deficiencies are already a commonality during the mid-summer months there.

Interestingly, irrigation seems to be more effective at maximizing crop yields during periods of more ample precipitation for Dallam Co., TX sorghum than Liberty Co., MT spring wheat (relevant respective periods being June-July for wheat and the entire growing season for sorghum). Specifically, irrigation improved mean sorghum yield residuals from +3.2 bushels/acre to +10.3 bushels/acre for the five highest growing season precipitation anomalies, while more negative spring wheat yield residuals were associated with the irrigated spring wheat crops than non-irrigated during the five highest precipitation anomalies for June-July in Liberty County, MT (Fig. 49e).

These seemingly negative impacts of irrigation on crop yield for northern Montana spring wheat can likely be attributed to over-irrigation when not needed by the crops, which is a common problem of the modern cereal grain farm in the Great Plains, where periods of midsummer dryness often coincide with heat waves (i.e., Appendix, Sections b-c).

The impacts from the ten highest/lowest monthly PDI values for the growing season monthly periods with the highest correlations with local crop yield are a consequence of the more direct relationship between soil moisture content and crop vigor (Table 8; Chapter 3, Section e, above). Figure 50 shows the impacts from PDI extremes on crop yield residual for the relevant months determined from the above correlation analysis, and support many of the patterns identified from the monthly precipitation impact analyses. For example, the largest discrepancies in the direct impacts of soil moisture on crop yields are found for the cereal grains (Fig. 50e,f), and are even more prominent than those of precipitation given the inherent month-to-month persistence of PDI. Interestingly, consistently higher crop yield residuals are found for the ten lowest April PDI values for Blue Earth County, MN corn, likely because of the importance of relatively dry soils at planting encouraging for robust and vertical root systems in moisture-demanding corn crops. The largest discrepancies between the moist and dry subsets of years are for the focus crops of greatest overall moisture demand, such as the corn and cotton crops of AAPLEX Farmers #2 and 3, respectively.

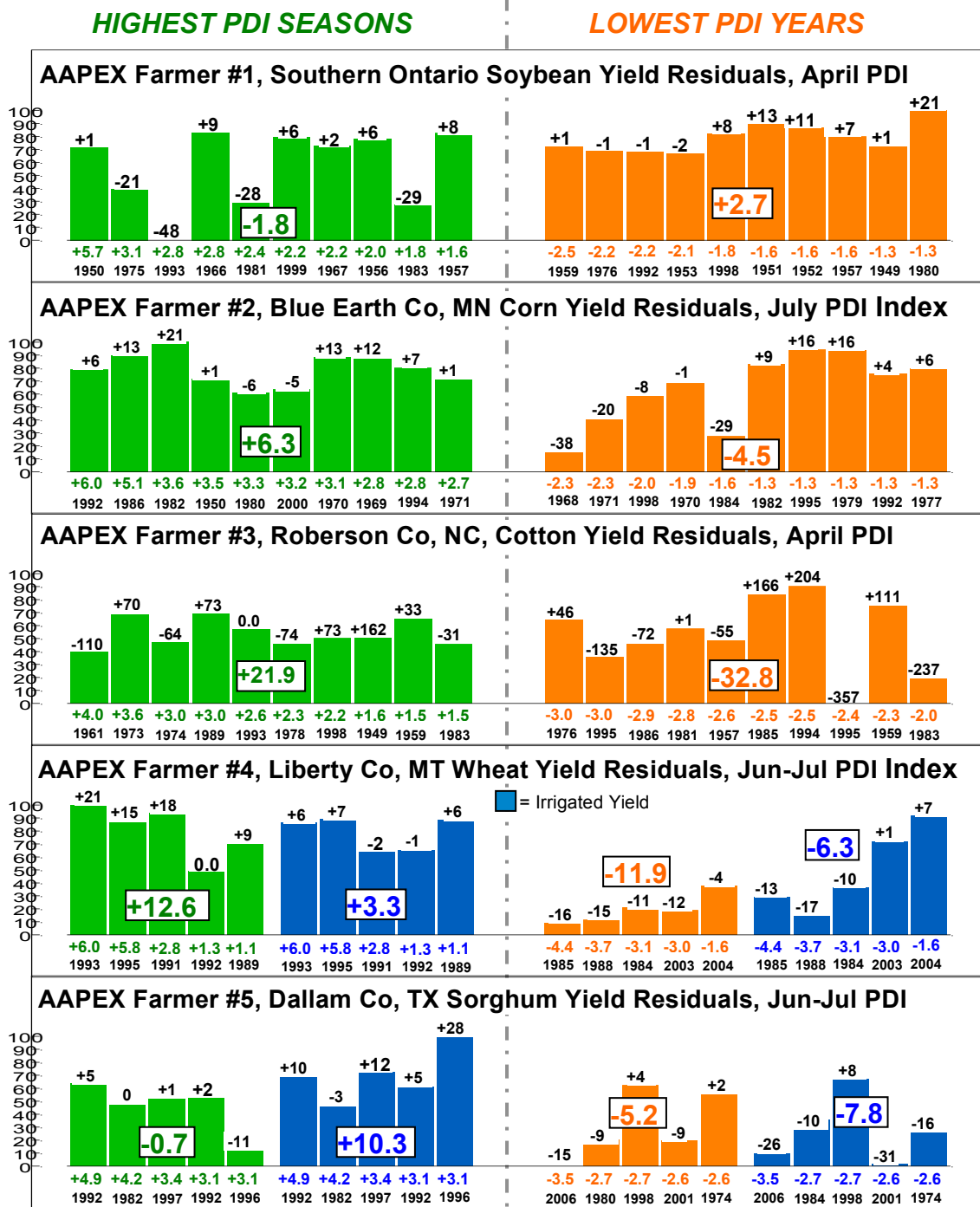


Figure 50. Raw and average crop yield residuals for the ten highest and ten lowest monthly PDI for relevant months for each focus crop, with ordinates representing scaled (0-100) crop yield residual for comparative purposes (Heim et al., 2003). Years of each GDD anomaly are listed below the associated bar.

Figure 51 shows the local crop yields for the growing seasons with the fifteen hottest flowering windows at the six AAPEX farming locations and focus crops (i.e., St. Clair Co., MI soybeans: July-August; Blue Earth Co., MN corn: July-August; Robeson Co., NC and Nueces Co., TX: June-July; Liberty Co., MT spring wheat: July; Dallam Co., TX: June-July), as specified by the AAPEX farmers themselves and through an exhaustive literature review on specific crop sensitivities to extreme heat during pollination (Appendix, Sections c; Chapter 3, Section f; Table 5, above). Interestingly, southern Ontario/St. Clair County, MI soybeans (Fig. 51a) are the only crop not locally impacted by extreme summer heat, likely because of the northern farming location and moderating influence from Lake Huron. Upland Cotton flowering/pollination appears particularly sensitive to extreme midsummer heat (Fig. 51c,d), with relatively much lower crop yield residuals on average across the fifteen hottest reproductive periods at the North Carolina and South Texas locations of AAPEX Farmer #3 (Roberson County, NC: -56.4 pounds/acre; Nueces County, TX: -15.9 pounds/acre).

Compared with the similar analyses above for monthly GDD, precipitation, and PDI (Fig. 48-50), extreme midsummer heat during these specific flowering windows overall is more detrimental to local crop yield for all AAPEX farming locations except southern Ontario, which is characterized by a uniquely moderate prevailing growing climate given the Great Lakes influence (Appendix, Section b). This result is expected, since pollen sterilization will decimate fruit/kernel/boll/grain development regardless of how favorable are the conditions the rest of the growing season (Chapter 3f, above). Also, the very heat-resilient grain sorghum crops of the Texas Panhandle (Fig. 36f) are much less impacted by hot midsummer temperatures compared with other focus crops.

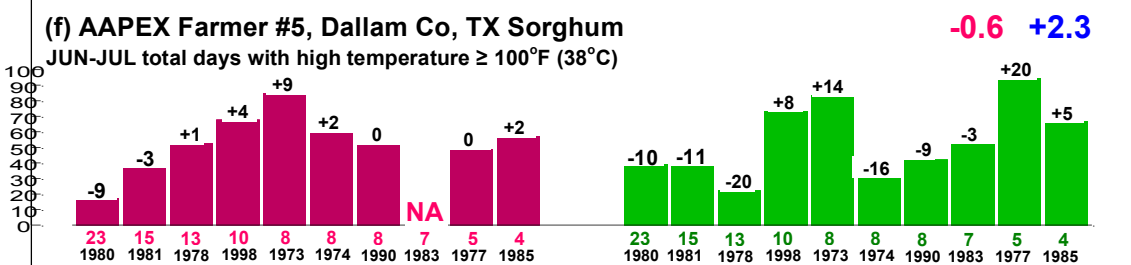
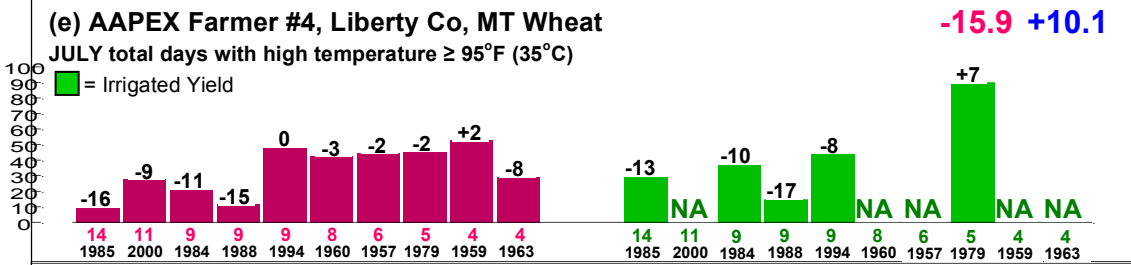
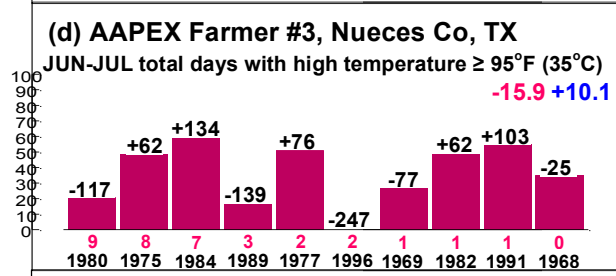
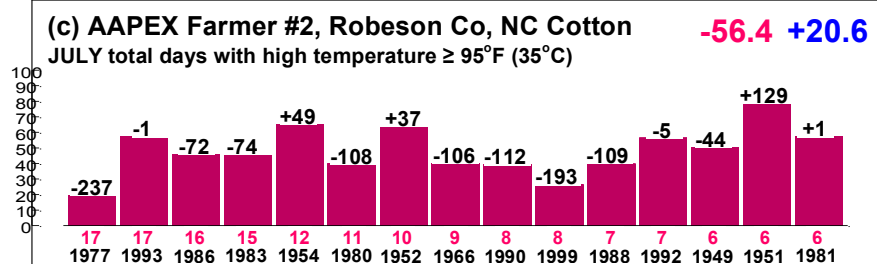
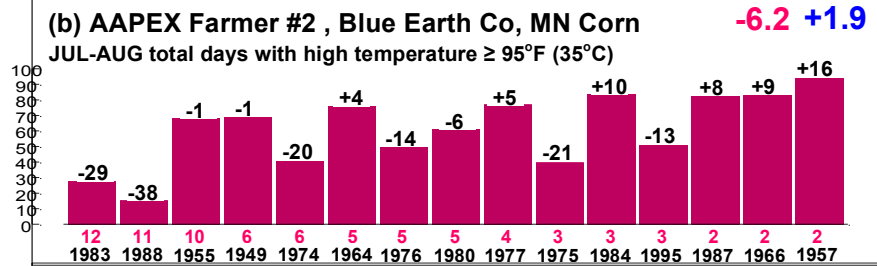
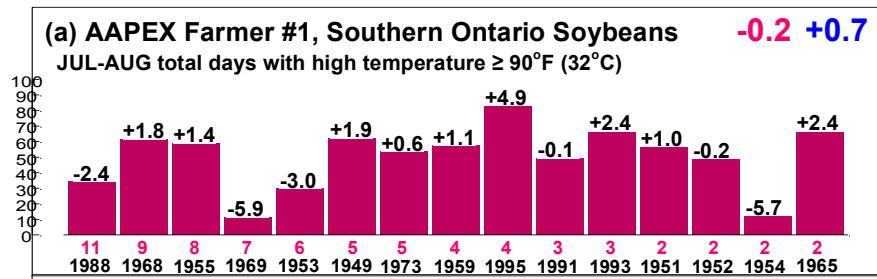


Figure 51. Raw and average crop yield residuals for the 15 highest number of days above crop-specific flowering-abortion thresholds for relevant months for each focus crop, with ordinates representing scaled (0-100) crop yield residual for comparative purposes (Heim et al., 2003). Years of each case are listed below the associated bar. Red (blue) numbers at upper right are average crop yield residuals for the 15 cases of extreme heat (remaining years).

Comparison of the crop yield residuals between the irrigated and non-irrigated subsets for Liberty County, MT spring wheat and Dallam County, TX grain sorghum (Fig. 51e,f), shows that irrigation likely has limited effectiveness at limiting pollen sterilization from extreme heat. Hence, given advanced knowledge of detrimental midsummer heat waves, adjustment of planting dates may be the best option for farmers to minimize crop yield loss. The predictive potential of these most impactful extremes in local agroclimate (i.e., extreme midsummer heat, Fig. 51) for each AAPEX farm location and focus crop, including those identified above for GDD, precipitation, and PDI (Figs. 48-50), is discussed below in terms of strength and time-lags of the preceding regional Pacific Ocean SST teleconnections (Chapters 4-6).

Chapter 8. Predictability of Impactful Agroclimate and Conclusions

a. Predictability of Locally Impactful Agroclimate Extremes

The recently infamous Droughts of 1988 and 2012-14 are the two most costly natural disasters in U.S. history ahead of even Hurricane Katrina (2005) and Super Storm Sandy (2012). Along with the agriculturally devastating Flood of 1993 in the Upper Mississippi River Basin, they show the enhanced sensitivity of modern farming to short-term agroclimate extremes. However, optimization of modern farming practices such as the adjustment of sowing dates/plant populations, irrigation, hybridization, and fertilization can help to minimize crop yield losses from warm season agroclimate extremes, as well as maximize gains during periods of favorable growing conditions. Table 9 provides a summary of the predictive potential of the most impactful monthly agroclimate extremes (GDD, precipitation, PDI) identified above in Chapter 7, Section d, inferred via the strength and time-lags of the above growing season (March-October) monthly teleconnections with modes of Pacific Ocean SST variability (Chapters 4-6, Sections c-f). The specific farming practices recommended for optimization based on this predictive agroclimate information for the AAPEX farming locations/focus crops also are included in the last column of Table 9, below.

The most striking result in Table 9 is for the cereal grains (i.e., sorghum, spring wheat) with much stronger positive crop yield residuals for the non-irrigated crops compared with irrigated during the wettest ten midsummer (June-July) periods since 1949. Hence, the most straightforward recommendation here is for these AAPEX farmers is to cease irrigation altogether during the growing seasons of midsummer soil moisture surplus. Adjustment of planting dates and selection of appropriate hybrids

before the growing season based on accurate predictive information such as developed above in Chapters 4-6 for monthly GDD, precipitation, and PDI will also shift those critical crop maturation windows away from periods of detrimental extreme agroclimate to coincide with favorable growing conditions, universally for any farming location or crop variety cultivated in the study region and beyond.

Table 9. Notable monthly agroclimate extremes of historical impact at each AAPEX farming location, strongest locally relevant teleconnections (Chapters 4-6, Sections c-f, above), and very basic suggestions of farming practice optimization.

Monthly PDI						
AAPEX farm crop yield impacts and predictability						
Location	Crop	Critical Period	Yield Residual (10 wettest years)	Yield Residual (10 driest years)	Strongest Pacific Ocean Teleconnection Pattern	Practice to Optimize (months)
Middlesex, ON	Soybeans	April	-1.8	+2.7	Jan-Mar PDO	Planting/fertilization
Blue Earth, MN	Corn	July	+6.3	-4.5	Jan-Mar mature ENSO	Planting/irrigation
Robeson, NC	Cotton	April	+21.9	-32.8	Jan-Mar mature ENSO	Planting/irrigation
Nueces, TX	Cotton	NA	NA	NA	NA	NA
Liberty, MT	Wheat	June-July	+12.6 +3.3	-11.9 -6.3	Jan-Mar PDO	Irrigation
Dallam, TX	Sorghum	June-July	-0.7 +10.3	-5.2 -7.8	Jan-Mar/Mar-May mature ENSO	Irrigation

Precipitation						
Location	Crop	Critical Period	Yield Residual (10 wettest years)	Yield Residual (10 driest years)	Strongest Pacific Ocean Teleconnection Pattern	Practice to Optimize (months)
Middlesex, ON	Soybeans	July	+1.5	-1.0	Apr-Sep decaying ENSO	Planting/irrigation
Blue Earth, MN	Corn	October	+7.3	-9.7	Apr-Sep decaying ENSO	Planting/fertilization
Robeson, NC	Cotton	July	+42.1	-6.5	Mar-May mature ENSO	Adjust planting
Nueces, TX	Cotton	July-Aug.	+57.7	-8.4	Jan-Mar mature ENSO	Adjust planning
Liberty, MT	Wheat	June-July	+9.5 -1.0	-7.1 -6.6	Jan-Mar PDO	Adjust planting
Dallam, TX	Sorghum	Growing Season	+3.2 +10.3	-6.9 -1.0	Jan-Mar PDO	Hybridization

GDD						
Location	Crop	Critical Period	Yield Residual (10 warm years)	Yield Residual (10 cold years)	Strongest Pacific Ocean Teleconnection Pattern	Practice to Optimize (months)
Middlesex, ON	Soybeans	JUL	+3.4	-3.8	Mar-May PDO	Planting/hybridization
Blue Earth, MN	Corn	AUG	-8.2	+2.0	Nov-Apr mature ENSO	Planting/hybridization
Robeson, NC	Cotton	JUL-AUG	-27.4	+58.4	Mar-May NPO	Planting/hybridization
Nueces, TX	Cotton	MAR-APR	+121.0	-48.2	Jan-Mar mature ENSO	Planting/hybridization
Liberty, MT	Wheat	JUN-JUL	-8.2 -5.5	+11.1 +4.9	Mar-May NPO	Planting/hybridization
Dallam, TX	Sorghum	AUG	-2.6 -5.7	-2.6 -5.7	Mar-May PDO	Planting/hybridization

The predictability of these most impactful agroclimate extremes are assessed using the above strongest, most coherent Pacific Ocean teleconnection patterns that also are characterized by consistent time lags from the 3- or 6-month SST periods (i.e., monthly GDD, precipitation, PDI; Chapters 4-6, Sections c-f), a method which could be employed similarly by any North American farmer of one of the five focus crops studied here. Several strong monthly-to-seasonal teleconnection patterns were identified for these agroclimate extremes with not only mature and transitional El Niño/La Niña patterns, but also the cold and warm phases of the Pacific Decadal Oscillation (PDO) and North Pacific Oscillation (NPO) as uniquely clarified with present treatment of Varimax-rotated Principal Component Analysis (PCA). The most prominent teleconnections include the ENSO Spring GDD (“ESG”) and ENSO Spring Precipitation (“ESP”) anomaly patterns, especially with winter-spring 3-month mature El Niño modes and the corresponding wetness (monthly precipitation anomalies > 1.25 inches) and anomalously low GDD composite totals across the Great Plains Region and southern U.S (GDD < -30); as well as large-scale moderate to severe agricultural drought indicated throughout the study region associated with preceding or concurrent cold-phase PDO.

Overall, the most impactful (both detrimental and beneficial) aspects of growing season agroclimate variability at the six AAPEX farming locations are summer (June-August) GDD monthly anomalies for all crops and spring (March-April) GDD for South Texas cotton yields; midsummer (June-July) monthly PDI for central Montana spring wheat; and the monthly totals of days with daily mean temperatures above highly-specific pollen sterilization thresholds for all focus crops except for southern

Ontario soybeans. Each of these specific growing season extremes in agroclimate show predictive potential based on teleconnection lags with the 3- and 6-month Pacific Ocean SSTA patterns computed in Chapter 2, specifically the January-March and March-May modes of mature ENSO and PDO. The negative impacts on agricultural production from heat stress coincident with flowering/pollination phases, as identified in the present study for the six AAPEX farming locations and five focus crops (corn, soybeans, cotton, spring wheat, grain sorghum), has been well-documented in previous literature (Trenberth et al., 1988; Ropelewski, 1988; Hall, 1992; Stewart et al., 1993; Porter and Gawith, 1999).

b. Conclusions: Summary and Future Work

Even if the impacts on crop yields from agroclimate variability are objectively and comprehensively understood for a specific crop type and farming location, this information is operationally useful from the perspective of the farmer only if the impactful climate extremes can be predicted. Lagged and concurrent monthly teleconnections with dominant modes of Pacific Ocean SST variability (mature/decaying ENSO, PDO, NPO phases) are employed in the present study to assess quantitatively the predictive potential for the most robust growing season agroclimate extremes. This methodology is uniquely feasible here because of the convenient study region location “downstream” of the Pacific Ocean relative to the prevailing westerlies of the Polar Front Jet Stream, which also happens to be the largest and deepest by far of the Earth’s ocean basins accounting for 46% of total water surface area with depths of greater than 10,000 meters (Rasmusson and Carpenter, 1982;

Namias et al., 1988; Fye et al., 2004). Consequently, the cold and warm phases of large-scale Pacific Ocean SST patterns are of heightened relative persistence compared with climate variability in the overlying atmosphere and a convenient predictive tool for monthly-to-seasonal agroclimate predictability.

The dependence of North American climate on Pacific Ocean SST variability has been well documented in previous literature on timescales from monthly to decadal, especially for El Niño and La Niña patterns during the cold season (Rasmusson and Carpenter, 1982; Horel and Wallace, 1981; Karoly and Hoskins, 1981; Ting and Wang, 1997; Barlow et al., 2001; Chen and Li, 2008), but this prior research lacks the basin-wide approach needed to identify coherent monthly teleconnections particularly during the warm season (i.e., March-October). Beyond the winter season as the Polar Front Jet Stream begins to migrate northward across the North Pacific Ocean, mid-latitude SSTA patterns become increasingly relevant in the modulation of North American agroclimate (Namias et al., 1976; 1988; Wallace and Gutzler (1981); and Barlow et al., 2001). As discussed above in Chapter 5, Section e, North American warm-season agroclimate is also found here to be particularly sensitive to the intermodulation between subtropical/tropical and mid-latitude Pacific Ocean SSTAs, as well as their evolution and prevalence relative to the seasonal cycle.

Complexities such as these with warm-season teleconnections of North American extreme climate are a desired result of the present study's uniquely comprehensive treatment of monthly-to-seasonal Pacific Ocean SST variability, derived through a multitude of Principal Components Analyses on six separate 3- and 6-month SST time periods (January-March, March-May, June-August, November-April,

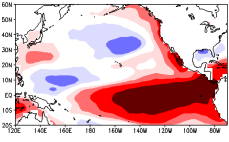
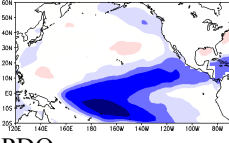
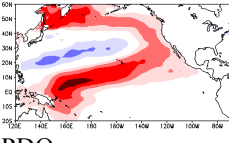
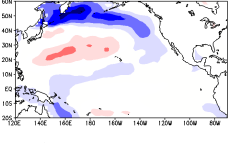
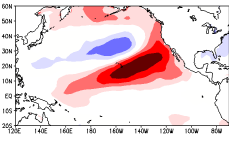
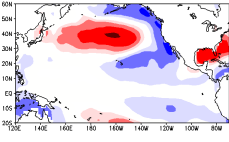
January-June, April-September; Chapter 2, Section c). The basin-wide treatment of Pacific Ocean SST variability and unique extraction of the NPO and PDO is intended also to provide much-needed insight on extratropical SSTA patterns, which are vastly under-represented in previous related research compared with El Niño and La Niña. A majority of this previous research even quantifies extratropical SST variability in the North Pacific Ocean with a single aggregate mode on the seasonal and shorter time-scales (e.g, Mantua et al., 1997; Papineau, 2001; Gutzler et al., 2002; Zhang et al., 1996), that includes both PDO and NPO variability as defined in the present study. This well-documented North Pacific aggregate SST pattern is termed the PDO by Mantua et al. (1997) and Papineau (2001) and the “North Pacific Mode” by Zhang et al. (1996), and assumes that the “PDO horseshoe” and “NPO oval” vary as one single mode. The present study’s comprehensive analysis of Pacific Ocean SST variability from the tropics through mid-latitudes, including the extraction of a multitude of PDO and NPO modes that vary independently on the seasonal scale, helps to clarify the vast oversimplification of extratropical SST variability in the North Pacific in previous research. Analysis these SST patterns for six 3- and 6-month SST periods also provides much needed insight on the evolution of these Pacific Ocean SST modes relative to the seasonal cycle, which is largely unexplored in previous research on PDO and NPO of sub-annual time scales.

Despite being much less researched, the relatively transient extratropical Pacific Ocean modes are more complex than El Niño and La Niña in terms of seasonal SST morphology, as inferred here through disparities in the spatial patterns of the six 3- and 6-month SST periods for each mode. The PDO as defined in the present study is the

most seasonally transient of the tropical and extratropical Pacific Ocean SST patterns considered, with the northern and southern PDO branches emphasized equally in only the March-May SST mode (Fig. 52). The northern/mid-latitude PDO branch is represented exclusively in the January-March mode, while the southern/subtropical branch dominates the November-April and January-June PDO modes (Fig. 52), each of which are teleconnected uniquely with warm season monthly agroclimate in the study region. These PDO horseshoe asymmetries can be attributed to increased seasonal persistence of the subtropical PDO branch relative to the mid-latitudes, and have not been identified in previous literature despite their relevance to North American climate.

While Namias et al. (1976) more generally associated a warm (cold) PDO with a ridge (trough) of high pressure over western North America and a trough (ridge) to the east, the present study's teleconnection analyses show very different results in the study region depending on the relative emphases of the northern/southern PDO branches in the base characteristic SST patterns. For example, the January-March cold PDO of northern SST branch emphasis is teleconnected most strongly with widespread patterns of spring-early summer dryness/drought across most of the central/southern study region (Chapter 5e, Fig. 31), with much weaker counterpart monthly precipitation and PDI anomaly patterns associated with a March-May cold PDO. Contrastingly, for warm PDO, the strongest spring-summer teleconnections for monthly precipitation and PDI are associated with the March-May SST mode (Chapter 5e, Fig. 30), when the PDO horseshoe is most symmetric between northern and southern branches. GDD spring-summer teleconnections with PDO generally exhibit a similar strengthening/dampening relationship with PDO asymmetry depending on SST phase (Chapter 4, Section e).

Table 10. Pacific Ocean SST mode and growing season (March-October) monthly agroclimate teleconnection summary, including the crop types and critical crop maturation windows impacted.

SST Mode	SST Period	Strongest GDD Teleconnection	Strongest Precipitation Teleconnection	Strongest PDI Teleconnections	Impacted Crops and Growth Period
Mature ENSO 	Jan-Mar	March-April ESG anomaly pattern: Below (above) normal GDD central to south U.S. cold (warm) SST phase	March-April ESP anomaly pattern: Wet (dry) central to southern U.S. for cold (warm) SST phase	March-August central/southern Great Plains to SW U.S. wetness (warm phase)	Spring planting through early growth: Cotton, S. Plains sorghum, wheat, central U.S. soybeans
Decaying ENSO 	Jan-Jun	March-May ESG anomaly pattern but focused only in southern U.S.	March-May ESP anomaly pattern but focused only in southern U.S.	Same as mature ENSO but focused Deep South and in spring only	Spring planting through early growth: Upland Cotton, S. Plains sorghum
PDO (symmetric) 	Mar-May	April-July central/northern U.S. positive GDD anomalies (cold SST phase)	April-July dryness (wetness) central U.S. for cold (warm) SST phase	April-July widespread dryness (wetness) most of U.S. for cold (warm) SST phase	Planting through midsummer flowering: all crops grown in study region (Fig. 1)
PDO (N. branch emphasis) 	Jan-Mar	May-September below normal GDD central/east U.S., above normal western Canadian Prairies warm SST phase	May-June strong dryness south-central U.S. for cold SST phase; wetness east U.S., dryness S. Plains warm phase	April-July central U.S. dryness cold SST phase; NW U.S. wetness and SW U.S. dryness warm phase	Planting through midsummer flowering: Upland cotton, sorghum, wheat, soybeans, corn
PDO (S. branch emphasis) 	Jan-Jun	April-June below normal GDD NW study region for warm SST phase. Weak teleconnections for cold SST phase	May-June wetness southern U.S. for warm SST phase. Weak teleconnections for cold SST phase	PDI teleconnections relatively incoherent	Planting through midsummer flowering: Upland cotton, sorghum, wheat, soybeans, corn
NPO 	Mar-May	April-July positive GDD anom. NW study region advancing south/east by August for cold SST phase	April-July extreme dryness (wetness) southern U.S. for cold (warm) SST phase	PDI teleconnections relatively incoherent compared with other SST modes	Planting through midsummer flowering: All crops grown in study region

Different than the PDO, SST variability associated with the NPO is confined entirely to mid-latitudes, regardless of SST time period, but exhibits a relatively subtle west-to-east shift across the Dateline from winter-to-spring. Despite linkages found

between the NPO oval and northwestern Pacific Ocean SSTAs by Linkin and Nigam (2008), this longitudinal shift in the NPO also has not been documented in previous related literature. The present study reveals that this NPO shift from 160°E to east of the Dateline from winter-to-spring, supported by the January-March and March-May SST modes, is important for the materialization of NPO warm season teleconnections in the study region. This seasonal NPO oval transition is not present in the 6-month SST periods, likely attributed to the overall more transient nature of mid-latitude Pacific Ocean SSTA patterns.

Contrary to the PDO and NPO, the mature and decaying El Niño patterns computed in the present study are substantially more consistent between the six SST time periods, indicating much less seasonal transience for these purely tropical/subtropical Pacific modes. As such, the strongest and most robust spring teleconnections found for monthly GDD, precipitation, and PDI are associated with the mature ENSO modes of both cold and warm phase. Termed the ENSO Spring GDD (“ESG”) and ENSO Spring Precipitation (“ESP”) anomaly patterns, and also present with greater persistence in the counterpart monthly composite patterns of PDI, these patterns are focused over the agriculturally-intensive Great Plains and southern U.S. “cotton belt”. The widespread spring wetness across the southern Great Plains and much of the southern U.S. with the ESP anomaly pattern is a well-documented El Niño teleconnection that is strongest during winter (Rasmusson and Carpenter, 1982; Ropelewski and Halpert, 1982; Montroy et al., 1998; Barlow et al., 2001; DeFlorio et al., 2013), and is shown here to extend through spring with a sharp cessation by summer. The La Niña counterpart ESP anomaly pattern is focused across the same areas

and opposite in sign (strong dryness), but is characterized by less pattern robustness overall especially during the March composite month. The ESG anomaly pattern is even stronger and more widespread for both phases of mature ENSO than the ESP, with strong negative (positive) composite GDD anomalies across much of the central/southern U.S. during spring with most mature El Niño (La Niña) modes.

The mechanisms behind the ENSO pattern teleconnections with North American climate are different than the PDO and NPO, since there is an absence of SST variability at mid-latitudes with this most dominant mode in the central and eastern tropical/subtropical Pacific Ocean. More specifically, the ESG and ESP anomaly patterns (as well as counter PDI teleconnection) are related predominantly to the modulation of Subtropical Jet Stream strength/moisture content by tropical and subtropical diabatic heating minima/maxima. Consequently, when the SSTAs in the mature or decaying El Niño/La Niña region dissipate, the North American warm season teleconnections quickly vanish, and vice-versa. Since the Subtropical Jet Stream typically weakens by summer with the seasonal cycle, these ENSO-related teleconnections also are confined to the spring and fall seasons, and have lesser predictive potential than the extratropical Pacific SST modes.

On the other hand, the NPO and PDO modes (especially March-May warm PDO) are characterized by enhanced predictive potential with the strongest teleconnections of monthly GDD, precipitation, and PDI, since Rossby Waves can be excited in the Polar Front Jet Stream by mid-latitude SSTAs much later in the growing season (Namias et al., 1976; 1988; Oakley and Redmond, 2014). The longest teleconnection lags are found for the March-May warm PDO, when Rossby Waves

excited by SSTAs in the northern PDO branch interact with a stronger-than-normal Subtropical Jet Stream induced by the warm subtropical branch. The strongest growing season (March-October) monthly composite anomaly patterns found for each of the dominant tropical and extratropical modes of Pacific SST variability (i.e. mature and decaying ENSO, PDO, and NPO), along with their associated teleconnections lags and impacted crops/critical farming windows are summarized below in Table 10.

These Pacific Ocean teleconnections of warm-season monthly agroclimate extremes are most impactful on crop yields in the study region when they coincide with certain climate-sensitive farming windows, such as planting, early growth, flowering/reproduction, and harvest. These critical crop maturation windows and the physiological plant responses to climate extremes are highly specific to each crop type, hence motivating the consideration of five very different focus crops in the local crop yield-agroclimate analyses of Chapter 7, above. In general, the most detrimental of the agroclimate extremes is extreme soil moisture dryness during midsummer flower/reproduction for all focus crops, with southern U.S. cotton characterized by particularly high moisture requirements. The more leafy soybean crop yields are most susceptible to cool, damp conditions from flowering through harvest, because of decimating fungus outbreaks, while the cereal grains are particularly susceptible to fungal and bacterial outbreaks like “Black Chaff” when farmers desperately over-irrigate during hot/dry periods.

Table 9 above shows how the local crop yield impacts from certain monthly-to-seasonal extremes in agroclimate can be related to the teleconnections analyses above for GDD, precipitation, and PDI for an assessment of predictive potential, realizing that

climate information is most useful to farmers if provided with sufficient lead time to effectively optimize cultivation strategies. While the analyses of crop yield impacts above are on the local level for five focus crops and six AAPEX farming locations, these results can benefit any farmer throughout the study region. The five AAPEX farmers and their crop locations (Chapter 7, Section b) were selected to represent a wide variety of crop types, growing climates, and cultural farming practices, such that the associated local analyses of crop yield impacts can benefit a vast majority of farmers throughout the study region.

Even though a majority of the monthly-to-seasonal agroclimate information is proven here to be theoretically beneficial to local and regional agricultural production in the study region, crop yield benefits are only realized if this climate information translates into action and farming optimization. A substantial amount of meteorological, biological, geological, and even sociological information as related to growing season (March-October) monthly agroclimate variability is presented in this manuscript, and streamlining these multifaceted results to benefit crop production beyond the local level will be an immense long-term challenge. One option is to convert the above meteorological teleconnections into monthly composite patterns of county crop yield data throughout the entire study region for every main crop hybrid, such that the predictive information is directly understandable by any farmer. A long-term approach would be to optimize the crop hybrids available to farmers prior to spring planting based on high-confidence predictive information of extreme agroclimate, which would circumvent the need to educate every farmer on the fundamentals of agroclimate variability. Given the multi-disciplinary nature of this applied climate research, there

are countless directions for future work that can build on this foundation of agrometeorological information, with topics ranging from Pacific Ocean SST variability to the regulation of growth inhibitors on Upland Cotton to the trading of agricultural futures.

References

- AAPEX. (2015) 'Association of Agricultural Production Executives', [online] Available from: <http://aapex.tamu.edu>.
- Akinremi, O. O., S. M. McGinn, and A. G. Barr, 1996: Evaluation of the Palmer Drought Index on the Canadian Prairies. *J. of Climate*, 9, 897-905.
- ASA. (2015) 'American Soybean Association', [online] Available from: <http://soygrowers.com>.
- Anderson, P. M., E. A. Oelke, and S. R. Simmons, 1985: Growth and Development Guide for Spring Barley. *Univ. Minn. Agric. Ext.*, [online] Available from: <http://www.extension.umn.edu/distribution/cropsystems/DC2547.html>.
- Anderson, J., 2007: A Mesoscale Analysis of the April 13, 2006 Eastern Iowa Severe Weather Outbreak. *J. Atmos. Oceanic Sciences, Univ. Wis. Madison*, 3,1-17. [online] Available from <http://www.aos.wisc.edu/uwaosjournal>.
- Armah-Agyeman, G., J. Loiland, R. Karow, W. A. Payne, C. Trostle, and B. Bean, 2002: Grain Sorghum. *Dryland Cropping Systems*, EM8794, 1-5.
- Arsyid, M. A., F. T. Camacho, and P. Guo, 2009: Corn Basics: Stages of Growth. *Growing Knowledge-Corn Basics by Dekalb-Asia*, [online]. Available from: http://www.dekalb-asia.com/pdf/CB1_StagesofGrowth.pdf.
- Ashley, R. O., Robertson, L. D., Seyedbagheri, M. M., and I. C. Hopkins, 2001: Estimating Water Requirements of Hard Red Spring Wheat for Final Irrigation. *Univ. of Idaho Coop. Ext. Sys.*, Bull. 833.
- Atallah, E. H. and L. F. Bosart, 2003: The Extratropical Transition and Precipitation Distribution of Hurricane Floyd. *Mon. Wea. Rev.*, 131, 1063-1081.
- Barlow, M., S. Nigam, and E. H. Berbery, 2001: ENSO, Pacific Decadal Variability, and U.S. Summertime Precipitation, Drought, and Stream Flow. *J. of Climate*, 14, 2105-2128.
- Bates, G. T., M. P. Hoerling, and A. Kumar, 2001: Central U.S. Springtime Precipitation Extremes: Teleconnections and Relationships with Sea Surface Temperature. *J. Climate*, 14, 3751-3766.
- Bauer, A. C., Fanning, C., Enz, J. W., and C. V. Eberlein, 1984: Use of Growing-Degree Days to Determine Spring Wheat Growth Stages. *North Dakota Coop. Ext. Ser.*, EB-37. Fargo, ND.

- Bauer, A., Frank, A. B., and A. L. Black, 1992: A Crop Calendar for Spring Wheat and for Spring Barley. *Farm Research*, 49.
- Bennett, D., 2008: Recognizing and Minimizing Soybean Stresses. *Delta Farm Press*, Feb. 6, 2008. [online] Available from: <http://deltafarmpress.com>.
- Bonsal, B. R., X. Zhang, L. A. Vincent, and W. D. Hogg, 2001: Characteristics of Daily and Extreme Temperatures over Canada. *J. Climate*, 14, 1959-1976.
- Borthwick, H. A. and M. W. Parker, 1940: Floral initiation in Biloxi Soybeans as Influenced by Age and Position of Leaf Receiving Photoperiodic Treatment. *Bot. Gaz.*, 101, 806-812.
- Bradley, C. A., 2009: Conditions Favorable for Sclerotinia Stem Rot (White Mold). *Illinois Natural History Survey, University of Illinois*, No. 18, Article 8, July 24, 2009.
- Brooks, T. D., M. C. Willcox, W. P. Williams, P. M. Buckley, 2005: Quantitative Trait Loci Conferring Resistance to Fall Armyworm and Southwestern Corn Borer Leaf Feeding Damage. *Crop Sci.*, 45, 2430-2434.
- Buell, C. E., 1975: The Topography of Empirical Orthogonal Functions. *Preprints of Fourth Conf. on Probability and Statistics in Atmospheric Sciences*, Amer. Meteor. Soc., 188-193.
- Buell, C. E., 1979: On the Physical Interpretation of Empirical Orthogonal Functions. *Preprints of Sixth Conf. on Probability and Statistics in Atmospheric Sciences*, Amer. Meteor. Soc., 112-117.
- Bunkers, M. J., J. R. Miller Jr., and A. T. DeGaetano, 1996: An Examination of El Niño-La Niña-Related Precipitation and Temperature Anomalies Across the Northern Plains. *J. Climate*, 9, 147-160.
- Byrd, G. P., 1985: An Adjustment for the Effects of Observation Time on Mean Temperature and Degree-Day Computations. *J. Appl. Meteor. Climatol.*, 24, 869-874.
- Chen, G. and H. Li, 2008: Fine Pattern of Natural Modes in Sea Surface Temperature Variability: 1985-2003. *J. Phys. Oceanogr.*, 38, 314-336.
- Conley, S. P., Scharf, P., Mansfield, C., and E. Christmas, 2005: Wheat Tiller Number and Spring Nitrogen Recommendations. Agronomy Department, Purdue University. [online] Available from: <http://agry.purdue.edu/ext/corn/news/articles.05/wheattopdressN-0128.pdf>].

- Cox, W. J., 2006: Using the Number of Growing Degree Days from the Tassel/Silking Date to Predict Corn Silage Harvest Date. *What's Cropping Up?*, 16, 1-3.
- Davis, R. E., 1976: Predictability of Sea Surface Temperature and Sea Level Pressure Anomalies over the North Pacific Ocean. *J. of Physical Oceanography*, 6, 249-266.
- DeFlorio, M. J., Pierce, D. W., Cayan, D. R., and A. J. Miller, 2013: Western U.S. Extreme Precipitation Events and their Relation to ENSO and PDO in CCSM4. *J. Climate*, 26, 4231-4243.
- Dettenger, M. D., 2013: Atmospheric rivers as drought busters on the U.S. West Coast. *J. of Hydrometeor.*, 14, 1721-1732.
- Economic Research Service/USDA, 2004: The Seed Industry in U.S. Agriculture. *U.S. Department of Agriculture*.
- Environmental Protection Agency, 2000: Major Crops Grown in the United States. [online] Available from: <http://www.epa.gov/agriculture>.
- Folland, C. K., Renwick, J. A., Salinger, M. J., and A. B. Mullan, 2002: Relative Influences of the Interdecadal Pacific Oscillation and ENSO on the South Pacific Convergence Zone. *Geophysical Research Letters*, 29, 21-1-21-4.
- Fehr, W. R. and C. E. Caviness, 1977: Stages of Soybean Development. *Iowa Agric. Exp. Stn. Special Rep.* 80.
- Fokar, M., Blum, A., and H. T. Nguyen, 2006: Heat Tolerance in Spring Wheat II. Grain Filling. *Euphytica*, 104, 9-15.
- Fosse, E. R. and S. A. Changnon, 1993: Potential Impacts of Shifts in Climate on the Crop Insurance Industry. *Bull. Amer. Meteor. Soc.*, 74, 1703-1708.
- Fye, F. K., D. W. Stahle, and E. R. Cook, 2004: Twentieth Century Sea Surface Temperature Patterns in the Pacific during Decadal Moisture Regimes over the United States. *Earth Interact.*, 8, 1-22.
- Frank, A. B. and L. Hofmann, 1989: Relationship among Grazing Management, Growing Degree-Days, and Morphological Development for Native Grasses on the Northern Great Plains. *J. of Range Management*, 42, 199-202.
- Gershunov, A. and T. P. Barnett, 1998: ENSO Influence on Intraseasonal Extreme Rainfall and Temperature Frequencies in the Contiguous United States: Observations and Model Results. *J. Climate*, 11, 1575-1586.

- Gibson, L. R. and R. E. Mullen, 1996: Soybean Seed Quality Reductions by High Day and Night Temperature. *Crop Sci.*, 36, 1615-1619.
- Gilford, D. M., Smith, S. R., Griffin, M. L., and A. Arguez, 2013: Southeastern U.S. Daily Temperature Ranges Associated with El Niño-Southern Oscillation. *J. Appl. Meteor. Climatol.*, 52, 2434-2449.
- Gong, Xiaofeng and Richman, Michael B., 1995: On the Application of Cluster Analysis to Growing Season Precipitation Data in North America East of the Rockies. *J. Climate*, 8, 897-931.
- Gray, A. J., 2005: Hybridization between Crops and Wild Plants in the Age of Genetic Engineering: New Risks or New Paradigms? *Amer. J. Botany*, 92,768-771.
- Griffin, T. S. and C. W. Honeycutt, 2000: Using Growing Degree Days to Predict Nitrogen Availability from Livestock Manures. *Soil Science Society of America Journal*, 64, 1876-1882.
- Guerrero, B. Wright, A. Hudson, D., Johnson, J. and S. Amossan, 2010: The Economic Value of Irrigation in the Texas Panhandle. *Southern Agricultural Economics Association Annual Meeting*, Orlando, FL, Feb 6-9, 2010.
- Gutzler, D. S., Kann, D. M., and C. Thornbrugh, 2002: Modulation of ENSO-based long-lead outlooks of Southwestern U.S. winter precipitation by the Pacific Decadal Oscillation. *Wea. Forecasting*, 17, 1163-1172.
- Heddinghaus, T. R. and P. Sabol, 1991: A review of the Palmer Drought Severity Index and where do we go from here? Proceedings of the Seventh Conference on Applied Climatology, pp. 242-246.
- Heddinghaus, T. R., and D. M. Le Comte, 1992: A Century of Monitoring Weather and Crops: The Weekly Weather and Crop Bulletin. *Bull. Amer. Meteor. Soc.*, 73, 180-186.
- Hayes, M. J., M. D. Svoboda, D. A. Wilhite, and O. V. Vanyarkho, 1998: Monitoring the 1996 Drought Using the Standardized Precipitation Index. *Bull. Amer. Meteor. Soc.*, 80, 429-438.
- Heim Jr., R. R., 2002: A Review of Twentieth-Century Drought Indices Used in the United States. *Bull. Amer. Meteor. Soc.*, 8, 1149-1165.
- Heim Jr., R. R., Lawrimore, J., Wuertz, D., Waple, A., and T. Wallis, 2003: The REDTI and MSI: Two New National Climate Impact Indices. *J. Appl. Meteor.*, 42, 1435-1442.

- Hicks, D. R., 2006: Planting Dates and Minnesota Average Corn Yields, 1968-2005. *Minnesota Crop News*, Univ. Minnesota. [online] Available from: <http://www.extension.umn.edu/cropenews/2006/06MNCN08.htm>.
- Hill, H. S. J., J. W. Mjelde, W. Rosenthal, and P. J. Lamb, 1999: The Potential Impacts of the Use of Southern Oscillation Information on the Texas Aggregate Sorghum Production. *J. Climate*, 12, 519-530.
- Hill, H. S. J., J. Park, J. W. Mjelde, W. Rosenthal, H. A. Love, and S. W. Fuller, 2000: Comparing Value of Southern Oscillation Index-Based Climate Forecast Methods for Canadian and US Wheat Producers. *Agric. for Meteor.*, 100, 261-272.
- Hodges, H. F., K. R. Reddy, J. M. McKinion, and V. R. Reddy, 1993: Temperature Effects on Cotton. *Department of Information Services, Division of Agriculture, Forestry, and Veterinary Medicine, Mississippi State University*, 990, 1-15.
- Horel, J. D. and J. M. Wallace, 1981: Planetary-Scale Atmospheric Phenomena Associated with the Southern Oscillation. *Mon. Wea. Rev.*, 109, 813-829.
- Hoskins, B. J. and D. J. Karoly, 1981: The Steady Linear Response of a Spherical Atmosphere to Thermal and Orographic Forcing. *J. Atmos. Sci.*, 38, 1179-1196.
- Hu, Q. and S. Feng, 2001: Variations of Teleconnection of ENSO and Interannual Variation in Summer Rainfall in the Central United States. *J. Climate*, 14, 2469-2480.
- Hutmacher, B., M. Keeley, and R. Delgado, 2002: Heat Unit Averages and Time to Mature Bolls. *California Cotton Review*, June 2002, 1-4.
- Isard, S. A., and W. E. Easterling, 1989: Predicting Large-Area Corn Yield with a Weighted Palmer Z-index. *J. Climate*, 2, 248-252.
- Kaiser, H. F., 1958: The Varimax criterion for analytic rotation in factor analysis. *Psychometrika*, 23, 187-200.
- Kalnay, E., 1996: The NCEP/NCAR Reanalysis 40-year Project. *Bull. Amer. Meteor. Soc.*, 77, 437-471.
- Karl, T. R., 1983: Some Spatial Characteristics of Drought Duration in the United States, *J. Appl. Meteor. Climatol.*, 22, 1356-1366.
- Karl, T. R., 1986: The Sensitivity of the Palmer Drought Severity Index and Palmer Z-index to their Calibration Coefficients Including Potential Evapotranspiration. *J. Appl. Meteor. Climatol.*, 25, 77-86.

- Karl, T. R., Williams, C. N., Young, P. J., and W. Wendland, 1986: A model to estimate the time of observation bias associated with monthly mean maximum, minimum, and mean temperatures for the United States, *J. Appl. Meteor. Climatol.*, 25, 145-160.
- Kiladis, G. N. and H. van Loon, 1988: The Southern Oscillation. Part VII: Meteorological Anomalies over the Indian and Pacific Sectors Associated with the Extremes of the Oscillation. *Mon. Wea. Rev.*, 116, 120-136
- Kiniry, J. R. and R. L. Musser, 1988: Response of Kernel Weight of Sorghum to Environment Early and Late in Grain Filling. *J. Agron.*, 80, 606-610.
- Krishnamurti, T. N., 1961: The Subtropical Jet Stream of Winter. *J. Climate.*, 18, 172-191.
- Kucharik, C. J. and N. Ramankutty, 2004: Trends and Variability in U.S. Corn Yields over the Twentieth Century. *Earth Interact.*, 9, 1-29.
- Kucharik, C. J. and S. P. Serbin, 2008: Impacts of Recent Climate Change on Wisconsin Corn and Soybean Yield Trends. *Environ. Res. Letters*, 3, Jul.-Sep. 2008.
- Kunkel, K. E., Changnon, S. A., and J. R. Angel, 1994: Climatic Aspects of the 1993 Upper Mississippi River Basin Flood. *Bull. Amer. Meteor. Soc.*, 75, 811-822.
- Kunkel, K. E., Changnon, S. A., Hollinger, S. E., Reinke, B. C., Wendland, W. M., and J. R. Angel, 1995: A Regional Response to Climate Information Needs during the 1993 Flood. *Bull. Amer. Meteor. Soc.*, 76, 2415-2421.
- Kucharik, C. J. and S. P. Serbin, 2008: Impacts of Recent Climate Change on Wisconsin Corn and Soybean Yield Trends. *Environ. Res. Letters*, 3, Jul.-Sep. 2008.
- Lawrence, M. B., Avila, L. A., Beven, J. L., Franklin, J. L., Guiney, J. L., and R. J. Pasch, 2001: Atlantic Hurricane Season of 1999. *Mon. Wea. Rev.*, 129, 3057-3084.
- Linkin, M. E. and S. Nigam, 2008: The North Pacific Oscillation - West Pacific Teleconnection Pattern: Mature-Phase Structure and Winter Impacts. *J. Climate*, 21, 1979-1997.
- Lipps, P. E. and D. R. Mills, 2001: Anthracnose Leaf Blight and Stalk Rot of Corn. *Ohio State University Extension*. [online] Available from: <http://ohioline.osu.edu/ac-fact/0022.html>.

- Livezey, R. E. and W. Chen, 1983: Statistical Field Significance and its Determination by Monte Carlo Techniques. *Mon. Wea. Rev.*, 111, 46-59.
- Livezey, R. E., A. Leetmaa, M. Masutani, H. Rui, M. Ji, and A. Kumar, 1997: Teleconnective response of the Pacific-North American region atmosphere to large central equatorial Pacific SST anomalies. *J. Climate*, 10, 1787-1820.
- Malone, R. W., Meek, D. W., Hatfield, J. L., Mann, M. E., Jaquis, R. J., and L. Ma, 2009: Quasi-biennial Corn Yield Cycles in Iowa. *Agricultural and Forest Meteorology*, 149, 1087-1094.
- Mantua, N. J., S. R. Hare, Y. Zhang, J. M. Wallace, and R. C. Francis, 1997: A Pacific Interdecadal Climate Oscillation with Impacts on Salmon Production. *Bull. Amer. Meteor. Soc.*, 78, 1069-1079.
- Mauget, S. A. and J. Ko, 2008: A Two-Tier Statistical Forecast Method for Agricultural and Resource Management Simulations. *J. Appl. Meteor. Climatol.*, 47, 1573-1589.
- Mavromatis, T., S. S. Jagtap, and J. W. Jones, 2002: El Niño-Southern Oscillation Effects on Peanut Yield and Nitrogen Leaching. *Climate Research*, 22, 129-140.
- McKee, T. B., N. J. Doesken, and J. Kliest, 1993: The Relationship of Drought Frequency and Duration to Time Scales. *Preprints, Eighth Conf. on Applied Climatology, Anaheim, CA, Amer. Meteor. Soc.*, 179-184.
- Meyer, S. J. and A. L. Dutcher, 1998: Soil Temperatures and Spring Planting Dates. *Historical Materials from Univ. of Neb.-Lincon Ext.*, Year 1998. [online] Available from: <http://www.extension.unl.edu/publications>.
- Meza, F. J., J. W. Hansen, and D. Osgood, 2008: Economic Value of Seasonal Climate Forecasts for Agriculture: Review of Ex-Ante Assessments and Recommendations for Future Research. *J. Appl. Meteor. Climatol.*, 47, 1269-1286.
- Mjelde, J. W., D. S. Peel, S. T. Sonka, and P. J. Lamb, 1993: Characteristics of Climate Forecast Quality: Implications for Economic Value to Midwestern Corn Producers. *J. Climate*, 6, 2175-2187.
- Mo, K. C. and R. E. Livezey, 1986: Tropical-Extratropical Geopotential Height Teleconnections during the Northern Hemisphere Winter. *Mon. Wea. Rev.*, 114, 2488-2515.
- Montroy, D. L., Richman, M. B., and P. J. Lamb, 1998: Observed Nonlinearities of Monthly Teleconnections between Tropical Pacific Sea Surface Temperature

- Anomalies and Central and Eastern North American Precipitation. *J. Climate*, 11, 1812-1835.
- Namias, J., Yuan, X, and D. R. Cayan, 1988: Persistence of North Pacific Sea Surface Temperature and Atmospheric Flow Patterns. *J. Climate*, 1, 682-703.
- NCDC, (2014) 'National Climatic Data Center' [online] Available from: <http://www.ncdc.gov>.
- NCCA, (2015) 'National Cotton Council of America' [online] Available from: <http://www.cotton.org>.
- National Soybean Research Library, University of Illinois. Soybean Production: Planting, growing and harvesting soybeans. [online] Available from: <http://www.nsrli.uiuc.edu/aboutsoy/production02.html>.
- Neild, R. E. and D. T. Smith, 1983: G83-673 Maturity Dates and Freeze Risks Based on Growing Degree Days. *Univ. of Neb.-Lincoln Ext.* [online] Available from: <http://digitalcommons.unl.edu/extensionhist/715>.
- Nielsen, R. L., 2010: Heat Unit Concepts Related to Corn Development. *Corny News Network Articles*, Purdue University, Dept. of Agronomy, May 2010.
- Newman, M., Compo, G. P., and M. A. Alexander, 2003: ENSO-forced variability of the Pacific Decadal Oscillation. *J. Climate*, 16, 3853-3857.
- Oakley, N. S. and K. T. Redmond, 2014: A Climatology of 500-hPa Closed Lows in the Northwestern Pacific Ocean, 1948-2011. *J. Appl. Meteor. Climatol.*, 53, 1578-1592.
- Ostlie, K., 2002: Managing Soybean Aphid. *Univ. Minn. Agric. Ext. Service*. [Available at http://www.soybeans.umn.edu/pdfs/SBAMgmtFacts_2.pdf].
- Palmer, W. C., 1965: Meteorological Drought. *Res. Pap.*, 45, U.S. Weather Bureau, Washington, D.C.
- Papineau, J. M., 2001: Wintertime Temperature Anomalies in Alaska Correlated with ENSO and PDO. *Int. J. Climatol.*, 21, 1577-1592.
- Parcell, J. and V. Pierce, 2009: An Introduction to Hedging Agricultural Commodities with Futures. *University of Missouri Dept. of Agricultural Economics Series*, [online] Available from: <http://agebb.missouri.edu/mgt/risk/introfut.htm>.
- Phair, J., 2010: Twynstra presented with Lifetime Achievement Award. *Today's Farmer*, article ID # 2615593. [online] Available from: <http://farmmarketnewspaper.com>.

- Phillips, J., B. Rajagopalan, M. Crane, and C. Rosenzweig, 1998: The Role of ENSO in Determining Climate and Maize Yield Variability in the U.S. Corn Belt. *Int. J. Climatol.*, 19, 877-888.
- Pitts, T., 2008: Thrips in Cotton. *Integrated Pest Management*, Southwest Research and Extension Center. [online] Available from: <http://osu.altus.ok.us/publications>.
- Pohl, S. and G. R. Durland, 2002: Grain Drying Guidelines for a Wet Fall Harvest. *Extension Extra, College of Agriculture & Biological Sciences/South Dakota State Univ.*, 1014.
- Rankin, M., 2009: High Moisture Corn Harvest and Storage Considerations. *University of Wisconsin Ext.-Fond Du Lac., Co.*, Oct. 2009. [online] Available from: <http://columbia.uwex.edu/ag/documents/HMcorn09.pdf>.
- Rathjen, F. W., 1973: The Texas Panhandle Frontier. *University of Texas Press*, Austin, TX.
- Roberson, R. and R. Smith, 2006: First 40 Days Critical for Cotton Plant. *Southwest Farm Press*, Feb. 2, 2006. [Available at http://southwestfarmpress.com/mag/farming_first_days_critical_2].
- Roberts, M. J. and W. Schlenker, 2009: The Evolution of Heat Tolerance of Corn: Implications for Climate Change. *The Economics of Climate Change: Adaptations Past and Present*.
- Rasmusson, E. M. and T. H. Carpenter, 1982: Variations in Tropical Sea Surface Temperature and Surface Wind Fields Associated with the Southern Oscillation/El Niño. *Mon. Wea. Rev.*, 110, 354-384.
- Reddy, K. R. and V. R. Reddy, 1998: Cotton Phenology and Growth Processes: Model Development. *Soil Science*, 526-529.
- Reiter, E. R. and L. F. Whitney, 1969: Interaction between Subtropical and Polar-Front Jet Stream. *Mon. Wea. Rev.*, 97, 432-438.
- Reynolds, R. W., N. A. Rayner, T. M. Smith, D. C. Stokes, and W. Wang, 2002: An Improved In Situ and Satellite SST Analysis. *J. Climate.*, 15, 1609-1625.
- Richman, M. B. and P. J. Lamb, 1985: Climatic Pattern Analysis of Three- and Seven-Day Summer Rainfall in the Central United States: Some Methodological Considerations and a Regionalization. *J. Appl. Meteor.*, 24, 1325-1343.

- Richman, M. B. and P. J. Lamb, 1987: Pattern Analysis of Growing Season Precipitation in Southern Canada. *Atmos.-Ocean*, 25, 137-158.
- Richman, M. B., 1986: Rotation of principal components. *J. Climatol.*, 6, 293-333.
- Richman, M. B. and W. E. Easterling, 1988: Procrustes Target Analysis: A Multivariate Tool for Identification of Climate Fluctuations. *J. Geophys. Res. Lett.*, 93, 10898-11003.
- Ritchie, G. L., Bednarz, C. W., Jost, P. H., and S. M. Brown, 2004: Cotton Growth and Development. [online] Available from: <http://www.spar.msstate.edu/class/EP-2008>.
- Roberson, R. and R. Smith, 2006: First 40 Days Critical for Cotton Plant. *Southwest Farm Press*, Feb. 2, 2006. [online] Available from: http://southwestfarmpress.com/mag/farming_first_days_critical_2.
- Ropelewski, C. F. and M. S. Halpert, 1986: North American Precipitation and Temperature Patterns Associated with the El Nino/Southern Oscillation (ENSO). *Mon. Wea. Rev.*, 114, 2352-2362.
- Ropelewski, C. F., 1988: The Global Climate for June-August 1988: A Swing to the Positive Phase of the Southern Oscillation, Drought in the United States, and Abundant Rain in the Monsoon Areas. *J. Climate*, 1, 1153-1174.
- Sakamoto, C. M., 1978: The Z-Index as a Variable for Crop Yield Estimation. *Agric. Meteor.*, 19, 305-314.
- Salinger, M. J. and A. B. Mullan, 1999: New Zealand Climate: Temperature and Precipitation Variations and their Links with the Atmospheric Circulation. *Int. J. Climatol.*, 19, 1049-1071.
- Salinger, M. J., Renwick, J. A., and A. B. Mullan, 2001: Interdecadal Pacific Oscillation and South Pacific Climate. *Int. J. Climatol.*, 21, 1705-1721.
- Schaal, L. A. and R. F. Dale, 1977: Time of Observation Temperature Bias and "Climate Change". *J. Appl. Meteor.*, 16, 215-222.
- Schoonover, V., 2009: Talkin' Cotton. *Southwest Farm Press*, Jul. 14, 2009. [online] Available from: <http://SouthwestFarmPress.com>.
- Shin, S., Sardeshmukh, P., and R. Webb, 2010: Optimal tropical sea surface temperature forcing of North American drought. *J. Climate*, 23, 3907-3917.

- Slattery, M. C., Gares, P. A., and J. D. Phillips, 2001: Slope-Channel Linkage and Sediment Delivery on North Carolina Coastal Plain Cropland. *Earth Surf. Process Landforms*, 27, 1377-1387.
- Small Grains, 2010. [Available at <http://www.smallgrains.org>].
- Smith, T. M. and R. W. Reynolds, 2003: Extended Reconstruction of Global Sea Surface Temperatures Based on COADS Data (1854-1997). *J. Climate*, 16, 1495-1510.
- Smith, T. M. and R. W. Reynolds, 2004: Improved Extended Reconstruction of SST (1854-1997). *J. Climate*, 17, 2466-2477.
- Smith, S. R., Brolley, J., O'Brien, J. J., and C. A. Tartaglione, 2007: ENSO's Impact on Regional U.S. Hurricane Activity. *J. Climate*, 20, 1404-1414.
- Solow, A., R. M. Adams, K. J. Bryant, D. M. Legler, J. J. O'Brien, B. A. McCarl, W. Nayda, and R. Weiher, 1998: The Value of Improved ENSO Prediction to U.S. Agriculture. *Climate Change*, 39, 47-60.
- Statistics Canada. (2012) [online] Available from: <http://www.statcan.gc.ca>.
- Stewart, J. , T. Kerby, J. Mauney, D. Oosterhuis, J., and J. Timpa, 1993: Cotton Fruit Development – The Square. *Cotton Physiology Today*, 4, 1-4.
- Terando, A., Keller, K., and W. E. Easterling, 2012: Probabilistic projections of agrometeorological indices in North America. *J. of Geophys. Res.*, 117, 16 pp.
- Thomas, J. M. G., Boote, K. J., Allen, Jr., L. H., Gallo-Meagher, M., and J. M. Davis, 2003: Elevated Temperature and Carbon Dioxide Effects on Soybean on Soybean Seed Germination and Transcript Abundance. *Crop Sci.*, 43, 1548-1557.
- Thut, A. S., 1996: The Oakfield Tornado of 18 July 1996. *J. Atmos. and Oceanic Sciences, Univ. Wis. Madison*, 1,1-7.
[Available _____ at http://www.aos.wisc.edu/uwaosjournal/volume1/AOS453/FCS_Thut.pdf].
- Ting, M., and H. Wange, 1997: Summertime U.S. Precipitation Variability and Its Relation to Pacific Sea Surface Temperature. *J. Climate*, 10, 1853-1873.
- Trenberth, K. E., Branstator, G. W., and P. A. Arkin, 1988: Origins of the 1988 North American Drought. *Science*, 242, 1640-1645.
- Trenberth, K. E. and G. W. Branstator, 1992: Issues in Establishing Causes of the 1988 Drought over North America. *J. Climate*, 5, 159-172.

- Trenberth, K. E. and C. J. Guillemot, 1996: Physical Processes Involved in the 1988 Drought and 1993 Floods in North America. *J. Climate*, 9, 1288-1298.
- U.S. Grains Council. [Available at <http://www.grains.org>].
- USDA, 2008: Soil Quality Indicators. *Natural Resources Conservation Service*, June 2008. [Available online: <http://www.soils.usda.gov>]
- USDA, 2009: Economic Research Service. [Available at <http://www.ers.usda.gov>].
- Viator, R. P., R. C. Nuti, K. L. Edmisten, and R. Wells, 2005: Predicting Cotton Boll Maturation Period Using Degree Days and Other Climatic Factors. *Agron Journal*, 97, 494-499.
- Wallace, J. M. and D. S. Gutzler, 1981: Teleconnections in the Geopotential Height Field during the Northern Hemisphere Winter. *Mon. Weather Review*, 109, 784-812.
- Wilks, D. S., 1995: *Statistical Methods in the Atmospheric Sciences*. Academic Press, New York, 467 pp.
- Yeh, S., Wang, X., Wang, C., and B. Dewitte, 2005: On the Relationship between the North Pacific Climate Variability and the Central Pacific El Niño. *J Climate*, 28, 663-677.
- Womach, J., 2004: Cotton Production and Support in the United States. *CRS Report for Congress*, June 24, 2004. [Available at <http://nationalaglawcenter.org/assets/crs/RL32442.pdf>].
- Workneh, F. and C. M. Rush, 2006: Weather Factors Associated with Development of Sorghum Ergot in the Texas Panhandle. *Plant Disease*, 90, 717-722.
- Wrona, A. F., Boman, R. K., Hutmacher, R. B., Jones, M. A., Padgett, G. B., 1998: Weather Extremes Dock 1998 Crop. *Cotton Physiology Today*, 9, 21-32.
- Zangvil, A., Portis, D. H., and P. J. Lamb, 2004: Investigation of the Large-Scale Atmospheric Moisture Field over the Midwestern United States in Relation to Summer Precipitation. Part II: Recycling of Local Evapotranspiration and Association with Soil Moisture and Crop Yields. *J. Climate*, 17, 3283-3301.
- Zeihner, C. A., Brown, P. W., Silvertooth, J. C., Matumba, N., and N. Mitton, 1994: The Effect of Night Temperature on Cotton Reproductive Development. *Cotton: A College of Agriculture Report*, University of Arizona, Series P-96, 26-32.

- Zeiger, C. A., Matumba, N., Brown, P. W., and J. C. Silvertooth, 1995: Response of Upland Cotton to Elevated Night Temperature II. *Beltwide Cotton Conferences*, National Cotton Council, 4-7 Jan. 1995, San Antonio, TX, Vol. 2.
- Zhang, T., Hoerling, M. P., Perlwitz, J., Sun, D., and D. Murray, 2011: Physics of U.S. Surface Temperature Response to ENSO. *J. Climate*, 24, 4874-4887.
- Zhang, L. R. Wang., and J. D. Hesketh, 2001: Effects of Photoperiod on Growth and Development of Soybean Floral Bud in Different Maturity. *Agronomy Journal*, 93, 944-948.
- Zhang, Y, Wallace, J. M., and N. Iwasaka, 1996: Is Climate Variability over the North Pacific a Linear Response to ENSO? *J. Climate*, 9, 1468-1478.
- Zhang, Y, Wallace, J. M., and D. S. Battisti, 1997: ENSO-like Interdecadal Variability: 1900-93. *J. Climate*, 10, 1004-1020.

Appendix

a. AAPEX Crop Significance in U.S. and Canadian Agriculture

The AAPEX crops included in the agroclimate analyses of the present study (soybeans, feed corn, cotton, spring wheat, grain sorghum; Chapter 6c) represent five of the top six leading crop varieties for total acres harvested and total sales in the U.S., with corn and soybean crops totaling 73 million acres as of the new millennium, followed by wheat, cotton, and grain sorghum at 53, 13, and 8 million acres, respectively (Environmental Protection Agency, 2000). In terms of domestic and exported sales, 40% of the total U.S. annual crop sales are from these five crop varieties, thus their sensitivities to climate extremes are also very important from an economic standpoint. The U.S. is by far the largest corn producer in the entire world, producing 10 billion bushels of the world's 12 billion bushels, while 50% of the world's soybeans farms are found in the U.S. U.S. grown wheat, cotton, and sorghum account for 13%, 20%, and 19%, respectively, of the total world product for each crop in 2000 (EPA, 2000; U.S. Grains Council, 2010). The rise to prominence for each of these crops in U.S. agriculture can be attributed to the versatility in their use for end products, ranging from food to soaps to biodiesel oil. Since the U.S. is the leading world producer for most of these crops, high-impact climate extremes within their respective growing regions could have significant impacts on the global food market, as well as for inedible derivative products.

Soybeans are a relatively insignificant cash crop for Canadian agriculture as a whole, but the soybean study location (southwest Ontario, Table 4) is located in the only climate region of Canada with ideal growing conditions for this versatile bean, less

than 50 miles east of southeast Michigan. Soybeans in Canada are primarily grown in southern Ontario, as the only difference between this region and the prime soybean region of the U.S. Midwest is the mere International Border. Growing conditions across the rest of Canada are either too dry or too cold during the spring and summer to cultivate soybeans, but in the last decade new genetically modified soybean hybrids have been successful in southern Manitoba. Ontario contributes around 90% of total annual Canadian soybean production, grown on a little under 2.2 million acres of farmland as of 2006 (Statistics Canada, 2012). By contrast, soybean production exploded in the U.S. beginning in the 1940s and 1950s given a domestic and worldwide increase in demand for soybean oil, with the U.S. quickly becoming the leading producer in the world, as soybean farm acreage increased from 4.8 to 18.6 million acres between 1940 and 1955 (American Soybean Association). The top soy producing states are Iowa, Illinois, Minnesota, Indiana, Nebraska, and Michigan, where the high moisture demand of soybeans can be satisfied in the fertile clay-loam soils with high available water capacities.

The food uses for soybeans are mainly for tofu and soymilk, as well as cooking oil and the recently popular soy-based imitation meats and yogurt. While the recent health food popularity has resulted in increased demand for soybeans in soy-based health foods, the negative media attention for trans-fatty acids has hurt the soybean oil market. Still though, the versatility of soybeans, not only in their edible and inedible derivative products, but also in the wide variety of growing conditions that can support them, will make this controversial legume a leading contributor for worldwide agriculture throughout the foreseeable future.

The food uses for corn are equally as versatile as soybeans in terms of derivative food products, and even more tolerant of extreme temperatures and moisture shortages. The world-leading U.S. corn crop is grown in a region called the “Corn Belt” characterized by fertile loam soils, adequate precipitation, and relatively less extreme summer temperatures as compared to farther west over the heart of the Great Plains. 75% of the U.S. corn production occurs across eastern South Dakota, southern Minnesota, Iowa, eastern Nebraska, Illinois, Indiana, and western Ohio, which accounts for more than 90% of the total value and production of feed grains (USDA, 2009). The food products derived from corn include starch, sweeteners, corn oil, and beverage alcohol, thus corn also contributes substantially to obesity in the U.S. which has been linked closely to the sweetener high fructose corn syrup.

The extensive corn crops over the U.S. Heartland have also been proven to have a significant impact on the local moisture climate, boosting low-level dew point values as much as 5-10°F through evapotranspiration during the summer. In fact, dewpoint increases attributed to corn evapotranspiration have even been linked to tornado occurrence in the Corn Belt (Thut, 1996; Anderson, 2007). While the impacts of corn on tornadoes or obesity are not of particular interest for the present study, the agroclimate-crop yield analysis below could shed light on the influences of corn evapotranspiration on crop yield over the Corn Belt during certain periods of anomalous soil moisture. Zanguil et al. (2004) applied the traditional atmospheric moisture budget to derive a “recycling equation” for the Corn Belt and surrounding areas, used to compare the locally-evapotranspired water vapor between four growing seasons with very different precipitation and crop yield values. This study showed that local

evapotranspiration is weakly related to precipitation on the monthly and seasonal time-scales, but strikingly consistent between the different growing seasons even with vastly different precipitation and corn yield values.

While the present study's agroclimate-crop yield analysis would be relatively ineffective at assessing the impacts of local evapotranspiration on corn yield, systematic changes in the impacts of agroclimate extremes on corn yield could be attributed indirectly to Corn Belt farm expansion. Since the atmospheric moisture content surrounding plants determines the stomata aperture (the tiny pores that plants use to transpire), which affect the sensitivity of the crop to extreme heat, it would seem feasible that the impacts of extreme hot temperatures during summer flowering/reproduction of corn could be influenced locally by long-term changes in Corn Belt evapotranspiration. Climate feedback mechanisms driven by agriculture are unique to every growing climate region and on the local scale, thus motivating further the local focus of the below agroclimate-crop yield analyses.

Similar to soybeans and corn, cotton is also versatile in terms of derivative products, but primarily for the cotton fiber rather than food. Despite all the advances in developing synthetic fibers for apparel, products made from the natural fiber of cotton are still the preeminent choice of apparel for comfort. Interestingly, only 32,000 farms exist across the U.S. in 17 southern states from California to Florida, but the U.S. is still the second leading cotton producer worldwide behind China (Environmental Protection Agency, 2000). Around 20 million bales (500 pounds per bale) of cotton are produced in the U.S. every year, equating to over \$3 billion in annual exports and enough cotton fiber for 4 billion pairs of jeans (National Cotton Council). Cotton requires summers

with warm nights and hot days to reach maturity, thus are confined to the extreme southern U.S., with Texas being the largest state producer of cotton at a little over 6 million bales per year on average (National Cotton Council). Cotton plants also have a relatively complex reproductive cycle for floral initiation through boll development, with each phase being uniquely sensitive to temperature and moisture, as will be shown below in the agroclimate-crop yield analysis.

A staggering 240,000 wheat farms are operational across the U.S., which account for 13% of worldwide wheat production. These wheat farms also include a vast diversity of crop varieties and hybrids, defined by the hardness, color, and shape of the kernels, as well as the time of year they are sown and harvested. The wheat crop varieties cultivated extensively in the study region include Hard Red Winter, Hard Red Spring, Soft Red Winter, Durum, Hard White Wheat, and Soft White Wheat (Small Grains, 2010). Spring wheat classes are planted in spring and harvested by late summer-to-early fall, and are typically more ideal for bread-making given their superior milling and baking characteristics (Environmental Protection Agency, 2000). The winter wheat is sown in the fall, after which the seeds require a period of cold (38-46°F) before germinating in the late winter/early spring, reaching maturity by spring (Anderson et al., 1985). Hard Red Winter wheat is the largest contributor to U.S. imports, mainly because of its relatively large growing area across the entire Great Plains from the Mississippi River to the Rocky Mountains, and Mexico to Canada, but Hard Red Spring Wheat is of particular value for bread-making (Small Grains, 2010). Hard Red Spring Wheat was chosen to represent the wheat focus crop, since yields are especially sensitive to agroclimate extremes and are cultivated in a growing climate

characterized by frequent periods of anomalous temperature and moisture, and thus will provide “worst-case scenario” information for other wheat varieties grown throughout the U.S. Great Plains and Canadian Prairies. The study location representing Hard Red Spring wheat is located (northern Montana, Table 4) in the heart of its primary growing region -- central/eastern Montana, South Dakota, North Dakota, and western Minnesota (U.S. Grains Council).

Grain sorghum is the third largest produced cereal grain in the U.S., and an ideal crop variety for the present study given its unique resilience to drought and necessity of hot temperatures. Thus, sorghum thrives in one of the most extreme spring-summer climates in North America in the central/southern Great Plains, with 90% of domestic sorghum production stemming from Nebraska, Kansas, Oklahoma, Texas, and Missouri (U.S. Grains Council, 2010). Irrigation can substantially increase crop yields, especially when timed optimally during particularly moisture-sensitive sorghum growth phases, but can also be detrimental to yields when excessive, as discussed in detail below. Sorghum is a particularly versatile grain, and can be used to make porridge, break, cookies, cakes, couscous, and malted beverages; is also gluten-free and high in antioxidants, and thus an ideal grain for the many people worldwide with an allergy to gluten.

b. Focus Crop Physiological Adaptations to Prevailing Agroclimate

The five focus crops considered in the present study are each very uniquely adapted to survive agroclimate extremes that characterize their respective growing regions, with highly-specialized physiological plant characteristics that have evolved

since the advent of their cultivation. Specifically, the hearty grains such as sorghum and wheat are characterized by thick, rigid husks and seed coats that trap moisture to thrive in semi-arid, hot summer climates such as the North American high plains, Middle East, and northern India, and tolerate the more frequent heat waves and soil moisture shortages of these growing climates. Conversely, the more “leafy” focus crops such as soybeans, cotton, and corn, have very different plant physiological characteristics than the drought-tolerant grain sorghum and spring wheat crops, specialized for the more humid agroclimates in which they are typically cultivated. For example, the substantially larger leaf areas of these focus crop varieties are covered with tiny pores or stomata regulate accelerated photosynthesis rates and plant moisture surpluses that result from an abundance of precipitation.

i. Soybeans

Soybean plants (*Glycine Max*) are a legume, similar to the pea and clover, and thus are characterized by nitrogen-fixing bacteria called Rhizobium in their root nodules that have a symbiotic relationship with the plant (National Soybean Research Library). These bacteria transform atmospheric nitrogen into ammonium-based nitrogen, which is the usable form for plants, and in return the plant provides sugars and minerals to support the bacteria population. Ammonium-based nitrogen is a macronutrient (required in large quantities throughout the growing season) required for the normal growth of nearly all crops, and makes up a large part of most fertilizers. Thus, the extensive fertilization process required for the healthy growth of most crops to boost

ammonium-based nitrogen and other macronutrients, the effectiveness of which is highly dependent on temperature and soil moisture, is not necessary for soybean crops.

Soybeans are a relatively slow-growing crop, with northern varieties such as those grown at the study location in the Great Lakes and upper Midwest requiring four to five months for sowing to harvest. Given typical planting dates in early May and harvest in early October in the southern Great Lakes Region (Table 5) assuming typical growing conditions, cool summers with below normal GDD totals or insufficient precipitation can extend harvest dates into the late fall. Late harvests are more prone to fungal infestations during the vital “bean drying” phase, because of the frequent cold, damp conditions of late fall in the Great Lakes Region. These slower growing rates also prolong specific climate-sensitive growth phases that are unique to the soybean life cycle (Table 9).

The life cycle of the soybean is split into the vegetative and reproductive phases, with the latter representing all growth periods from flower bud appearance until maturity. Sowing of soybeans should not be executed until soil temperatures reach at least 55-60°F, which typically occurs in late April into early May in the Great Lakes Region (Table 6). Sufficiently warm soil temperatures and adequate soil moisture are required for the quick germination and emergence of soybean plants, or the increased time in the soil exposes the vulnerable seedling to pests and fungus. The vigor of the young seedlings determine the health of the rest of the crop through maturity, thus soybean farms should delay sowing dates given anomalously cold conditions through early May.

Table 11. Critical soybean growth phases and number of days since sowing marking the beginning of each phase, representative of the soybeans grown in Ailsa Craig, Ontario (Fehr and Caviness, 1977; National Soybean Research Library).

Soybean Life Cycle		
AAPEX Farm: Steve Twynstra, Ailsa Craig, ON		
Stage	Days since Sowing	Description
Emergence	5-10	Shoots appear above ground
First trifoliolate	15-20	First photosynthesizing leaves
5-Branch trifoliolate	45-60	Plants 10-12 inches tall
Flowering	90-100	Plants 1-22 inches tall; vertical root systems develop; flower located at every node and branch from base to top of plant.
Pod formation	100-110	Plants 23-32 inches tall; 65-75% of all flowers abort; Seeds begin to form when pods are 1 inch long.
Seed filling	120-130	Significant moisture and nutrient uptake; plant less resilient to stress and vegetative damage; plants reach maximum height.
Maturity	150-160	Rapid leaf yellowing; pod weight peaks; Need warm and dry weather for 5-10 days of drying after full maturity

The first few months after emergence is called the vegetative stage, the timing of which is measured through the number of branches with trifoliolates, or the compound leaves of soybean plants composed of three leaflets and attached to the main stem (Fehr and Caviness, 1977). The first trifoliolate appears a few weeks after sowing, with the beginning of the flowering phases typically coincident with the plants having six to ten branches of trifoliolates (Table 7). The soybean crops are relatively resilient to climate-extremes, pests, and fungus during the vegetative stage, until the reproductive stage

begins as flower buds appear on the main plant nodes 90-100 days after sowing. The subsequent two months from flowering to maturity, and especially the “bean fill” stage which directly dictates the bean mass and harvest, is especially sensitive to temperature and moisture stress with the biggest impacts on crop production.

Extreme heat is particularly stressful for soybean crops during flowering and early pod formation, where any disruption of pollination will have significant impacts on crop yield as is the case for each of the five focus crops. Gibson and Mullen (1996) and Thomas et al (2003), who performed heat-sensitivity experiments on soybeans in climate-controlled growth chambers, showed a reduction in yield of 27% when soybean crops were subjected to temperatures of greater than 35°C for at least 10 hours during the day, and delayed seed formation with prolonged temperatures of 30-40°C, respectively. Borthwick and Parker (1940) indicated a reduction in flower initiation with persistent high temperatures greater than 32°C, but for southern varieties of soybeans. Thus, one of the agroclimate variables included in the crop production impact analyses for Steve Twynstra’s soybean farm location, representing extreme summer heat during flowering through early pod formation, were the number of July-August days with maximum temperatures above 32°C (90°F).

Soil moisture shortages during the “seed fill” stage (beginning 1-2 weeks after the appearance of the first flowers – Table 7) through pod maturity have potentially devastating impacts on yield, given the increased moisture demand for heightened photosynthesis as the plants pump sugars and proteins into the seeds for 30-40 days until maturity is achieved (National Soybean Research Library). Kucharik and Serbin (2008) correlated county-level monthly precipitation with soybean yield in northern

Wisconsin, and found statistically significant correlations between yield and September-October rainfall, attributing this relationship to water stress shortening the period of seed filling. Bennett (2008) showed that moisture stress during the first week of pod development decreases yield by 19%, by 36% during the first week of seed fill, and 39-45% during the second through fourth week of seed fill. Irrigation of soybean crops in the Great Lakes Region is extremely rare, even the very large commercial farms. Thus, the only way to limit high-impact moisture shortages during the critical pod and bean development phases is to adjust planting dates based on predictive information for seasonal climate, such as developed in the present study via the above regional teleconnection analyses. As such, the below agroclimate impact analyses for the study locations (Table 4) quantify the impacts of anomalous moisture on yield (via monthly Palmer Z Index and precipitation) during these moisture-sensitive bean fill stages, as well as for every month during the growing season.

The final, and often the most impactful growth phase on soybean yields of the Great Lakes Region, is typically around five months after sowing (Table 7) because early onsets of cool fall temperatures more commonly coincide with the period of bean-drying for edible bean crops. After a month or more of mass accumulation during the previous bean fill stage, which directly dictates crop yields at harvest, much of the moisture in the pods and beans must be allowed to evaporate to facilitate harvesting. If a period of extended dampness occurs when the soybeans reach their maximum mass, thus delaying harvest, yields can be negatively impacted by the increased exposure to pests and fungus as well as the breakdown of non-water mass prior to drying. Thus,

warm and dry conditions are preferred for soybeans in the Great Lakes Region during early October, which is the typical time for harvest there (Table 7).

Soybeans are affected particularly by a fungus called “Downy Mildew”, and not only can be a negative impact during the soybean-drying phase, but also during any growth phase from trifoliolate-appearance through harvest. Downy Mildew (*Peronospora manshurica*) is a biotrophic fungus, which means it can only grow on soybean plants, and can result in significant negative impacts on crop yield especially during wet and damp conditions and given spreading to the bean pods (UW Soybean Plant Health, 2008). The fungus appears first on the upper surfaces of young leaves as small pale green to light yellow spots, turning gray and slightly fuzzy during high humidity, with contaminated beans turning dull white from the coating of fungal spores (UW Soybean Plant Health, 2008). Fungicide is mildly effective at managing Downy Mildew, as well as the planting of specific fungus-resistant hybrids, and both practices could be optimized given prior knowledge of wet, damp conditions and their specific impacts on yield throughout the growing season.

In addition to fungal outbreaks, soybeans also face a variety of pests, some of which can have significant impacts on yield with their likelihood and extent dependent on specific climate conditions. Aphids are the most significant insect pests for soybean crops, decreasing yields by up to 50% for untreated crops, and the timing of their colonization of soybean plants are largely dependent on local climate (Ostlie, 2002). Aphids have the greatest impact on yield when the maximum colony populations are coincident with the critical flowering through seed filling phases, since they feed from the “veins” of the plant that contain the sugars and starches from photosynthesis that

fuel healthy growth of reproductive parts, as well as directly determine the mass of the eventual beans. Aphids typically colonize soybeans in the Great Lakes Region around early June after overwintering in Buckthorn plants, with populations reaching several thousand per plant by early August with up to 15 generations per plant (Ostlie, 2002). Two climate factors impact the timing of aphid colonization, including heavy rains during late spring into summer, which directly curtail the migration of the populations from Buckthorn to soybeans, and warm, dry springs, which lead to an earlier colonization of soybeans than early June and more rapid reproduction. Soybean farmers can adjust the timing and extent of insecticide application based on concurrent and forecast measures of temperature and precipitation to ensure that colonization is not coincident with flowering and seed development beginning in early August, and adjust the volume of insecticide purchased prior to the growing season.

ii. Feed Corn

Feed corn has a much faster life cycle than soybeans, with around 100 days from sowing to maturity as compared to 150 days for soybeans. Similar to soybeans, the life cycle of corn is split into the vegetative and particularly moisture-demanding reproductive phases, encompassing several shorter growth phases each with unique sensitivities to moisture and temperature (Table 8). In general, high temperatures equate to faster, more robust corn crop growth assuming adequate soil moisture conditions, with high photosynthesis rates satisfying the heightened nutrient demand of the reproductive phases. Corn requires around 110-120 GDD to emerge, 1300 from emergence to flowering, and 2800 total GDD for the kernels to reach maturity (Cox,

2006). However, Roberts and Schlenker (2009) showed a sharp decrease in corn yield with mean temperatures above 29°C, and Kucharik and Serbin (2008) revealed negative correlations (-0.51) between June-August temperature and county corn yield in central Wisconsin, thus fast growth rates do not necessarily correspond to higher yields. These negative relationships between corn yield and temperature are likely attributed to extreme hot temperatures aborting reproductive processes despite the faster observed growth rates, as summarized below.

Corn crops are typically planted in late April through early May in southern Minnesota. However, earlier planting dates are associated with higher yields in the Corn Belt, likely since the kernel development phases will coincide with warmer temperatures, as the more climate-resistant corn hybrids of modern times are less vulnerable to extreme heat (Hicks, 2006). The relatively dry soils of earlier in the spring also promote vertical root structures and vigor in early season growth, which determines resiliency to moisture shortages throughout the life cycle, and moist soils promote fungal growth that can abort seedlings. Very late season freezes are not much of a concern for corn sowing in late April because of the lag in time between planting and emergence, and the growing region of the seedling remains under the surface of the soil for an extended period of time (Nielsen, 2010). Thus, more flexibility exists to adjust planting dates of corn based on predictive climate information to avoid detrimental agroclimate extremes to take better advantage of optimal growing conditions, but planting later than mid-May typically has a negative impact on corn yield (Kucharik and Serbin, 2008).

Corn from emergence through the whorl stage is relatively resilient to heat stress, with higher temperatures promoting rapid leaf expansion and increased photosynthesis during the vegetative and later reproductive stages. The whorl stage is named after the bunches of rapidly emerging leaves in a “whorl” pattern at the nodes of the branches and main stalk, and exhibits some of the fastest growth rates of the entire life cycle, thus soil moisture demand is particularly high. The whorl phase is especially vulnerable to pests given the abundance of early leaf growth, especially from the Southwestern Corn Borer (*Diatraea grandiosella*) with the correspondence in timing of its early larvae stage (Brooks et al., 2005). The larvae of this especially destructive pest of corn feed on the newly emerged leaves of the whorls, causing substantial vascular and leaf damage leading to reduced yield potential. The first generation larvae typically hatch in early June in southern Minnesota, but earlier (later) arrival is possible with anomalously warm (cold) conditions, so insecticide application should be adjusted accordingly -- another possible use of predictive climate information.

The reproductive phase begins about two months after sowing for corn at the study location (southern Minnesota, Table 4) as the tassel emerges from the last whorl at the top of the stalk. The tassel is the male reproductive part of the corn plant that produces the very heat-sensitive pollen that can make or break crop yields at the end of the growing season. The silk and ear are the female portions of the plant, which can receive pollen from the tassel for up to ten days for pollination and kernel development, with the whole pollination phase lasting a few weeks given lagged emergence of the silk from the bottom to the top of the ear (Arsyid et al., 2009). Frequent days with

maximum temperatures over 95°F during flowering can decimate corn yields, causing pollination to sterilize and florets to abort.

Table 12. Critical corn growth phases and number of days since sowing marking the beginning of each phase, representative of the corn grown in Blue Earth County, MN (Arsyid, M. A. et al., 2009; Iowa State University Agronomy Extension).

Corn Life Cycle		
AAPEX Farm: Patrick Duncanson, Blue Earth County, MN		
Stage	Days since Sowing	Description
Emergence	6-7	Water uptake is substantial; seed absorbing 30% of its mass; 21-32°C is ideal.
Knee-high stage	25-40	Number of leaves increases from 5 to 10; stem girth increases substantially.
Whorl stage	40-50	Whorls of quickly growing leaves at the top of the plant; tassel has developed but is concealed in the last whorl; crop growth and moisture demand is high.
Flowering	50-60	Tassel appearance and pollen shredding occur; the silk and husks begin to develop. Pollination highly sensitive to extreme temperature.
Blister kernel	65-75	Kernel visible and looks like a blister on the cob; filled with clear fluid; 85% moisture content; climate stress can cause abortion of kernels.
Milk kernel	70-80	Kernels yellow on the outside and milky white inside; starch (“dry mass”) rapidly accumulating replacing water mass; stress can cause abortion of kernels
Dough kernel	75-85	Kernels dented at the top; climate stress can only limit yield by slowly accumulation of dry mass.
Dent kernel	85-95	Dent appears at the top of kernel and have begun drying down; reached maximum dry mass; 30-35% moisture in the kernel. Stress will not limit yield.

Thus, extreme heat is a significant contributing factor for the negative correlations between summer temperature and corn yield found by Kucharik and Semin

(2008) and Roberts and Schlenker (2009). The only techniques truly effective at avoiding the impacts of extreme summer heat during late June/July flowering is to adjust planting dates or hybrid selection accordingly, which is feasible with the relatively short two-week flowering period assuming accurate predictive climate information.

The subsequent reproductive stages are not quite as vulnerable to extreme heat as pollination, but corn yields are extremely sensitive to moisture deficiencies starting with early kernel development. Inadequate soil moisture during the blister and milk stages of kernel development are the most impactful on corn yield (first 2-3 weeks after silking – Table 8), since kernels are aborted from the top of the ear to the bottom to alleviate the moisture stress on the rest of the plant (Arsyid et al., 2009; Iowa State University Agronomy Extension). Moisture stress during the dough and dent stages will not result in kernel abortion, but will lead to smaller kernel mass at harvest since the attendant slower photosynthesis rates decrease the rate of starches and protein accumulation in the kernel. This rate of starch and protein accumulation, called “dry mass”, ultimately determines the mass of the mature kernel, since a moisture content of 30-35% defines the kernel at maturity (Iowa State University Agronomy Extension). Therefore, not only is moisture availability important, but GDD must still be sufficiently high to encourage a fast plant metabolism and maximum sugar production.

After the kernels reach maturity, a substantial period of drying is needed before harvest, which typically is required well into September or even October from north to south across the Corn Belt, since moisture levels of around 15-18% are desired for feed corn (Pohl and Durland, 2002). Given wet fall conditions or corn that is maturing late,

harvesting of corn with moisture levels of greater than 30% can result in undesired fermentation of the kernels in the silos and broken corn, so warm and dry falls are strongly beneficial for the post grain filling stage (Pohl and Durland, 2002; Rankin, M., 2009). Moisture-laden corn for an extended period of time is also susceptible to Anthracnose (*Colletotrichum graminicola*), which is a fungus that thrives in rainy, damp conditions (Lipps and Mills, 2001). Anthracnose not only affects corn at maturity, but can impact crop yield during any stage of development, thus fungicide application should be managed according to concurrent or forecast periods of wetness.

The county-level agroclimate impact analyses of the present study show the significance of each climate-sensitive growth phase above, such that further optimization of farming strategies can be facilitated. The impacts on yield from anomalous GDD, precipitation, Palmer Z Index, and number summer days above 95°F are quantified below for each month of the growing season (March-October) to identify additional climate-sensitive phases. In addition, alternatives for planting date are also to be recommended given a multitude of extreme agroclimate scenarios, and predictability is investigated using concurrent and lagged monthly local teleconnection analyses, for each focus crop variety and study location.

iii. Upland Cotton

Cotton is a very unique crop in terms of ancestry and farm management, since many of its wild characteristics have been retained throughout its history of cultivation, including the continued vegetative growth through well after seed production. The genetic code of cotton is very complex and difficult to modify, originating from

perennial vines several centuries ago that were native to Africa, Arabia, Australia, and Middle America (Ritchie et al., 2004). Upland cotton (*Gossypium hirsutum*) is one of four main cotton varieties developed from these ancient vines, and is the primary species thriving across much of the Southern U.S. from the Pacific to the Atlantic Ocean (Reddy and Reddy, 1998). Given the relative ineffectiveness of hybridization of cotton, tailoring of crop growth rates for different temperature climates and cultural practices has been limited, thus farmers of cotton must uniquely use growth regulators to control undesirably rapid growth in high temperatures and vegetative growth even after pollination. Most crops reach a maximum plant size during flowering/reproduction, after which vegetative growth ceases for ease of harvesting, but cotton has retained its perennial growth characteristics since its ancient origin. Cotton growth is highly dependent on temperature with high soil moisture intake, requiring the high GDD totals associated with warm nights and hot days of the humid southern U.S. Specifically, accumulation of 800 GDD is required from planting to flowering, with around 2200 for boll maturation and harvesting for the varieties grown in the study regions (North Carolina coastal plain and extreme southern Texas, Table 4).

Cotton crops can be planted as early as March 1 in extreme southern Texas and April 1 in southern North Carolina, as 50-60 GDD are required for emergence. El Nino is particularly impactful for cotton yields in southern Texas, as supported in the analyses below, since earlier planting dates are more feasible with the warm and moist late winter soils of El Nino winters. Earlier planting dates are typically associated with higher yield in both cotton locations, especially in the southern coastal plains of Texas, since the attendant timing of flowering and boll filling would better coincide with the

ample rainfall of spring, with higher temperatures experienced during later boll maturation phases where growth rates determine boll size, mass, and quality of fiber (Table 9).

Early sowing also can also minimize thrip infestations during the particularly vulnerable seeding through early growth period, particularly in cotton growing regions of the Great Plains with nearby wheat crops. The Western Flower Thrip colonizes winter wheat plants during the early spring, before migrating to cotton plants when wheat matures and cotton experiences early growth, the relative timing of which determines the severity of the crop yield impacts (Pitts, 2008). The thrip colonies feed from the plants and stems, causing slower growth and disfigured foliage on early growth with significant impacts on yield through the 4-5 leaf stage two to three weeks after sowing. Conversely, if migration of the thrips from winter wheat occurs later in the cotton life cycle they feed on mite eggs instead of the cotton plants, which can be beneficial for cotton yield (Pitts, 2008). Thus, because Western Flower thrips are particularly tolerant of insecticides, the timing of early growth for cotton crops relative to wheat maturation is a key method of thrip management, which is highly dependent on climate conditions during late winter into early spring.

Planting prior to the typical planting dates of a particular location (i.e., April 1 for North Carolina coastal plain and March 1 for extreme southern Texas) must be approached with caution given the importance of germination to seedling establishment in the formation of healthy root systems, which support reproductive vigor and robust boll growth closer to maturity when mid-summer soil moisture shortages are quite frequent across the entire southern U.S. Planting in cool, moist soils typically results in

underdeveloped root systems for cotton crops that struggle to reach the desired root depth of 24 to 30 inches by square development (Table 9), and exhibit weak axial stems that are especially vulnerable to stalk rot diseases later in crop life in the “crusty” clay soils of the Southern U.S. (Roberson and Smith, 2006). Decreased seedling vigor in crusty soils also results in a condition called “big shank” or “thick-legged” cotton with impaired growth rates from the shading of adjacent taller plants (Ritchie et al., 2004).

Table 13. Critical Upland Cotton growth phases and number of days since sowing marking the beginning of each phase, representative of the cotton grown in Robeson Co., NC and Nueces Co., TX (Ritchie et al., 2004; Reddy and Reddy, 1998).

Cotton Life Cycle		
AAPEX Farm: Allan Baucom, Robeson County, NC and Nueces County, TX		
Stage	Days since Sowing	Description
Emergence	5-10	Cotyledons emerge from the soil and support the subsequent growth immediately after emergence. First leaf appears 1 week after emergence.
5-leaf plants		Leaves grow on every node of the main stem. Once 5 leaves or nodes have developed, the vulnerability of the crop to extreme climate dramatically decreases.
Square development	35-45	Squares or flower buds are produced every 6 days from fruiting branches.
Flower formation	55-65	White flower day 1, pink on day 2, and red on day 3. Pollination happens a few hours after anthesis. Flowers fall off when boll develops.
Boll development	95-105	Occurs in three phases: enlargement, filling, and maturation. Fibers produced in first two for first 6 weeks after flowering.
Harvest	150-170	Defoliant applied to stop plant growth and prepare crop for harvesting. The effectiveness of defoliant is proportional to temperature.

Generally, a longer duration between planting and emergence for cotton crops equates to a greater chance of plant impairment and yield losses, which is strongly dependent on early spring climate. As such, Ritchie et al. (2004) recommends a soil temperature of 65°F for at least three consecutive days before even considering the planting of cotton. The growth of weeds during early cotton growth is also highly dependent on late winter-early spring climate, a period when seedlings and young plants are particularly sensitive to competition for moisture and nutrients from adjacent weed growth. Roberson and Smith (2006) noted that yields exposed to weed competition at the 5-leaf stage (Table 9) can experience yield reductions as large as 23%.

Cotton plants grow relatively slowly during early growth, and as a consequence are vulnerable to crop stress for a longer duration. Sensitivity of crop yield to early spring climate is of particular interest here, since concurrent agroclimate information is typically sufficient for adjustment of planting dates, unless labor and equipment management changes require substantial lead-time. Motivated by these strong associations between crop yield and local agroclimate, the present study quantifies the impact of a myriad of agroclimate variables for individual months beginning in late winter (March), to explore their relative importance for the cultivation of crops such as cotton.

Cotton plants experience rapid crop growth after their sluggish beginning that is highly dependent on temperature, especially between the 5-leaf stage and square development. Cotton growth is measured by the number and distribution of nodes on the main stem, from which either vegetative (monopodia) or fruiting branches (sympodia) emerge (Ritchie et al., 2004). Normal cotton maturation typically results in

a new node everyday on the main stem and branches, with greater separation in hotter temperatures. The ratio of vegetative to fruiting branches is also determined by agroclimate during this period of rapid cotton growth, with more of the vegetative branches produced during periods of moisture or temperature stress. Each fruiting branch can produce a maximum of four squares, or flower buds, so the increased ratio of vegetative branches can decimate cotton yields (Ritchie et al., 2004). Consequently, cotton farmers use growth regulators and other management practices to limit the height of their crops, as well as increase the ratio of fruiting to vegetative branches, all of which could be optimized with detailed and relevant agroclimate information.

Squares typically first appear on cotton crops in the southern U.S. around 40 days after sowing, with the highly temperature-sensitive flowering period occurring three weeks later (Table 9). The white, pink, and red flowers each pollinate for a few days, but during a relatively long flowering period of 6 weeks for the entire plant (Reddy and Reddy, 1998). Crop yields are especially impacted by extended extreme heat during this six-week period, since squares and flowers can fall off the fruiting branches with pollen sterilization for those that survive in extreme hot temperatures. Reddy (1992) and Hodges et al. (1993) showed that persistent exposure to temperatures above 97°F, beginning as early as 15 days prior to anthesis (blooming), typically results in little or no pollination and the abortion of 3-5 day old bolls up to two weeks following the stress. Even provided effective pollination, Zeiher (1994) and Zeiher et al. (1995) showed that fruit retention, seed number, and boll size are drastically reduced when nearly developing bolls are consistently exposed to mean temperatures of greater than 90°F, especially during the enlargement and filling stages of the first three weeks

of boll development (Table 9). Similar results are associated with moisture deficiencies during these critical reproductive phases of cotton (Reddy and Reddy, 1998; Richie et al., 2004).

Large-scale irrigation of cotton crops east of West Texas is not common, but still largely ineffective at reducing the temperature-related stress of cotton crops despite satisfying the increased moisture requirements. Surprisingly, irrigation can actually increase the damage of extreme heat during cotton reproduction, since the higher vapor pressures surrounding the plants and increased photosynthesis rates cause wider stomata aperture, as introduced above. Other than selecting more heat-resilient cultivars, the only effective farming practice that can reduce the impacts of mid-summer extreme heat is choosing an optimum planting date based on accurate predictive climate information - a seemingly consistent theme across all focus crops and study locations (Table 4).

iv. Cereal Grains (Spring Wheat and Grain Sorghum)

The life cycle phases and physiology of reproductive features are very similar between spring wheat and grain sorghum, but with slight differences in timing and tolerance to extreme agroclimate (Table 10, 11). Wheat and sorghum crops are relatively resilient to moisture shortages and tolerant of extreme heat, except during their respective reproductive stages, both of which are characterized by a relatively short (less than 1 week) flowering period, followed by several weeks of grain fill with rapid sugar and protein accumulation highly dependent on temperature and soil moisture conditions. Despite wheat being accustomed to much cooler growing environments than Sorghum, hence the latitudinal difference in their native growing

areas (northern High Plains and Southern Plains, respectively), both varieties of cereal grains reach their critical growth phases in a very similar number of days since planting (Table 10, 11). This similarity in life cycle timing shows the disparity in the accumulated heat requirements of spring wheat compared to sorghum; wheat (sorghum) requiring around 1800 (2600) between planting and kernel maturity (Neild and Smith, 1983).

The typical planting date range for Hard Red Spring wheat at the northern Montana study location is May 1 to May 15, and April 15 to June 1 for sorghum crops at its Texas Panhandle study location, but with vastly different soil temperatures for proper emergence (Table 10, 11). Since Hard Red Spring wheat growth rates are adapted for much cooler spring temperatures, planting dates after May 15 in northern Montana and the rest of the Northern Plains result in substantially decreased yield, mainly attributed to undesirably fast life cycles and insufficient accumulation of nutrients for grain fill (Meyer and Dutcher, 1998). On the other hand, the ideal date range for grain sorghum planting is twice as large and can be planted as late mid-June, despite the hot late spring and summer of the Southern Plains. The difference in spring agroclimate between these wheat and sorghum growing climates at the time of planting leads to contrasting concerns regarding soil conditions at planting. Specifically for spring wheat, cool and rainy conditions during spring often result in overly moist soils for planting in early May, which cause poor seedling establishment and increased likelihood for disease, while delayed planting also results in yield losses.

Table 14. Critical spring wheat growth phases and number of days since sowing marking the beginning of each phase, representative of the spring wheat grown in Liberty Co., MT (Bauer et al., 1992; Anderson et al., 1985; Meyer and Dutcher, 1998).

Spring Wheat Life Cycle		
AAPEX Farm: Carl Mattson, Liberty County, MT		
Stage	Days since Sowing	Description
Emergence	3-5	Ideal soil temperatures are 45-55°F, minimum is 40°C; winter-spring rainfall is vital for recharging soil moisture.
Seedling establishment and leaf production	5-10	Critical phase for establishment of root system. 8-9 leaves are produced on main stem.
Tillering	15-20	Tillers are leaves that grow on the main stem at each node, and allow crops to take full advantage of good growing conditions; vital for supplying nutrients.
Rapid stem elongation and head emergence	30-40	Most rapid crop growth occurs here just as the heads are preparing for pollination; florets develop and mature.
Flowering	50-60	Characterized by an extension of the awns from the floret; each head can be pollinated for 4 days.
Grain filling	60-70	4 weeks from pollination to maturity; includes watery, milk, and dough stage similar to corn.
Maturity	90-100	Requires around four weeks of drying; at 30-40% “dry weight” the grain can be harvested without yield loss.

The development of tillers around two to three weeks after planting is a critical stage for both spring wheat and sorghum crops, the extent of which is highly dependent on local agroclimate (Anderson et al., 1985; Prasad et al., 2004; Conley et al., 2005). Tillers are elongated, peripheral leaves that develop along the growth nodes on the main stem that function entirely to supply the plant with nutrients during the subsequent stem elongation and reproductive stages, as well as take full advantage of ideal growing conditions with the presence of more photosynthesizing leaves. Temperature or

moisture stress during the tillering stage typically causes insufficient tiller coverage throughout wheat and sorghum growth, and in turn, inadequate stored nutrient supply for the important grain fill stage. Selection of planting density is a farming practice that can be used to adjust tiller coverage given prior knowledge of extreme temperature or moisture shortages during early crop growth, since lower plant populations are typically associated with more extensive tillering (Bauer et al., 1992; Conley et al., 2005). Thus, not only can lower plant populations offset the decreased tillering from climate-related stress, but can also ensure that maximum tiller coverage during expected periods of ideal growing conditions.

The reproductive phases of both spring wheat and grain sorghum are characterized by the emergence of the head or panicle at the end of the rapid stem elongation phase, followed by the appearance of florets or tiny self-pollinating flower structures around two months after planting, and concluded with the critical grain fill stage when the developing kernels accumulate starch and protein until maturity (lasting around 4 weeks for spring wheat and 6-8 weeks for grain sorghum; Anderson et al., 1985; Bauer et al., 1992; Prasad et al., 2004). Interestingly, the flowering and grain fill stages are similarly sensitive to extreme heat for both spring wheat and sorghum, with an impedance or abortion of respective reproductive processes in persistent maximum temperatures greater than 90-95°F (32-35°C; Bauer et al., 1984; Kiniry and Musser, 1988; Prasad et al., 2004; Fokar et al., 2006).

Table 15. Critical grain sorghum growth phases and number of days since sowing marking the beginning of each phase, representative of the grain sorghum grown in Dallam Co., TX (Prasad et al., 2004; Meyer and Dutcher, 1998).

Grain Sorghum Life Cycle		
AAPEX Farm: Mark Lowe, Dallam County, TX		
Stage	Days since Sowing	Description
Emergence	3-5	Ideal soil temperatures are 70-80°F, minimum is 65°F; winter-spring rainfall is vital for recharging soil moisture.
Seedling establishment and leaf production	5-10	Critical phase for establishment of root system. # leaves grow on main stem.
Tillering	10-15	Tillers are leaves that grow on the main stem at each node, and allow crops to take full advantage of good growing conditions; vital for supplying nutrients.
Rapid stem elongation and head emergence	15-20	Rapid crop growth occurs until a “boot” covering the panicle at the apex of the plant is revealed; bulge forms in this boot 6-10 days before harvest.
Flowering	50-60	Duration of six days; flowering structure also called panicle or head, or “inflorescence”; pre-flowering period 10 days before is also heat-sensitive.
Grain filling	60-70	6-8 weeks to; first 2 weeks is a period of rapid starch and protein accumulation; includes watery, milk, and dough stage similar to corn.
Maturity	100-120	Grain moisture must drop below 25% of total mass before harvesting to maximize “dry weight” and yield.

Specifically, Kiniry and Musser (1988) identified the physiological and yield impacts of extreme temperature on grain sorghum grown in growth chambers, and found that temperatures above 91°F (33°C) during early stages of panicle development induce floret and embryo abortion -- around late May for late April planting in the Texas Panhandle. Given average high temperatures increasing from 77°F (25°C) to 86°F (30°C) from May to June at the sorghum study location (Dallam County, TX), the

late April planting option appears much more favorable for panicle development realizing these findings. Prasad et al. (2004) and Fokar et al. (2006) indicated high temperatures greater than 97°F (36°C) and 93°F (34°C) during the grain fill stages negatively impact grain sorghum and spring wheat yield, respectively, attributed to decreased seed size and number at maturity. These extreme hot temperatures suppress photosynthesis in sorghum and wheat, and thus the supply of starch and protein for kernel development is limited to stem reserves, which cannot be efficiently distributed to the heads throughout the plant (Fokar et al., 2006). Thus, earlier than average planting dates are preferable for both spring wheat and sorghum so the phases of panicle development through grain filling are less likely to experience temperatures greater than 90-95°F (32-35°C), assuming adequate soil moisture conditions during spring.

Increasing irrigation concurrent to the above heat stress beyond that needed to satisfy moisture demand is ineffective at reducing the yield impacts, and excessive irrigation during periods of hot temperature enhances the likelihood and severity of wheat and sorghum diseases such as *Rhizoctonia* root rot, bacteria leaf blight, and “black chaff”, capable of decimating grain yield even more severely than the heat stress (Ashley et al., 2001). Yet another example of potentially irrigation-encouraged fungus that is especially significant in the Texas Panhandle is sorghum ergot (*Claviceps africana*), a potentially devastating sorghum fungus of occasionally epidemic proportions (Workneh and Rush, 2006). Untimely or excessive irrigation are extremely common mistakes of grain farmers not realizing the negative impacts of surplus soil moisture for moisture resilient crop varieties such as wheat and grain sorghum, especially since much of even modern irrigation of these crops is based on visual

inspection of the stem nodes or panicles (Ashley et al., 2001). Discoloration of grain crop nodes and panicles can be caused by many factors in addition to soil moisture stress, such as Nitrogen deficiency and various plant diseases, so adjusting farming practices such as irrigation based on this visual inspection can be reckless. Hence, irrigated and non-irrigated crop yield impacts from different aspects of locally relevant agroclimate are compared in the present study to assess the relative benefit or detriment of irrigation during different stages of the growing season. These analyses could be used to optimize irrigation strategies, especially when supplementing the earlier predictive GDD and precipitation information.

Fertilizer application is an additional farming technique that could be optimized based on the climate information developed here, since its effectiveness is highly dependent on temperature and timing relative to critical growth phases. Nitrogen-fertilizer has particularly effective applications for wheat and sorghum such as manipulating the tiller growth to match the quality of growing conditions, as well as supplying nutritional needs during critical reproductive phases (Conley et al., 2005). Since soil denitrification rates are proportional to temperature, supplemental fertilizer is likely needed during extended periods of extreme heat, especially during periods of high nutrient demand. Additionally, farmers utilizing crop rotation techniques should be aware of past agroclimate regimes in addition to future, since the vigor of previous crops has a significant impact on soil nitrogen levels during subsequent crops.

c. AAPEX Farm Growing Region Summaries

i. AAPEX Farmer #1, Soybeans, Southern Ontario

The Great Lakes Region is an ideal growing climate for the analysis of climate-related soybean impacts, because of the local complexities in agroclimate that characterize this region, as well as the increased curiosity and anticipation felt as a scientist just prior to exploring the unique climate-sensitivities of a crop located next to one of the largest bodies of water in the world (Lake Huron). The positioning of the soybean study location in the northern third of the large soybean growing area centered over the Midwest is also of particular interest here, since the relative impacts of a slighter cooler growing season climate can be examined. The significance of this study for Canadian agriculture is also enhanced with this study location, especially since southwest Ontario is the predominant growing region contributing to the entire Canadian soybean market. Soybeans are the second leading crop produced in Ontario with around 2.2 million acres (~870,000 hectares) of total dedicated farmland, and new genetically-modified cultivars have recently been developed that have experienced success as far west as the southeastern Canadian Prairies in southern Manitoba (Statistics Canada).

Soybean yield data for St. Clair County in southeastern Michigan (on the border of Michigan and Ontario just south of Lake Huron) was used to represent the AAPEX farming location in Ailsa Craig, Ontario, located only 40 miles to the east of the International Border, since province-level yield data was the most local Canadian crop yield data of sufficient time record. However, given the similar proximities to Lake Huron and latitude within the southern Great Lakes Region, St Clair County is quite

representative of the local agroclimate in southwest Ontario, as will be supported further objectively in the appropriate section below. The growing season average soybean yields of Table 6 show relatively similar field efficiencies for St. Clair County (34.6 bu/acre), Michigan (37.4 bu/acre), and the U.S (38.8 bu/acre), and thus the southern Great Lakes are fairly representative of the U.S. soybean growing region as a whole. The slightly lower field efficiency in St. Clair county compared to the state and national values, however, is likely attributed in part to the local moderation of daytime high temperatures from the lake breeze off the cooler Lake Huron, making this study location particularly desirable for analyses of local agroclimate.

ii. AAPEX Farmer #2, Corn, Southern Minnesota

The corn study location, Blue Earth County, Minnesota, is situated in the heart of the U.S. Corn Belt; a region characterized by flat, fertile farmland but an extreme, highly variable spring and summer climate. The local climate-yield analyses for this location are of particular importance, since the climate division containing this county has one of the largest contributions to U.S. National corn yield with over 100,000 bushels produced annually on average during 1991-2000 (Heim et al., 2003). Annual average Minnesota corn production (950.6M bushels, Table 8) contributes nearly 10% of the national total at over 10 billion bushels annually, with Blue Earth County corn production (26.8M bushels) typically around 3% of the Minnesota total.

Located at nearly 44°N latitude, Blue Earth County is sufficiently north to be affected by storm systems in the prevailing Westerlies even during mid-summer, but can also experience paralyzing drought conditions when stagnant anticyclones park

overhead. These persistent dry periods are not depicted in the relatively ample growing season average precipitation for Blue Earth County (Table 8), nor do the moderate average daily maximum and minimum temperature values show the susceptibility of this location for extreme summer heat. Located in the northeastern Great Plains, this region of the Corn Belt is characterized by extreme weather and climate variability during the growing season, thus detailed knowledge of local agroclimate is of particular value for local farmers such as Patrick Duncanson, whose livelihood hinge on the impacts to crop yields from extreme agroclimate.

iii. AAPEX Farmer #3, Upland Cotton, Southern Texas and North Carolina

The Robeson County, NC and Nueces County, TX are situated in coastal plain regions of their respective states -- eastern North Carolina and extreme southern Texas - - with prime soil conditions and favorable growing climates for cotton to thrive. Coastal plains are typically characterized by fertile sandy loam soils of relatively high available water capacities as well as ample organic content, thus provide ideal growing conditions for the moisture- and nutrient-demanding cotton crops (Slattery et al., 2001). Over two feet of rain falls on average during the cotton growing season in Robeson County, NC, stemming mostly from strong coastal storms that strengthen offshore over the Atlantic Gulf Stream during the spring, and also the air mass thunderstorms during summer that develop almost daily along the sea breeze front with its migration inland across the North Carolina coastal plains each afternoon. Even though the rain from air mass thunderstorms are not of the preferred persistent and gradual variety, the high

water capacity of the sandy loam soils there allow for the cotton crops to take full advantage of these short-duration, heavy rains during summer.

Different from the North Carolina coastal plain, Nueces County, TX receives much of its growing season precipitation during spring (March-May), with highly variable summer soil moisture content dependent on highly sporadic tropical systems that happen to meander westward through the Gulf of Mexico. Therefore, despite the coastal location, late spring into summer is especially prone to drought in extreme southern Texas as persistent hot, dry air from descending flow over the Mexican Plateau hinders the daily thunderstorm development that characterizes other coastal locations of similar latitude, such as southern Florida. As a consequence, the vigor of cotton crops during the period of rapid growth just prior to flowering, as well as the robustness of boll maturation even later in the growing season, are largely dependent on stored soil moisture from late-winter/spring rainfall in Nueces County, TX.

Two of the leading cotton producing states in the U.S. are represented in the local agroclimate analyses for Robeson County, NC and Nueces County, TX, each with substantial differences in their growing climates and soil geology with associated disparities in average cotton yield (Table 8). Texas and North Carolina are consistently in the top six in the U.S. annually in terms of cotton production. In 2003, for example, Texas was the leading cotton producing state and North Carolina was sixth, contributing 24% and 6% to the national total production of 18.25 million bales that year (Womach, 2004). Given the U.S. is the second leading cotton producer in the world, exporting 20% of the world cotton production each year, the growing climates of these regions are

driving factors for not only the national cotton market, but for cotton agribusiness worldwide.

The growing conditions are not uniformly ideal between these two major cotton-producing states, or between the study counties they encompass. Specifically, higher field efficiencies are noted on average for North Carolina (699.2 lbs/ac) compared to Texas (552.1 lbs/ac), and to a lesser extent on the county level for Robeson County, NC (614.4 lbs/ac) and Nueces County, TX (558.3 lbs/ac), attributed largely to the more ample and consistent growing season precipitation of the North Carolina coastal plains. On the county level, Robeson County receives 25.8 inches (April-September) on average, with 16.3 inches (March-August) in Nueces County. Despite similar growing season rainfall totals on average, the slightly lower yield values closer to 600 lbs/acre as compared to the North Carolina and U.S. averages (Table 8), can be attributed to slightly sandier soils in Robeson County as compared to the rest of the Carolina coastal plains. Specifically, Robeson County is uniquely covered by undulating sand hills and ancient coastal dunes with less ideal water retention, rapid runoff during rainfall, and increased tendency for erosion. While the cotton fields are likely maintained with soils closer to loams than the surrounding sand hills, the soil conditions are not quite comparable to the “textbook” sandy loams of farther north on the Coastal Plain, where ideal proportions of organic matter and larger sand particles are found naturally. These differences in the local soil characteristics and climatology between Robeson Co., NC and Nueces Co., TX contribute to the uniqueness of their respective impacts from agroclimate extremes, as quantified below.

iv. AAPEX Farmer #4, Grain Sorghum, Texas Panhandle

The Texas Panhandle study location for grain sorghum (Dallam County, TX; Table 6) is located in the heart of the semiarid growing region for this important cereal grain crop and is perfectly adapted for survival in the extreme temperatures and frequent moisture shortages that characterize the southern High Plains growing season. Sorghum became the leading cereal grain crop in Texas in the 1940s, with much of the production supporting the economically significant cattle industry in the Texas Panhandle (The Handbook of Texas Online).

The spring and early summer weather/climate in Dallam County of the northern Texas Panhandle is one of the most tumultuous growing environments in North America, with radical temperature changes of greater than 20-30°F relatively common during spring on the hourly to weekly time scales, which needless to say has a significant impact on crop growth. Severe thunderstorms, tornadoes, and even late season snowstorms are quite common during spring, followed by extended periods of extreme heat during summer, especially those during La Niña events. The soils across the High Plains are sandy, loamy, deep, and calcareous (porous), thus have limited storage capacity for soil moisture, thus the heavy rains of short duration that fall from thunderstorms have limited benefit for moisture accessible by crops (Rathjen, 1973). The seemingly ideal growing conditions depicted by the growing season average temperatures and precipitation for Dallam County, TX in Table 8 do not reveal such impactful extremes in local agroclimate.

v. AAPEX Farmer #5, Spring Wheat, Central Montana

Similarly, the relatively cool average growing season-aggregate temperatures of Liberty County, Montana (Table 8) fail to show the extreme summer heat, which can also build across the northern High Plains during spring wheat flowering, and can cripple late-maturing crops. The growing climate for Red Spring Wheat, over central/eastern Montana, and Dakotas is also semiarid, with the study location in Liberty County, MT receiving the least amount of growing season average precipitation (7.1 inches, Table 8) of all local agroclimates investigated here. Spring wheat crops thrive in the semiarid northern High Plains, despite the limited growing season precipitation; hence central Montana is called the “Golden Triangle”, renowned for its ability to produce high quality grains that have remarkably high protein content (www.MatsonFarms.com). The semiarid growing climates for spring wheat and grain sorghum, as well as the sensitivity of midsummer flowering to extreme heat for both crops, contribute largely to the heightened impacts from extreme agroclimate during summer (Chapter 6e).